Greenhouse gas emission rate estimates from airborne remote sensing in the short-wave infrared

Thomas Krings

Universität Bremen 2012

Greenhouse gas emission rate estimates from airborne remote sensing in the short-wave infrared

Vom Fachbereich für Physik und Elektrotechnik
der Universität Bremen

zur Erlangung des akademischen Grades eines

Doktor der Naturwissenschaften (Dr. rer. nat.)

genehmigte Dissertation

von

Dipl. Geophys. Thomas Krings

aus Schierwaldenrath

1. Gutachter:	Prof. Dr. J. P. Burrows
2. Gutachter:	Prof. Dr. J. Notholt
Eingereicht am:	09.10.2012
Tag des Promotionskolloquiums:	30.01.2013

Abstract

The quantification of emissions of the greenhouse gases carbon dioxide (CO_2) and methane (CH_4) is essential for attributing the roles of anthropogenic activity and natural phenomena in global climate change. The current measurement systems and networks, whilst having improved during the last decades, are deficient in many respects. For example, the emissions from localised and point sources such as fossil fuel exploration sites are not readily assessed. A tool developed to better understand point sources of CO_2 and CH_4 is the optical remote sensing instrument MAMAP, operated from aircraft. With a ground scene size of the order of 50 m and a relative accuracy of the column-averaged dry air mole fractions of about 0.3 % for XCO_2 and less than 0.4 % for XCH_4, MAMAP can make a significant contribution in this respect.

Detailed sensitivity studies showed that the modified WFM-DOAS retrieval algorithm used for MAMAP has an approximate accuracy of about 0.24 % for XCH_4 and XCO_2 in typical atmospheric conditions. At the example of CO_2 plumes from two different power plants and CH_4 plumes from coal mine ventilation shafts, two inversion approaches to obtain emission rates were developed and tested. One is based on an optimal estimation scheme to fit Gaussian plume models from multiple sources to the data and the other is based on a simple Gaussian integral method.

Compared to CO_2 emission estimates as reported by the power plants' operator within the framework of emission databases (24 and 13 Mt CO_2 yr^{-1}), the results of the individual inversion techniques were within ±10 % with uncertainties of ±20–30 % mainly due to insufficient wind information and non-stationary atmospheric conditions. Measurements at the coal mine included on-site wind observations by an aircraft turbulence probe that could be utilised to calibrate the wind model. In this case, the inversion results have a bias of less than 1 % compared to the reported CH_4 emissions (50 kt CO_2 yr^{-1}) with an uncertainty of approximately ±13.5 %. In cases where no elevated CO_2 or CH_4 is observed, MAMAP data are useful to provide upper limit constraints as was shown for a marine gas seep.

The inversion techniques developed in this work have the potential to provide the basis for quantification and independent validation of anthropogenic and natural point source emission rates. These concepts are not restricted to airborne applications and are of particular value also for future satellite remote sensing missions.

Publications

Articles in peer-reviewed journals

Krings, T., Gerilowski, K., Buchwitz, M., Reuter, M., Tretner, A., Erzinger, J., Heinze, D., Burrows, J. P., and Bovensmann, H.: MAMAP – a new spectrometer system for column-averaged methane and carbon dioxide observations from aircraft: retrieval algorithm and first inversions for point source emission rates, Atmos. Meas. Tech., 4, 1735–1758, doi:10.5194/amt-4-1735-2011, 2011.

Gerilowski, K., Tretner, A., Krings, T., Buchwitz, M., Bertagnolio, P. P., Belemezov, F., Erzinger, J., Burrows, J. P., and Bovensmann, H.: MAMAP – a new spectrometer system for column-averaged methane and carbon dioxide observations from aircraft: Instrument description and performance analysis, Atmos. Meas. Tech., 4, 215–243, doi:10.5194/amt-4-215-2011, 2011.

Bovensmann, H., Buchwitz, M., Burrows, J. P., Reuter, M., Krings, T., Gerilowski, K., Schneising, O., Heymann, J., Tretner, A., and Erzinger, J.: A remote sensing technique for global monitoring of power plant CO_2 emissions from space and related applications, Atmos. Meas. Tech., 3, 781–811, doi:10.5194/amt-3-781-2010, 2010.

Velazco, V. A., Buchwitz, M., Bovensmann, H., Reuter, M., Schneising, O., Heymann, J., Krings, T., Gerilowski, K., and Burrows, J. P.: Towards space based verification of CO_2 emissions from strong localized sources: fossil fuel power plant emissions as seen by a CarbonSat constellation, Atmos. Meas. Tech., 4, 2809–2822, doi:10.5194/amt-4-2809-2011, 2011.

Hoffmann, A., Clifford, D., Aulinas, J., Carton, J. G., Deconinck, F., Esen, B., Hüsing, J, Kern, K., Kox, S., Krejci, D., Krings, T., Lohrey, S., Romano, P., Topham, R., Weitnauer, C.: A Novel Satellite Mission Concept for Upper Air Water Vapour, Aerosol and Cloud Observations Using Integrated Path Differential Absorption LiDAR Limb Sounding, Remote Sens., 4(4), 867–910, doi:10.3390/rs4040867, 2012.

Under review

Krings, T., Gerilowski, K., Buchwitz, M., Hartmann, J., Sachs, T., Erzinger, J., Burrows, J. P., and Bovensmann, H.: Quantification of methane emission rates from coal mine ventilation shafts using airborne remote sensing data, Atmos. Meas. Tech. Discuss., 5, 7383-7429, doi:10.5194/amtd-5-7383-2012, 2012. (Under review for Atmos. Meas. Tech.)

Technical Reports

Gerilowski, K., Krings, T., Bovensmann, H.: Qualitative methane flux upper limit constraints from airborne remote sensing data acquired over the 22/4B emission site, Final Report, IFE-FR-KGTKHB-24052012-BO_EXXON_R2.0, University of Bremen, 26 pp., 2012.

Conference Contributions

Krings, T., Gerilowski, K., Buchwitz, M., Bovensmann, H., Burrows, J. P., Tretner, A., Sachs, T., Erzinger, J.: Airborne demonstration of carbon dioxide (CO_2) point source emission rate estimations from MAMAP remote sensing data, 7th International Workshop on Greenhouse Gas Measurements from Space (IWGGMS-7), 16–18 May 2011, University of Edinburgh, Edinburgh, UK, 2011.

Krings, T., Gerilowski, K., Buchwitz, M., Bovensmann, H., Burrows, J. P., Tretner, A., Sachs, T., Erzinger, J.: Carbon dioxide (CO_2) emission rate estimates for coal fired power plants and analysis from MAMAP airborne instrument data, European Geoscience Union General Assembly, 03–08 April 2011, Vienna, Austria, 2011.

Krings, T., Gerilowski, K., Buchwitz, M., Bovensmann, H., Burrows, J.P., Tretner, A., Sachs, T., and Erzinger, J.: Passive airborne remote sensing and plume model inversion of CO_2 from coal fired power plants measured by the MAMAP/CarbonMapper instrument, DPG Spring Meeting of the Section AMOP and the Divisions Environmental Physics and Physics Education, 08–12 March 2010, Hannover, Germany, 2010.

Krings, T., Buchwitz, M., Gerilowski, K., Bovensmann, H., Burrows, J.P., Tretner, A., Sachs, T., and Erzinger, J.: Passive airborne remote sensing and plume model inversion of CO_2 from coal fired power plants measured by the MAMAP instrument, European Geoscience Union General Assembly, 02–07 May 2010, Vienna, Austria, 2010.

Contents

Introduction

With the improvement of the steam engine by James Watt at the dawn of the industrial revolution in 1765 by adding a separate condensing chamber, the foundation was laid for a progressing admission of machines into manufacturing and transport. By utilising fossil fuels, production processes in factories and mines as well as associated transport of goods became more independent of human and horse power. Since then, electricity was harnessed and countless other machines and technical devices were invented, modified and improved with respect to their efficiency making their way into everyday life. While the industrial revolution with its enormous socio-economic impact is considered to be over after about 1850, the industrialisation of the globe, particularly in developing countries, is still progressing with an increasing demand of energy which, to a large extend, is still satisfied by combustion of fossil fuels. In 2009, about 81 % of the global primary energy supply was based on oil, coal and natural gas (International Energy Agency, 2011).

As a consequence, the greenhouse gas carbon dioxide (CO_2), that is released as a combustion product, is constantly accumulating in the atmosphere. Since pre-industrial times, CO_2 concentrations have increased by about 40 % and have been identified as the main man-made contributor to global climate change (Forster et al., 2007). The enhanced fossil fuel mining as well as increased agriculture to feed the world population give rise to increased methane emissions. Methane (CH_4) is a greenhouse gas that is about 25 times more effective than CO_2 on a 100-year time horizon and has increased by about 150 % relative to pre-industrial levels (Forster et al., 2007). Combined, the two compounds are the most important anthropogenic greenhouse gases. The enhanced greenhouse effect results in a net global warming that has various implications for the earth system like sea ice and ice sheet retreat in the polar regions and sea level rise, for example, due to thermal expansion and melt water. More frequent flooding at the coasts and inland droughts may be the consequence. Complex positive and negative feedback mechanisms interact with the rate of global warming and are often not completely understood in their magnitude. For example, beside the anthropogenic sources, CH_4 is also naturally released in large quantities due to microbial activity in wetlands that may spatially increase when the climate is changing (Denman et al., 2007).

Accurate quantification and attribution of CO_2 and CH_4 sources and sinks is therefore essential to be able to assess the impact of these greenhouse gases on the earth system. Model simulations need detailed input to produce reliable projections for the future climate like they are periodically published and refined for the reports of the Intergovernmental Panel of Climate Change (IPCC) based on measurements.

Global warming predictions and observations have not only drawn scientific but increasingly also political and public interest. The Kyoto protocol negotiated in 1997 is likely the most prominent outcome of global political discussions to mitigate climate change. By ratifying the protocol, member states committed to reduce greenhouse gas

emissions by a total of at least 5 % below 1990 levels in the period from 2008–2012. Emissions trading schemes (ETS) – usually implemented to facilitate fulfilment of the Kyoto commitments such as the European ETS – aim at creating economic incentives to reduce greenhouse gas emissions. This requires accurate and objective measurement techniques for greenhouse gas emissions needed for the implementation of independent validation techniques. While the Kyoto commitment is likely to be reached, global greenhouse gas emissions are still rising, amongst others because China and the USA did not participate, although having the largest CO_2 output.

Estimates for emissions or uptake are generally obtained using the top-down or the bottom-up approach. The bottom-up approach facilitates national inventories and statistical data (for example, fuel consumption, surface type, etc.) in conjunction with emission factors or microscale information with subsequent upscaling. However, bottom-up emissions can differ by a factor of two compared to the observed accumulation in the atmosphere and, for example, in the case of industrial greenhouse gases tend to underestimate actual emissions (Nisbet and Weiss, 2010, and references therein).

Top-down estimates on the other hand rely on a network of atmospheric measurements such as ground based or airborne in-situ measurements and remote sensing observations from satellites or aircraft. To operate models that can invert these measurements for accurate emission estimates, high temporal and spatial resolution is key (Bergamaschi et al., 2005; Bréon and Ciais, 2010). While a dense and uniform coverage of the globe is not likely to be reached with in-situ measurements, in particular over the ocean, satellite measurements can remedy this issue by providing global coverage on appropriate time scales. For satellite remote sensing of greenhouse gases, active and passive measurement concepts in the short-wave and thermal infrared exist with different advantages.

Passive satellite instruments that rely on thermal infrared emissions such as the Fourier transform spectrometers TES (Worden et al., 2012) and IASI (Crevoisier et al., 2009) as well as the grating spectrometer AIRS (Strow et al., 2006; Xiong et al., 2010) and the multispectral sounder HIRS/TOVS (Chédin et al., 2003) have the advantage that they can measure day and night and can potentially give height resolved profiles. However, due to the lack of temperature contrast, they only have very limited sensitivity at near surface layers where the regional and local source and sink signals are largest (Crevoisier et al., 2003; Bréon and Ciais, 2010). In contrast to thermal infrared observations, instruments relying on solar backscatter in the short-wave infrared to measure CO_2 and CH_4 such as SCIAMACHY onboard ENVISAT (2003–2012) (Buchwitz et al., 2005a; Schneising et al., 2011; Reuter et al., 2011) and TANSO onboard GOSAT (Morino et al., 2011) exhibit relatively even sensitivity throughout the atmosphere down to the surface but require sunlight.

Although CH_4 data from SCIAMACHY have already been successfully used for inverse modelling (Bergamaschi et al., 2007, 2009), the resolution of 60 km × 30 km (1000 km swath) was too coarse to resolve localised sources like power plants or landfills that account for about 50 % of total CO_2 emissions and 40 % of total CH_4 emissions (EC-JRC/PBL, EDGAR version 4.2. http://edgar.jrc.ec.europa.eu/, 2011; Wuebbles and Hayhoe, 2002). GOSAT with a ground scene diameter of 10 km, but with a gap of about 160–320 km in between in nominal mode, is not suitable for evaluation of point sources either.

Future satellite missions with increased resolution such as OCO-2 (to be launched in 2014 earliest) with a ground scene of $< 3\,\mathrm{km}^2$ (10 km swath) (Crisp et al., 2009) and

to a limited extent the TROPOMI instrument onboard the Sentinel 5 Precursor satellite mission (to be launched in 2015) with a ground scene of 7 km × 7 km will help to partly overcome this problem for CO_2 and CH_4, respectively. The French-German future active LIDAR CH_4 satellite mission MERLIN (to be launched in 2016) with a ground scene of about 50 km × 125 m (Kiemle et al., 2011), on the other hand, is not ideal for "hot spot" measurements.

The observational gap for point sources is also not filled by available airborne remote sensing instruments. Airborne active systems designed for pipeline leakage detection (Meyer et al., 2006; Zimig and Ulbricht, 2006; Ershov, 2007) are typically limited to 300 m altitude and hence cannot cover the complete planetary boundary layer where most of the mixing takes place and which has a thickness of 100–3000 m (Stull, 1988). High altitude DIAL (differential absorption LIDAR) systems are under development (see, for example, Sakaizawa et al., 2012; NRC, 2010) but have not yet been tested for localised sources. Results from passive airborne Fourier transform spectrometers such as the TSUKUBA instrument for GOSAT validation and calibration (Suto et al., 2008) or NASA's instrument for CARVE (Carbon in Arctic Reservoirs Vulnerability Experiment, http://science.nasa.gov/missions/carve/, retrieved: March, 2012) have not been published yet. Recently, a band ratio approach was used to map CH_4 plumes with the hyperspectral airborne imager AVIRIS in solar glint geometry over the ocean (Bradley et al., 2011) but column concentrations were not quantitatively retrieved.

The lack of suitable quantification instruments and methods for localised sources was also stressed by Babilotte et al. (2010) who compared five different state-of-the-art measurement techniques (in-situ and remote sensing) to quantify the local CH_4 emissions of a particular landfill in France. Resulting emission estimates differed by an order of magnitude and Babilotte et al. (2010) conclude that further research on each method is necessary to provide reliable results for emission rates. Similar results were obtained by Börjesson et al. (2000) who found that CH_4 emission estimates for a Swedish landfill differ by a factor of 4 between tracer gas techniques and closed chamber measurements. Using the example of Canadian natural gas processing plants and a refinery, Chambers and Strosher (2006a,b) showed that emission estimates may be 4–9 times higher when computed using DIAL instruments compared to calculations from emission factors.

Uncertainties in greenhouse gas emission estimates from localised sources become of particular relevance in the context of carbon emissions trading. In the European Union (EU), the greenhouse gas emission allowance trading scheme (European Commission, 2007) gives mandatory guidelines on how greenhouse gas emissions have to be reported. For strong emitters as a result of combustion ($> 500\,\mathrm{kt\,CO_2\,yr^{-1}}$) like, for example, power plants, the uncertainty in fuel consumption, which serves as input data for greenhouse gas calculations, is allowed to be 1.5 % at maximum. An additional error is caused by the uncertainty of the emission and oxidation factors. However, Evans et al. (2009) noticed that the uncertainties of the EU ETS are not referring to the accuracy ("closeness to truth") but to the precision ("repeatability of the data"). Furthermore, Evans et al. (2009) observed at different coal-fired power plants a negative bias of emissions calculated from emission factors compared to emissions derived from continuous emissions monitoring systems (CEMS) of 15 % and more. Ackerman and Sundquist (2008) found that emission estimates for individual US power plants differ by about 20 % and recommend different independent approaches to more reliably quantify emissions.

A remote sensing instrument that can retrieve precise column information with a ground scene size of the order of the source heterogeneity, and is able to measure on a regional scale at an ample speed can add significant knowledge to our understanding of surface fluxes of the two most important anthropogenic greenhouse gases. On that account the MAMAP instrument was built to improve the quantification and understanding of current CO_2 and CH_4 sources and to provide the opportunity of a monitoring system for local source regions, which are vulnerable and influenced by global warming. Bertagnolio (2008) gave a first overview of the technical setup of MAMAP and data pre-processing steps. The retrieval algorithm developed by M. Buchwitz and applied there to allow a first evaluation of data quality was the starting point for this work. Beside that, a completely separate approach to MAMAP data analysis than by Bertagnolio (2008) is undertaken.

The aim of this work is to establish an improved retrieval based on a pre-existing, preliminary algorithm version to obtain accurate CO_2 and CH_4 information and to allow for a detailed instrument specification and performance assessment. This comprises also the possible range of application within the framework of existing measurement capabilities. The second focus is the development of data analysis methodologies to obtain emission rate estimates for greenhouse gas point sources using MAMAP data including an in-depth evaluation of capabilities and possible limitations. Experience gained with the MAMAP instrument and data have direct implications for potential future satellite missions such as CarbonSat (Bovensmann et al., 2010) for which MAMAP can serve as a proof of concept.

Outline

This thesis is divided into four parts.

Part I presents background information necessary to understand the importance of the atmospheric greenhouse gases CO_2 and CH_4 for the greenhouse effect and associated climate change. The relevance within a more political context is shortly discussed. Furthermore, the basic concepts of remote sensing are given.

Part II introduces the MAMAP instrument and gives a short overview of the technical specifications. The retrieval algorithm to obtain total column information on CO_2 and CH_4, as it was developed for this work, is explained in detail including an in-depth sensitivity study with respect to various atmospheric parameters. This part concludes with the possible range of application where MAMAP can make a significant contribution to current knowledge.

Part III describes the development and application of two approaches inverting for emission rates from point sources using MAMAP total column measurements. At the example of two coal fired power plants emitting CO_2 and coal mine ventilation shafts emitting CH_4, the inversion techniques are tested and validated against data reported within the framework of greenhouse gas emission databases. The application of MAMAP data to obtain upper limit constraints on emission rates using simulations is demonstrated for a marine CH_4 seep. Results and major conclusions will be summarised at the end including implications for future research.

In Part IV supplementary material and additional background information is given.

Part I

Fundamentals

1

Earth's atmosphere

The planet Earth is a complex system which may be divided into five domains: geosphere, hydrosphere, cryosphere, biosphere and atmosphere (Figure 1.1). The geosphere (sometimes also referred to as lithosphere) comprises the densest part of the planet consisting on the exterior of continental and oceanic crust and on the interior of the highly viscous mantle, the liquid outer core and the solid inner core. The hydrosphere refers to the liquid water part of the Earth such as subaerial oceans, lakes or rivers, but also to subsurface water reservoirs. The extent of frozen water masses is often separately considered in the cryosphere, for example, including the large ice sheets on Greenland and Antarctica as well as mountain glaciers. All forms of life combined form the biosphere. And finally – most important for the present work – the gases surrounding the Earth constitute the atmosphere.

The domains are not enclosed systems, but they are interconnected by different interaction and feedback mechanisms. In particular, all of them directly or indirectly influence the atmosphere where the so-called greenhouse effect takes place. The natural greenhouse effect is crucial for life on Earth as we know it. On the other hand, it is also the greenhouse effect which is responsible for a global climate change that is observed and predicted to continue in the future. The impact is not limited to the atmosphere. It influences more or less all other parts of the Earth system, where often the exact mechanisms and consequences are not well understood – both quantitatively and qualitatively (IPCC, 2007).

This chapter focuses on the fundamentals that are necessary to understand the importance of the atmospheric greenhouse gases carbon dioxide and methane for the greenhouse effect and climate change.

Figure 1.1: The Earth system comprising croysphere, biosphere, geosphere, hydrosphere and the atmosphere where the important greenhouse effect takes place. (Figure courtesy of ESA).

1.1 Composition and vertical structure

The Earth's atmosphere surrounding the planetary surface is formed by gases that are retained by means of gravitation (see Table 1.1). Up to about 80 km, the dry atmosphere, that is, water vapour free atmosphere, mainly consists of a homogeneous mixture of molecular nitrogen (N_2, 78.09 % by volume), molecular oxygen (O_2, 20.95 %) and trace amounts of other gases of which argon (Ar, 0.93 %) is the most abundant (Roedel and Wagner, 2011). The remaining 0.03 % are formed by other so called trace gases such as the greenhouse gases carbon dioxide (CO_2) with an average mole fraction of currently[1] 394 ppm (parts per million[2]) and methane (CH_4) with 1774 ppb (parts per billion[3]) (Forster et al., 2007). Despite their rather low abundances, CO_2 and CH_4 are of great importance for atmospheric processes, in particular, for the natural and anthropogenic greenhouse effect and associated climate change. The concentration of water vapour, which is also an important natural greenhouse gas, varies by several orders of magnitude on a spatial and temporal scale and is generally not included in the permanent species of the atmosphere. The mixture of gases in the atmosphere is referred to as *air*. In addition to gaseous compounds, the atmosphere also contains aerosols (suspensions of liquid droplets or solid particles in the air) of which clouds, that mostly consist of liquid water drops or frozen ice crystals, are a special case.

As a consequence of the weight of the air in the Earth's gravitational field, each layer of air imposes a pressure on the layers beneath. The average atmospheric pressure at sea level ($h_0 = 0$ m) is $p_0 \approx 1013$ hPa. Assuming an atmosphere at constant temperature T_0, the barometric formula gives the exponential decrease of pressure p with altitude h (compare also Figure 1.2):

$$p(h) = p_0 \cdot \exp\left(-\frac{h}{h_s}\right) \tag{1.1}$$

where $h_s = \frac{RT_0}{Mg} \approx 8.4$ km is the scale height with the universal gas constant $R = 8.315\,\mathrm{J\,K^{-1}\,mol^{-1}}$, molar mass of air M (see Table 1.1), temperature T_0 =288 K and gravitational acceleration $g = 9.81\,\mathrm{m\,s^{-2}}$.

According to the temperature variation, the atmosphere is divided into several vertical layers (see Figure 1.2). The lowermost layer, the troposphere, reaches from the surface to about 9 km at the poles and about 18 km in the tropics, respectively. The troposphere is defined by a decreasing temperature with height, where the surface temperature is about 14 °C (Jones et al., 1999) and the lapse rate about -7 $\mathrm{K\,km^{-1}}$ on average (Wallace and Hobbs, 1977). This thermal layering is mainly caused by heating from the ground with subsequent rise of air and cooling during expansion in the decreasing pressure, with additional radiative cooling in the mid and upper troposphere due to water vapour. As a result, this convection leads to a well mixed troposphere and, in conjunction with high abundances of water vapour, gives rise to the weather phenomena.

Transport and mixing through the tropopause, a zone with rather constant temperature and which separates the troposphere from the stratosphere above, is usually inhibited.

[1] August 2012, corrected for average seasonal cycle, Dr. Pieter Tans, NOAA/ESRL (http://www.esrl.noaa.gov/gmd/ccgg/trends/) and Dr. Ralph Keeling, Scripps Institution of Oceanography (http://scrippsco2.ucsd.edu/) (see also Keeling et al., 1976; Thoning et al., 1989).

[2] 1 ppm=1 $\mu\mathrm{mol\,mol^{-1}}$

[3] 1 ppb=1 $\mathrm{nmol\,mol^{-1}}$

Table 1.1: A selection of important constituents of the atmosphere and their abundances compiled from Roedel and Wagner (2011); Forster et al. (2007) and Tans and Keeling, 2012 (see text). (*Note that the abundances for carbon dioxide and methane are given in mole fractions which slightly differ from volume mixing ratios. If CO_2 and CH_4 behaved like ideal gases, volume mixing ratios and mole fractions would be equal.)

Constituent	Symbol	Abundance (by volume)	Molar mass [g/mol]
Nitrogen	N_2	78.09 %	28.02
Oxygen	O_2	20.95 %	32.00
Argon	Ar	0.93 %	39.94
Carbon dioxide	CO_2	394 ppm*	44.01
Methane	CH_4	1774 ppb*	16.04
Water vapour (global average)	H_2O	0.4 %	18.02
Dry air			28.97

The reason is the increasing temperature in the stratosphere that leads to a very stable layering. Exceptions are, for example, transport through the tropical tropopause layer (TTL) (Tzella and Legras, 2011, and references therein) or – particularly important for aerosol transport – strong volcanic eruptions like Mt. Pinatubo in 1991. Overshooting events in intense storm systems do occur but are accepted to be no major contributor to transport through the tropopause (only 0.5 % or less of total convective events (Gettelman et al., 2002; Liu and Zipser, 2005; Fu et al., 2007)).

The stratosphere is chemically characterised by low water vapour and high ozone (O_3) content. The increasing temperature is built up by cooling from the upper troposphere and heating from absorption of radiation from the sun in the range of 200–310 nm mainly by ozone which has a maximum concentration in the region of the ozone layer (see Figure 1.2) protecting the Earth from the ultraviolet (UV) radiation.

The temperature reaches a maximum at the stratopause, located at about 50 km altitude, and then decreases in the mesosphere to its absolute minimum in the mesopause at about 85 km. In the thermosphere above, the temperature rapidly increases again. From about 500 km upwards is the Exosphere where the atmosphere is so thin that it is technically already part of space.

1.2 Stability conditions in the lower troposphere

The actual temperature profile in the troposphere may vary significantly from the average presented in Section 1.1 with large consequences for the atmospheric stability. Since the stability determines the ability of air to mix, the atmospheric stability plays an important role in dispersion of gaseous or particulate constituents.

The lowest part of the troposphere is also called the planetary boundary layer or

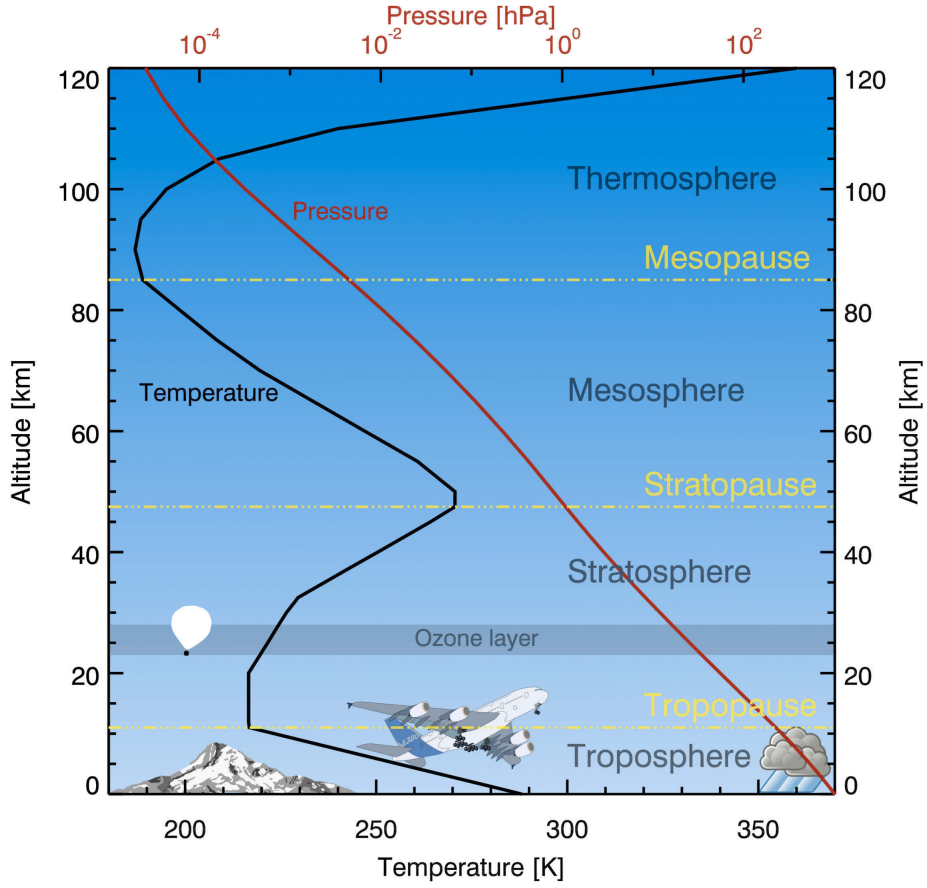

Figure 1.2: Vertical structure of the atmosphere including mean temperature (black) and pressure (red) as a function of altitude according to the 1976 U.S. Standard Atmosphere (U.S. Committee on Extension to the Standard Atmosphere, 1976).

mixed layer (as opposed to the free troposphere above). It exhibits a thickness of about 100–3000 m and is defined by its response to surface forcings on timescales of an hour or less (Stull, 1988). Generally, the boundary layer is subject to more turbulence than the free troposphere from which it is separated by a stable layer (Stull, 1988; Foken, 2006). This has direct impact on tracer concentrations with surface sources such as the greenhouse gas methane. Nocturnal and winter boundary layers are generally thinner than at day time or in summer, respectively. Assuming accumulation within the boundary layer but no instantaneous mixing with the free troposphere, total tracer amounts can only be inferred with knowledge of the boundary layer height (compare, for example, Lloyd et al., 2001).

Assuming dry air, the atmosphere is considered *stable* if the actual air temperature is decreasing slower with height compared to the adiabatic lapse rate (see Figure 1.3, Panel A). An air parcel that rises, for example, due to turbulences consequently cools adiabatically. It then becomes cooler and therefore denser than the surrounding air and sinks back. *Adiabatically* means that there is no heat transfer from or to the respective air parcel which is usually a good approximation. Accordingly, sinking air stays warmer

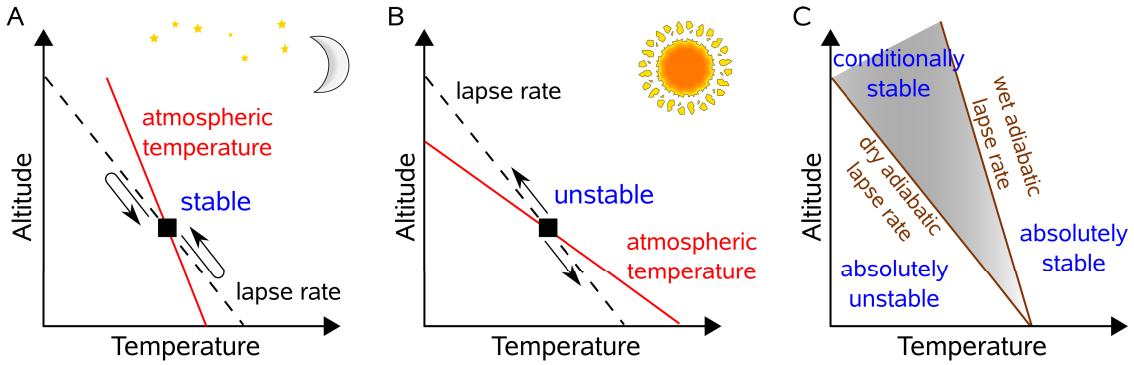

Figure 1.3: Sketch of atmospheric stability. Generally during night time (Panel A), the air is cooled from the ground and the temperature profile is steeper than the lapse rate leading to stable conditions. During day time (Panel B), solar insolation heats the ground which warms the atmosphere from below. The temperature profile is then often less steep than the lapse rate which gives unstable conditions. In practice, the concept of atmospheric stability is more complex and also depends on the water vapour content which can, for example, release latent heat during condensation. Hence, there are two different lapse rates, the dry adiabatic and the wet adiabatic, with a conditionally stable region in between (Panel C), depending on water vapour content.

than the surrounding air and subsequently rises back up. An extreme case of a stable atmospheric layering is given during inversion conditions where temperature is increasing with height. This frequently occurs, for example, for relatively warm air above cool water surfaces or over land during night time in the absence of clouds when the strong radiative cooling of the surface leads to lower air temperatures close to the surface than aloft. Persistent stable conditions, for example, around cities, can lead to smog events where airborne pollutants cannot disperse but keep building up.

If the air temperature is decreasing faster with height than the adiabatic lapse rate, conditions are *unstable* (see Figure 1.3, Panel B). A rising air parcel cools less than the surrounding air and is therefore less dense which keeps it rising. On the other hand, a sinking air parcel will keep on sinking. Unstable conditions can usually be observed during daytime when solar radiation heats the ground and subsequently heats the atmosphere from below giving rise to convection processes.

If air temperature profile and lapse rate are similar, conditions are called *neutral*. Air parcels keep on sinking or rising until the external force, which may be induced, for example, by orography, ceases.

However, in practice, the concept of stability is more complex since the presence of water vapour can lead to latent heat release due to condensing water vapour, whereas altered thermodynamic properties of moist air only play a minor role[4]. Therefore, it has to be distinguished between the dry and the wet adiabatic lapse rate. The latter has to be applied when the air parcel becomes saturated with respect to water vapour and condensation occurs. The dry adiabatic lapse rate is about -10 $\mathrm{K\,km^{-1}}$ while the wet adiabatic is about -5 $\mathrm{K\,km^{-1}}$ between 0 °C and 10 °C (Roedel and Wagner, 2011). Air parcels exhibiting a temperature profile between the wet and dry adiabatic are called *conditionally stable* (see

[4]For example, a typical deviation from the adiabatic lapse rate due to presence of water vapour and the corresponding change in the specific heat is of the order of only 0.86 % (Roedel and Wagner, 2011).

Figure 1.3, Panel C) since their actual stability additionally depends on the water vapour saturation.

1.3 Climate and climate change

The expression *climate* is generally understood as the "average weather" (IPCC, 2007) over time scales of typically at least 30 years, where weather defines a current state of the atmosphere. This definition of climate is somewhat diffuse since it depends on the period of time under consideration as well as the extent of the areas comprised for a certain climatic zone. Associated with the climate is also the natural variability in the parameters that define the state of the atmosphere such as temperature, humidity, precipitation, wind and cloud cover. Only when the natural variability is exceeded and the average conditions change over longer time periods, the premises for a *climate change* are given.

Temperature is often acknowledged as one of the most concise single parameters describing the climate. On Earth, the temperature at the surface is primarily determined by the radiative balance between incoming solar energy on the one hand and the energy reflected or radiated back to space on the other hand[5]. The average incoming solar energy per unit time and area at the top of atmosphere of the Earth is described by the solar constant $I_0 \approx 1368\,\mathrm{W\,m^{-2}}$, which is $I \approx 342\,\mathrm{W\,m^{-2}}$ averaged over the Earth's surface, where the variation due to the Earth's elliptical orbit is about $\pm 3.4\,\%$ (Roedel and Wagner, 2011).

Using the Stefan-Boltzmann law for a black body with emissivity $\epsilon = 1$ to compute the amount of energy E_{out} radiated by the Earth per unit area and assuming an average planetary albedo (reflectivity) of $\alpha = 30\,\%$, the energy balance is determined by:

$$E_{\mathrm{in}} = E_{\mathrm{out}} \tag{1.2}$$

$$\Rightarrow (1-\alpha)\cdot I = \epsilon\sigma_{\mathrm{SB}} T^4 \tag{1.3}$$

where E_{in} is the incoming solar energy per unit area and $\sigma_{\mathrm{SB}} = 5.670\,\mathrm{W\,m^{-2}\,K^{-4}}$ the Stefan-Boltzmann constant. This would lead to an average surface temperature of about $T \approx -19\,^{\circ}\mathrm{C}$. However, the actual observed surface temperature is about $+14\,^{\circ}\mathrm{C}$ (Jones et al., 1999). The reason is the natural greenhouse effect that accounts for about $+33\,\mathrm{K}$. In the absence of clouds, it is mainly caused by water vapour and carbon dioxide (see Section 1.4). This natural greenhouse effect is essential for life on Earth in its wide diversity of species.

An increase of the global mean temperature has a large and complex impact on the climate system. The most direct possible impact probably being more frequent droughts, severe precipitation events and flooding. Although it is accepted that a global warming leads to sea level rise due to thermal expansion as well as melting of glaciers and inland ice sheets, the exact mechanisms of heat transfer to the ocean are not completely understood. A recent, unexpected decline in ocean warming and sea level rise, for instance, appears to be connected to El Niño Southern Oscillation events during the last years (Katsman and van Oldenborgh, 2011). However, it is expected that the sea level rise will resume in the near future.

[5] Neglecting, for example, the surface heat flux of geothermal energy amounting to comparably low $0.09\,\mathrm{W\,m^{-2}}$ (Davies and Davies, 2010).

Direct fresh water input into the ocean from inland ice is not in a simple relationship to surface temperature either. While rising temperatures lead to higher melting rates, they also tend to cause higher precipitation rates, for example, in the interior of Antarctica, that can lead to more accumulation of ice and snow. On the other hand, this may be offset by enhanced ice flow velocities (Rignot et al., 2008) and destabilising ice sheets when their ice shelves break away as did, for example, the Larsen A and B ice shelves at the east coast of the Antarctic Peninsula. It is generally assumed that the west Antarctic ice sheet is more vulnerable to global warming, whereas the larger east Antarctic ice sheet is assumed to remain rather stable (Joughin and Alley, 2011). Complete melting of the west Antarctic ice sheet would correspond to a sea level rise of 4–6 m (Oppenheimer, 1998). Melting of the Greenland ice corresponds to a sea level rise of about 7 m, and the east Antarctic ice sheet has potential to rise the sea level by more than 50 m (Lemke et al., 2007).

A warming ocean is potentially feeding more intense hurricanes while enhanced westerly winds and wind shear may lead to a reduced number of tropical storms (Elsner et al., 2012; Trenberth et al., 2007) but with potentially different landfall patterns compared to the past.

Although global warming and climate change itself is evident in measurements (see Figure 1.4 and Santer et al., 2011), the understanding of the complex mechanisms of the consequences and their interplay is far from complete. In particular, also feedback effects cause a high degree of uncertainty as, for example, the positive ice-albedo feedback where melting ice reduces the planetary albedo leading to warming and enhanced melting. An example for a possible negative feedback is the cloud-albedo feedback which indicates that an increased formation of clouds in a warmer and moister climate may lead to a higher albedo and hence subsequent cooling. Other positive feedback mechanisms may arise from thawing permafrost and melting methane hydrates in the ocean, both leading to a potentially increased release of the greenhouse gas methane to the atmosphere (Denman et al., 2007). Up to now, however, there is no evidence that a state of sustained, enhanced CH_4 emissions from methane hydrates and melting permafrost has been reached (Dlugokencky et al., 2009).

That makes projections for future climate very challenging and especially the drivers of climate change must be identified and quantified in detail to reliably predict and potentially be able to mitigate climate change effects.

1.4 Greenhouse effect and other climate drivers

As already mentioned in Section 1.3, the greenhouse effect is responsible for a surface temperature that is about 33 K warmer compared to an atmosphere that would contain no greenhouse gases at all. It was first quantitatively described by Arrhenius (1896) who also discovered the great importance of carbon dioxide, although his work was not motivated by future climate change, but by an explanation for the ice ages. In a later work, Arrhenius (1906) estimated an increase of temperature of about 2.1 °C for a doubling of CO_2 in the atmosphere which is close to the estimate of more recent studies of 2.0–4.5 °C (Hegerl et al., 2007).

Greenhouse gases are generally understood as gases that absorb in the infrared but are more or less transparent for short-wave radiation from the sun which has a maximum at

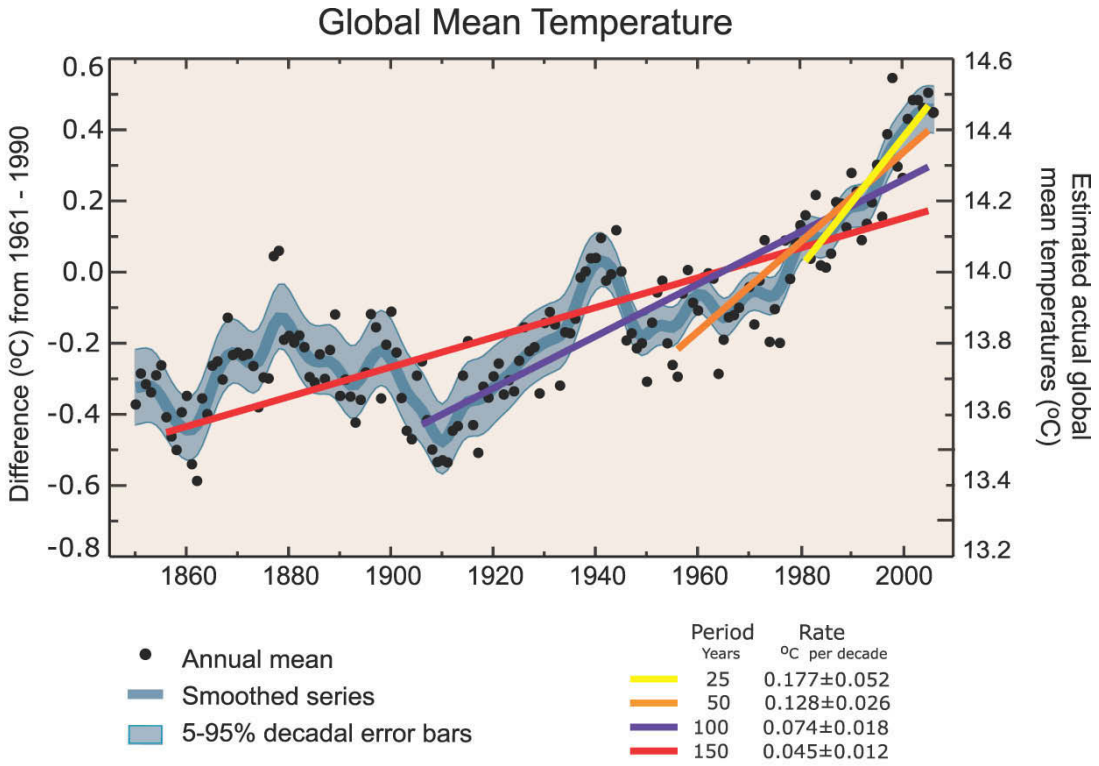

Figure 1.4: "Annual global mean observed temperatures (black dots) along with simple fits to the data. The left hand axis shows anomalies relative to the 1961 to 1990 average and the right hand axis shows the estimated actual temperature. Linear trend fits to the last 25 (yellow), 50 (orange), 100 (purple) and 150 years (red) are shown. Note that for shorter recent periods, the slope is greater, indicating accelerated warming. From about 1940 to 1970 the increasing industrialisation following World War II increased pollution in the Northern Hemisphere, contributing to cooling, and increases in carbon dioxide and other greenhouse gases dominate the observed warming after the mid-1970s." (IPCC, 2007)

about 500 nm. As a consequence, a large portion of the sunlight can pass the atmosphere, but the thermal radiation from the Earth – having a maximum at about 10 μm according to Planck's Law – is absorbed and re-emitted to all directions, including back downwards. In this way, part of the energy is trapped in the lower part of the atmosphere and can then heat the surface. This process is called *natural greenhouse effect*. Figure 1.5 shows the radiative budget for the Earth. The sum of incoming and outgoing energy does not exactly equal zero (Trenberth et al., 2009) indicating that the Earth is radiatively not in balance and slowly heating up (until a new equilibrium is reached). The most important greenhouse gases are water vapour (H_2O), carbon dioxide (CO_2), methane (CH_4), ozone (O_3) and nitrous oxide (N_2O), whereas the most abundant gases in the atmosphere, oxygen (O_2) and nitrogen (N_2), are no greenhouse gases. Ozone is to some extent special because it also plays an important role in absorption of short-wave (UV) radiation from the sun. Table 1.2 lists the contribution of greenhouse gases to the natural greenhouse effect in the absence of clouds.

When the abundance of greenhouse gases is elevated due to anthropogenic activity, the portion of energy radiated back to Earth is increased further and leads to an additional enhancement in surface temperatures. This is referred to as the *anthropogenic greenhouse*

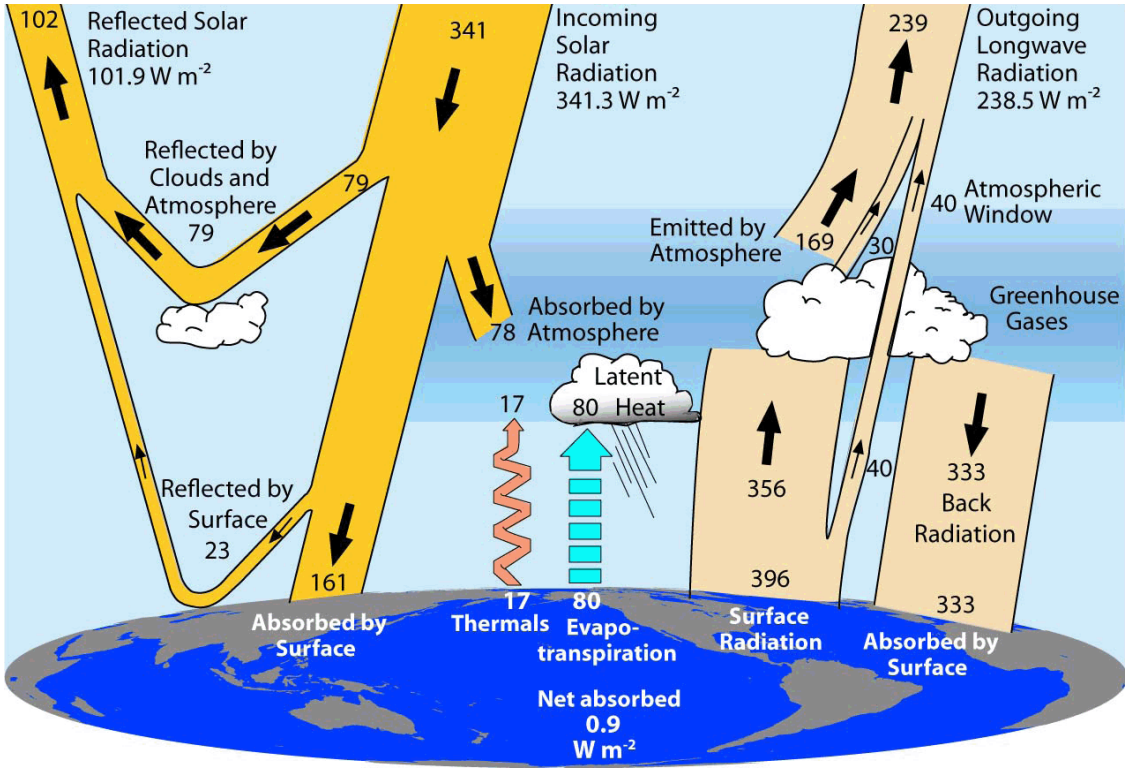

Figure 1.5: Global energy flows (in W m^{-2}) including the greenhouse effect. The imbalance for the period 2000–2004 is about +0.9 ±0.15 W m^{-2} net absorption by the Earth (Trenberth et al., 2009).

effect as opposed to the natural greenhouse effect. Beside the greenhouse gases, also non-gaseous compounds such as aerosols (especially clouds) impact the greenhouse effect.

To assess and compare the effect of greenhouse gases and other drivers of climate, the concept of *radiative forcing* has been introduced. It refers to the change in the radiative energy balance per unit area of the Earth at the height of the tropopause (IPCC, 2007) where a positive value indicates an increase of energy in the system. Figure 1.6 shows the

Table 1.2: Contribution of the most important greenhouse gases to the natural greenhouse effect in the absence of clouds (after Roedel and Wagner, 2011, and references therein). For a contribution by species to the anthropogenic greenhouse effect, see Table 2.2.

Greenhouse gas species	Contribution to natural greenhouse effect [%]
H_2O	62 %
CO_2	22 %
O_3	7 %
N_2O	4 %
CH_4	2.5 %

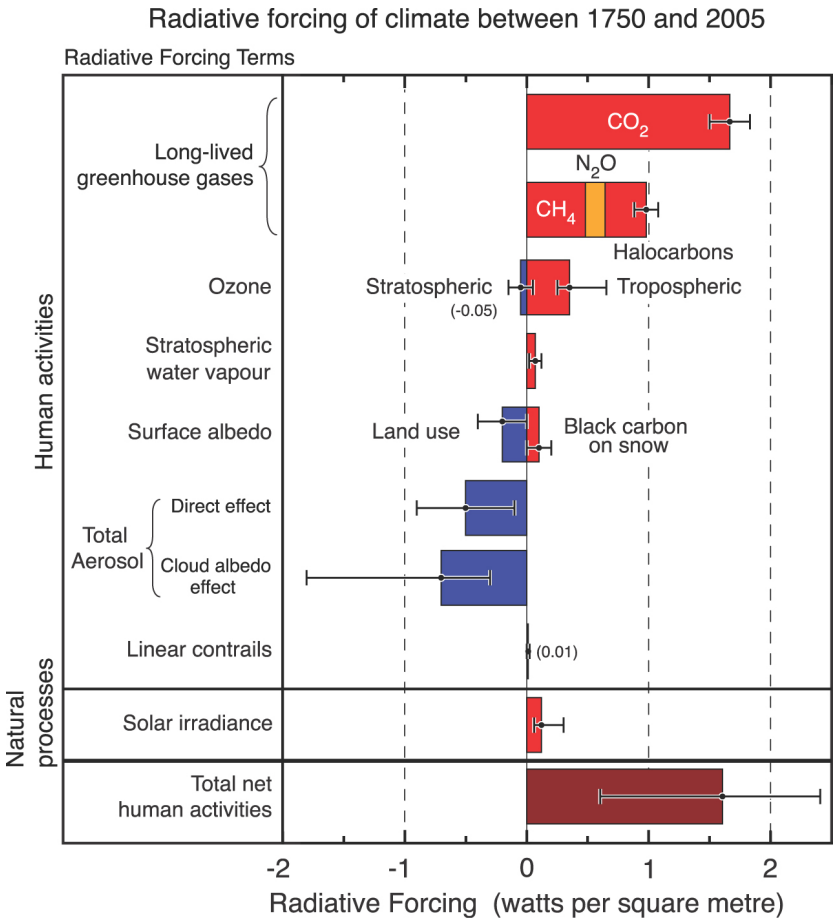

Figure 1.6: Radiative forcing for different components in the climate system from 1750–2005 A.D.. The only significant natural source is the change in solar irradiance which, however, is small compared to the anthropogenic influence being dominated by long lived greenhouse gases. (IPCC, 2007)

radiative forcing for different components in the climate system since the beginning of the industrialisation. It shows that anthropogenically released greenhouse gases carbon dioxide and methane have the largest impact on climate.

The net human activities exceed the natural forcing of climate by far. The only natural source large enough to be included in this figure is the change in the solar irradiance which can generally be induced by solar variability directly or from a change in the parameters of the Earth's orbit around the sun. A natural effect that transiently imposes a negative radiative forcing is the injection of aerosols into the stratosphere due to explosive volcanic eruptions, the most prominent in recent history being the Mt. Pinatubo eruption in 1991. This effect lasts only 2–3 years so that currently the stratosphere is free of volcanic sulphate aerosols (IPCC, 2007).

The predominance of anthropogenic influence on climate change is also consistent with the fact that the global mean temperature increase shown in Figure 1.4 cannot be satisfactorily modelled by the natural radiative forcing alone. The observed surface temperature increase can only be adequately explained when the large effect of human activities is included, with the anthropogenic greenhouse gas forcing very likely having

the largest impact (Hegerl et al., 2007). This is further confirmed by the fact that the troposphere is measurably warming, whereas the stratosphere is cooling (Randel et al., 2009). This would not be in accordance with, for example, increased solar irradiance being the main driver (Solanki and Krivova, 2003). But on the other hand, it is the expected consequence of an increased concentration of greenhouse gases in the atmosphere and an enhanced greenhouse effect (Shine et al., 2003). Part of the stratospheric cooling may be attributed to the depletion of ozone, for example, caused by anthropogenic chlorofluorocarbons (CFCs), which leads to less absorption of short-wave solar radiation and hence less heating. But even though the ozone is recovering as a consequence of the Montreal Protocol (1989) and its amendments (Yang et al., 2006), the stratosphere continues to cool for an enhanced greenhouse effect. The main reason is that increased CO_2 in the stratosphere shifts the balance between heating from absorption of solar radiation (mainly by O_3) on the one hand and cooling by infrared emission on the other hand to cooler temperatures. In addition, accumulated CO_2 in the troposphere reduces the upwelling radiation in the CO_2 absorption bands, which is then not available for stratospheric warming any more. While, in principal, valid for all greenhouse gases, these effects are most effective for CO_2 with its high abundances in the troposphere and deep absorption bands blocking most of the upwelling radiation, and also high concentrations in the stratosphere providing an effective cooling (compare also Shine et al., 2003).

Water vapour is the strongest greenhouse gas contributing about 62 % to the natural greenhouse effect (Roedel and Wagner, 2011, and references therein). However, its tropospheric component is not included in Figure 1.6, even though it is apparently increasing in global mean concentrations. This is because H_2O is generally not considered a driver but its increase is mainly attributed to feedback mechanism to a warmer climate (Forster et al., 2007).

Recently, special attention has been given to stratospheric water vapour (compare, for example, Hoffmann et al., 2012) of which one major source is oxidation of CH_4 (see Section 2.2 and Trenberth et al., 2007) and where it is not clear if its variations are a forcing or a feedback mechanism (Solomon et al., 2010).

The next chapter will discuss in detail the most important anthropogenic greenhouse gases contributing to climate change: carbon dioxide and methane.

2

The greenhouse gases carbon dioxide and methane

2.1 Relevance for climate change

Human activity has raised the atmospheric concentrations of several greenhouse gases in the atmosphere (see Table 2.1 and Figure 2.1). Among these, carbon dioxide and methane have the biggest impact on the greenhouse effect and associated climate change. Since the beginning of the industrial revolution after 1750 A.D., atmospheric CO_2 has increased by about 37 % to a concentration of 379 ppm in 2005, whereas CH_4 has increased by 148 % to an amount of 1774 ppb for the same period. The increase has been confirmed by various independent measurements of which the "Keeling curve" for CO_2 started at the Mauna Loa Observatory on Hawaii (located at 19.5° N) in 1958 under the supervision of Charles David Keeling is probably the most prominent.

Table 2.2 lists the contribution of several long-lived greenhouse gases to the

Table 2.1: Increase of atmospheric concentrations of long-lived greenhouse gases since the start of the industrial era (Forster et al., 2007). The unit of the concentration for the purely human made SF_6 refers to *parts per trillion* (1 ppt = 1 pmol mol^{-1}).

Greenhouse gas species	Concentration 2005	Concentration 1750	Increase [%]
CO_2 [ppm]	379 ± 0.65	277 ± 1.2	+ 37
CH_4 [ppb]	1774 ± 1.8	715 ± 4	+ 148
N_2O [ppb]	319 ± 0.12	270 ± 7	+ 18
SF_6 [ppt]	5.6 ± 0.038	0	—

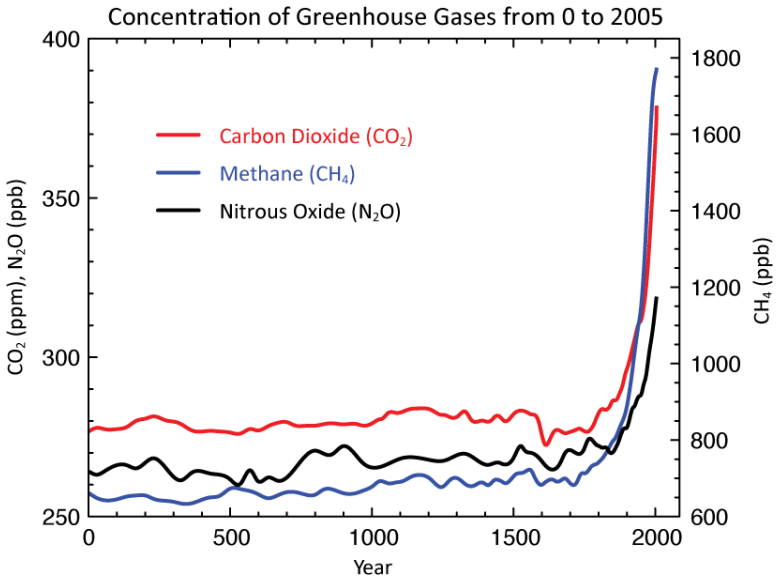

Figure 2.1: Time series of greenhouse gases carbon dioxide (red), methane (blue) and nitrous oxide (black) for the last two thousand years, including the sudden increase with the beginning of the industrialisation (Forster et al., 2007).

anthropogenic radiative forcing. In total, the group of long-lived greenhouse gases consists of CO_2, CH_4, N_2O, SF_6, chlorofluorocarbons (CFCs), hydrochlorofluorocarbons (HCFCs), hydrofluorocarbons (HFCs) and perfluorocarbons (PFCs). Carbon dioxide and methane are most important contributing about 63 % and 18 %, respectively, whereas N_2O contributes about 6 %. Ozone is not a long-lived greenhouse gas, but included in Table 2.2 for comparison.

To compare the contribution of same amounts of different trace gases to climate change, the *global warming potential* (GWP) has been introduced. In contrast to the concept of radiative forcing, which has been described in Section 1.4, the GWP additionally takes into account the atmospheric lifetime of the forcing agents (Forster et al., 2007). It describes the integrated radiative forcing over a given period from a unit mass pulse emission relative to CO_2. Hence, per definition, carbon dioxide has a GWP of unity.

Table 2.3 shows the lifetime and GWP for different time frames of CO_2, CH_4 and several other greenhouse gases. For guidelines, often the 100-year time horizon is used to compare different greenhouse gases. In this time period, methane has a GWP that is 25 times higher than that for carbon dioxide and may be even higher according to more recent studies (Shindell et al., 2009). The highest GWP and lifetime has sulphur hexafluoride (SF_6) which is of purely anthropogenic origin from use as an electrical insulator or as an inert tracer gas to study atmospheric and oceanic processes. However, due to its very low concentrations (see Table 2.1), the contribution to the total anthropogenic radiative forcing from long-lived greenhouse gases is only about 0.1 % (Table 2.2).

The GWP is also used to compute the so-called *carbon dioxide equivalent* which is the amount of CO_2 that has the same impact on climate as a certain amount of another greenhouse gas. This offers the possibility to compare the severity of emissions of different greenhouse gas species. For example, taking into account the GWP of 25, one ton of CH_4

Table 2.2: Contribution of the most important greenhouse gases to the anthropogenic radiative forcing between 1750 and 2005 (after Forster et al., 2007) (compare also Figure 1.6). Note that O_3 does not belong to the group of long-lived greenhouse gases. For a contribution by species to the natural greenhouse effect, see Table 1.2.

Greenhouse gas species	Contribution to radiative forcing [$W\,m^{-2}$]	Share among long-lived greenhouse gases [%]
CO_2	1.66	63 %
CH_4	0.48	18 %
N_2O	0.16	6 %
SF_6	0.0029	0.1 %
CFCs	0.268	10 %
HFCs	0.039	1.5 %
tropospheric O_3	0.35	
stratospheric O_3	-0.05	

has the equivalent impact on climate as 25 tons CO_2.

2.2 Sources, sinks and distribution

Due to its long lifetime, carbon dioxide is, on average, a well mixed atmospheric trace gas. The vertical profile (see Figure 2.2, Panel A) shows that its mean mixing ratio is almost constant with altitude up to the upper mesosphere. However, due to the time delay of transport of CO_2 from the troposphere into the stratosphere of about 5–6 years (Bischof et al., 1980), the concentrations in the stratosphere can be several ppm lower compared to the troposphere depending also on the season. Inside the troposphere, measurements showed that annual mean surface concentrations are slightly higher than aloft by about 0.7 ppm (Stephens et al., 2007).

Carbon dioxide does not play an important role in atmospheric chemistry. Only in the lower thermosphere, where CO_2 is photolysed (wavelength $\lambda < 240\,nm$), it can be a source for carbon monoxide (CO), although CO can rapidly react with an hydroxyl radical (OH) back to CO_2 (Hewitt and Jackson, 2009; Brasseur and Solomon, 2005):

$$CO_2 + h\nu \longrightarrow CO + O \tag{2.1}$$

$$CO + OH \longrightarrow CO_2 + H \tag{2.2}$$

where hν denotes the input of light of the frequency ν and energy $h\nu$ with Planck's constant $h \approx 6.626 \cdot 10^{-34}\,Js$.

The sources of CO_2 are not uniformly distributed and lead to variations in time and space as they can be observed, for example, by satellite (see Figure 2.3). The most prominent features are (i) the seasonal variability, (ii) the interhemispheric gradient with higher average concentrations in the northern hemisphere and (iii) the linear increase of CO_2 concentrations with time.

Table 2.3: Lifetime and global warming potential for several greenhouse gases and different time horizons (modified after Forster et al., 2007). The GWP of CH_4 given here also contains the indirect effects from enhancements of ozone and water vapour.
* Even though the lifetime of an individual CO_2 molecule is only about 5 years before it gets exchanged by the ocean (Craig, 1957), the net lifetime of an extra CO_2 pulse emitted to the atmosphere is much longer. This *turnover time* is much more difficult to specify and depends on assumptions for different uptake and feedback mechanisms. A more accurate equation for the lifetime of a CO_2 pulse based on models can be found in Forster et al. (2007, and references therein). According to this, after about 100 years, the net amount of a CO_2 pulse has decreased to e^{-1} of the original amount.

Greenhouse gas species	Lifetime [years]	GWP for given time period 20 years	100 years	500 years
CO_2	$\sim 100^*$	1	1	1
CH_4	12	72	25	7.6
N_2O	114	289	298	153
SF_6	3200	16300	22800	32600

The reason for the annual cycle (i) is the influence of photosynthetically active land plant species which consume CO_2 in the growing seasons combined with subsequent release of carbon in autumn and winter (Keeling et al., 2005). This seasonal concentration change is more pronounced in the northern hemisphere where most of the continental land mass with vegetation is located. At the Mauna Loa observatory, the seasonal cycle is currently about ± 3 ppm[1]. Column-averaged dry air mole fractions (XCO_2) seasonally vary by about $\pm$(3–4) ppm for the northern hemisphere and $\pm$(1–1.5) ppm for the southern hemisphere (Schneising et al., 2011). For comparison, the diurnal cycle of XCO_2 can amount to a few ppm (Geibel et al., 2010) and is mainly caused by photosynthesis.The (increasing) interhemispheric gradient (ii) represents the distribution of carbon dioxide sources and sinks and is primarily due to the greater anthropogenic fossil fuel combustion in the northern hemisphere[2], for example, for energy production, and amounts to about $+$(2.0–3.0) ppm (Keeling et al., 2011). The enhancement of these CO_2 emissions leads to globally increased atmospheric carbon dioxide concentrations which can be observed in a linear trend (iii) of about $+1.4\,\mathrm{ppm\,yr^{-1}}$ (Forster et al., 2007) and which accelerated to about $+2\,\mathrm{ppm\,yr^{-1}}$ for the last decade measured at Mauna Loa Observatory[1].

In 2005, anthropogenic emissions were about $36\,\mathrm{Pg\,CO_2\,yr^{-1}}$ (see Table 2.4), 55 % of which were taken up by the ocean (30 %) and terrestrial ecosystems (25 %) (Denman et al., 2007)[3]. The remaining 45 % accumulated in the atmosphere.

Up to three quarters of the CO_2 increase since the pre-industrial era have been attributed to combustion of fossil fuels (for example, in power plants but also steel plants, etc.), gas

[1] Dr. Pieter Tans, NOAA/ESRL (http://www.esrl.noaa.gov/gmd/ccgg/trends/) and Dr. Ralph Keeling, Scripps Institution of Oceanography (http://scrippsco2.ucsd.edu/), 2012.

[2] There is evidence that before anthropogenic influence, the natural gradient was reversed with higher CO_2 concentrations in the southern hemisphere (Keeling and Heimann, 1986; Taylor and Orr, 2000).

[3] The mass unit 1 Pg (petagram) is equivalent to 10^{15}g or 1000 Mt (megatons) or 1000 Tg (teragrams) or 10^6 kt (kilotons).

Table 2.4: Global anthropogenic sources of atmospheric carbon dioxide for the year 2005 by sector according to the EDGAR database (Source: EC-JRC/PBL. EDGAR version 4.2. http://edgar.jrc.ec.europa.eu/, 2011). Fractions do not add up to exactly 100 % due to rounding inaccuracies. The last column shows the IPCC 1996 codes that are often officially used to uniquely designate source types.

Source	Emissions [$TgCO_2$/year]	[%]	IPCC code 1996
Fuel combustion			
Public electricity and heat production	11200	30.9	1A1a
Manufacturing industries and construction (incl. steel plants)	4580	12.6	1A2
Residential and other sectors	3300	9.1	1A4
Other energy industries (incl. refineries)	1320	3.6	1A1b, 1A1c
Road transportation	4670	12.9	1A3b
Aviation	764	2.1	1A3a, 1C1
Navigation	645	1.8	1A3d, 1C2
Offroad transportation	163	0.4	1A3e
Rail transportation	134	0.4	1A3c
Land use change & forestry			
Forest fires	2890	8.0	5A
Forest fires – post burn decay	2630	7.3	5F2
Peat fires and decay of drained peatland	1400	3.9	5D
Industrial processes			
Cement production	958	2.6	2A1
Chemicals	422	1.2	2B
Lime & other minerals	294	0.8	2A2, 2A7
Metals	191	0.5	2C
Fugitive emissions (mining, exploration, venting, etc.)			
Fugitive emissions from oil and gas	314	0.9	1B2
Fugitive emissions from solid fuels	140	0.4	1B1
Agriculture			
Direct soil emissions (e.g. from urea application and soil liming)	112	0.3	4D4
Other			
Non-energy use of lubricants, solvents, etc.	69	0.2	2G, 3A, 3B 3C, 3D
Fossil fuel fires	48	0.1	7A
Waste			
Waste incineration	30	0.1	6C
TOTAL	$\approx$ 36000	100.1	

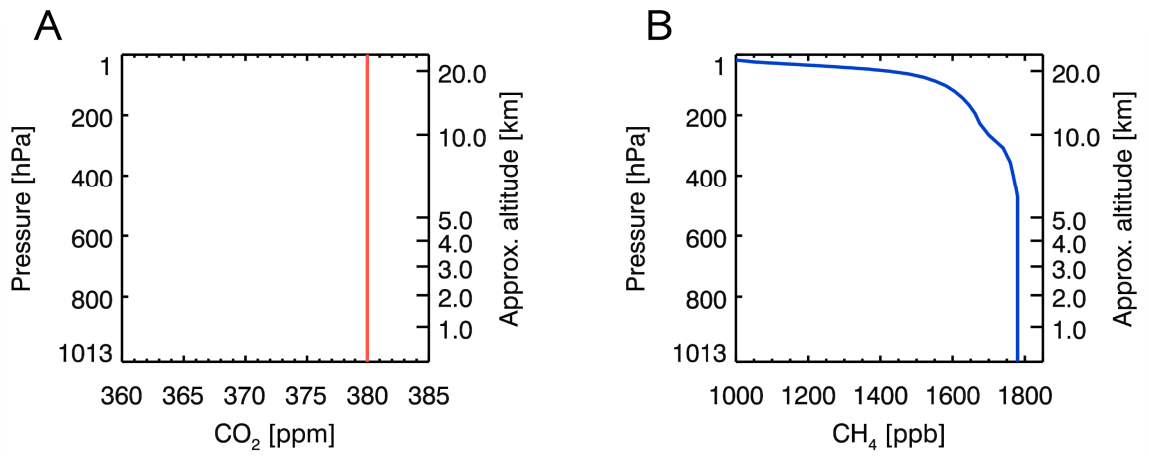

Figure 2.2: Vertical profiles of carbon dioxide (Panel A) and methane (Panel B) in the atmosphere based on the 1976 U.S. Standard Atmosphere (U.S. Committee on Extension to the Standard Atmosphere, 1976) scaled to actual values as used in Krings et al. (2011).

flaring (at refineries, oil platforms, etc.) and cement production (Forster et al., 2007) where CO_2 is chemically released during the transition of limestone (calcium carbonate, $CaCO_3$) to the main cement ingredient quicklime (calcium oxide, CaO). The total amount of CO_2 emissions from fossil fuel combustion was about 27.5 Pg CO_2 in 2005 (not including flaring and cement production) with high degree of consistency between different inventories and accounting methods (Andres et al., 2012). Other important sources are land use change and land-cover change, biomass burning and deforestation, which are often tightly linked. Where emissions due to fossil fuel combustion are still rising (Olivier et al., 2011), emissions from land use and land-cover change recently showed a downward trend (Houghton et al., 2012). Compared to these anthropogenic sources, global release of CO_2 from volcanoes and degassing of the lithosphere, is about two orders of magnitude lower, but may be underestimated (Mörner and Etiope, 2002).

Attribution to specific sources is, for example, accomplished by making use of the fact that due to a preference of land plants for the isotope ^{12}C during photosynthesis, CO_2 from fossil fuel combustion has a measurably lower $^{13}C/^{12}C$ isotope ratio compared to most other sources. This can then be traced in the isotopic composition of atmospheric carbon dioxide. Furthermore, also the increase and decline of O_2 due to photosynthesis and burning of fossil fuels, that is, the oxidation of carbon, respectively, can be measured, offering a possibility to assess the importance of the oceanic CO_2 sink (Forster et al., 2007).

In the global carbon cycle (see Figure 2.4), the anthropogenic emissions may seem relatively small compared to the natural fluxes. However, they disturb the natural balance of sources and sinks and lead to a net accumulation of carbon dioxide in the atmosphere. Figure 2.4 also shows that with rising atmospheric carbon content the ocean reservoir has increased indicating that natural sinks may change under altered environmental conditions. Without the enhanced oceanic carbon sink, atmospheric concentrations would have increased even more.

In contrast to CO_2, the mixing ratio of methane is only constant up to an altitude

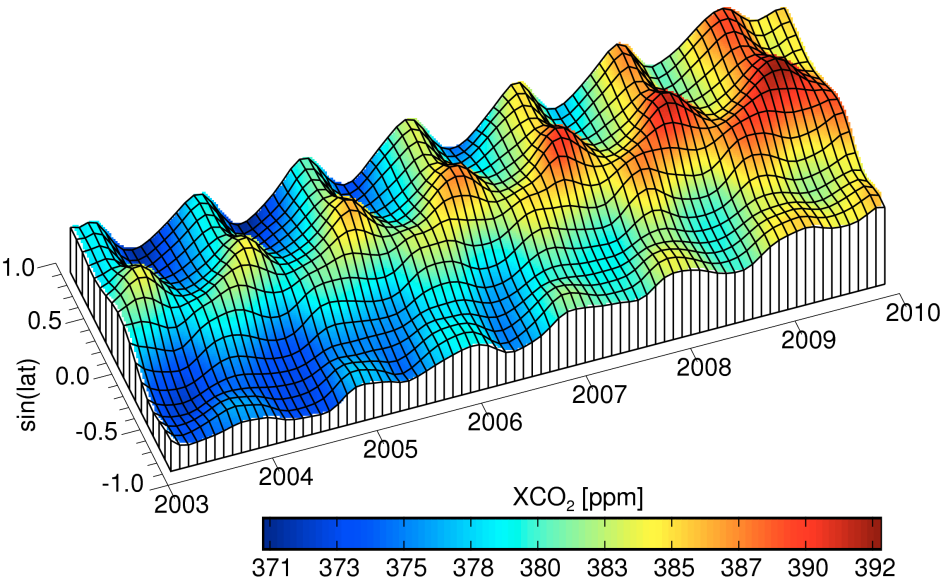

Figure 2.3: Column-averaged dry air mole fractions of carbon dioxide as a function of time and latitude observed by the SCIAMACHY instrument on ENVISAT. (Figure courtesy of O. Schneising, 2011.)

of about 7 km and then decreases with height (see Figure 2.2, Panel B). Since there are no sources of methane within the atmosphere, this is a direct consequence of the equilibrium between transport upward from the sources at the surface and photochemical destruction in the atmosphere. Carbon dioxide, on the other hand, is produced, for example, from oxidation of CO and from destruction of CH_4 throughout the atmosphere (about 3900 Tg CO_2 yr^{-1}, Nassar et al., 2010).

With a seasonal variation, an interhemispheric gradient and an increase of atmospheric concentrations in time, the global distribution of CH_4 (see Figure 2.5) shows similar patterns as for CO_2. The seasonal variation (about ±(10–13) ppb for column-averaged dry air mole fractions XCH_4 (Schneising et al., 2011) and ±(30–60) ppb for surface observations (Dlugokencky et al., 1994)) is mainly induced by photochemical production of the hydroxyl radical OH which acts as a CH_4 sink (see Equation (2.3)) and seasonally varying methane emissions (Dlugokencky et al., 1994), for example, of methanogenic microorganisms (*archaea*) in northern boreal wetlands where temperature strongly affects the release of methane to the atmosphere. The interhemispheric gradient (about +90 ppb in the northern hemisphere) is caused by the domination of sources in the northern hemisphere (Dlugokencky et al., 1994). Increasing methane emissions, for example, due to intensified fossil fuel mining and extension of the warm period of wetlands lead to a positive trend in time. While the trend has been steady for CO_2, atmospheric methane concentrations were stable between 1999 and 2006 (Bousquet et al., 2006) but increased again from 2007 onwards as could be shown in surface measurements (Rigby et al., 2008; Dlugokencky et al., 2009; Terao et al., 2011) and satellite observations (Schneising et al., 2011). In 2007 and 2008 global CH_4 concentrations increased by about +8 ppb and +4 ppb respectively (Dlugokencky et al., 2009). The reasons are not completely understood but might be based, for example, on changed methane emissions from rice

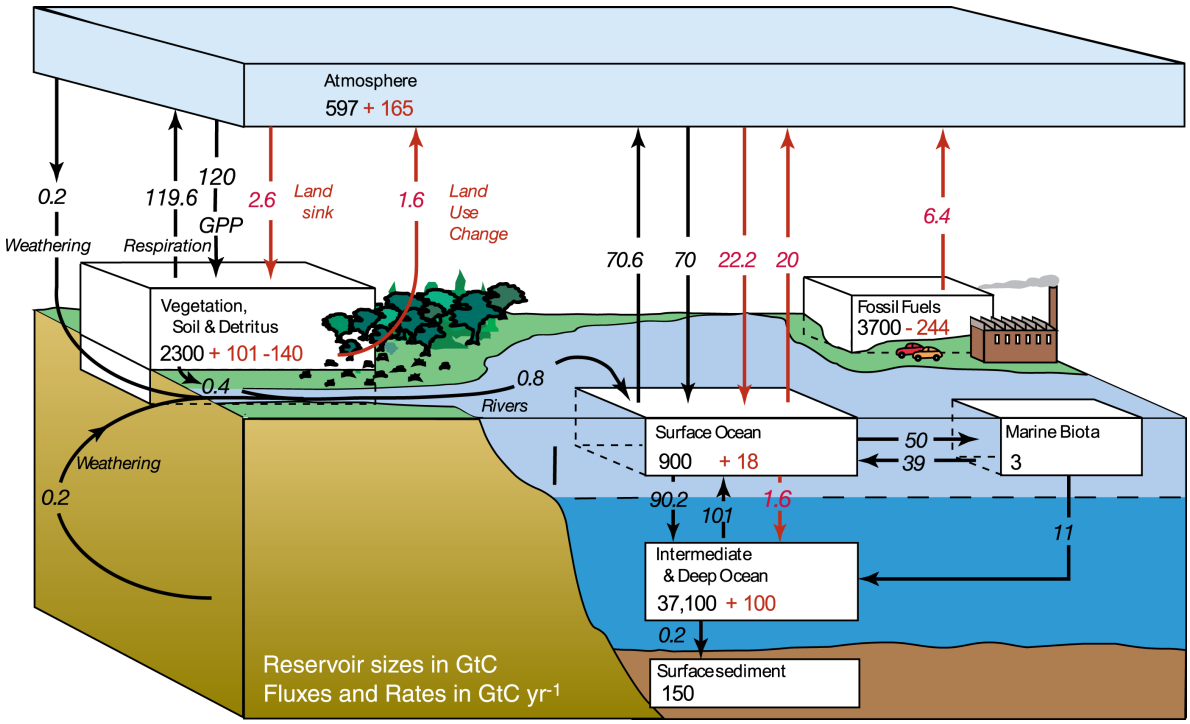

Figure 2.4: The global carbon cycle for the 1990s showing the pre-industrial, undisturbed reservoir sizes and fluxes (black) and the anthropogenic perturbation (red) in Pg C (or Gt C) and Pg C yr^{-1} respectively (Denman et al., 2007). *GPP* is the annual gross (terrestrial) primary production. Even though the perturbations may seem small with respect to natural fluxes, they disturb the balance of sources and sinks.

agriculture (Kai et al., 2011) or fossil fuels (Aydin et al., 2011) or variability in the annual mean OH concentrations (Rigby et al., 2008). The diurnal cycle of CH_4 is highly dependent on location. For example, in eastern Poland, $X\,CH_4$ varied by about 10 ppb during the day (Geibel, 2011).

Sources of CH_4 can be divided into anthropogenic and natural (see Table 2.5). Natural sources of methane are dominated by spatially extended wetlands (100 Tg CH_4 yr^{-1}) and geological local sources (19 Tg CH_4 yr^{-1}) like seeps and mud volcanoes, and also destabilised methane hydrates. The latter may be further enhanced by global warming (Wuebbles and Hayhoe, 2002). Anthropogenic sources like landfills (61 Tg CH_4 yr^{-1}), rice agriculture (60 Tg CH_4 yr^{-1}), biomass burning (50 Tg CH_4 yr^{-1}), ruminant animals (81 Tg CH_4 yr^{-1}) and release of CH_4 due to fossil fuel production and distribution (106 Tg CH_4 yr^{-1}) (Wuebbles and Hayhoe, 2002) are usually localised. All in all, natural and anthropogenic localised sources account for about 40 % of the total yearly methane emissions of 503 Tg CH_4, the remainder being extended area sources (Wuebbles and Hayhoe, 2002). Landfills alone account for more than 12 % of the total yearly emissions.

The following paragraphs regarding the atmospheric chemistry of methane have been adopted from the standard text books Brasseur and Solomon (2005) and Seinfeld and Pandis (1998).

Besides the uptake from soil and the photolysis above the stratopause (particularly by the Lyman α line from the sun at 121.6 nm), the dominant sink (about 85 %) for methane is the destruction by reaction with the OH radical mainly in the troposphere. The hydroxyl

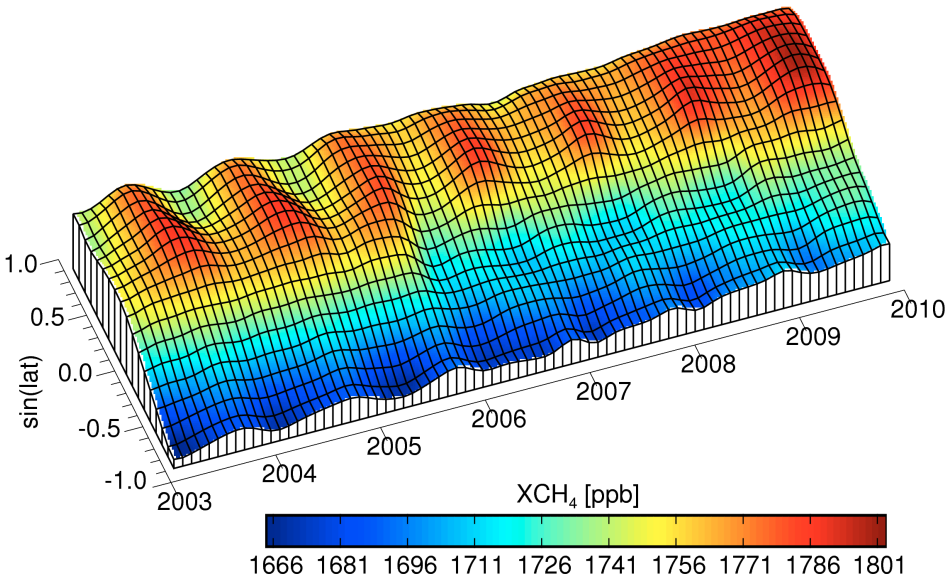

Figure 2.5: Column-averaged dry air mole fractions of methane as a function of time and latitude observed by the SCIAMACHY instrument on ENVISAT. (Figure courtesy of O. Schneising, 2011.)

radicals react with CH_4 and the generated methyl radical, CH_3, then instantaneously reacts with O_2 to yield the methyl peroxy radical, CH_3O_2:

$$CH_4 + OH \longrightarrow CH_3 + H_2O \tag{2.3}$$
$$CH_3 + O_2 + M \longrightarrow CH_3O_2 + M \tag{2.4}$$

where M denotes a third molecule that carries off the excess energy of the reaction, or concisely written as:

$$CH_4 + OH \xrightarrow{O_2} CH_3O_2 + H_2O \tag{2.5}$$

Under tropospheric conditions, subsequent reactions with NO_x and hydroperoxyl radicals (HO_2) are most important. When levels of nitric oxide, NO, are sufficiently high, the reaction of CH_3O_2 with NO dominates. The complete reaction chain can be written as:

$$CH_4 + OH \xrightarrow{O_2} CH_3O_2 + H_2O \tag{2.6}$$
$$CH_3O_2 + NO \longrightarrow CH_3O + NO_2 \tag{2.7}$$
$$CH_3O + O_2 \longrightarrow HCHO + HO_2 \tag{2.8}$$
$$HO_2 + NO \longrightarrow OH + NO_2 \tag{2.9}$$
$$2\,(NO_2 + h\nu) \longrightarrow 2\,(NO + O) \tag{2.10}$$
$$2\,(O + O_2 + M) \longrightarrow 2\,(O_3 + M) \tag{2.11}$$

$$\text{Net :} \qquad CH_4 + 4\,O_2 \longrightarrow HCHO + 2\,O_3 + H_2O \tag{2.12}$$

Table 2.5: Sources of atmospheric methane. Estimate ranges for wild fire emissions are not specified. Adapted from Wuebbles and Hayhoe (2002, and references therein).

	Source	Emissions [$TgCH_4$/year]	Range of estimate [$TgCH_4$/year]
Natural	Wetlands	100	92–232
	Termites	20	2–22
	Geological sources	14	12–36
	Marine Sediments	5	0.4–12.2
	Oceans	4	0.2–2.0
	Wild fires	2	*
	Total natural	145	
Anthropogenic	Ruminants	81	65–100
	Waste disposal	61	40–100
	Rice cultivation	60	25–90
	Biomass burning	50	27–80
	Coal mining	46	15–64
	Natural gas	30	25–50
	Other fossil fuels	30	6–60
	Total anthropogenic	358	

This reaction chain is important considering, for example, flight corridors of aircraft which not only contribute more than 2 % to global CO_2 emissions (compare, for example, Gössling and Upham, 2009) but also emit significant amounts of NO_x.

In NO-poor environments, the methyl peroxy radical reacts with the HO_2 radical instead leading to one of the following two simplified reactions where the resulting methyl hydroperoxide, CH_3OOH, is photolysed or reacts with OH, respectively:

$$CH_4 + OH \xrightarrow{O_2} CH_3O_2 + H_2O \tag{2.13}$$
$$CH_3O_2 + HO_2 \longrightarrow CH_3OOH + O_2 \tag{2.14}$$
$$CH_3OOH + h\nu \longrightarrow CH_3O + OH \tag{2.15}$$
$$CH_3O + O_2 \longrightarrow HCHO + HO_2 \tag{2.16}$$

$$\text{Net :} \quad CH_4 + O_2 \longrightarrow HCHO + H_2O \tag{2.17}$$

$$CH_4 + OH \xrightarrow{O_2} CH_3O_2 + H_2O \tag{2.18}$$
$$CH_3O_2 + HO_2 \longrightarrow CH_3OOH + O_2 \tag{2.19}$$
$$CH_3OOH + OH \longrightarrow HCHO + H_2O + OH \tag{2.20}$$

$$\text{Net :} \quad CH_4 + OH + HO_2 \longrightarrow HCHO + 2\,H_2O \tag{2.21}$$

In all cases, Formaldehyde (HCHO) is the first major product of CH_4 with a lifetime longer than a few seconds. It can be further oxidised to CO which eventually is oxidised to the

final product CO_2. The generation of the greenhouse gases ozone and water vapour from CH_4 is another important outcome of these reactions and leads to an indirect radiative forcing effect.

Despite their importance, the knowledge on the sources and sinks of the greenhouse gases CO_2 and CH_4 still has significant gaps as indicated, for example, by the range of estimates given in Table 2.5 that often differ by an order of magnitude or more.

2.3 Carbon emissions inventoring and trading

Although climate change may not be a challenge for earth itself, it is for many life forms and in particular for mankind. This is why authorities started to debate on national and international grounds about measures for mitigation. The first step towards this is a precise reporting, for example, in the framework of emissions inventories and trading to better identify, localise and quantify sources of greenhouse gases. Not only does this help to raise opportunities for emission reductions, it also assists scientists in improving the understanding of the carbon cycle. This is key to be able to predict future climate and mitigate effects and hazards coming along with global climate change. One example for such an inventory gathering data from various sources is the *Emissions Database for Global Atmospheric Research* (EDGAR) by the Joint Research Centre of the European Commission (JRC) and the Netherlands Environmental Assessment Agency (PBL) (compare, for example, Olivier et al., 2005). Figure 2.6 and 2.7 illustrate the distribution of anthropogenic sources for the greenhouse gases carbon dioxide and methane, respectively, according to this database.

However, the climate debate is to a large extent also driven – or slowed down – by economical and financial interests. To support any political approach, economic incentives must be provided to stimulate the reduction of substances that accelerate climate change. *Carbon emission trading* is aimed at this point: saving carbon dioxide emissions can lead to financial benefits in the future.

The *Kyoto Protocol*, negotiated in 1997 at the Conference of Parties (COP) to the United Nations Framework Convention on Climate Change (UNFCCC), has been the first international environmental treaty with the goal to reduce emissions of the greenhouse gases carbon dioxide, methane, nitrous oxide, sulphur hexafluoride, hydrofluorocarbons and perfluorocarbons. Among other agreements, the participating *Annex I countries*[4], as specified in Annex B of the protocol, committed to reduce the CO_2-equivalent of "their overall emissions of such gases by at least 5 per cent below 1990 levels in the commitment period 2008 to 2012" (United Nations, 1998, Article 3). While some countries only limited their increase (Iceland +10 %, Australia +8 %), the European Union, for example, committed to a reduction of -8 % and Canada to -6 %. All in all, the commitments aim at a collective decrease of -4.2 % CO_2 equivalent of greenhouse gas emissions, excluding USA which never actually ratified the protocol. This target is very likely to be achieved (Olivier et al., 2011).

The Kyoto Protocol is an important step for international environmental protection. However, global greenhouse gas emissions, of which the countries with a Kyoto target

[4]Annex I countries: industrialised countries and economies in transition, as classified by the UNFCCC.

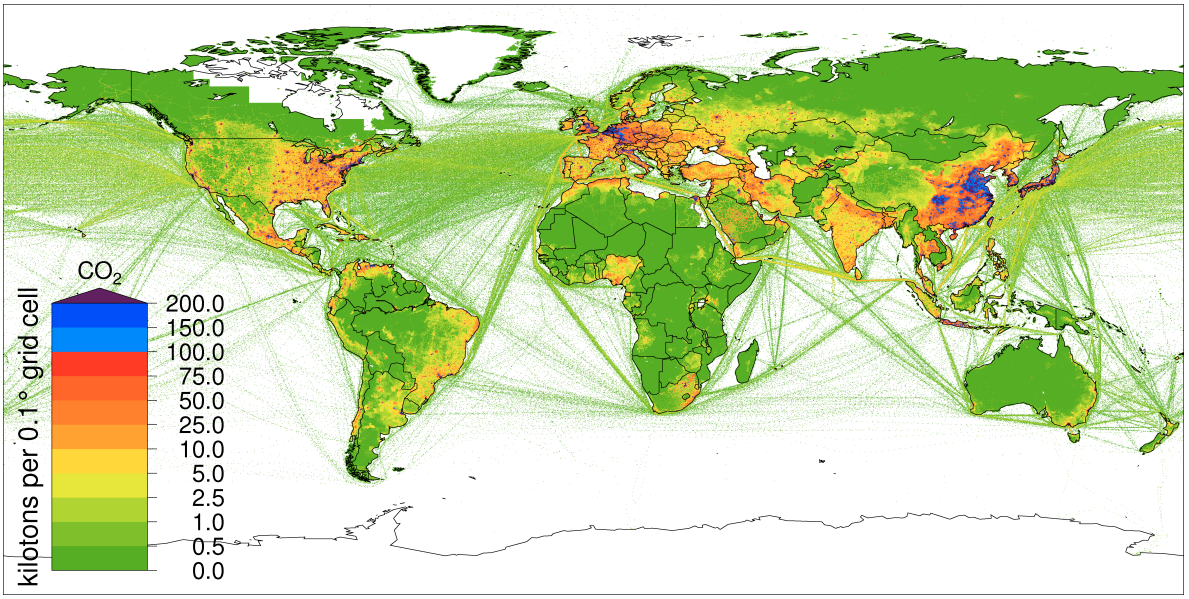

Figure 2.6: Global map of anthropogenic carbon dioxide emissions gridded to boxes of $0.1° \times 0.1°$ for the year 2005. White areas denote regions where there are no data available. (Data source: European Commission, Joint Research Centre (JRC)/Netherlands Environmental Assessment Agency (PBL). Emission Database for Global Atmospheric Research (EDGAR), release version 4.0. http://edgar.jrc.ec.europa.eu, 2009.)

shared less than 25 % in 2008[5], keep on rising (compare, for example, Olivier et al., 2011, for CO_2). It is unfortunate that the biggest contributors to global greenhouse gas emissions, China and the USA, did not take part in this agreement. Furthermore, in December, 2011, one year before the end of the first commitment period, Canada decided to withdraw from the obligations according to Article 27 of the protocol after which a withdrawal is permitted with one year's notice. Amongst others, due to Canada's efforts to expand its profitable oil production from tar and oil sands (bituminous sands), whose treatment leads to relatively high greenhouse gas emissions compared to regular fuel production (Charpentier et al., 2009), the country was behind the Kyoto goal already before its withdrawal (Environment Canada, 2011). Nevertheless, the Kyoto countries altogether – including Canada and the USA – are still well on track to achieve their target reductions (Olivier et al., 2011).

As an outcome of the 17th UNFCCC Conference of Parties (COP17/CMP7) in Durban, South Africa, 2011, the Kyoto Protocol, though with a reduced number of participating countries, is proposed to continue with the formal commitments for each country still to be quantified (CMP, 2011). Furthermore, a working group was formed to elaborate a new treaty and to "complete its work as early as possible but no later than 2015 in order to adopt this protocol, legal instrument or agreed outcome with legal force [...] and for it to come into effect and be implemented from 2020" (COP, 2011).

Shortly after the acceptance of the Kyoto Protocol by the European Union to jointly fulfil

[5]Source: European Commission, Joint Research Centre (JRC)/PBL Netherlands Environmental Assessment Agency. Emission Database for Global Atmospheric Research (EDGAR), release version 4.2. http://edgar.jrc.ec.europe.eu, 2011.

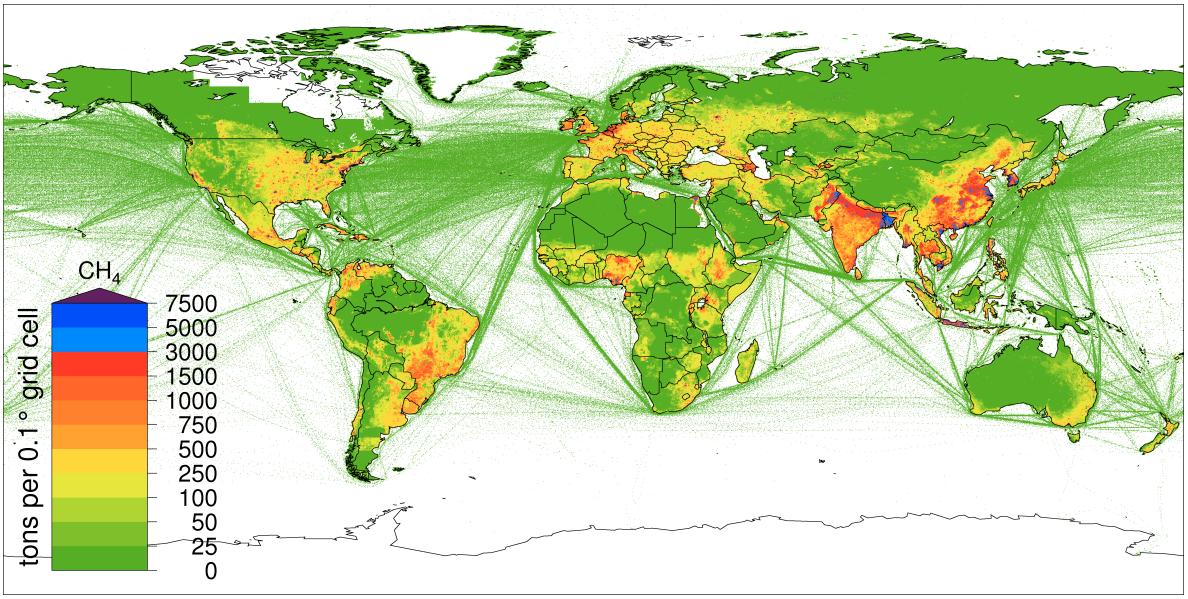

Figure 2.7: Global map of anthropogenic methane emissions gridded to boxes of 0.1 °× 0.1 ° for the year 2005. White areas denote regions where there are no data available. (Data source: European Commission, Joint Research Centre (JRC)/Netherlands Environmental Assessment Agency (PBL). Emission Database for Global Atmospheric Research (EDGAR), release version 4.0. http://edgar.jrc.ec.europa.eu, 2009.)

the commitments (*Burden Sharing Agreement,* European Commission, 2002), an emission allowance trading system was negotiated by the European Parliament and Council. The *European Union Emission Trading Scheme* (EU ETS) for carbon dioxide emission allowances is meant to "contribute to fulfilling the commitments of the European Community and its Member States [under the Kyoto Protocol] more effectively" (European Parliament and Council of the European Union, 2003). Following a *cap & trade* principle, emissions should be saved where it is economically most efficient. In Germany, it has been formally accepted in 2004 (Deutscher Bundestag, 2004).

The ETS program has been divided into three periods. The first three year trial period started in 2005 and ended in 2007, whereas the second EU ETS trading period (2008–2012) coincides with the Kyoto Protocol commitment period. From 2013–2020 the EU ETS is entering the third period (European Parliament and Council of the European Union, 2009) where allowances are going to further increase in price and probably also more greenhouse gases, besides CO_2, will be included. Until the end of 2011, CO_2 emissions from energy activities (electric power, oil refineries, coke ovens), production and processing of ferrous metals (metal ore and steel), mineral industry (cement kilns, glass, ceramics) and industrial plants that produce paper and pulp fell under the ETS. Beginning in 2012, also emissions from aviation have been included (European Commission, 2011a) with consequences also for airlines originating from outside the EU. Emissions from oil and gas exploration, for example, are not included so far.

In a preliminary assessment of the EU ETS, Ellerman and Buchner (2007) stated that the actual trading was less than expected due to sufficient allowances that have been distributed by the national authorities (under supervision by the European Commission) also in order not to compromise national industries in global competition. This initial

allocation of allowances was based on the so-called *grandfathering* approach that takes into account the emissions of each facility in previous years. However, Ellerman and Buchner (2007) also state a likely decline in carbon dioxide emissions already during the trial period and acknowledge that the EU ETS is world wide the first successful implementation of a price on CO_2 emissions. In 2011, the prices for 1 EUA (European Union Allowance) that allows for an emission of 1 t CO_2 ranged between about 7 € and 17 €[6]. In the case that emissions exceed the allowances held by the according institution, the fine per missing EUA was 40 € in the trial period and since 2008 the fine is 100 €, additionally to the obligation to surrender the according amount of missing allowances for the next calendar year (European Parliament and Council of the European Union, 2003).

A similar, notable step was recently made by Australia whose government passed a law that introduces a carbon trading scheme beginning in July, 2012. At the beginning, prices will be fixed by the government because of which it is sometimes misleadingly referred to as a *carbon tax*. However, after a step by step rise, the cost for emission allowances will eventually be regulated by the market itself as of July, 2015 (The Parliament of the Commonwealth of Australia, 2011).

It has been discussed if the implementation of carbon trading schemes might lead to the so-called *carbon leakage*, a relocation of production in sectors that are energy-intensive and in global competition to countries not imposing such a trading scheme[7]. This matter is difficult to quantify and different views have been published in the past. However, the German environmental agency (Umweltbundesamt) comes to the conclusion that the problem is less pronounced when investigated in detail (Görlach et al., 2008). Where for the United Kingdom, Helm (2008) claimed a significant carbon leakage problem, Görlach et al. (2008) could not verify the same for Germany on the basis of empirical data where the export outweighs the import of energy content in products. Additionally, the European Union takes measures against carbon leakage in the third EU ETS trading period by allocating free emission allowances to sectors that are "deemed to be exposed to a significant risk of carbon leakage" (European Commission, 2011b). Where for other sectors the free allocation gradually decreases from 80 % in 2013 to 30 % in 2020, sectors vulnerable to carbon leakage like the cement industry will transitionally receive free allowances according to the full (100 %) emissions of the most effective facilities of the corresponding sector (*benchmarking*). The power sector, that presumably is the least affected by non-EU competition (Ellerman and Buchner, 2007), will be subject to 100 % auctioning of allowances from 2013 on (European Commission, 2011b).

The procedure collecting the required emission data in order to allow trading is usually based on a bottom-up approach relying on emission factors and in-situ measurements only. It does generally not include remote sensing data for a top down estimate. Remote sensing techniques may therefore serve as an independent validation technique and might possibly even play a more standard role in the compilation of future emissions inventories where direct data are, for one reason or another, inaccessible.

[6]European Energy Exchange (EEX): http://www.eex.com/en/Market%20Data/Trading%20Data/Emission%20Rights/EU%20Emission%20Allowances%20|%20Spot (retrieved: January, 2012)

[7]The expressions *pollution haven* and *race to the bottom* originate from a similar globalisation debate, that started in the 1990s, arguing if production is being relocated to countries with rather low environmental standards that in turn might reduce these standards more and more to attract further investments (Görlach et al., 2008).

3
Basic concepts of remote sensing

Generally, the term *remote sensing* refers to non-intrusive and contactless methods for retrieval of information about the object under consideration. This includes, for example, measurements of the Earth's gravitational field, as well as seismo-acoustic waves, to explore the Earth's interior on scales of a few metres down to the core. More specifically, and most important for this work, remote sensing denotes the gathering of data of the Earth and the atmosphere by aerial measurements. Thereby, platforms for these measurements can be, for example, satellites or, as used in this work, aircraft.

Remote sensing of atmospheric gases generally relies on propagation of electromagnetic radiation in the atmosphere and its characteristic interaction with the gas species of interest. For this study, absorption bands in the short-wave infrared were used to quantify amounts of carbon dioxide and methane. Additionally, observations of oxygen in the near infrared can be used for reference purposes.

In order to do so, also other atmospheric effects like elastic and inelastic scattering from molecules and aerosol particles have to be taken into account. When operating passive instruments that rely on reflected radiation from the sun, additionally the type of surface spectral reflection is important.

The following chapters introducing the basic concepts of molecular physics and radiative transfer in the atmosphere are largely adopted from standard textbooks (Haken and Wolf, 2003; Banwell, 1983; Herzberg, 1950, 1956; Liou, 2002), unless otherwise noted.

3.1 The electromagnetic spectrum

The spectrum of electromagnetic radiation can be divided with respect to its frequency ν, or, according to the fundamental relation $c = \lambda \cdot \nu$, to its vacuum wavelength λ where $c \approx 3 \cdot 10^8\,\mathrm{m\,s^{-1}}$ refers to the vacuum speed of light. The energy of electromagnetic radiation is quantised and the energy of the corresponding photons can be computed as $E = h \cdot \nu$ with Planck's constant h. In infrared (IR) spectroscopy, also the wavenumber

Table 3.1: The electromagnetic spectrum including the sub-bands in the infrared. Of special interest for this work is the short-wave infrared (SWIR) region where CO_2 and CH_4 absorption bands are located. Note that the partitioning of the electromagnetic spectrum is not entirely uniform throughout literature and may slightly differ in different publications.

Frequency ν [Hz]	Wavenumber $\bar{\nu}$ [cm^{-1}]	Notation	Wavelength λ	Sub-division
		Gamma rays		
$3 \cdot 10^{19}$	10^9		0.01 nm	
		X-rays		
$3 \cdot 10^{16}$	10^6		10 nm	
		Ultraviolet (UV)		
$7.5 \cdot 10^{14}$	$2.5 \cdot 10^4$		400 nm	
		Visible		
$4.3 \cdot 10^{14}$	$1.4 \cdot 10^4$		700 nm	
			1.4 µm	Near IR (NIR)
			3 µm	Short-wave IR (SWIR)
		Infrared (IR)	8 µm	Mid IR (MIR)
			15 µm	Thermal IR (TIR)
				Far IR (FIR)
$3 \cdot 10^{11}$	10		1 mm	
		Microwave		
$3 \cdot 10^8$	10^{-2}		1 m	
		Radio		

$\bar{\nu} = \lambda^{-1}$ (in cm^{-1}) is frequently used. Table 3.1 shows the range and notation of the electromagnetic spectrum as it is used in this work.

The infrared part of the spectrum, being located between the visible and the microwave region, ranges from about 700 nm to 1 mm wavelength. It is further divided into sub-bands of which, for example, the near infrared (NIR) is located between 700 nm and 1.4 µm and the short-wave infrared (SWIR) between 1.4 µm and 3 µm.

Molecular (or atomic) absorption of electromagnetic radiation can only take place if the photon energy matches the energy difference of two excitation states of the molecule. Different excitation mechanisms are associated to different spectral regions and their corresponding photon energy (see Table 3.2). Radiation in the UV, visible and X-ray range are generally associated with electronic transitions, whereas in the infrared the responsible transitions are vibrational and combined vibrational-rotational transitions. Absorption and emission of electromagnetic radiation are opposed processes corresponding to excitation and disexcitation of molecular states.

Where radiation in the thermal infrared is mainly emitted from the Earth and the atmosphere, energy in the SWIR region is predominantly originating from the sun. Figure 3.1 shows the spectrum of the sun as it can be observed at the top of the Earth's atmosphere and at the surface, respectively. It basically follows a Planck emission curve of a black-body with an effective temperature of 5800 K. Deviations from the black-body spectrum are mainly in the X-ray, far UV as well as the radio bands of the spectrum and particularly pronounced during flares and burst activity at the sun (Shu, 1982). Additionally, chemical elements in the sun's atmosphere remove energy from distinct

Table 3.2: Approximate electromagnetic spectral ranges and corresponding molecular excitation mechanisms and energies.

Spectral range	Energy [eV]	Excitation mechanism
Gamma rays	$> 10^5$	nuclei decay
X-rays, UV	$10^2 - 10^5$	electronic transitions
Visible, NIR	$1 - 10^2$	
Infrared	$10^{-3} - 1$	vibrational transitions
Microwave	$< 10^{-3}$	rotational transitions

wavelengths due to absorption resulting in the dark so called *Fraunhofer lines*.

3.2 Infrared spectroscopy

While in the NIR region also few electronic transitions are important, most of the absorption and emission in the infrared part of the electromagnetic spectrum are associated to coupled transitions in the vibrational and rotational states of molecules.

The energy states of a molecule can be derived as eigenvalues from the time independent Schrödinger equation assuming, for example, that nuclear and electronic motion can be decoupled due to the considerably lower mass of electrons (Born-Oppenheimer approximation). If, accordingly, also the fast vibration and the comparably slow rotation of the molecule are assumed to be independent, the total energy can be described as the sum:

$$E = E_{\mathrm{el}} + E_{\mathrm{vib}} + E_{\mathrm{rot}} \tag{3.1}$$

with the electronic energy component E_{el}, the vibronic energy E_{vib} and the energy associated with the rotation of the molecule E_{rot} where generally holds:

$$E_{\mathrm{el}} \gg E_{\mathrm{vib}} \gg E_{\mathrm{rot}} \tag{3.2}$$

This is also reflected in the wavelength of the corresponding absorbed or emitted radiation (see Table 3.2). Generally, the energy levels of the higher energetic state are denoted with one dash (E'), the lower energetic state with two dashes (E''). For transitions, the higher energetic state is followed by the lower one where the direction of the transition is indicated by an arrow, for example, $E'_{\mathrm{vib}} \longleftarrow E''_{\mathrm{vib}}$ for an absorption process.

Molecular vibrations can be understood as oscillations within the molecular potential well. If this potential was parabolic, the solution of the Schrödinger equation would equal the quantum mechanical harmonic oscillator. Empirically, however, the potential well is better described by the *Morse potential* as a function of the interatomic distance R:

$$V = D_{\mathrm{e}} \left[1 - \exp\left(-a\left(R - R_{\mathrm{e}}\right)\right)\right]^2 \tag{3.3}$$

where D_{e} is the dissociation energy, R_{e} the equilibrium distance between the atoms and a a molecule specific constant. The asymmetric Morse potential takes into account that with decreasing distance the potential rises leading to a stable equilibrium distance. For

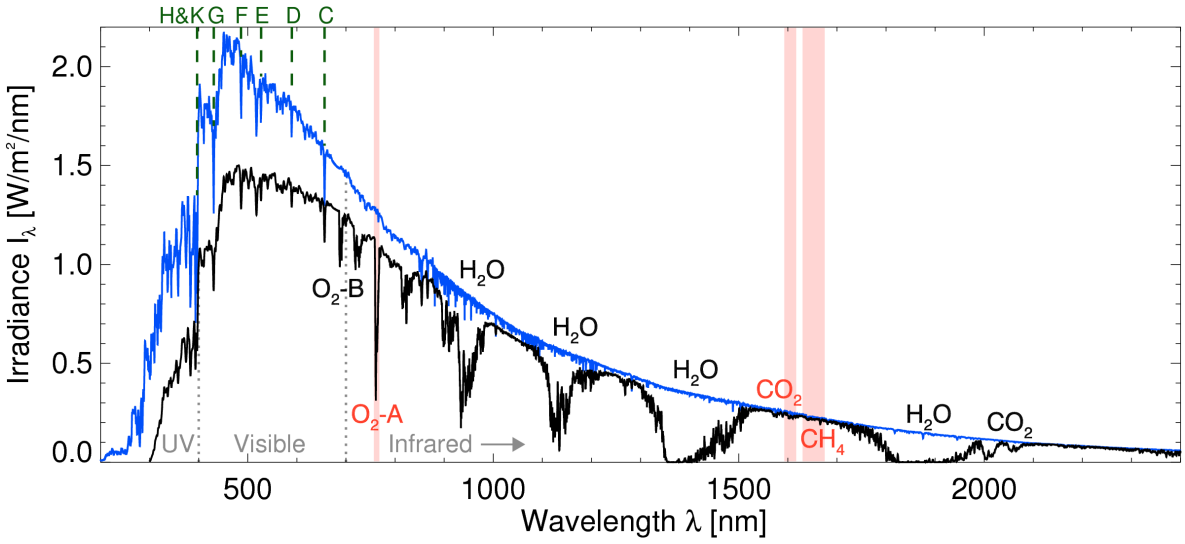

Figure 3.1: Solar spectrum as observed at the top of atmosphere (blue) and at the surface (black). The dashed green lines and letters on top denote the position and notation of a few so called Fraunhofer lines (see, for example, Jenkins and White, 2001), where elements in the sun's atmosphere remove energy from particular wavelengths. Several absorption features in the Earth's atmosphere due to particular molecules are pointed out. Most important for this work are the wavelength regions shaded in light red including absorption bands of CO_2, CH_4 and O_2. The displayed solar spectrum is the MODTRAN Thuillier plus corrected Kurucz ("thkur.dat") (Berk et al., 2000, and references therein). The surface spectrum has been computed from this solar spectrum using the radiative transfer model SCIATRAN (Rozanov et al., 2005) for low rural aerosol load and a solar zenith angle of 0°.

increasing distance from the equilibrium, the potential asymptotically reaches a maximum at the dissociation energy D_e until the molecule actually dissociates.

Using the Morse potential the resulting vibrational Energy becomes in a good approximation:

$$E_{\text{vib}} = \underbrace{\hbar\omega_e \left(v + \frac{1}{2}\right)}_{\text{harmonic oscillator}} \underbrace{- \frac{\hbar^2\omega_e^2}{4D_e}\left(v + \frac{1}{2}\right)^2}_{1^{\text{st}}\text{ order anharmonic}} \tag{3.4}$$

where ω_e denotes the angular frequency of the corresponding harmonic oscillator and $\hbar = \frac{h}{2\pi}$ the reduced Planck constant. Similar to the harmonic oscillator, the vibrational quantum number can take integral numbers[1] $v = 0, 1, 2, \ldots$, where the ground state $v = 0$ yields the zero point energy $E_{\text{vib},0} \neq 0$. The total vibrational energy of a molecule can then be computed as the sum over all normal modes including also anharmonic vibrational coupling to combination bands (see, for example, Sathyanarayana, 2005).

Figure 3.2 shows the characteristics of the Morse potential including a sketch of the vibrational states for two different electronic states. Transitions between electronic states are governed by the *Franck-Condon principle* assuming that the electron transition happens virtually instantaneously compared to the nuclei movement. It is most likely between

[1] The Latin, italic letter v denoting the vibrational quantum number is not to be confused with the Greek letter ν denoting the frequency.

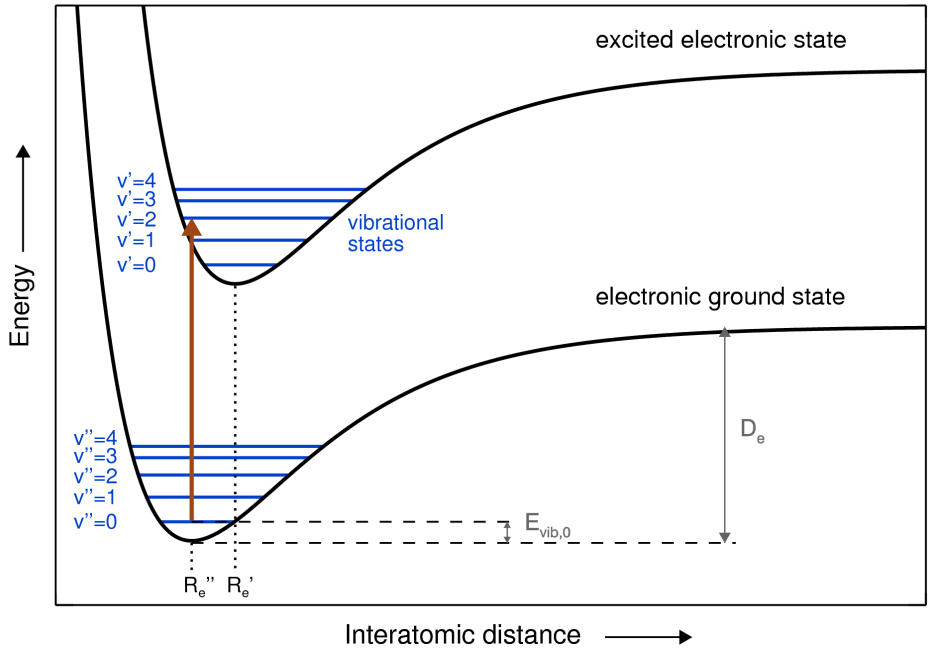

Figure 3.2: Vibrational Morse potential of a diatomic molecule for two different electronic states and indicated non-equidistant vibrational energy levels (not to scale). The brown arrow denotes a possible transition from the vibrational ground state $v'' = 0$ to the vibrational level $v' = 2$ of the excited electronic state. $E_{\text{vib},0}$ denotes the zero-point energy and D_e the dissociation energy. The equilibrium distances between the atoms in the excited and ground state are denoted by R'_e and R''_e, respectively. Electronic transitions generally correspond to X-rays, UV, visible or NIR spectral range.

vibrational levels whose wave functions, and hence the probability density for the location, largely overlap.

Applying a semi-classical approach, the rotational energy can be expressed analogue to the classical rotational energy assuming the molecule to be a rigid rotor with moment of inertia I:

$$E_\text{rot} = \frac{\boldsymbol{J}^2}{2I} \tag{3.5}$$

but with the quantised total angular momentum $\boldsymbol{J}$ where $|\boldsymbol{J}| = \hbar\sqrt{J\,(J+1)}$ introducing the rotational quantum number $J = 0, 1, 2, \ldots$.

In contrast to atoms that possess only 3 degrees of freedom for translational motion, molecules consisting of N atoms additionally have 3 degrees of freedom for rotational motion. If the molecule structure is linear, the rotation about the axis of symmetry is called *frozen* and the rotational degrees of freedom reduce to 2. The moment of inertia of the frozen rotation is very low and hence the corresponding energy for a transition, according to Equation (3.5), very high and may even reach the dissociation energy for the molecule. Generally, such transitions do not occur.

For symmetric top molecules with two equal principal moments of inertia ($I_\text{A} = I_\text{B} \neq I_\text{C}$), additionally the quantised projected angular momentum about the c-axis with the corresponding quantum number k (where $-J \leq k \leq J$) has to be taken into account.

Introducing the rotational constants $B = A = \frac{\hbar}{4\pi c I_B}$ and $C = \frac{\hbar}{4\pi c I_C}$, the corresponding rotational energy can be expressed as:

$$E_{rot} = hcBJ(J+1) + hc(C-B)k^2 \tag{3.6}$$

Purely rotational spectra can be observed in the microwave region provided that the molecule has a permanent electrical dipole moment which can interact with the electromagnetic radiation.

Coupled transitions between rotational and vibrational energy levels of a symmetric top molecule

$$E = E_{vib} + E_{rot} \tag{3.7}$$

$$= \hbar\omega_e\left(v+\frac{1}{2}\right) - \frac{\hbar^2\omega_e^2}{4D_e}\left(v+\frac{1}{2}\right)^2 + hcBJ(J+1) + hc(C-B)k^2 \tag{3.8}$$

give rise to infrared spectra as they are typically observed. Figure 3.3 shows the characteristic features for an infrared absorption spectrum with the so-called P-branch and R-branch corresponding to transitions with $\Delta J = -1$ and $\Delta J = +1$, respectively. Vibrational-rotational bands are only observed if the electric dipole moment is changing during the vibration. The vibrational mode is then called *infrared active*. A molecule consisting of N atoms has $3N-6$ vibrational normal modes (degrees of freedom) in the nonlinear and $3N-5$ in the linear case. The modes are denoted as parallel or perpendicular depending on the orientation of the oscillating dipole relative to the symmetry axis.

Transitions can be evaluated as forbidden or allowed by computing the transition moment integral leading to the so-called selection rules for molecular transitions. Forbidden transitions may actually occur but are much less likely than the allowed transitions. The selection rules for rotational-vibrational transitions are:

parallel vibrations	$\Delta v = \pm1, \pm2, \pm3, \ldots$	$\Delta J = \pm1$ $\Delta J = 0, \pm1$	$\Delta k = 0$	for $k = 0$ for $k \neq 0$
perpendicular vibrations	$\Delta v = \pm1, \pm2, \pm3, \ldots$	$\Delta J = 0, \pm1$	— $\Delta k = \pm1$	linear molecules otherwise

In contrast to the harmonic potential, for the anharmonic Morse potential also vibrational overtones $\Delta v = \pm2, \pm3, \ldots$ are possible. The pure vibrational transition ($\Delta J = 0$) is only allowed under certain conditions and gives, if present, rise to a Q-branch[2] (see Figure 3.3) that is rather strong due to the superimposing of lines from all rotational quantum numbers J. Due to interactions between vibrational and rotational motion, that have been neglected so far, the lines of the Q-branch are slightly displaced forming a broader absorption feature.

Equation (3.8) can be reduced in the case of a linear molecule (such as CO_2 or O_2) where there is no rotation about the axis of symmetry ($k = 0$) and for spherical tops

[2] An exception from the strict selection rules above are molecules where there is a contribution to the total angular momentum by the electrons as, for example, in the diatomic molecule NO for which a Q-branch can be observed at about 1875 cm^{-1} (Gillette and Eyster, 1939).

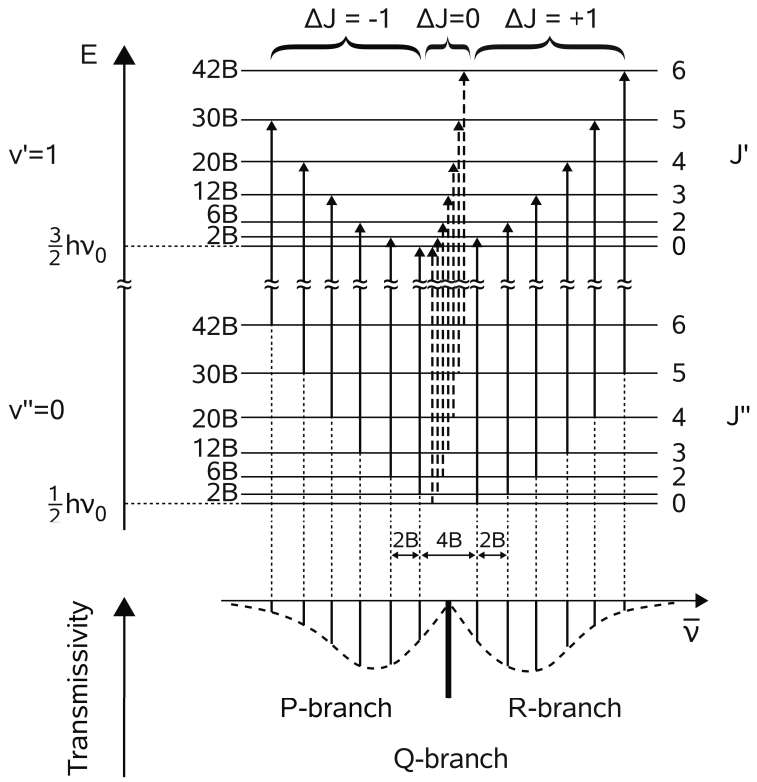

Figure 3.3: Schematic diagram of vibrational-rotational transitions giving rise to P- and R-branches with transitions of $\Delta J = -1$ and $\Delta J = +1$, respectively. The Q-branch ($\Delta J = 0$) cannot always be observed. The distance between rotational lines in P and R branch is approximately $2B$. The relative line strength indicated here is a direct consequence of the population and degeneracy of energy levels. Rotational-vibrational transitions generally correspond to the infrared spectral range.

(such as CH_4) where all principal moments of inertia are equal ($I_A = I_B = I_C$ and hence $A = B = C$):

$$E = \hbar\omega_e \left(v + \frac{1}{2}\right) - \frac{\hbar^2\omega_e^2}{4D_e}\left(v + \frac{1}{2}\right)^2 + hcBJ\,(J+1) \tag{3.9}$$

The relative line strength is mainly depending on the population level N_J of the originating rotational state and its degeneracy g_J, the number of states that have the same energy E_J. Assuming a local thermodynamic equilibrium, the population is governed by the temperature following a Boltzmann distribution:

$$\frac{N_J}{N_0} = \frac{g_J \exp\left(-\frac{E_J}{kT}\right)}{g_0 \exp\left(-\frac{E_0}{kT}\right)} = g_J \exp\left(-\frac{BhcJ\,(J+1)}{kt}\right) \tag{3.10}$$

where $g_J = 2J+1$ for linear and $g_J = (2J+1)^2$ for spherical top molecules. For small J, the degeneracy term g_J is dominating while for larger J, the exponential term dominates with a population and hence intensity maximum in between, as can also be seen schematically in Figure 3.3 for the P-branch and R-branch. Typically, the upper vibrational state (v') is not thermally excited due to its high energy level and hence largely unoccupied. *Hot bands* based on transitions with a ground state of $v \geq 1$ are therefore far less intense.

For a more accurate treatment of molecular absorption, more molecular characteristics have to be taken into account as, for example, the coupling of vibrations and rotations that both affect the interatomic distance. For example, due to the influence of vibrations on the interatomic distance, the spacing between lines is not exactly $2B$. For the P-branch, lines are slightly diverging for larger J (decreasing wavenumber) while for the R-branch, lines slightly converge with increasing J (increasing wavenumber). Furthermore, the nuclear spin contributing to the symmetry of the total wave function, which has to satisfy Pauli's principle, impacts the statistical population of rotational levels for molecules with a centre of symmetry. In case of $^{12}C^{16}O_2$ or $^{16}O_2$, for example, every other rotational level J is unoccupied so that every other rotational line in the spectrum cannot be observed leading to a spacing of $4B$ instead of $2B$ between lines. Note that vibrational levels v also contribute to the symmetry so that vibrational-rotational transitions with $\Delta v = \pm 1$ and $\Delta J = \pm 1$ are still possible (see, for example, Varandas and Xu, 2003).

Line broadening and mixing

In practice, lines are not infinitesimal narrow but span a certain energy (frequency) range. The natural line width ($\sim 1/t_0$), which is a consequence of the finite lifetime t_0 of a molecular state, is enhanced by pressure broadening that further reduces the lifetime due to molecular interaction and collisions ($\sim p/T^n$, $n = 0.5 \ldots 1$ depending on the molecule type) leading to a *Lorentz profile*. The directional movement of molecules additionally gives rise to a Doppler effect ($\sim \sqrt{T}$). In altitudes of about 20 to 50 km, both, pressure and Doppler broadening have to be considered which can be expressed in a *Voigt profile*. Below 20 km altitude, pressure broadening dominates (Liou, 2002).

When pressure broadened lines of, for example, a rotational fine structure overlap, line mixing occurs due to rotational inelastic collisions leading to an overall narrowing of lines (see, for example, Hartmann et al. (2008); Pine (1997) and for the impact of line mixing on CO_2, CH_4 and O_2 also Hartmann et al. (2009); Tran et al. (2010, 2006)).

Aside from line spectra introduced here, also continuum absorption, for example, for H_2O with relatively strong, continuous absorption bands in the infrared occurs. This continuum absorption is not well understood but might be due to formation of water vapour dimers or the cumulative absorption from line wings of strong absorption lines (see, for example, Cormier et al., 2005, and references therein).

3.3 Absorption spectra of carbon dioxide, methane and oxygen

Carbon dioxide

Carbon dioxide is a triatomic linear molecule and has three normal modes of vibration: a symmetric stretch $\bar{\nu}_1$, a doubly degenerate bending mode $\bar{\nu}_2$ and an asymmetric stretch $\bar{\nu}_3$ (Figure 3.4). The symmetric stretch $\bar{\nu}_1$ is not associated with a change in the dipole moment and is hence infrared-inactive only appearing in combination bands (Martin and Barker, 1932). The other modes are infrared-active and the perpendicular band $\bar{\nu}_2$ additionally gives rise to a Q-branch. Since CO_2 does not exhibit a permanent dipole

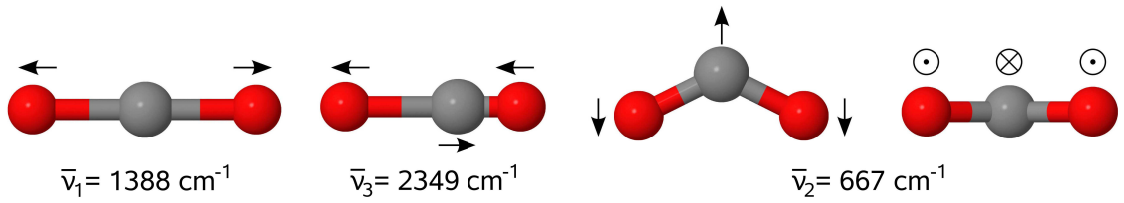

Figure 3.4: Vibrational modes of CO_2: symmetric stretch ($\bar{\nu}_1$), asymmetric stretch ($\bar{\nu}_3$) and the doubly degenerate bending mode ($\bar{\nu}_2$).

moment, a pure rotational spectrum cannot be observed. The vibrational modes are summarised in Table 3.3. Due to the spectral proximity of $\bar{\nu}_1 \approx 2\bar{\nu}_2$, large Fermi resonance takes place leading to spectral bands that are grouped in polyads. Using the notation by Amat and Pimbert (1965), the different bands can be described by $(\nu_1 \nu_2^l \nu_3)_r$ (see also McCluskey and Stoker, 2006, and references therein), with the vibrational quantum numbers ν_i of the associated fundamental mode and $l = \nu_2, \nu_2 - 2, \ldots, 0$ or 1 the angular momentum associated with the degenerated bending mode. The rank $r \in \{1, 2, \ldots, \nu_1 + 1\}$ given in Roman numerals denotes the level in the Fermi polyad $\{(\nu_1 \nu_2^l \nu_3), ((\nu_1 - 2)(\nu_2 + 2)^l \nu_3), \ldots, (0(\nu_2 + 2\nu_1)^l \nu_3)\}$ sorted by decreasing energy.

For this work, the absorption band in the SWIR around 1.6 µm (centred at 6228 cm^{-1}) has been measured corresponding to the transition from the ground state (00^00) to the vibrational level $(30^01)_{\mathrm{III}} = (14^01)$ of the Fermi tetrad (see Figure 3.6). The P-wing for this absorption band is overlapped by weak absorption corresponding to the transition $(31^11)_{\mathrm{III}} \longleftarrow (01^10)$ centred at 6196 cm^{-1} (see, for example, Régalia-Jarlot et al., 2006; Toth et al., 2008). Note that Q-branches for CO_2 occur only when $\Delta\nu_2$ is odd (Martin and Barker, 1932) and hence are not observed for the transitions mentioned above.

Methane

Methane is a spherical top molecule with tetrahedral symmetry (bonding angle 109.5°) and four normal modes of vibration: a symmetric stretching mode $\bar{\nu}_1$, a doubly degenerate

Table 3.3: Vibrational modes of CH_4 and CO_2 (after Rothman et al., 2009; Toth et al., 2008; Albert et al., 2009).

Molecule	Mode	Type	$\bar{\nu}$ [cm^{-1}]	λ [µm]	Degeneracy	Activity
CH_4	$\bar{\nu}_1$	symmetric stretch	2916	3.4	–	Raman
	$\bar{\nu}_2$	symmetric bend	1533	6.5	2	Raman
	$\bar{\nu}_3$	asymmetric stretch	3019	3.3	3	IR, Raman
	$\bar{\nu}_4$	asymmetric bend	1310	7.6	3	IR, Raman
CO_2	$\bar{\nu}_1$	symmetric stretch	1388	7.2	–	Raman
	$\bar{\nu}_2$	bend	667	15.0	2	IR
	$\bar{\nu}_3$	asymmetric stretch	2349	4.3	–	IR

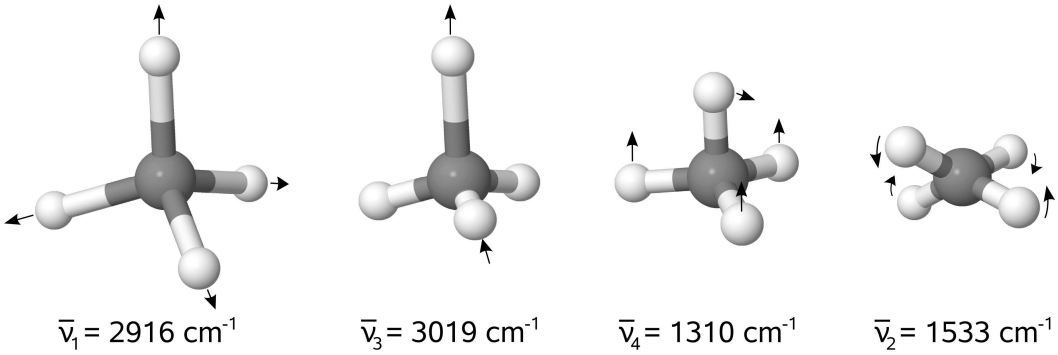

Figure 3.5: Schematic of vibrational modes of CH_4: symmetric stretch $\bar{\nu}_1$ ("breathing"), triply degenerate asymmetric stretch $\bar{\nu}_3$, triply degenerate asymmetric bending mode $\bar{\nu}_4$ ("umbrella mode") and doubly degenerate symmetric bending mode $\bar{\nu}_2$ ("twisting"). Small movements of the H-atoms and the C-atom are not shown (see, for example, Wu et al., 2006, for a more detailed illustration).

symmetric bending mode $\bar{\nu}_2$, a triply degenerate asymmetric stretching mode $\bar{\nu}_3$ and a triply degenerate asymmetric bending mode $\bar{\nu}_4$ (see Figure 3.5). Only the asymmetric vibrations are infrared-active (see Table 3.3). CH_4 has no permanent dipole moment and hence no pure rotational spectrum.

The corresponding fundamental frequencies exhibit a simple approximate relation $\bar{\nu}_1 \approx \bar{\nu}_3 \approx 2\bar{\nu}_2 \approx 2\bar{\nu}_4$ leading to a polyad structure with polyads P_n defined by $n = 2(v_1 + v_3) + v_2 + v_4$ and the vibrational quantum numbers v_i (Boudon et al., 2006). The number of vibrational levels $(v_1 v_2 v_3 v_4)$ depends on n and are further divided into sublevels due to the degeneracy of the normal vibrations and vibrational angular momentum l.

Relevant for this work is the transition from the ground state (0000) to a sublevel of the overtone in the $\bar{\nu}_3$ mode (0020) around 1.66 µm (centred at 6005 cm^{-1}) in the tetradecad P_4. The transition exhibits a strong Q-branch as can be seen in Figure 3.6. Accurate line positions of P-, Q- and R-branch are given, for example, in Frankenberg et al. (2008). This band is overlapped by other weak bands from the same tetradecad (see, for example, Boudon et al., 2006). The spectral proximity of the $2\bar{\nu}_3$ band to the above mentioned CO_2 absorption is of advantage for the retrieval described later.

Oxygen

Oxygen (O_2) is present in the atmosphere as a homonuclear, diatomic molecule and hence exhibits no pure rotational or rotational-vibrational spectrum due to the lack of permanent or vibrational dipole moment. However, unlike most other molecules, O_2 has a strong absorption line in the NIR region associated with the electronic transition from the triplet ground state exhibiting two unpaired electrons with parallel spin to a metastable singlet state: $O_2(b^1\Sigma_g^+) \longleftarrow O_2(X^3\Sigma_g^-)$ where Σ denotes a total orbital angular momentum about the molecule axis of $\Lambda = 0$. The subscript g denotes the even ("gerade") parity of the wave function with respect to inversion and the superscript + the symmetry with respect to reflection on the molecule plane. The leading capital X and the lower case b denote the ground state and the second deepest excited energetic state with multiplicity (1) different from the ground state (3), respectively. This transition is associated to the O_2-A absorption

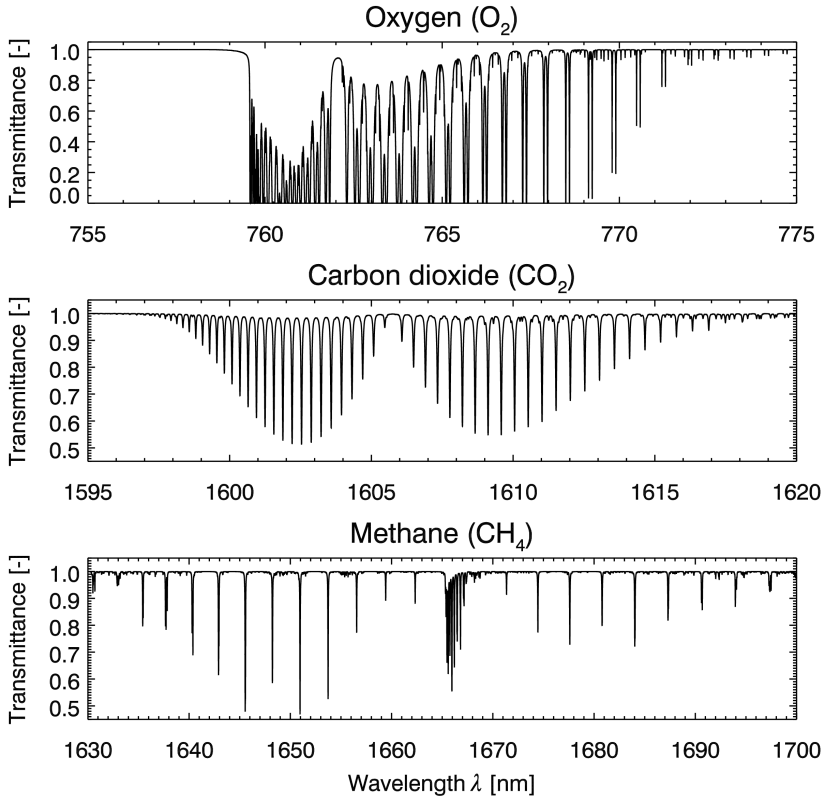

Figure 3.6: Transmittances of oxygen, carbon dioxide and methane for 900 hPa and 282 K for relevant wavelengths. The oxygen transition is $O_2(b^1\Sigma_g^+) \longleftarrow O_2(X^3\Sigma_g^-)$. For the CO_2 transition $(30^01)_{III} \longleftarrow (00^00)$ and for the $2\bar{\nu}_3$ band of CH_4, the P- and R-branch are clearly visible. For CH_4, additionally the strong Q-band at about 1666 nm can be observed. (Spectroscopic data taken from the HITRAN 2008 database, Rothman et al., 2009.)

band ($\Delta v = 0$, $0 \longleftarrow 0$) at 762 nm (13122 cm^{-1}). An overtone band of this transition leads to the weaker O_2-B band ($\Delta v = 1$, $1 \longleftarrow 0$) at 687 nm (14550 cm^{-1}).

During the electronic transitions, the rotational constants decrease ($B' < B''$) giving rise to a shading to the red of branches. Additionally, the change in spin leads to a more complex branch structure with ^{R}R-, ^{R}Q-, ^{P}P- and ^{P}Q-branches with the notation $^{\Delta N}\Delta J$, where J is the total angular momentum, and N the angular momentum excluding spin. Accordingly, the doublets in the P-wing in Figure 3.6 are due to overlapping ^{P}P- and ^{P}Q-branches with a spacing of about 2 cm^{-1}. Additional transitions overlapping with the P-wing are due to the hot band $O_2(^1\Sigma_g^+, v' = 1) \longleftarrow O_2(^3\Sigma_g^-, v'' = 1)$ (see Babcock and Herzberg, 1948; Ritter and Wilkerson, 1987).

3.4 Radiative transfer in the atmosphere

Modelling the transfer of electromagnetic radiation through the atmosphere requires the consideration of various interaction mechanisms of which the most important are specified in the following. Their influence is evaluated with respect to the change dL_λ they cause in

the monochromatic radiance L_λ (given in $\mathrm{W\,m^{-2}\,sr^{-1}\,nm^{-1}}$) for a particular wavelength interval from λ to $\lambda + \mathrm{d}\lambda$ (Liou, 2002):

$$L_\lambda = \frac{\mathrm{d}E}{\cos\theta \; \mathrm{d}A \, \mathrm{d}\Omega \, \mathrm{d}t \, \mathrm{d}\lambda} \tag{3.11}$$

where $\mathrm{d}E$ is the radiant energy emitted from an element of area $\mathrm{d}A$ into the solid angle $\mathrm{d}\Omega$ at an angle of θ to the normal of $\mathrm{d}A$ during the time interval $\mathrm{d}t$.

Molecular absorption

The absorption by molecules as introduced in the previous sections is described by the molecular absorption cross-section $\sigma^{\mathrm{a}}_\lambda$ (given in $\mathrm{cm^2}$) which strongly depends on the wavelength but generally also is a function of pressure p and temperature T that control line shape and population of molecular states (see Section 3.2).

Taking into account the number density n (in molecules $\mathrm{cm^{-3}}$) of the respective gas species and integrating over a path $\mathrm{d}s$ yields the dimensionless optical depth (or optical thickness) τ_λ:

$$\tau_\lambda = \int_{s_1}^{s_2} \sigma^{\mathrm{a}}_\lambda(s)\, n(s)\, \mathrm{d}s = \int_{s_1}^{s_2} \kappa^{\mathrm{a}}_{\lambda(s)}\, \mathrm{d}s \tag{3.12}$$

with the absorption coefficient $\kappa^{\mathrm{a}}_\lambda$.

Elastic scattering

Elastic scattering in the atmosphere refers to a change of direction of the incident radiation while no energy exchange takes place. Elastic scattering of electromagnetic plane waves by homogeneous, spherical particles with radius r is treated in the Mie-theory (Mie, 1908) that analytically solves the Maxwell equations by a series of cylindrical functions. While for large size parameters $a = 2\pi r \lambda^{-1} \gg 1$ the solution approaches the geometric optics, for $a \ll 1$ it passes into the result for Rayleigh scattering from small particles[3] (Rayleigh, 1871). Rayleigh scattering of unpolarised light can be described by the scattering cross-section $\sigma^{\mathrm{sc}}_{\mathrm{Ra}}$ and the phase function P (normalised to 4π) that describes the angular distribution of the scattered light depending on the scattering angle θ (Liou, 2002; Goody and Yung, 1989):

$$\sigma^{\mathrm{sc}}_{\mathrm{Ra},\lambda} \approx \frac{8\pi^2 \left(m_r^2 - 1\right)^2}{3n^2} \cdot \frac{1}{\lambda^4} \cdot f(\delta) \tag{3.13}$$

$$P_{\mathrm{Ra},\lambda}(\theta) = \frac{3}{2} \cdot \frac{(1+\delta) + (1-\delta)\cos^2\theta}{2+\delta} \tag{3.14}$$

where m_r denotes the real refractive index of the scatterer, n its number per unit volume and $f(\delta) = (6+3\delta)/(6-7\delta)$ the King correction (King, 1923) accounting for anisotropy characterised by the depolarisation factor δ ($\delta_{\mathrm{air}} \approx 0.035$ (Liou, 2002)).

[3] Strictly speaking, Rayleigh scattering being based on the polarisability of a scatterer includes also inelastic components like the rotational Raman lines (see below) and the Brillouin doublet even though these phenomena were not known at the time of the original work (see Young, 1980).

Rayleigh scattering being proportional to λ^{-4} accounts for the blue colour of the sky and consequently also leads to a strongly reduced scattering efficiency in the infrared.

For scattering by particles with intermediate size parameters $a \approx 1$, often simply termed Mie scattering, the wavelength dependence is much weaker and Mie phase functions generally exhibit a stronger forward peak than Rayleigh scattering. The exact solution is computationally expensive and not available for many particle shapes. Therefore, often the Mie phase function is approximated by a Henyey-Greenstein function (Henyey and Greenstein, 1941) (see Appendix A).

Inelastic scattering

In contrast to elastic scattering, inelastic scattering involves a change of energy and hence gives rise to a frequency shift of the scattered radiation compared to the incident radiation. For example, Raman scattering leads to less deep Fraunhofer lines in scattered sunlight as compared to direct sunlight (Grainger and Ring, 1962), known as the Ring effect.

In Raman scattering events, a molecule changes its energetic state and the corresponding energy is associated with a frequency change in the scattered light. Raman scattering accounts for only a small fraction of the total scattering in the atmosphere. For the most abundant species in the atmosphere, N_2, the ratio of Raman and elastic Rayleigh scattering is 2.3 % for rotational and 0.07 % for vibrational Raman scattering at 500 nm (Sneep and Ubachs, 2005; Moosmüller, 1994). Similar to Rayleigh scattering, the Raman cross section is proportional to λ^{-4} (see, for example, Schrader and Moore, 1997) and becomes less important in the infrared spectrum. In the short-wave infrared at 2.36 µm, for example, the rotational Raman effect on radiances is generally less than 0.1 % for an instrumental slit function of 0.2 nm (Buchwitz et al., 2000; Buchwitz, 2000).

Inelastic Brillouin scattering (see, for example, Vieitez et al., 2010) as a result of an inhomogeneous index of refraction (acoustic modes, thermally induced density fluctuations) in the air occurs but only plays a minor role.

Aerosols

Aerosols of sizes between about 0.001 µm and 20 µm originating from various natural and anthropogenic sources have been observed in the atmosphere. Their influence on the radiative transfer is predominantly due to scattering (mainly Mie scattering). Absorption generally plays a minor role, except, for example, for mineral and water-soluble particles and, in particular, for black carbon (soot).

By introducing a complex refractive index, the Mie theory allows a detailed treatment of aerosol scattering and absorption only in special cases. The general application to the atmosphere is complex due to varying microphysical properties such as composition, shape, size and inhomogeneity of the particles. However, the wavelength dependence of aerosol extinction, which is the combined effect of scattering and absorption described by the extinction cross-section $\sigma_\lambda^{\text{ext}}$, approximately follows a $\lambda^{-\alpha}$ law, where α is the Ångström exponent (Ångström, 1929, and references therein). The Ångström exponent varies for different wavelength ranges (see, for example, Schuster et al., 2006) and has typical values between 0 and 1.5 (Hess et al., 1998). The phase function can be approximated, for example, by a Henyey-Greenstein function (see Appendix A).

Clouds

Clouds are a special case of aerosols and can be divided into liquid and ice clouds (cirrus). Single liquid water droplets can be described by the Mie theory with respect to their radius a but clouds with particle size distributions that generally feature various sizes of drops are better described by the effective radius $a_{\text{eff}} = \langle a^3 \rangle / \langle a^2 \rangle$, where $\langle \cdot \rangle$ denotes the mean throughout the distribution. Combining the effective radius with the liquid water content (LWC, given in $\mathrm{g\,cm^{-3}}$), the extinction coefficient can be approximately derived independently of the exact distribution (Kokhanovsky, 2006, and references therein).

Computing extinction for cirrus clouds consisting of ice crystals additionally requires knowledge on the crystal shape. Ice crystals exhibit numerous types of shapes that may be approximated by irregularly shaped, fictive particles such as fractals (Kokhanovsky, 2006). The SCIATRAN radiative transfer model (Rozanov et al., 2005), that has been used for this work, can utilise regularly shaped tetrahedrons of the 2nd fractal generation, the optical properties of which (phase function, extinction coefficient, etc.) have been determined statistically via a Monte Carlo technique (see also Reuter et al., 2010).

Cirrus clouds can be characterised by the integral of the ice water content (IWC, in $\mathrm{g\,cm^{-3}}$) along a (vertical) light path, referred to as the ice water path (IWP, in $\mathrm{g\,cm^{-2}}$):

$$\mathrm{IWP} = \int_{z_1}^{z_2} \mathrm{IWC}\, \mathrm{d}z \tag{3.15}$$

where z_1 and z_2 can be defined as cloud base height and cloud top height, respectively, with a cloud geometrical thickness of $z_2 - z_1$. The cloud optical thickness is analogue to Equation (3.12):

$$\tau_{\text{cl}} = \int_{z_1}^{z_2} \sigma^{\text{ext}}_{\lambda,\text{cl}}(s)\, n_{\text{cl}}(s)\, \mathrm{d}s \tag{3.16}$$

where $\sigma^{\text{ext}}_{\lambda,\text{cl}}$ and n_{cl} denote the extinction cross section and the number density of cloud particles, respectively.

Surface reflection

The simplified reflectivity as used in Equation (1.3) has to be refined for uses in remote sensing. Generally the surface reflection depends on wavelength, surface type, direction of the incident light (θ', ϕ') and direction of the reflected light (θ, ϕ). The directions are defined by the zenith angles θ, θ' towards the vertical and the azimuth angles ϕ, ϕ' relative to a distinguished horizontal direction (for example, sun direction or simply north). The resulting function is called a bi-directional reflectance distribution function (BRDF).

The BRDF can often be approximated by a spectral reflectance (or spectral albedo) α_λ assuming a perfect Lambertian reflector with an isotropic reflection (radiance independent of direction) and is defined as the ratio of the monochromatic radiance L_λ integrated over the hemisphere $\Omega = 2\pi$ and the incoming monochromatic irradiance (flux density) $I_\lambda \cos\theta'$ (in $\mathrm{W\,m^{-2}\,nm^{-1}}$):

$$\alpha_\lambda = \frac{\int_\Omega L_\lambda \cos\theta \,\mathrm{d}\Omega}{I_\lambda \cos\theta'} = L_\lambda \cdot \frac{\pi}{I_\lambda \cos\theta'} \tag{3.17}$$

Formulating the radiative transfer

A mathematical formulation of the radiative transfer problem yields in a simple form (Goody and Yung, 1989):

$$\frac{\mathrm{d}L_\lambda(\boldsymbol{s})}{\mathrm{d}s} = \kappa_\lambda^{\mathrm{ext}} \left(-L_\lambda(\boldsymbol{s}) + J_\lambda(L,\boldsymbol{s})\right) \tag{3.18}$$

where $-L_\lambda$ describes the losses of radiance in direction $\boldsymbol{s}$ due to absorption and scattering in a path element $\mathrm{d}s$ and J_λ denotes the source term describing the radiation gain due to thermal emission and due to light scattered into direction $\boldsymbol{s}$. The total extinction coefficient $\kappa_\lambda^{\mathrm{ext}}$ is the sum of all scattering and absorption coefficients from molecules, aerosols and clouds.

Thermal emission, in the most simple form, equals the Planck radiation but is more complex when thermodynamic equilibrium cannot be assumed (Goody and Yung, 1989). The scattering part of the source function J_λ^{sc} can be described using the phase function P_λ (Goody and Yung, 1989; Roedel and Wagner, 2011):

$$J_\lambda^{\mathrm{sc}}(L,\boldsymbol{s}) = \frac{\kappa_\lambda^{\mathrm{sc}}}{\kappa_\lambda^{\mathrm{ext}}} \int_{\Omega^*} L_\lambda(\theta^*,\phi^*) \frac{P_\lambda(\theta,\phi,\theta^*,\phi^*)}{4\pi}\,\mathrm{d}\Omega^* \tag{3.19}$$

where * denotes the direction relative to the direction of interest.

When source terms can be neglected, the radiative transfer Equation (3.18) simplifies to:

$$\frac{\mathrm{d}L_\lambda(\boldsymbol{s})}{L_\lambda(\boldsymbol{s})} = -\kappa_\lambda^{\mathrm{ext}}\,\mathrm{d}s \tag{3.20}$$

which is solved by the Lambert-Beer law of exponential attenuation:

$$L_\lambda(s) = L_0 \exp\left(-\tau_\lambda(s)\right) \tag{3.21}$$

where $\tau_\lambda(s) = \int_{s_1}^{s_2} \kappa_\lambda^{\mathrm{ext}}(s)\,\mathrm{d}s = \int_{s_1}^{s_2} \sigma_\lambda^{\mathrm{ext}}(s)\,n(s)\,\mathrm{d}s$ is the corresponding optical depth.

The Lambert-Beer law holds strictly only for monochromatic radiances. Generally, the measured L_λ is spectrally not fully resolved but given at instrument resolution (see Section 4.1). Then, the measured signal will no longer be a simple exponential function of the absorbers' number density profile $n(s)$ (see, for example, Richter and Wagner, 2011). This effect is particularly pronounced in the presence of strong absorption lines (see, for example, Frankenberg et al., 2005b) and absorption cross sections that are highly dependent on wavelength (Richter and Wagner, 2011).

Part II

Instrument and retrieval

4

The Methane Airborne Mapper instrument

The Methane Airborne Mapper (MAMAP) instrument is a passive remote sensing instrument designed for airborne applications to measure and retrieve columns of CH_4 and CO_2 particularly from point and localised sources. It builds on the heritage of the SCIAMACHY project, which has demonstrated that CH_4 and CO_2 can be measured and retrieved from space (Schneising et al., 2011; Burrows et al., 1995; Bovensmann et al., 1999). MAMAP was developed in a cooperation between the University of Bremen and the Helmholtz Centre Potsdam – GFZ German Research Centre for Geosciences.

Figure 4.1 shows the MAMAP system consisting of a spectrometer rack and a computer rack designed for flexible operations on a variety of airborne platforms. The system is equipped with down-looking telescopes for nadir observations and an up-looking inlet for zenith observations. In the following, the instrument and its specifications will be shortly described.

Parts of this chapter have been published in Krings et al. (2011) and Gerilowski et al. (2011) where additional information on the technical setup of MAMAP can be found.

4.1 Technical overview and measurement geometry

Using two separate grating spectrometers integrated into the spectrometer unit, MAMAP measures in the short-wave infrared (SWIR) and in the near infrared (NIR) region of the electromagnetic spectrum. The SWIR spectrometer covers the region of about 1590 nm to 1690 nm with a resolution of approximately 0.82 nm FWHM observing CH_4 and CO_2 absorption bands from which the CH_4 and CO_2 columns can be retrieved. The additional NIR spectrometer measures the O_2-A absorption band between about 757 nm and 768 nm with a resolution of approximately 0.46 nm FWHM. The retrieved O_2 columns can be used to convert the greenhouse gas columns into column-averaged dry air mole fractions (see Section 5). In contrast to the non-imaging SWIR spectrometer, the NIR spectrometer

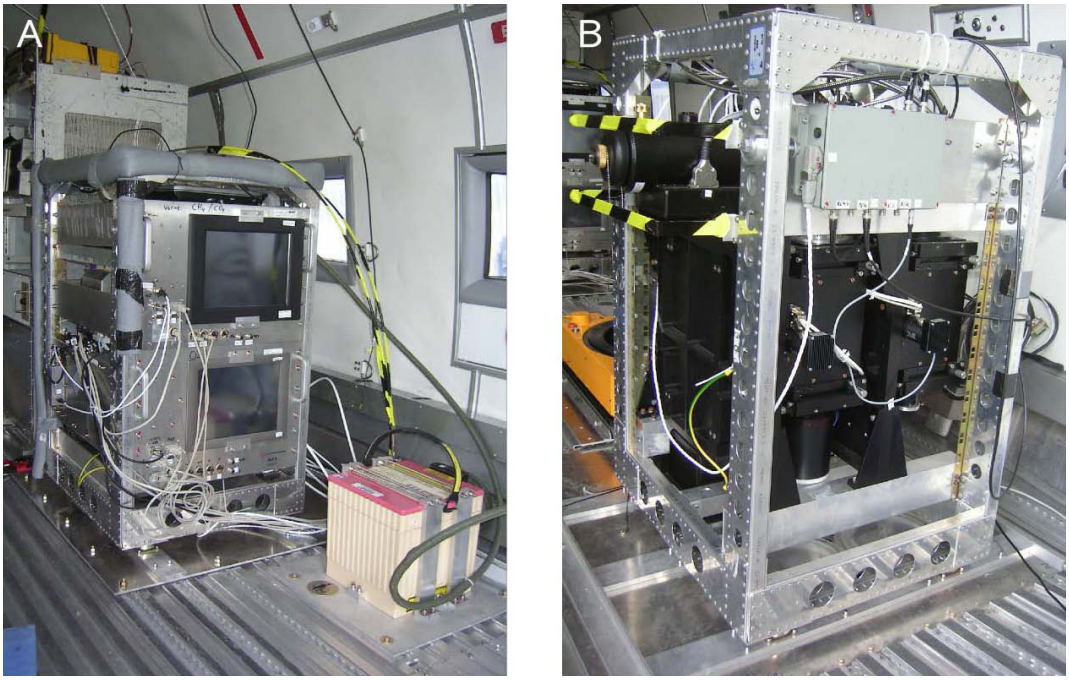

Figure 4.1: MAMAP computer rack and battery installed in the Polar 5 aircraft of the Alfred Wegener Institute for Polar and Marine Research (AWI) (Panel A). The green cable conduit connects the computer rack with the spectrometer rack (Panel B). The spectrometer rack is installed above two windows for the nadir telescopes.

is an imaging pushbroom sensor which means that it can simultaneously measure several adjacent ground scenes within its across track swath relative to flight direction.

MAMAP's nadir observation mode relies on solar backscatter as indicated in Figure 4.2. Light passes through the whole atmosphere before being reflected from the ground and reaching the instrument that hence measures the absorption spectra of the corresponding slant atmospheric column. Light passes twice below the aircraft, once before and once after reflection from the ground. This gives rise to an increased sensitivity below the aircraft compared to the atmospheric fraction above the aircaft with implications for the retrieval of column-averaged dry air mole fractions (see Section 5).

The instantaneous field of view (IFOV) of the SWIR spectrometer looking nadir is about $1.34° \times 0.02°$ (across track $\times$ along track). For an exposure time of about 0.6 s, a typical aircraft altitude of 1.25 km and 200 km h^{-1} ground speed, this results in a ground scene size of about 29 m $\times$ 33 m, where the along track extension is primarily determined by ground speed and exposure time. The parameters above are a valid configuration in most cases where the surface spectral reflectance is not significantly below 0.18 (assuming a Lambertian reflector), which is about the spectral albedo of vegetation. Over surfaces with lower spectral reflectance (mainly water), the exposure time has to be extended accordingly or the instrument can be operated in sunglint (see Section 10).

The imaging NIR sensor for O_2-A band measurements has a considerably larger field of view across track (5.85°) divided into 85 pixels of which about 1/4 are software binned. By selecting the corresponding pixels, an accurate field of view matching between NIR and SWIR spectrometer can be achieved. Later on, MAMAP has been modified for glass

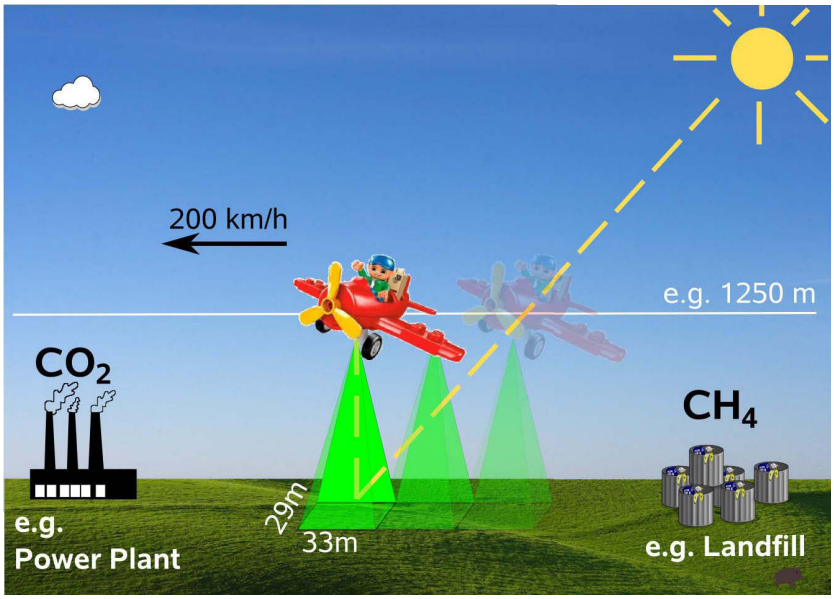

Figure 4.2: Sketch of the MAMAP measurement geometry. (Parts of the image ©2011 The LEGO Group. Used with permission.)

fibre coupled operation using a single telescope for both spectrometers (see Section 4.4).

Additionally, the instrument can be operated in zenith mode by internally switching a mirror (see Figure 4.3). Zenith sky observations can be utilised as reference measurements of the atmosphere above the sensor.

The instrument has been developed for airborne application up to altitudes of 4 km and more than 20 km for non-pressurised and pressurised cabins, respectively, and can generally fly well above the planetary boundary layer if necessary. To monitor position and pointing of the instrument, MAMAP is equipped with a 5 Hz GPS and a gyro-system recording the attitude (roll, pitch, yaw) in addition to a colour CCD pointing camera ($7.2° \times 5.7°$, across track $\times$ along track) that gives further information about the ground scene.

4.2 Selection of infrared channels

For both greenhouse gases, CH_4 and CO_2, absorption bands in the SWIR are used relying on solar backscatter. In this way, high sensitivity down to the surface can be achieved (see Section 5.2). Trace gas retrievals from thermal infrared bands, on the contrary, are strongly dependent on the temperature contrast to the ambient scene which is in particular challenging for the near surface layers (Crevoisier et al., 2003). The weak CO_2 band at 1.60 µm (see Section 3.3) is relatively free of absorption of other gases (in particular water vapour, see Figure 4.4), non-saturating and thermal emissions from atmosphere and instrument are small (Crisp et al., 2004) leading to less detector noise. The non-saturated absorption reacts almost linear to changes in CO_2 abundances compared to the saturated strong absorption band at around 2.0 µm (Crisp et al., 2004). As an addition, the 2.0 µm absorption can be useful in providing supplementary information on cloud and aerosol

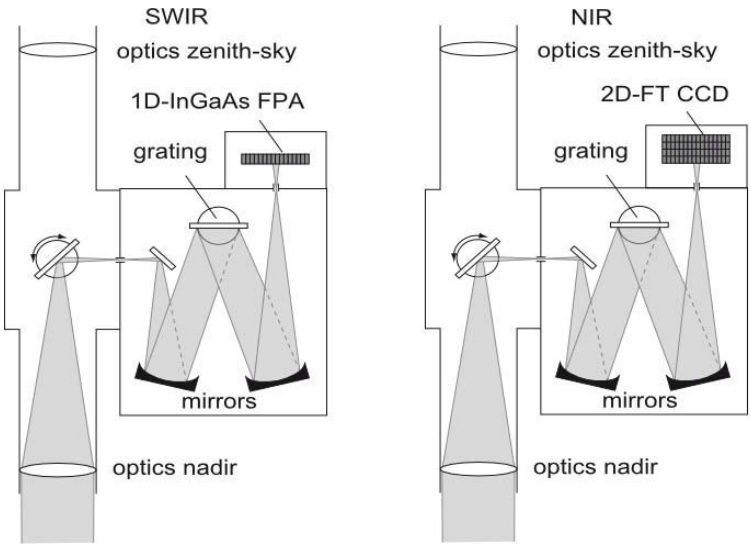

Figure 4.3: Sketch of the MAMAP spectrometer modules (Gerilowski et al., 2011). Both spectrometers have two separate light intake telescopes pointing towards nadir and zenith-sky directions for measurements of nadir and zenith radiances. A mirror enables switching between both modes. For zenith irradiance measurements, zenith optics can be equipped optionally with glass fibres and transmissive diffuser optical inlets (not shown in this sketch).

load (Bovensmann et al., 2010). However, this has not been implemented for the MAMAP sensor.

Note that the CO_2 absorption used for MAMAP is not identical with the band used for retrieval of CO_2 from SCIAMACHY at about 1.575 µm, where a different band was chosen due to detector degeneration of the 6+ channel (Schneising et al., 2009; Kleipool et al., 2007). The MAMAP band has the additional advantage that it completely avoids potential minor influence of oxygen singlet delta emissions[1] (airglow) at 1.58 µm (Vallance Jones and Harrison, 1958).

The CO_2 1.6 µm absorption band is located close to the CH_4 absorption band at 1.67 µm (see Section 3.3) so that both absorptions can be measured by one InGaAs line detector with good spectral resolution. Among others, this provides excellent bore-sighting and the spectral closeness ensures a similar light path for both bands having advantages for the retrieval of column-averaged dry air mole fractions.

4.3 Measured quantity

In nadir mode, MAMAP measures upwelling radiance (see Equation (3.11)). When operated in zenith sky mode, the instrument records downwelling radiance or, if using a diffuser plate, solar irradiance and diffuse downwelling irradiance. By geometry, the radiance received by the instrument from a homogeneous source subtending a solid angle

[1] These are emissions of excited oxygen molecules returning to ground state: $O_2(a^1\Delta_g,\ v' = 0) \longrightarrow O_2(X^3\Sigma_g^-,\ v'' = 0)$ at 1.27 µm and $O_2(a^1\Delta_g,\ v' = 0) \longrightarrow O_2(X^3\Sigma_g^-,\ v'' = 1)$ at 1.58 µm. The excited O_2 molecules originate predominantly from photolytic destruction of ozone and emission intensities are not any more well described using the assumptions of thermodynamic equilibrium.

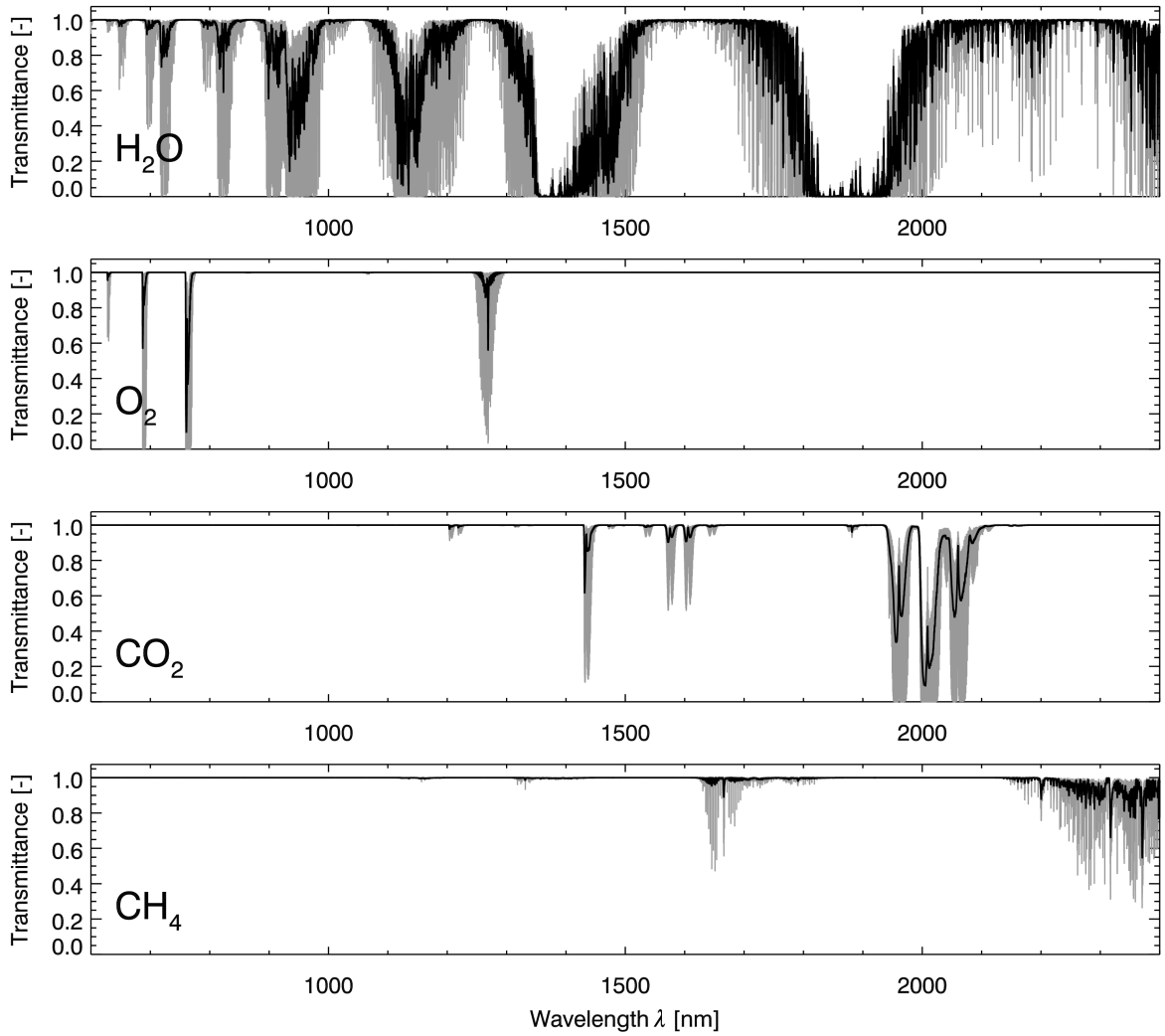

Figure 4.4: Transmittance of relevant absorbers for the MAMAP measurements for conditions at about 1 km altitude (900 hPa, 282 K) according to the 1976 U.S. Standard Atmosphere (U.S. Committee on Extension to the Standard Atmosphere, 1976). Monochromatic transmittances are shown in grey, convoluted with a Gaussian instrument slit function (FWHM=0.46 nm for H_2O and O_2, FWHM=0.82 nm for CO_2 and CH_4) in black.

given by the field of view thereby equals the radiance of a source element observed over a solid angle equivalent to the instrumental field of view.

The optics of the instrument focus the incoming light on the entrance slit of the spectrometer which is subsequently dispersed by a reflective grating and reimaged onto the detector. The shape of the imaged, monochromatic slit, and hence the spectral resolution of the instrument, is determined by the instrumental transfer function or slit function f so that the observed radiance is the convolution of the actual radiance with the (normalised) instrumental slit function.

For the SWIR channel, the slit function is best described by the sum of two slightly shifted Gaussian functions with an overall approximate FWHM of 0.82 nm (see Appendix B) while the preliminary slit function for the NIR channel is a single Gaussian function with FWHM

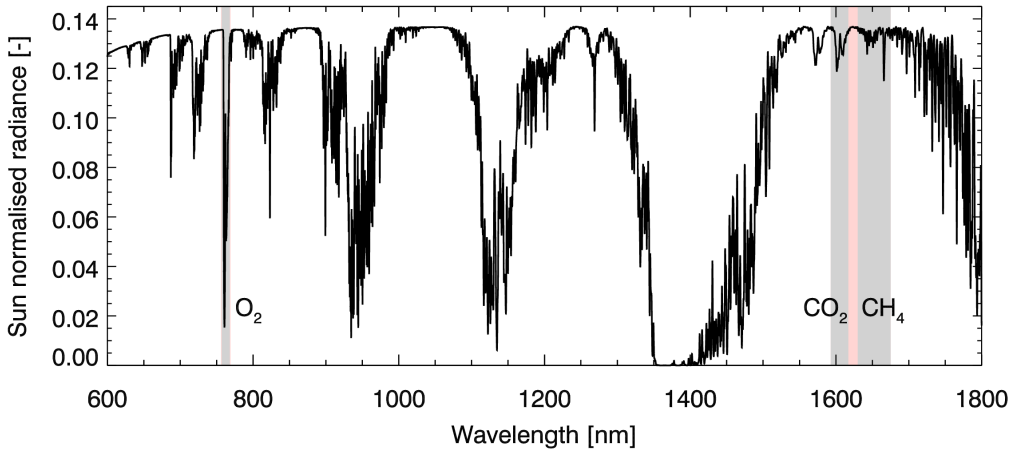

Figure 4.5: Simulated sun normalised radiances for a typical MAMAP setup with an aircraft altitude of 1250 m, solar zenith angle of 40 °, lambertian surface spectral albedo of 0.18 and using a background aerosol scenario. The shaded areas are covered by the MAMAP instrument, where grey indicates ranges used for the retrieval of CO_2, CH_4 and O_2. The simulation has been conducted using the SCIATRAN radiative transfer model. The wavelength region up to 1.05 µm has been convolved with the NIR channel slit function, for larger wavelengths with the SWIR channel slit function.

of 0.46 nm. The small FWHM guarantee a high spectral resolution capturing the relevant absorption features, while the oversampling of approximately 9 pixels per FWHM (see Table 4.1) enables an accurate wavelength calibration.

Figure 4.5 shows simulated, sun normalised radiances for a typical MAMAP setup where the shaded areas denote the wavelength regions covered by the instrument.

4.4 Recent improvement of the instrument

The MAMAP instrument is subject to ongoing modifications. After the instrument assessment by Gerilowski et al. (2011) and the analysis of data recorded over two coal fired power plants emitting CO_2 (see Section 8 and Krings et al., 2011), the MAMAP optical setup has been improved by adding a spatial scrambler to mitigate pseudo noise resulting from scene inhomogeneities as proposed by Gerilowski et al. (2011). The degraded performance in the original setup has been attributed to slit function variations due to optical *Smile* and *Keystone* effects of the spectrometer in combination with inhomogeneous slit illumination (Gerilowski et al., 2011; Schnisa, 2009). These improvements are not the focus of this thesis and will be discussed elsewhere.

However, important for this work is the improved instrument performance that could be achieved introducing the optical scrambler (slit homogeniser). Compensating the slightly reduced throughput of the instrument by an increased integration time, the instrumental precision could be enhanced by about a factor of 3 compared to the original setup (see Section 6.1).

For the updated optical configuration, a single glass fibre coupled telescope is used for both channels. In this setup, the IFOV of the SWIR and NIR channels is about $1.15° \times 1.15°$. For an aircraft altitude of 1250 m and ground speed of 200 km h^{-1}, this results in a ground

scene of about 25 m × 79 m (across track × along track). Taking into account the large along track IFOV, the along track sensitivity within a single ground scene is actually given by a trapezium function corresponding to the time that a ground scene element resides in the IFOV of the instrument. Mathematically, this can be described by a convolution of the IFOV with a rectangular function that describes the along track ground scene extent during the integration time.

The improved instrument has been used for subsequent measurements over coal mine ventilation shafts (see Section 9) and a natural gas blowout site in the North Sea (see Section 10) emitting CH_4.

The instrument parameters are summarised in Table 4.1. A more detailed technical description of MAMAP can be found in Gerilowski et al. (2011). Further photographs of the MAMAP instrument and the installation on aircraft are compiled in Appendix C.

Table 4.1: MAMAP sensor parameters. Bold information refers to the improved setup. See text for more information. Abbreviations: *LN*: liquid nitrogen, *TE*: thermoelectric, *F*: focal length of the spectrometer, *f*: f-number, *IFOV*: instantaneous field of view, *FWHM*: full width at half maximum of the instrumental slit function, *FPA*: focal plane array, *FT*: frame transfer.

CH_4/CO_2-SWIR-spectrometer	O_2-NIR-spectrometer
$F = 300$ mm temperature stabilised grating spectrometer system (f/3.9)	$F = 300$ mm temperature stabilised push broom imaging grating spectrometer system (f/3.9)
Grating: 600 grooves mm^{-1}	*Grating*: 1200 grooves mm^{-1}
Detector: LN cooled 1024 pixel InGaAs FPA	*Detector*: 512×512 pixel CCD FT Sensor, TE cooled, 6 pixel binned in imaging direction and 2 in spectral direction
Spectral range: ≈1590–1690 nm	*Spectral range*: ≈757–768 nm
Spectral resolution: ≈0.82 nm FWHM	*Spectral resolution*: ≈0.46 nm FWHM
Spectral sampling: ≈8.6 pixel/FWHM	*Spectral sampling*: ≈9 pixel/FWHM
Detector-SNR: ≈1000 at ≈0.6–0.8 s **(1 s)** integration time (10 detector readouts co-added, surface spectral reflectance 0.18)	*Detector-SNR*: >4000 (binned) at ≈0.6–0.8 s **(1 s)** integration time (10 detector readouts co-added, 1/4 of the 85 spatial rows binned, surface spectral reflectance 0.18)
IFOV: ≈1.34° across track × ≈0.02° along track	*IFOV*: ≈5.85° across track (divided into 85 pixel) × ≈0.072° along track
Spatial resolution: At 1.25 km **(1.1 km)** flight altitude, ground speed of 200 km h^{-1}, the co-added ground scene size is ≈33 m **(79 m)** along track over land (surface spectral reflectance 0.18) and larger for lower surface spectral reflectance. Across track ground scene size is ≈ 29 m **(25 m)**	*Spatial resolution*: At 1.25 km **(1.1 km)** flight altitude, ground speed of 200 km h^{-1}, the co-added ground scene size is ≈33 m **(79 m)** along track over land (surface spectral reflectance 0.18) and larger for lower surface spectral reflectance. Across track swath width is about ≈128 m **(25 m)** with ground scene sizes of ≈1.5 m
Size: 2 "Falcon" standard racks, 556 mm × 650 mm × 968 mm each	
Weight: ≈120 kg (each rack)	
Power consumption: ≈600–800 Watt at nominal operation, <1000 Watt at warm-up	

5

Retrieval of carbon dioxide and methane

A retrieval algorithm is used to convert the spectral radiances measured by MAMAP to the trace gas column information of interest. For the processing of MAMAP data, a modified version of the Weighting Function Modified Differential Optical Absorption Spectroscopy (WFM-DOAS) algorithm (Buchwitz et al., 2000) is used to obtain vertical column information of CH_4, CO_2 and also O_2.

The standard DOAS technique assumes that the absorption cross sections are independent of height. However, this is usually not valid for the strong absorbers in the infrared. Thus, WFM-DOAS additionally takes into account the pressure and temperature dependency of the absorption cross sections using linearisation points.

WFM-DOAS has been successfully applied to scientific retrieval of CO_2 and CH_4 column information (Buchwitz et al., 2005a,b; Schneising et al., 2008, 2009, 2010, 2011) from the SCIAMACHY satellite sensor onboard Envisat (Burrows et al., 1995; Bovensmann et al., 1999).

SCIAMACHY's WFM-DOAS uses a look-up table approach with multi dimensional interpolation for solar zenith angle, surface spectral reflectance, surface elevation. Water vapour is iteratively fitted before the final trace gas fit of, for example, CH_4 or CO_2. The MAMAP measurement flights described in this work cover only narrow regions and rather short time spans compared to SCIAMACHY observations, so that only a specific set of parameters for solar zenith angle, surface spectral reflection, surface elevation, water vapour, etc. was applied for each flight separately instead of an extended look-up table. However, for future surveys being larger in time and space, look-up tables can be used accordingly.

While the physical ideas of a pre-existing, preliminary MAMAP retrieval algorithm adopted from the satellite version of the WFM-DOAS algorithm and developed prior to this work by M. Buchwitz have been retained, large modifications had to be conducted to allow for a complete instrument assessment, algorithm sensitivity analysis and subsequent

inversion for point source emission rates. Among numerous modifications dealing with specifics of the instrument, such as the odd-even correction, the shift and squeeze procedure for the wavelength calibration has been updated to enable testing of higher order squeezing and dynamical changes to a predefined shift and squeeze over the full detector length or particular wavelength windows. Furthermore, a fit for the FWHM of the instrument function was implemented along with an improved treatment of bad pixels, dark spectra (continuous evaluation of in-flight dark current) and the implementation of a radiative transfer that is more conform to the instrument requirements including a high resolution altitude grid, updated spectroscopy, more complex aerosol scenarios and updated CO_2 and CH_4 profiles. The introduction of a conversion factor that takes into account the measurement geometry of an in-atmosphere aircraft instrument and assuming that changes in the target gas abundances predominantly happen below the aircraft has a large impact on the overall retrieval result. The completed MAMAP algorithm has first been presented in Krings et al. (2011) and will be introduced in the following.

5.1 Algorithm description

As for SCIAMACHY, the MAMAP version of the WFM-DOAS algorithm is based on a least squares fit of the logarithmic simulated radiance spectrum to the measurements after correction for dark signal and pixel to pixel gain. The fit parameters are:

1. desired atmospheric parameters: partial or total columns of CH_4, CO_2 and O_2,
2. additional trace gas atmospheric parameters for spectrally interfering gases (water vapour),
3. other atmospheric parameters (temperature),
4. a low order polynomial (usually of the second or third order) in wavelength to account for spectrally smoothly varying parameters which are not explicitly modelled or not well enough known. These parameters include, for example, the MAMAP absolute radiometric calibration function, aerosol scattering and absorption parameters and the surface spectral reflectance,
5. shift and squeeze parameters from an iterative wavelength calibration procedure,
6. and an alternating function (-1, 1, -1, 1, ...) accounting for a detector pixel odd even correction.

The last-mentioned odd-even effect is caused by the design of the SWIR detector where multiplexers of odd and even pixels are on opposed sides of the detector. If illumination is tilted, a residual light sensitivity can lead to a characteristic intensity shift between odd and even pixels. This matter has been resolved when using the instrument modification as discussed in Section 4.4.

The logarithm of the spectrum can be expressed as a linearised radiative transfer model plus a low order polynomial P_λ:

$$\ln R_\lambda^{\mathrm{mea}} = \ln R_\lambda^{\mathrm{mod}}(\bar{\mathbf{c}}) + \sum_j W_{\lambda,\bar{c}_j} \frac{c_j - \bar{c}_j}{\bar{c}_j} + P_\lambda(\mathbf{a}) + \epsilon_\lambda \tag{5.1}$$

On the left hand side of this equation, there is the logarithm of the measured spectral radiance R_λ^{mea} at a wavelength λ. On the right hand side, there is the WFM-DOAS linearised radiative transfer model, the low order polynomial P_λ with the free fit parameters $\mathbf{a}$ and an error term ϵ_λ. The expression $R_\lambda^{\text{mod}}(\bar{\mathbf{c}})$ denotes the radiative transfer model result at the linearisation point $\bar{\mathbf{c}}$. The vector-valued $\bar{\mathbf{c}}$ consists of typical values for relevant atmospheric parameters. These "first guess" values are referred to as $\bar{c}_j$. The second term on the right hand side describes the linearised model corrections depending on the fit parameters c_j. To each $\bar{c}_j$ exists a corresponding fit parameter c_j. The column weighting functions $W_{\lambda,\bar{c}_j}$ denote the derivatives of the radiance with respect to fit parameters c_j. They are computed by adding up all relevant atmospheric layer weighting functions $W_{\lambda,\bar{c}_j,z}$:

$$W_{\lambda,\bar{c}_j} = \sum_{z=z_{\text{low}}}^{z_{\text{up}}} W_{\lambda,\bar{c}_j,z} \tag{5.2}$$

where z_{low} and z_{up} denote the lower and upper limit of the relevant atmospheric layers. For a general MAMAP retrieval, the altitude range would reach from the lowest atmospheric layer to the top of atmosphere. As a consequence, the retrieval algorithm does not resolve different altitude levels but shifts the mean profile as a whole. The results of the algorithm are height-averaged increased or decreased profile scaling factors or a profile shift (in case of temperature).

The atmospheric layer weighting functions are computed as:

$$W_{\lambda,\bar{c}_j,z} = \left.\frac{\partial \ln R_\lambda}{\partial \ln c_{j,z}}\right|_{\bar{c}_j(z)} \cdot \Delta_z \tag{5.3}$$

This is basically the relative change of radiance due to a relative change of the according parameter c at altitude z times the quadrature weight Δ_z. The quadrature weights essentially correspond to the geometrical thickness of the layers of the model atmosphere.

Both the model radiances and the weighting functions are computed with the radiative transfer model SCIATRAN (Rozanov et al., 2005) using the HITRAN 2008 spectroscopic database (Rothman et al., 2009) and sun spectra by Livingston and Wallace (1991) for the SWIR bands and the MODTRAN Thuillier plus corrected Kurucz (Berk et al., 2000, and references therein) for the NIR band.

The error term ϵ_λ in Equation (5.1) accounts for all wavelength dependent differences between the measurement and the model which cannot be modelled or cannot be modelled without approximations (for example, aerosol effects). In an ideal case, the error term is identical to the instrument's detector noise.

Equation (5.1) can be expressed as a vector equation of the following form:

$$\mathbf{y} - \mathbf{A} \cdot \mathbf{x} = \epsilon \tag{5.4}$$

with each vector component corresponding to a specific wavelength λ. Here, $\mathbf{A}$ denotes a matrix whose columns consist of the weighting functions $W_{\lambda,\bar{c}_j}$ and of the polynomial base functions. The vector $\mathbf{y}$ is built up by the differences of logarithmic radiances of measurement and model at the linearisation point $\bar{c}$. The parameters $\mathbf{x}$ corresponding to

the (relative) change in the atmospheric parameters and the polynomial coefficients can be obtained by a least squares fit minimising the sum of the squared errors:

$$\sum_{i=\lambda_{\min}}^{\lambda_{\max}} \epsilon_i^2 = \|\epsilon\|^2 = \|\mathbf{y} - \mathbf{A} \cdot \mathbf{x}\|^2 \longrightarrow \min \tag{5.5}$$

The solution for $\mathbf{x}$ is then given by:

$$\mathbf{x} = \left(\mathbf{A}^T\ \mathbf{A}\right)^{-1} \mathbf{A}^t\ \mathbf{y} \tag{5.6}$$

The remaining measurement error ϵ is a measure for the quality of the spectral fit, which in practice is not only determined by noise but also influenced by systematic errors (for example, spectrometer slit function uncertainties or errors in spectroscopic parameters). Since the systematic measurement errors are not known, the statistical errors of fit parameter j have to be estimated from the residual ϵ:

$$\sigma_{\hat{x}_j} = \sqrt{\left(\mathbf{A}^T\ \mathbf{A}\right)^{-1}_{j,j} \frac{\|\epsilon\|^2}{m-n}} \tag{5.7}$$

where m is the number of spectral points used for the fit, n the number of fit parameters and $m - n$ the number of degrees of freedom of the linear least squares problem.

The WFM-DOAS equation is solved independently in three wavelength regions:

- 757–768 nm for O_2 retrieval,
- 1593–1617 nm for CO_2 retrieval and
- 1630–1675 nm for CH_4 retrieval.

Figures 5.1 and 5.2 show example results for a WFM-DOAS analysis of a single spectrum recorded by the MAMAP SWIR channel. The absorption features of CO_2 (Figure 5.1) and CH_4 (Figure 5.2) are clearly visible in the MAMAP spectrum. Interfering gases in the CH_4 fitting window are CO_2 and H_2O. In the CO_2 fitting window only H_2O interferes. Also fitted is the shift of the temperature profile (only shown for the CO_2 fitting window). The retrieved CO_2 profile scaling factor is 0.991 ± 0.022. The retrieved CH_4 profile scaling factor is 0.989 ± 0.014. The residuals (RES) are shown in the bottom panels and denote the relative difference between the MAMAP spectral measurements and the fitted radiative transfer model. The root-mean-square (RMS) of the residual is $\approx$0.6 % for both fitting windows. As can be seen, the fit residual is not only determined by measurement noise but also contains systematic features. This is attributed to wavelength calibration errors, slit function uncertainties, uncertainties of the spectroscopic line parameters or spectral structures of the white lamp calibration source.

For the interpretation of the MAMAP measurements with respect to sources and sinks of the greenhouse gases CO_2 and CH_4, the column-averaged dry air mole fractions (in ppm for CO_2 or ppb for CH_4) are the preferred quantity rather than the total columns (in molecules cm^{-2}). This is because dry air mole fractions are less affected by changes in surface topography, pressure and flight altitude compared to the absolute column.

To convert the obtained total columns, additional knowledge of the dry air column, that is the total number of molecules in the air column neglecting water molecules, is necessary. This knowledge can be obtained in several ways:

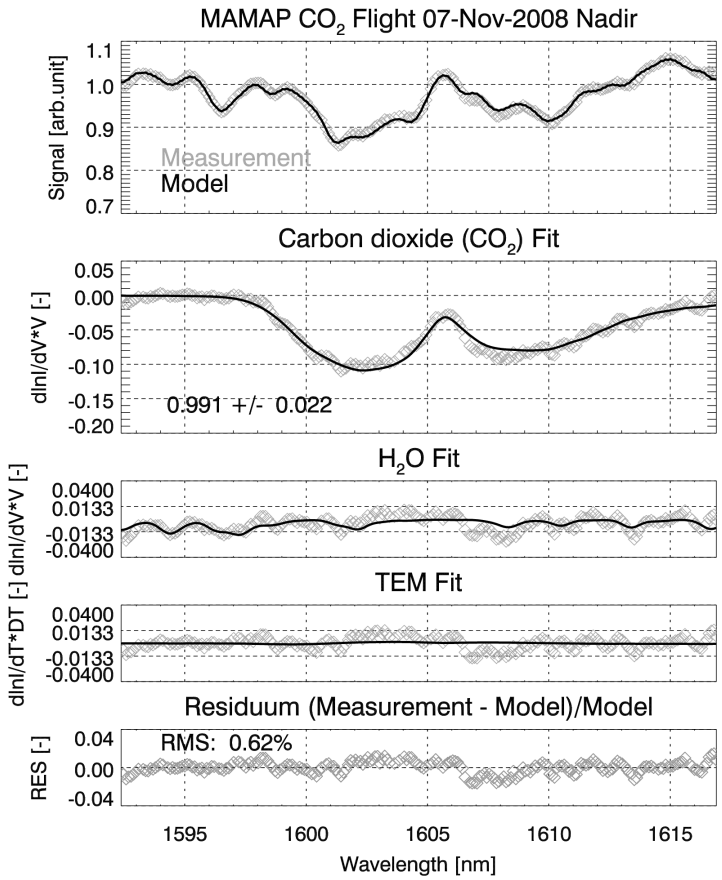

Figure 5.1: Example fits of the MAMAP WFM-DOAS algorithm for a single CO_2 spectrum. Data were obtained on November 7, 2008, during a flight from Oshawa to Wilmington (USA) on the Polar-5 aircraft of the Alfred-Wegener-Institute (AWI), Bremerhaven, Germany. The top panel shows a MAMAP nadir spectrum (grey symbols) and the fitted, linearised radiative transfer model (solid, black line). The bottom panel shows the fit residuum which is the relative difference between measurement and simulation after the fit (the root-mean-square (RMS) of the fit residuum (RES) is 0.62 %). The second panel shows details of the CO_2 fit. The solid line is the scaled derivative of the radiance with respect to a change of the CO_2 vertical column. The retrieved scaling factor for the CO_2 vertical profile is 0.991 ± 0.022. Hence, the retrieved columns is 0.9 % lower than the vertical column which was assumed for the radiative transfer simulations. The grey symbols show the CO_2 fit residuum which is identical with the black curve except that the spectral fit residuum has been added. The third panel displays the fit result for weak interference of H_2O and the fourth panel the retrieved temperature shift.

i. by using simultaneous measurements of the oxygen (O_2) column as reference,

ii. by using another well-mixed gas whose mole fraction is quite well known and varies significantly less than the trace gas of interest, or

iii. by considering external information on surface pressure obtained, for example, from meteorological analysis analogously to the method described in Barkley et al. (2006) utilising ECMWF surface pressure fields. However, very high resolution surface pressure data would be required in this case, especially in areas with high topographic variations.

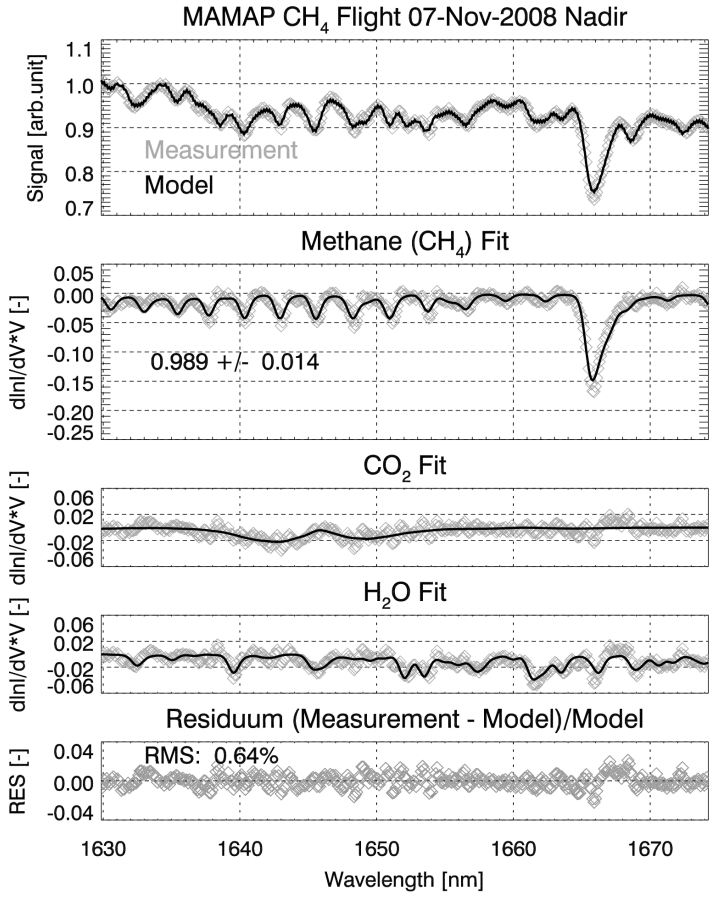

Figure 5.2: Same as Figure 5.1 but for CH_4. Here, the retrieved CH_4 vertical column is 98.9±1.4 % of the assumed column. The third and the fourth panel show the corresponding results for the interfering gases CO_2 and H_2O. The retrieved temperature shift is not displayed.

Successful utilisation of the O_2 column (i) (in the case of MAMAP to be obtained from the O_2-A band spectrally located at about 760 nm) has been demonstrated, for example, in Schneising et al. (2008) for SCIAMACHY column-averaged CO_2 retrieval. The mole fraction of O_2 in dry air is well known (20.95 %) and fairly constant in space and time up to about 100 km. However, due to the spectral distance of the O_2-A band at 760 nm and the CO_2 and CH_4 absorption bands located at about 1.6 µm, light paths will be different if not all scattering parameters are known. This can lead to total column retrieval errors (see Section 5.3 and Schneising et al., 2008, 2009, for a discussion).

In order to avoid these light path differences, another well-mixed gas which is measured spectrally close to the trace gas of interest can be used as reference (ii). For the determination of MAMAP CH_4 mole fractions, the CO_2 mole fractions can in many cases be assumed to be effectively constant and well mixed compared to CH_4 – at least in regions without large temporal or spatial CO_2 variations. Due to the spectral closeness, the photon paths can be assumed to be similar for both gases causing light path errors to cancel to

a large extent when computing the column-averaged dry air mole fractions ($X\mathrm{CH_4}$):

$$X\mathrm{CH_4}(\mathrm{CO_2}) = \frac{\mathrm{CH_4^{column}}}{\mathrm{CO_2^{column}}/\mathrm{CO_2^{aver.\ mole\ fraction}}} \tag{5.8}$$

This is also done for CH_4 mole fractions obtained from SCIAMACHY (Frankenberg et al., 2005a; Schneising et al., 2009).

In case of strong CO_2 sources like the power plants in this study away from strong local methane sources, CH_4 can be used to determine mole fractions for carbon dioxide ($X\mathrm{CO_2}$) accordingly:

$$X\mathrm{CO_2}(\mathrm{CH_4}) = \frac{\mathrm{CO_2^{column}}}{\mathrm{CH_4^{column}}/\mathrm{CH_4^{aver.\ mole\ fraction}}} \tag{5.9}$$

But also CH_4 area sources such as wetlands will not significantly bias the result of a strong CO_2 point source. For example, a 10 km wide wetland upwind of the point source will only result in a columnar CH_4 increase of 0.03 %–0.06 % CH_4, assuming a high summer wetland emission rate of 50–100 mg CH_4 m^{-2} day−1 (see, for example, Ringeval et al., 2010, for wetland emission rates), a wind speed of 2 m s^{-1} and a background column of about 9.75 g CH_4 m^{-2}.

For the power plant study (see Section 8), for example, the average mole fractions $\mathrm{CO_2^{aver.\ mole\ fraction}}$ and $\mathrm{CH_4^{aver.\ mole\ fraction}}$ were assumed to be ≈380 ppm and ≈1.7 ppm (with a surface value of 1.780 ppm), respectively. These values were used to scale a U.S. Standard Atmosphere (U.S. Committee on Extension to the Standard Atmosphere, 1976) to current mole fractions. The resulting vertical profiles determine the linearisation point for the radiative transfer model.

Mole fractions of CO_2 using O_2 as proxy, $X\mathrm{CO_2}(\mathrm{O_2})$, are computed similarly.

This method is also preferred to using external surface pressure data (iii) because of the higher accuracy that can be obtained if light path errors can be accounted for. The feasibility, however, depends strongly on the actual variability of CO_2 and CH_4.

5.2 Altitude sensitivity

As can be seen from Equation (5.2), the MAMAP WFM-DOAS retrieval does not resolve different altitude levels. However, the retrieval has different sensitivities for different altitudes. This behaviour can be characterised by the so called column averaging kernels (AK) as a function of altitude. They are defined as the variation of the retrieval parameter (the trace gas column) $c_{\mathrm{retrieved}}$ as a result of a perturbation of the true subcolumn $c_{\mathrm{true}}(z)$ at altitude z:

$$\mathrm{AK}(z) = \frac{\partial c_{\mathrm{retrieved}}}{\partial c_{\mathrm{true}}(z)} \tag{5.10}$$

The AK for MAMAP were computed by retrieving trace gas columns from measurement simulations that have been perturbed at various altitude levels z. An averaging kernel value equal to unity at a certain altitude indicates that the perturbation was correctly retrieved by the algorithm. Values lower or higher than unity indicate a decreased or increased sensitivity. In particular, there is a sharp step in the averaging kernels at the aircraft altitude (see Figure 5.3). Below the aircraft altitude, the averaging kernels are

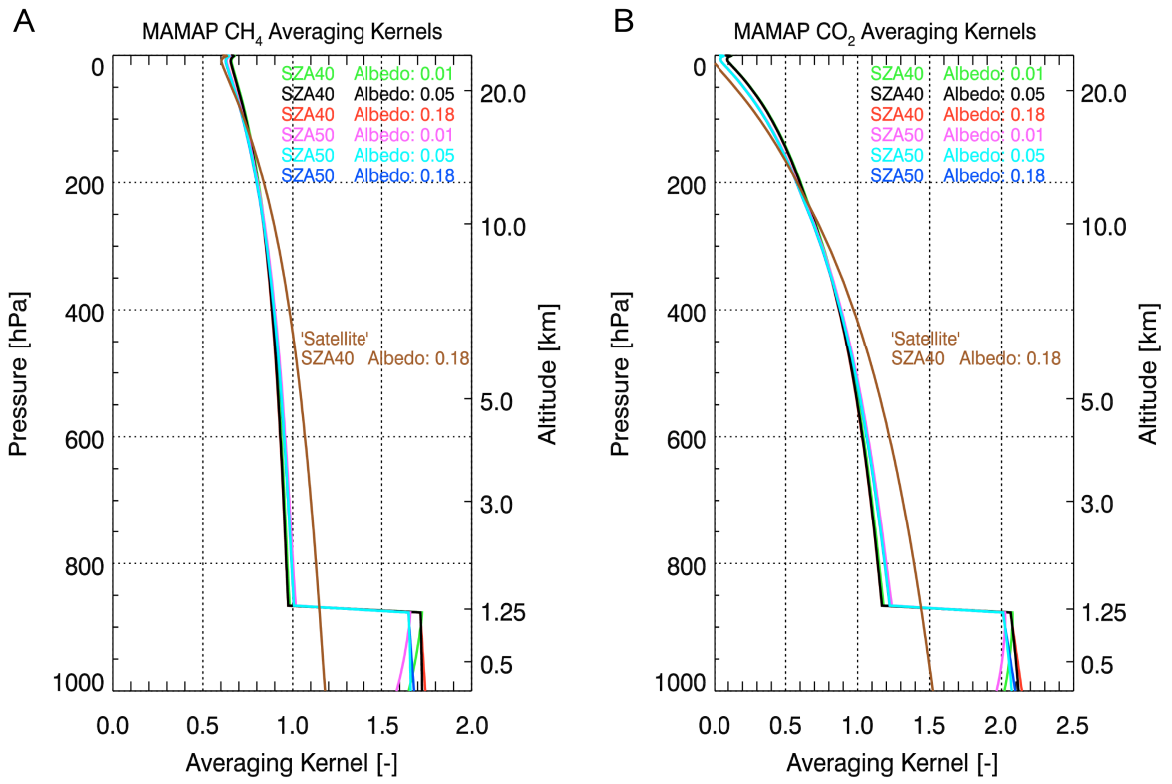

Figure 5.3: Averaging Kernels of MAMAP measurements for CH_4 (Panel A) and CO_2 (Panel B) for an aircraft altitude of 1.25 km and various solar zenith angles (SZA) and surface spectral albedos. For comparison, also the averaging kernels for a hypothetical aircraft altitude of 1000 km (satellite altitude) are shown.

increased by a factor of about 2 (for low aircraft altitudes). This is due to the fact that light from the sun passes through the absorber below the aircraft twice – once before and once after surface reflection. The higher the aircraft flies, the less pronounced the step becomes, since the height-averaged AK are about unity.

For a typical MAMAP measurement, elevated or decreased trace gas concentrations can be expected mainly below the aircraft due to activity at the surface, for example, power plants emitting CO_2 or landfills releasing CH_4. Since the retrieval is not height sensitive, the measurements will be weighted with the mean averaging kernel (ideally being close to unity). If the concentration changes occur evenly at all altitude levels, this gives the correct result. For changes only below the aircraft, this has to be accounted for, for example, by a conversion factor. Otherwise, the column-averaged mole fraction variations from the retrieval appear about twice as high as they actually are. This conversion factor k can be computed by:

$$k = \frac{1}{\overline{\mathrm{AK}_{\mathrm{low}}}} \tag{5.11}$$

where $\overline{\mathrm{AK}_{\mathrm{low}}}$ denotes the mean averaging kernel of altitude layers below the aircraft. Table 5.1 gives examples of conversion factors for various conditions (see also Appendix D). The aircraft altitude of 1.25 km, as used for Table 5.1, is valid for the measurements

Table 5.1: Conversion factors for retrieval output assuming an aircraft altitude of 1.25 km and that all deviations from standard mean column occurred below the aircraft. Conversion factors for various more conditions can be found in Appendix D.

Solar zenith angle [°]	Surface albedo [−]	Aerosol type	Conversion factor [−]	
			CH_4	CO_2
40	0.1	urban	0.580	0.477
		background	0.582	0.478
	0.18	urban	0.578	0.475
		background	0.581	0.477
	0.25	urban	0.577	0.474
		background	0.580	0.477
50	0.1	urban	0.603	0.488
		background	0.604	0.489
	0.18	urban	0.600	0.487
		background	0.603	0.488
	0.25	urban	0.599	0.485
		background	0.602	0.488
60	0.1	urban	0.629	0.502
		background	0.630	0.502
	0.18	urban	0.626	0.500
		background	0.628	0.501
	0.25	urban	0.625	0.498
		background	0.628	0.501

conducted over the power plants Jänschwalde and Schwarze Pumpe (see Section 8).

Note that the conversion factors given here and in Krings et al. (2011) are not identical to those in Gerilowski et al. (2011) since an improved radiative transfer was applied for the retrieval resulting in modified averaging kernels and hence also in slightly modified conversion factors k. The improvements include the update from the HITRAN 2004 (Rothman et al., 2005) to the HITRAN 2008 spectroscopic database (Rothman et al., 2009), an altitude grid with higher vertical resolution in lower altitudes and a more complex aerosol profile.

The actual variation in the column Δc can then be calculated by using observation geometry and averaging kernels:

$$\Delta c = (c - \bar{c})_{\text{corrected}} = k \cdot (c - \bar{c}) \tag{5.12}$$

or for the column-averaged dry air mole fractions:

$$X\text{CO}_2^{\text{corrected}} = \text{CO}_2^{\text{aver. mole fraction}} + k \cdot \left(X\text{CO}_2 - \text{CO}_2^{\text{aver. mole fraction}}\right) \tag{5.13}$$

$$X\text{CH}_4^{\text{corrected}} = \text{CH}_4^{\text{aver. mole fraction}} + k \cdot \left(X\text{CH}_4 - \text{CH}_4^{\text{aver. mole fraction}}\right) \tag{5.14}$$

Thereby, $\text{CO}_2^{\text{aver. mole fraction}}$ and $\text{CH}_4^{\text{aver. mole fraction}}$ are generally referring to local or regional background mole fractions against which variations are measured.

This will also enhance the precision σ (standard deviation) computed for the profile scaling factors by the same amount:

$$\sigma_{\text{corrected}} = k \cdot \sigma \tag{5.15}$$

Alternatively, it is possible to fix the column above the aircraft to background and retrieve only below. However, for this approach to be accurate, detailed knowledge of the above column is required. MAMAP's zenith observation mode potentially offers the opportunity to obtain and incorporate this information but has not been exploited yet.

5.3 Sensitivity and error analysis

Retrieval errors may generally arise from insufficient information and variations of the atmospheric state or the measurement geometry that are not accounted for in the reference radiative transfer model. To assess the sensitivity of the derived total columns of CO_2, CH_4 and O_2 to various atmospheric and other parameters, synthetic retrievals on data from different radiative transfer simulations were performed. The sensitivity study includes the impact of variations of the solar zenith angle, aerosol content, surface elevation, aircraft altitude, surface spectral reflectance, cirrus clouds and water vapour content in the atmosphere. If not stated otherwise, the retrieval was conducted using as reference a spectral albedo of 0.18 (assuming a Lambertian reflector), a solar zenith angle of 40° and an OPAC (Hess et al., 1998) continental background aerosol scenario (see below) as it is also used for recent WFM-DOAS SCIAMACHY satellite data retrieval of CO_2 and CH_4 (Schneising et al., 2011).

Tables 5.2–5.8 show the relative error on the retrieved background total columns of CO_2, CH_4 and O_2 and their column-averaged dry air mole fractions using the proxy method. Thereby, the relative error $\Delta_r^{a/b}$ on ratios a/b of two gases a and b was computed from the non-rounded relative errors for the single gases Δ_r^a and Δ_r^b in the following way:

$$\Delta_r^{a/b} = \frac{1 + \Delta_r^a}{1 + \Delta_r^b} - 1 \tag{5.16}$$

Note that for small relative errors Δ_r^a and Δ_r^b, Equation (5.16) simplifies to:

$$\Delta_r^{a/b} \approx \Delta_r^a - \Delta_r^b \tag{5.17}$$

so that for most purposes in this work the relative retrieval errors for column-averaged dry air mole fractions $X\text{CO}_2(\text{CH}_4)$ and $X\text{CH}_4(\text{CO}_2)$ are essentially equal except for the sign.

Table 5.2 shows the dependence on the solar zenith angle (SZA) for different aircraft altitudes if 40° is assumed for the retrieval but the true SZA is different. There is a rather large error on the single gas columns decreasing with higher aircraft altitude, since the fraction of the wrongly assumed light path (before reflection on the ground) becomes lower. The SZA can be determined very precisely when geolocation (for example, by using GPS) and time of measurement are known and can be considered for the retrieval reference scenario. However, in case of flights with a short temporal duration, a single reference scenario can be used if the proxy method of, for example, $X\text{CO}_2(\text{CH}_4)$ or $X\text{CH}_4(\text{CO}_2)$ is

Table 5.2: Solar zenith angle sensitivity of total column concentrations and their column-averaged dry air mole fractions using the proxy method for different aircraft altitudes if the true solar zenith angle is deviating from the 40 ° assumed for the retrieval.

Aircraft	Solar zenith	Sensitivities [%]					
altitude [km]	angle [°]	CO_2	CH_4	O_2	$XCH_4(CO_2)$	$XCO_2(CH_4)$	$XCO_2(O_2)$
0.85	35.0	−5.97	−6.02	−5.73	−0.05	0.05	−0.25
	40.0	0.00	0.00	0.00	0.00	0.00	0.00
	45.0	7.44	7.56	7.22	0.11	−0.11	0.21
1.25	35.0	−5.74	−5.82	−5.46	−0.08	0.08	−0.30
	40.0	0.00	0.00	0.00	0.00	0.00	0.00
	45.0	7.15	7.31	6.88	0.15	−0.15	0.25
3.0	35.0	−4.99	−5.14	−4.66	−0.16	0.16	−0.35
	40.0	0.00	0.00	0.00	0.00	0.00	0.00
	45.0	6.23	6.47	5.91	0.23	−0.23	0.30
4.5	35.0	−4.57	−4.75	−4.27	−0.19	0.19	−0.31
	40.0	0.00	0.00	0.00	0.00	0.00	0.00
	45.0	5.72	5.98	5.42	0.25	−0.25	0.28

applied, as was done for the analysis in this study. This method is also superior to the O_2 proxy method, provided that CH_4 or CO_2 variations are negligible, respectively.

Beside the aerosol OPAC background scenario with clean continental air (99.998 % water soluble, for example, sulfates and nitrates), also an OPAC urban scenario with polluted air in the boundary layer up to 2 km altitude (31.399 % water soluble, 68.6 % soot) and "average continental" aerosol (45.79 % water soluble, 54.2 % soot) in the free troposphere above as well as an OPAC desert scenario with aerosol of mineral composition in the boundary layer (93.19 % and 6.81 % mineral in the nucleation and the accumulation mode, respectively) and "clean continental" aerosol in the free troposphere were tested. Additionally, two LOWTRAN 7 (Kneizys et al., 1988) aerosol scenarios were used for comparison: a background scenario with maritime aerosol in the boundary layer (34 km visibility, 80 % humidity) and a scenario with an extremely polluted boundary layer (2 km visibility, 99 % humidity). While the OPAC aerosol scenarios use Mie phase functions, for LOWTRAN scenarios a Henyey-Greenstein approximation (see Appendix A) is applied (see Rozanov, 2012, and references therein for further details on the aerosol options in SCIATRAN). The same scenarios were also used to assess aerosol impact on greenhouse gas retrievals from satellite measurements (Schneising et al., 2008, 2009; Schneising, 2009; Reuter et al., 2010). For MAMAP, the aerosol dependency is generally rather low for the CH_4 and CO_2 proxy methods, respectively (Table 5.3). This is also confirmed in a simulation considering actual aerosol deployment in a power plant's vicinity (see Section 8.5.3). Usage of a standard background scenario or the urban polluted in industrial areas as general reference scenario seems justified.

Another parameter giving rise to potential errors is the surface elevation (Table 5.4). Unaccounted elevations of 100 m can lead to a bias of −0.34 % for $XCO_2(CH_4)$. However, surface elevation is a well known parameter if geolocation is known.

Table 5.3: Aerosol sensitivity of total column concentrations and their column-averaged dry air mole fractions using the proxy method for an aircraft altitude of 1.25 km and a solar zenith angle of 40 °. Lowtran (LT, using Henyey-Greenstein phase functions for a background scenario and a scenario with extreme aerosol load in the boundary layer (BL)) and OPAC (using Mie phase functions) aerosol scenarios were used (see Hess et al., 1998; Schneising et al., 2008; Schneising, 2009). The aerosol optical thickness at 0.8 µm and 1.6 µm is given in the second and third column for each scenario. For comparison, Rayleigh scattering optical thickness in all scenarios was 0.0271 at 0.8 µm and 0.00131 at 1.6 µm.

Aerosol	AOT [−] at		Sensitivities [%]					
scenario	0.8 µm	1.6 µm	CO_2	CH_4	O_2	$XCH_4(CO_2)$	$XCO_2(CH_4)$	$XCO_2(O_2)$
LT background	0.2491	0.1814	1.35	1.17	0.94	−0.18	0.18	0.41
LT extreme in BL	2.1922	1.0008	3.34	2.88	0.11	−0.44	0.44	3.23
OPAC background	0.0890	0.0240	0.00	0.00	0.00	0.00	0.00	0.00
OPAC urban	0.1783	0.0631	0.38	0.33	0.28	−0.05	0.05	0.10
OPAC desert	0.2560	0.1799	1.26	1.07	0.50	−0.18	0.18	0.76

Table 5.4: Surface elevation sensitivity of total column concentrations and their column-averaged dry air mole fractions using the proxy method for an aircraft altitude of 1.25 km and a solar zenith angle of 40 °.

Surface	Sensitivities [%]					
elevation [m]	CO_2	CH_4	O_2	$XCH_4(CO_2)$	$XCO_2(CH_4)$	$XCO_2(O_2)$
0	0.00	0.00	0.00	0.00	0.00	0.00
25	−0.63	−0.54	−0.83	0.09	−0.09	0.20
50	−1.25	−1.09	−1.66	0.16	−0.16	0.42
75	−1.87	−1.63	−2.49	0.24	−0.24	0.64
100	−2.50	−2.17	−3.31	0.34	−0.34	0.84
125	−3.12	−2.70	−4.13	0.43	−0.43	1.05
150	−3.74	−3.24	−4.95	0.52	−0.52	1.27
200	−4.97	−4.31	−6.59	0.69	−0.69	1.73

The aircraft altitude determines the length of the slant column to be measured and therefore has an impact on the retrieval results, as well. For the flight over two CO_2 emitting power plants (see Section 8), for example, the principal altitude of observation during the flight was kept constant at 1.25 km. This altitude was hence also chosen as default for the corresponding reference radiative transfer simulation in the retrieval. Table 5.5 shows the errors to be expected if the actual aircraft altitude is differing from this reference altitude. A variation of ±50 m, which will rarely be exceeded during measurement flights leads to an error of about ±0.06 % for $XCO_2(CH_4)$.

For the retrieval, solely a spectral albedo of 0.18 was applied assuming a Lambertian reflector and no spectral dependency. Obviously, this is not true for real surfaces although this is mitigated by the fit polynomial P_λ. To assess the influence of different surface types on the standard retrieval, spectral reflectances of various surfaces (see Figure 5.4) were applied to radiative transfer simulations for two different aerosol scenarios (Table 5.6).

Table 5.5: Sensitivity to aircraft altitude uncertainty for a spectral albedo of 0.18 and a reference altitude of 1.25 km.

Δ Aircraft	Sensitivities [%]					
altitude [m]	CO_2	CH_4	O_2	$XCH_4(CO_2)$	$XCO_2(CH_4)$	$XCO_2(O_2)$
−400	−3.81	−3.33	−4.57	0.49	−0.49	0.80
−250	−2.35	−2.06	−2.80	0.30	−0.30	0.46
−100	−1.40	−1.23	−1.65	0.17	−0.17	0.26
−50	−0.46	−0.41	−0.54	0.05	−0.05	0.08
0	0.00	0.00	0.00	0.00	0.00	0.00
50	0.46	0.40	0.54	−0.06	0.06	−0.08
100	1.37	1.20	1.58	−0.17	0.17	−0.21
250	2.26	1.99	2.60	−0.26	0.26	−0.33
400	3.15	2.77	3.59	−0.37	0.37	−0.43

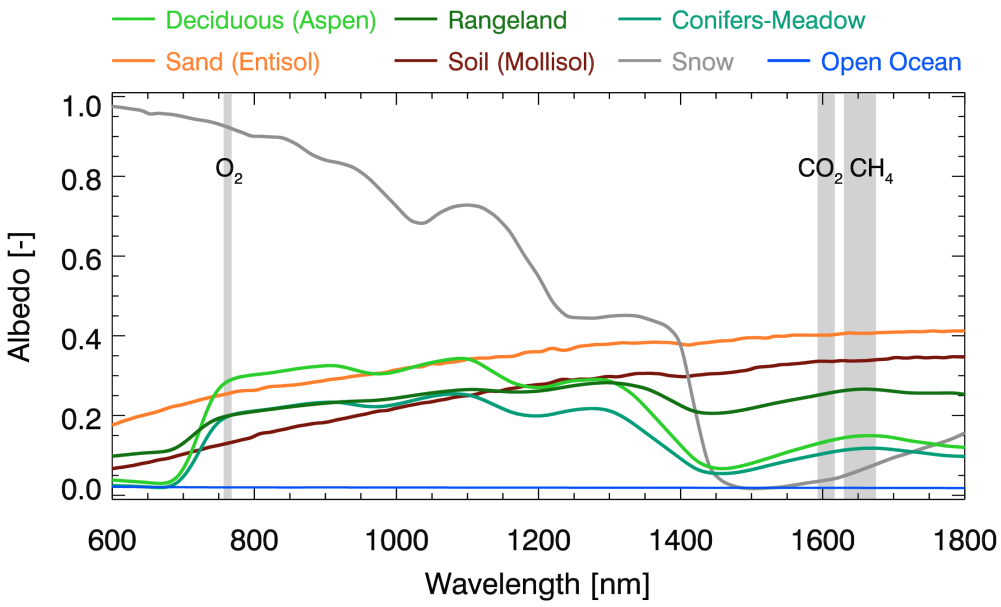

Figure 5.4: Surface spectral reflectances for different surface types with MAMAP fit windows shaded in grey. Reproduced from the ASTER Spectral Library through the courtesy of the Jet Propulsion Laboratory, California Institute of Technology, Pasadena, California (©1999, California Institute of Technology) and the Digital Spectral Library 06 of the US Geological Survey.

The surface types chosen here (soil, sand, snow, deciduous vegetation, conifer vegetation, rangeland and ocean) are based on the ASTER Spectral Library through the courtesy of the Jet Propulsion Laboratory, California Institute of Technology, Pasadena, California (©1999, California Institute of Technology) and the Digital Spectral Library 06 of the US Geological Survey in the same manner as used by Reuter et al. (2010). Where for the O_2 proxy method biases in case of MAMAP XCO_2 retrievals can be quite high, they are rather low for the CH_4 proxy method for both aerosol scenarios (background and urban). The

Table 5.6: Sensitivity to surface spectral albedo (surface type) reproduced from the ASTER Spectral Library through the courtesy of the Jet Propulsion Laboratory, California Institute of Technology, Pasadena, California (©1999, California Institute of Technology) and the Digital Spectral Library 06 of the US Geological Survey in the same form as used by Reuter et al. (2010). Thereby, the spectral albedo in the respective fit windows was smoothed by a polynomial of third order. Assumed solar zenith angle was 40° and the aircraft altitude was 1.25 km.

Aerosol scenario	Surface type	Sensitivities [%]					
		CO_2	CH_4	O_2	$XCH_4(CO_2)$	$XCO_2(CH_4)$	$XCO_2(O_2)$
OPAC background	Soil (Mollisol)	0.26	−0.23	−0.26	−0.03	0.03	0.52
	Sand (Entisol)	0.51	0.45	0.50	−0.06	0.06	−0.01
	Medium Snow	−0.26	−0.05	2.40	0.21	−0.21	−2.60
	Deciduous (Aspen)	−0.04	−0.08	0.43	−0.04	0.04	−0.47
	Conifers-Meadow	−0.09	−0.12	−0.09	−0.03	0.03	0.00
	Rangeland	0.10	0.08	0.07	−0.02	0.02	−0.03
	Open Ocean	−0.55	−0.46	−2.80	0.09	−0.09	2.31
OPAC urban	Soil (Mollisol)	0.39	0.34	−0.37	−0.05	0.05	0.76
	Sand (Entisol)	0.76	0.67	0.66	−0.09	0.09	1.43
	Medium Snow	−0.52	−0.17	2.96	0.35	−0.35	−3.38
	Deciduous (Aspen)	−0.09	−0.10	0.57	−0.01	0.01	−0.66
	Conifers-Meadow	−0.18	−0.18	−0.12	0.00	0.00	−0.06
	Rangeland	0.14	0.13	0.09	−0.01	0.01	0.05
	Open Ocean	−1.00	−0.85	−4.09	0.15	−0.15	3.22

largest errors are caused by snow due to the very low spectral albedo in the SWIR band.

Subvisual (and visual) cirrus can be a major challenge for remote sensing applications, since they are difficult to identify but can have a significant impact on the light path. Several cirrus cloud scenarios were tested (Table 5.7) using the radiative transfer model SCIATRAN. Thereby, the shape of the cirrus ice crystals was assumed to be fractal (fractal tetrahedron of the second generation) with an effective radius of $a_{\text{eff}} = 50\,\mu\text{m}$. Cirrus cloud base heights (CBH) were assumed to be at 6.0, 9.0, 12.0, 15.0, 18.0 and 21.0 km altitude. Each cirrus layer was assumed to be 500 m thick. The tested optical thickness (at a wavelength of λ =500 nm) and the corresponding ice water paths were 0.01, 0.05, 0.10, 0.30, 0.70 and 0.31, 1.54, 3.05, 9.20, 21.45 $\text{g}\,\text{m}^{-2}$, respectively. The CH_4 proxy method for XCO_2 also proves to be very robust in this case. For an optically thick (0.05) subvisual cirrus, errors to be expected range between −0.05 % and +0.05 % with respect to the background column.

Moreover, the water vapour influence on the retrieval result was investigated and has proven to be rather low (Table 5.8). For a water vapour enhancement of, for example, a factor of 2 compared to background, the error for XCO_2 applying the CH_4 proxy method is +0.02 %, showing that there is only little interference between water vapour and the XCO_2 product.

Table 5.9 lists typical uncertainties that may generally be expected for a retrieval of $XCO_2(CH_4)$ for small temporal and spatial scales. The total uncertainty estimate based on Table 5.9 is then about 0.24 % computed as the root of the sum of individual, squared uncertainties. The same is valid for the CO_2 proxy method in case of XCH_4 retrieval.

Table 5.7: Sensitivity to cirrus clouds for an aircraft altitude of 1.25 km, a solar zenith angle of 40° and a spectral albedo of 0.18 assuming a cirrus geometrical thickness of 500 m.

Optical thickness	Ice water	Cloud base	Sensitivities [%]					
[−]	path [g m^{-2}]	height [km]	CO_2	CH_4	O_2	$XCH_4(CO_2)$	$XCO_2(CH_4)$	$XCO_2(O_2)$
0.01	0.31	6.0	0.26	0.25	0.10	−0.01	0.01	0.16
		9.0	0.29	0.29	0.09	0.00	0.00	0.20
		12.0	0.30	0.31	0.10	0.01	−0.01	0.20
		15.0	0.31	0.32	0.10	0.01	−0.01	0.21
		18.0	0.31	0.33	0.10	0.02	−0.02	0.21
		21.0	0.33	0.31	0.10	0.02	−0.02	0.23
0.05	1.54	6.0	1.20	1.15	0.49	−0.05	0.05	0.71
		9.0	1.34	1.32	0.49	−0.02	0.02	0.85
		12.0	1.40	1.42	0.49	0.02	−0.02	0.91
		15.0	1.42	1.46	0.49	0.04	−0.04	0.93
		18.0	1.43	1.48	0.49	0.05	−0.05	0.94
		21.0	1.49	1.44	0.49	0.05	−0.05	1.00
0.10	3.05	6.0	2.18	2.09	0.95	−0.08	0.08	1.22
		9.0	2.44	2.42	0.95	−0.02	0.02	1.48
		12.0	2.56	2.59	0.96	0.03	−0.03	1.58
		15.0	2.60	2.68	0.96	0.07	−0.07	1.62
		18.0	2.61	2.72	0.96	0.10	−0.10	1.63
		21.0	2.73	2.62	0.96	0.11	−0.11	1.75
0.30	9.20	6.0	5.17	5.02	2.63	−0.15	0.15	2.47
		9.0	5.84	5.85	2.66	0.01	−0.01	3.10
		12.0	6.12	6.28	2.66	0.15	−0.15	3.37
		15.0	6.22	6.49	2.66	0.25	−0.25	3.47
		18.0	6.25	6.59	2.66	0.32	−0.32	3.50
		21.0	6.64	6.26	2.65	0.36	−0.36	3.89
0.70	21.45	6.0	8.90	8.74	5.29	−0.15	0.15	3.43
		9.0	10.04	10.24	5.35	0.18	−0.18	4.45
		12.0	11.53	10.06	5.35	0.48	−0.48	5.87
		15.0	10.70	11.44	5.34	0.67	−0.67	5.09
		18.0	10.76	11.63	5.39	0.78	−0.78	5.10
		21.0	11.72	10.78	5.38	0.85	−0.85	6.02

When applying the altitude correction as presented in Section 5.2 to compute $XCO_2(CH_4)$ or $XCH_4(CO_2)$ assuming all relevant greenhouse gas variation to occur below the aircraft, these errors further reduce according to Equation (5.15) to $\sigma_{XCH_4} = 0.14\%$ and $\sigma_{XCO_2} = 0.11\%$ for the given atmospheric conditions.

Table 5.8: Sensitivity of total column concentrations and their column-averaged dry air mole fractions using the proxy method to water vapour for a solar zenith angle of 40 ° and an aircraft altitude of 1.25 km. The H_2O scaling factors denote the scaling of the background water vapour profile, for example, due to emissions of water vapour from a power plant's cooling towers.

H_2O	Sensitivities [%]					
scaling	CO_2	CH_4	O_2	$XCH_4(CO_2)$	$XCO_2(CH_4)$	$XCO_2(O_2)$
0.5	0.00	−0.01	0.00	−0.01	0.01	0.00
1.0	0.00	0.00	0.00	0.00	0.00	0.00
1.5	0.00	−0.01	0.00	−0.01	0.01	0.00
2.0	−0.03	−0.05	−0.01	−0.02	0.02	−0.02
3.0	−0.13	−0.26	−0.01	−0.13	0.13	−0.12
4.0	−0.29	−0.59	−0.02	−0.30	0.30	−0.27

Table 5.9: Typical uncertainties to be generally expected in a standard retrieval of XCO_2 using the CH_4 proxy method and XCH_4 using the CO_2 proxy method for a spectral albedo of 0.18, an aerosol background scenario and a reference aircraft altitude of 1.25 km.

Parameter	Expected variation	Uncertainty [%]	
		$XCH_4(CO_2)$	$XCO_2(CH_4)$
Solar zenith angle	±5°	≈ +0.15 %	≈ −0.15 %
Aerosol	urban vs. background	≈ −0.05 %	≈ +0.05 %
Surface elevation	+50 m	≈ +0.16 %	≈ −0.16 %
H_2O profile	×2	≈ −0.02 %	≈ +0.02 %
Spectral albedo	Aspen vs. 0.18	≈ −0.04 %	≈ +0.04 %
Cirrus clouds (subvis.)	no cirrus vs. AOT 0.1, CTH 12 km	≈ +0.03 %	≈ −0.03 %
Aircraft altitude	±50 m	≈ −0.06 %	≈ +0.06 %
	total uncertainty estimate:	≈0.24 %	≈0.24 %

6 Range of application

6.1 Instrumental precision analysis

A key parameter to assess the performance of MAMAP and its possible range of application is the instrumental precision in combination with the observed ground scene size. The precision as defined by Gerilowski et al. (2011) with respect to MAMAP comprises all kind of random errors in measurement and retrieval including, although not truly random, errors resulting from variations of the surface spectral reflectance since they cannot be isolated. Using the algorithm described in detail in Section 5.1 and published in Krings et al. (2011), the instrumental precision was analysed in depth by Gerilowski et al. (2011). The results will be shortly summarised in the following.

Over homogeneous surfaces, the instrumental precision approaches the simulated value dominated by shot noise, dark signal shot noise and detector readout noise. For ground based measurements staring at a sun illuminated target, precisions of 0.33 % ($1\,\sigma$) could be derived for the retrieved profile scaling factor ratios (CH_4/CO_2 or CO_2/CH_4) while simulations predicted precisions of 0.27 %. This shows that the ground based performance of the instrument is as expected.

Most relevant for the analysis of data recorded over two coal-fired power plants in 2007 (Section 8) is the in-flight result for inhomogeneous land surfaces. This yielded a standard deviation of 1.74 % for profile scaling factor ratios using 10 co-added sequential measurements with a total integration time of about 0.6 s, whereas the simulated precision is 0.23 %. This large deviation between simulation and measurement was mainly attributed to errors resulting from inhomogeneous slit illumination.

The instrument improvement reducing pseudo noise resulting from inhomogeneous scenes (see Section 4.4) lead to an enhanced precision of about 0.6 % for 10 co-added measurements with a total integration time of 1 s over inhomogeneous land scenes even without using any filter on the fit quality. The precision is improved by about a factor of 3 compared to the original setup. This is visualised in Figure 6.1 which shows MAMAP $XCO_2(CH_4)$ retrieval results from the same power plant for the original and the

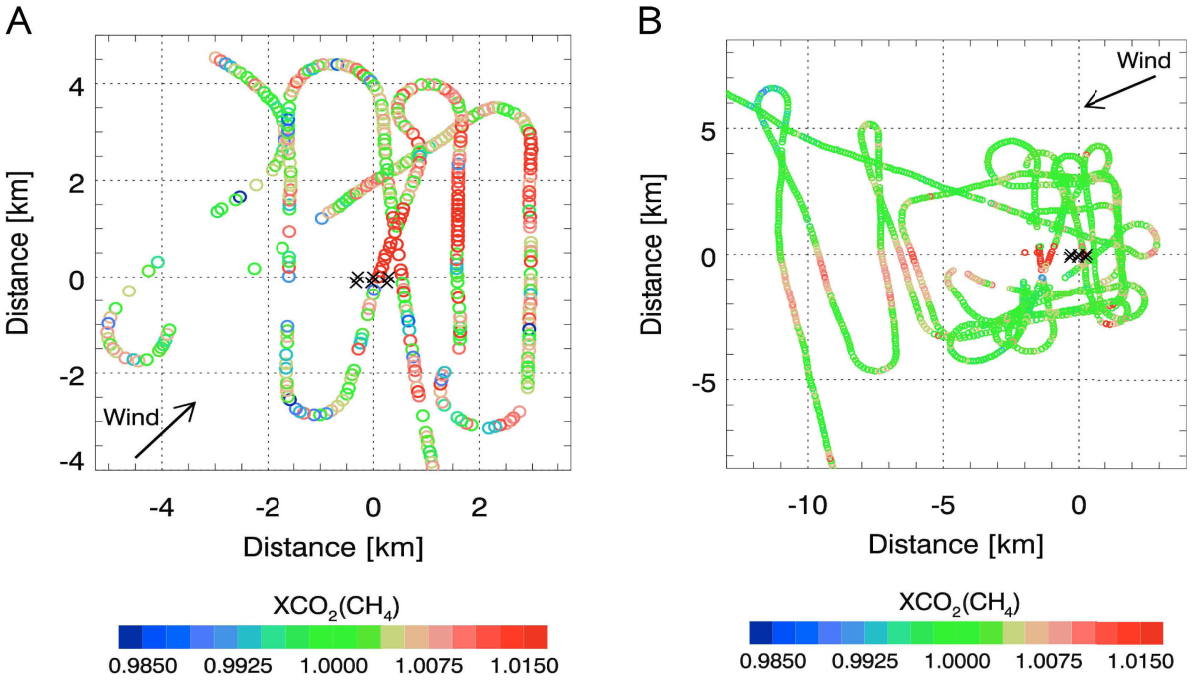

Figure 6.1: Panel A: Retrieved $XCO_2(CH_4)$ scaling factors relative to background over power plant Jänschwalde measured on 26 July 2007 using the original instrument setup. Black crosses denote the CO_2 releasing stacks. The data are unsmoothed but filtered for fit quality (RMS threshold was 0.95). Wind speed was about 4.5 m s^{-1} and the precision is about 0.83 %. Panel B: Preliminary data from the same power plant recorded with the improved instrument on 29 April 2011 with a precision of about 0.3 %. The data are unsmoothed and not filtered for fit quality. Wind speed was about 7.5 m s^{-1}.

improved instrument setup. While the unsmoothed result of measured data using the original instrument setup appears rather noisy in the shown scale, data recorded with the improved instrument exhibit a drastically reduced noise level even without applying a filter on the fit quality. Note that the precision for $XCO_2(CH_4)$ and $XCH_4(CO_2)$ can be determined from the profile scaling factor ratio precision multiplied with the conversion factor k ($\approx$ 0.5–0.6) that takes into account the aircraft altitude (see Equation 5.15).

6.2 Detection limits

The column detection limit of MAMAP refers to the minimum column variation that can be retrieved with reasonable certainty. In line with common definitions (IUPAC, 1997), a confidence limit of approximately 90 % can be reached for real data (which is usually not exactly Gaussian distributed) if variations relative to background are at the 3 σ level regarding the precision. This column variation can be translated into a minimum emission rate which would be necessary to create such a variation. However, the detection limit of MAMAP with respect to CO_2 or CH_4 emission rates from localised and point sources depends on various paramaters of the atmosphere and the measurement geometry such as wind speed, atmospheric stability and ground scene size (depending on aircraft altitude). In the following, detection limits for localised CH_4 and CO_2 sources based on simple

assumptions will be derived neglecting potential systematic errors which are less relevant when surveying point sources relative to the local background.

Methane

The minimum required, relative column enhancement in an entire MAMAP ground scene is defined as

$$\Delta V/V = 3\,\sigma \tag{6.1}$$

where σ denotes the precision of $X\mathrm{CH_4}$, V the $\mathrm{CH_4}$ vertical background column of approximately $3.67 \cdot 10^{19}$ molecules $\mathrm{cm^{-2}}$ and ΔV the column variation to be retrieved. Taking into account the $\mathrm{CH_4}$ molecular weight of about $16 \cdot 1.66 \cdot 10^{-27}$ kg, this results in a background column of 9.75 g $\mathrm{CH_4}$ $\mathrm{m^{-2}}$.

Assuming an air column to be continuously loaded with $\mathrm{CH_4}$ molecules by a flux F'_{area} per unit area and time (given in g $\mathrm{CH_4}$ $\mathrm{m^{-2}\,s^{-1}}$) during an accumulation time τ, this results in a column enhancement of $\Delta V = F'_{\mathrm{area}} \cdot \tau$:

$$\frac{\Delta V}{V} = \frac{F'_{\mathrm{area}}}{V} \cdot \tau \tag{6.2}$$

This is a good assumption when the source is larger than the instrument's ground scene and there is no diffusion to the sites (for example, assuming homogeneous area sources). The accumulation time τ can be regarded as the time an air column needs to move over a target. In this case, $\tau = l/u$ holds, where l is the linear dimension of the $\mathrm{CH_4}$ emitting target and u is the wind speed:

$$\frac{\Delta V}{V} = \frac{F'_{\mathrm{area}}}{V} \cdot \tau \tag{6.3}$$

$$\frac{\Delta V}{V} = \frac{F'_{\mathrm{area}}}{V} \cdot \frac{l}{u} \tag{6.4}$$

$$F'_{\mathrm{area}} = \frac{\Delta V}{V} \cdot V \cdot \frac{u}{l} \tag{6.5}$$

Hence, the detection limit is best for low wind speeds u and large accumulation lengths l.

For point sources with characteristic lengths of the order of the instrument's ground scene area $A = l_{\mathrm{CT}} \times l_{\mathrm{LT}}$ or smaller (for example, coal mine ventilation shafts), concentrations cannot be assumed to be constant perpendicular to wind direction. For very small point sources in a stable atmosphere where diffusion becomes relevant only far downwind from the source, the detection limit can be approximated similar to Equation (6.2) using the emission rate F_{point} in g $\mathrm{CH_4}$ $\mathrm{s^{-1}}$:

$$\frac{\Delta V}{V} = \frac{F_{\mathrm{point}}}{V \cdot A} \cdot \tau \tag{6.6}$$

$$F_{\mathrm{point}} = \frac{\Delta V}{V} \cdot V \cdot A \cdot \frac{u}{l_{\mathrm{LT}}} \tag{6.7}$$

where $\tau = l_{\mathrm{LT}}/u$ assuming that the wind direction coincides with the along-track direction (l_{LT}) of the ground scene. Similar to before, the accumulation time τ can be understood

as the time an air parcel covering an area of the instrument's ground scene size needs, to pass over a point source.

Considering a precision of 1.74 % (1σ) for the CH_4/CO_2 profile scaling factor ratios (see Section 6.1) and a typical aircraft altitude of 1.25 km, this gives a precision of about 1.0 % for $XCH_4(CO_2)$ assuming CH_4 to be constant above the aircraft (see Section 5.2). Or, following the instrument modification (see Section 4.4), the 1σ-precision is approximately 0.6 % for the profile scaling factors and about 0.35 % for $XCH_4(CO_2)$. This gives a minimum CH_4 column variation of $\Delta V/V = 3\,\sigma = 3.0\,\%$ for the old configuration and $\Delta V/V = 3\,\sigma = 1.05\,\%$ for the new configuration.

A reasonable characteristic length for localised targets is $l \approx 400\,\mathrm{m}$ (for example, landfills). Assuming further a wind speed of about $u \approx 2\,\mathrm{m\,s^{-1}}$ (approximately Beaufort 2), this gives an accumulation time of $\tau \approx 200$ s. From this, it follows that the corresponding emission rates at detection limit are:

old configuration ($3\,\sigma = 3.0$ %): $F'_{\mathrm{area}} > 130\,\mathrm{g\,CH_4\,m^{-2}\,day^{-1}} = 0.046\,\mathrm{t\,CH_4\,m^{-2}\,yr^{-1}}$

new configuration ($3\,\sigma = 1.05$ %): $F'_{\mathrm{area}} > 44\,\mathrm{g\,CH_4\,m^{-2}\,day^{-1}} = 0.016\,\mathrm{t\,CH_4\,m^{-2}\,yr^{-1}}$

For point sources, assuming the same wind speed of $u = 2\,\mathrm{m\,s^{-1}}$ and a ground scene size of $A = 29\,\mathrm{m} \times 33\,\mathrm{m}$ for the old configuration and $A = 25\,\mathrm{m} \times 79\,\mathrm{m}$ for the new configuration (see Section 4), this leads to detection limits of:

old configuration ($3\,\sigma = 3.0$ %): $F_{\mathrm{point}} > 17\,\mathrm{g\,CH_4\,s^{-1}} = 540\,\mathrm{t\,CH_4\,yr^{-1}}$

new configuration ($3\,\sigma = 1.05$ %): $F_{\mathrm{point}} > 5\,\mathrm{g\,CH_4\,s^{-1}} = 160\,\mathrm{t\,CH_4\,yr^{-1}}$

The obtained detection limits are highly dependent on wind speed. If wind speed is higher than assumed, the detection limits decrease according to Equations (6.5) and (6.7). Furthermore, it was implicitly assumed, that the MAMAP instrument took measurements in the direct vicinity downwind of the source.

Carbon dioxide

Corresponding calculations can be conducted for carbon dioxide assuming an aircraft altitude of 1.25 km and a CO_2/CH_4 profile scaling factor ratio precision of 1.74 % and 0.6 % for the old and new instrument configuration, respectively, as before. Assuming variations to occur below the aircraft, this yields 0.83 % and 0.3 % for the 1σ-precisions of $XCO_2(CH_4)$ and 2.5 % and 0.9 % for the corresponding $3\,\sigma$-neighbourhoods.

The background column of CO_2 is about $8.18 \cdot 10^{21}\,\mathrm{molecules\,cm^{-2}}$ or about $6\,\mathrm{kg\,CO_2\,m^{-2}}$. Since MAMAP measurements are relative to background, the sensitivity to CH_4 is about 220 times higher than to CO_2 with respect to molecule numbers because of the higher background load for CO_2. With respect to mass, MAMAP is about 600 times more sensitive to CH_4 due to the lower molecular mass of CH_4. When taking into account the altitude sensitivity factor, which is different for CO_2 and CH_4, the sensitivity to enhancements below the aircraft with respect to mass is approximately 500 times higher for CH_4.

Assuming the characteristic length of a localised CO_2 area source is about $l \approx 400\,\mathrm{m}$ and wind speed about $u \approx 2\,\mathrm{m\,s^{-1}}$, this results in a detection limit for CO_2 emission rates of:

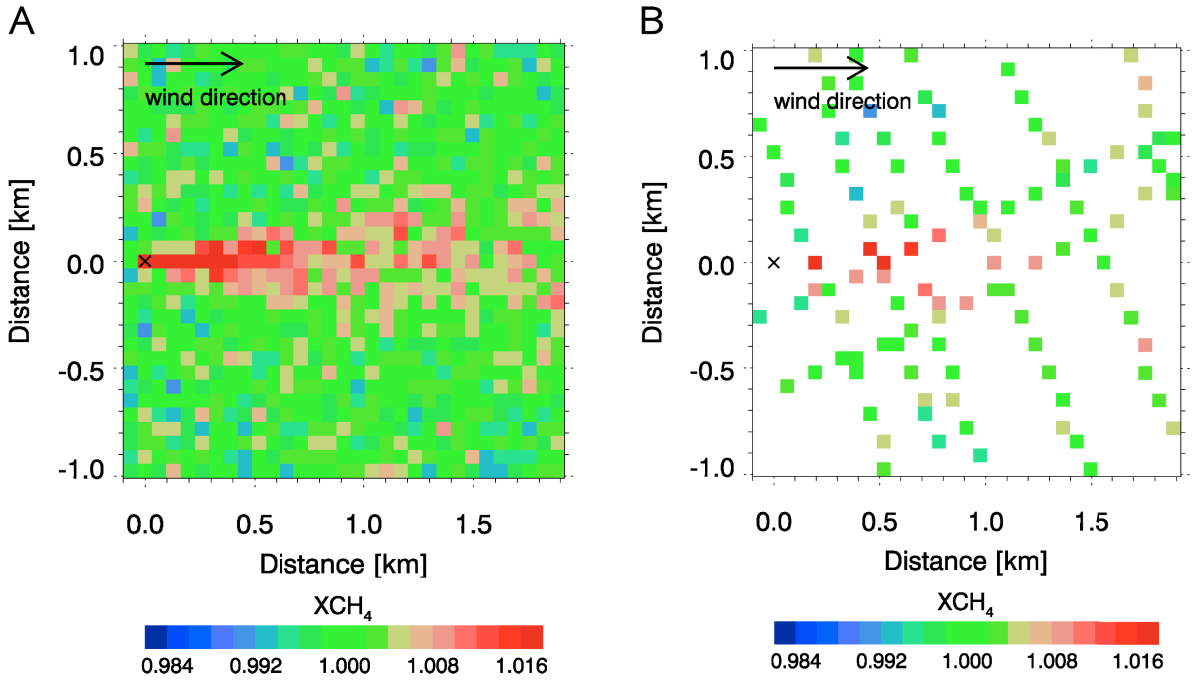

Figure 6.2: Panel A: Gaussian plume dispersion simulation (see Section 7) for a point source with an emission rate of F =4 kt CH_4 yr^{-1} as seen by an imaging instrument with a precision of 0.35 % (1 σ) for single ground scene XCH_4 observations. The resolution (65 m × 65 m) is equivalent to an approximate MAMAP ground scene. For the simulation, wind speed was set to 4 m s^{-1} and the atmospheric stability to slightly unstable. Panel B: Corresponding measurements using a non-imaging instrument like MAMAP based on a real flight track.

old configuration $(3\,\sigma = 2.5\,\%)$: $F'_{\text{area}} > 24\,\text{t}\,CO_2\,\text{m}^{-2}\,\text{yr}^{-1}$

new configuration $(3\,\sigma = 0.9\,\%)$: $F'_{\text{area}} > 9\,\text{t}\,CO_2\,\text{m}^{-2}\,\text{yr}^{-1}$

For a CO_2 point source assuming a wind speed of 2 m s^{-1}, the detection limit is:

old configuration $(3\,\sigma = 2.5\,\%)$: $F_{\text{point}} > 240\,\text{kt}\,CO_2\,\text{yr}^{-1}$

new configuration $(3\,\sigma = 0.9\,\%)$: $F_{\text{point}} > 90\,\text{kt}\,CO_2\,\text{yr}^{-1}$

6.3 Inversion limit

Generally, not only the detection but also the quantification of an emission source is desirable. In order to obtain a measurement signal well above noise level in a sufficient number of observations that allow for a stable inversion result, higher emission rates than just the detection limit are necessary. The minimum emission rate that still allows for an inversion, however, is not only influenced by atmospheric conditions but is also dependent on the flight track. Figure 6.2 (Panel A) shows a simulated CH_4 plume at instrument resolution including instrument noise of 0.35 % XCH_4 (1 σ) for a 4 kt CH_4 yr^{-1} source and a wind speed of 4 m s^{-1} as seen by an imaging instrument with a sufficiently large swath. However, MAMAP is non-imaging and only records one ground scene in across flight track

direction per overpass. Moreover, MAMAP data exhibit a mall spacing between adjacent along track measurements. The correspondingly sparser sampling of MAMAP is shown in Figure 6.2 (Panel B) based on a real flight track. The plume is still visible despite the noise but the figure illustrates the challenges that arise for detection and quantification of small sources.

Empirically, a plume can generally be identified if about 5–10 measurements inside the plume are above the detection limit. Based on this assumption, according to simulations, accurate inversions for point sources ($l \approx 50\,\mathrm{m}$) with a minimum emission rate of about 3–5 kt CH_4 yr^{-1} or about 2–3 Mt CO_2 yr^{-1} are feasible with the methods that will be described in Section 7 given a sufficient spatial sampling and wind speeds not more than $4\,\mathrm{m\,s^{-1}}$. In favourable atmospheric conditions, weaker sources can be quantified accordingly.

6.4 Potential targets

Having defined MAMAP's capabilities to measure and quantify particularly localised sources of CH_4 and CO_2, a wide range of potential target types with assumed emissions exceeding the MAMAP inversion limits (3–5 kt CH_4 yr^{-1} or 2–3 Mt CO_2 yr^{-1}) that are currently not well monitored can be identified.

For methane, for example, large landfills are interesting targets. In Europe, they are officially quantified in the E-PRTR[1] but exhibit large uncertainties in their emissions. The same is true for methane release from fossil fuel exploration and transport, like fugitive emissions from west Siberian gas fields and deposits that account for about 10 Mt CH_4 yr^{-1} (Jagovkina et al., 2000, and references therein).

Furthermore, refineries, compressor stations, offshore production platforms and blowout sites of natural gas (see Section 10) as well as coal mine ventilation shafts (see Section 9) can have emissions of up to 20 kt CH_4 yr^{-1} and more (E-PRTR). Marine, methane bearing sediments can lead to CH_4 concentrations of 3–8 ppm in the atmospheric surface layer on a few square kilometres (Shakhova et al., 2010) potentially large enough to produce total column increases detectable with MAMAP. Natural, geological seepage (Leifer et al., 2006a,b) and mud volcanoes (Etiope, 2009) have emissions that are hard to quantify but often are in the range of MAMAP's measurement capabilities. Seam gas emissions from open cut coal mines exhibiting similar features as landfills with respect to the source heterogeneity in time and space are complex to quantify. In Australia, for example, these open cut mines are responsible for an estimated amount of 360 kt CH_4 yr^{-1} in 2009 solely based on emission factors (Australian Government, 2011) (assuming all fugitive emissions to be CH_4). This is more than 30 % of Australia's total greenhouse gas emissions from mining activities.

Most carbon dioxide sources originate from localised combustion of fossil fuels, for example, at (coal fired) power plants that can easily reach emissions of 20 Mt CO_2 yr^{-1} and more (see Section 8 or E-PRTR). Steel plants, cement factories and flares on oil platforms (Villasenor et al., 2003) or refineries are further potential targets.

MAMAP may not only give rise to a better quantification of these sources but also to an increased understanding of physical processes governing emissions from similar targets.

[1] European Pollutant Release and Transfer Register, http://prtr.ec.europa.eu/, last access: May, 2012.

Part III

Inversion for point source emission rates

7

Developing two inversion approaches

In addition to the column-averaged dry air mole fractions $X\mathrm{CO}_2$ and $X\mathrm{CH}_4$ that can be inferred from MAMAP data using the retrieval algorithm presented in Section 5, particularly the actual emission rates of sources under investigation are of interest. To obtain point source emission rates using MAMAP $X\mathrm{CO}_2$ and $X\mathrm{CH}_4$ data, two inversion approaches have been implemented within the scope of this work: an inverse Gaussian plume model using an optimal estimation method and a Gaussian integral approach based on mass budgets (Krings et al., 2011).

7.1 Gaussian plume inverse modelling

The CO_2 or CH_4 concentrations downwind of a point source such as the coal-fired power plants under investigation in this study (see Section 8) can be estimated by a quasi-stationary Gaussian plume model (Sutton, 1932; Hanna et al., 1982; Masters, 1998, and references therein). Since MAMAP measures columns, the plume model equation for concentrations (mole fractions) C with vertical coordinate z

$$C(x,y,z) = \frac{F}{\pi\sigma_y(x)\sigma_z(x)u} \exp\left(-\frac{1}{2}\left(\frac{y}{\sigma_y(x)}\right)^2\right) \exp\left(-\frac{1}{2}\left(\frac{z}{\sigma_z(x)}\right)^2\right) \tag{7.1}$$

can be integrated to the total vertical column V (in $\mathrm{g\,m^{-2}}$) and equals:

$$V(x,y) = \int_0^\infty C(x,y,z)\,\mathrm{d}z = \frac{F}{\sqrt{2\pi}\sigma_y(x)u} \exp\left(-\frac{1}{2}\left(\frac{y}{\sigma_y(x)}\right)^2\right) \tag{7.2}$$

where the x-direction is parallel to the wind direction and the y-direction is perpendicular to the wind direction. The advantage of the vertically integrated form is the independence of the actual vertical distribution of the plume. The difficulty to estimate vertical transport and plume rise, in particularly in the presence of water vapour emitted from cooling

Table 7.1: Stability parameters for different atmospheric stabilities of the Pasquill classification (Martin, 1976; Masters, 1998).

			$x \leq 1\,\text{km}$			$x \geq 1\,\text{km}$		
Stability	Description	a	c	d	f	c	d	f
A	very unstable	213	440.8	1.941	9.27	459.7	2.094	−9.6
B	moderately unstable	156	106.6	1.149	3.3	108.2	1.098	2.0
C	slightly unstable	104	61.0	0.911	0	61.0	0.911	0
D	neutral	68	33.2	0.725	−1.7	44.5	0.516	−13.0
E	slightly stable	50.5	22.8	0.678	−1.3	55.4	0.305	−34.0
F	stable	34	14.35	0.740	−0.35	62.6	0.180	−48.6

towers (Stephen and Moroz, 1976), causes increased complexity for in-situ methods (see, for example, Weil and Jepsen, 1977; Leifer et al., 2006b). For MAMAP observations, the vertical distribution is only important in terms of wind shear assuming variations in concentrations primarily occurring below the aircraft and acknowledging that the averaging kernels (see Section 5.2) are rather constant below the instrument.

The total, vertical column V depends on the emission rate F (in $\text{g}\,\text{s}^{-1}$), the across wind distance y, wind speed u, and the horizontal dispersion coefficient (standard deviation) in y-direction σ_y (in m). The standard deviation $\sigma_y = \sigma_y(x)$ is a function of the along wind distance x and depends on the atmospheric stability parameter a (Martin, 1976) which is a measure for the mixing rate with ambient air:

$$\sigma_y = a \cdot x^{0.894} \tag{7.3}$$

where x must be specified in kilometres to obtain σ_y in meters. In contrast, the vertical dispersion is not directly needed for the inversion process but has been applied for simulations (see Section 8.5.3). The vertical dispersion coefficient (standard deviation) σ_z (in m) is given by (Martin, 1976):

$$\sigma_z = c \cdot x^d + f \tag{7.4}$$

with the distance x given in km and stability parameters c, d and f. The corresponding empirical stability parameters a, c, d and f are given in Table 7.1 depending on the atmospheric stability conditions.

A simplified classification of atmospheric stability (see Section 1.2) can be obtained by assessing solar insolation and surface wind speeds (see Table 7.2). Thereby, “Strong” insolation corresponds to a clear summer day with solar zenith angles lower than 30°, “Moderate” to a summer day with few broken clouds or a clear day with SZA of 30°–55° and “Slight” to an autumn afternoon, a cloudy summer day or a clear summer day with SZA of 55°–75° (Turner, 1970; Masters, 1998). In overcast conditions, stability class D can generally be assumed independent of wind speed (Turner, 1970).

This classification is predominantly valid for conditions over land. For applications over sea, where, for example, warm air over cold sea surface layers can lead to very stable conditions, a similar classification scheme based on wind speed and air-sea temperature difference is available (see Hasse and Weber, 1985).

Table 7.2: Simplified atmospheric stability classification (Turner, 1970). Surface wind speeds refer to a height of 10 m above ground.

Surface wind speed	Solar insolation		
[m/s]	Strong	Moderate	Slight
< 2	A	A–B	B
2–3	A–B	B	C
3–5	B	B–C	C
5–6	C	C–D	D
> 6	C	D	D

The equations presented above are valid for emissions originating from point sources. In order to simulate an emission source with a horizontal cross section y_0 at the plume's origin ($x = 0$ m), an offset x_0 is added in Equation (7.3):

$$\sigma_y = a \cdot (x + x_0)^{0.894} \tag{7.5}$$

The offset distance x_0 can then be computed as follows:

$$x_0 = \left(\frac{y_0}{4a}\right)^{\frac{1}{0.894}} \tag{7.6}$$

The factor of 4 is introduced so that the source width is described by a $\pm 2\sigma$ environment, that is, about 95.45 % of total emissions are confined along the source width at distance $x = 0$ m from the source.

The typical appearance of a simulated Gaussian plume for moderately unstable conditions (stability class B) is shown in Figure 7.1 (Panel A) using the example of a 50 m wide CO_2 source emitting 10 Mt CO_2 yr^{-1}. This corresponds, for example, to CO_2 emissions from a medium sized coal fired power plant. Also at approximate instrument resolution of the MAMAP instrument, the plume can clearly be identified (see Figure 7.1, Panel B).

Often, there is not only one separated source, but several emission sources are located close to each other like, for example, a number of CO_2 emitting stacks belonging to different blocks of the same coal fired power plant. When having such a network of N sources, the individual dispersion plumes can overlap and the vertical column V is a result of all contributing sources F_j. In this case, Equation (7.2) changes to:

$$V(x,y) = \sum_{j=1}^{N} \frac{F_j}{\sqrt{2\pi}\sigma_y(x_j)u} \exp\left(-\frac{1}{2}\left(\frac{y_j}{\sigma_y(x_j)}\right)^2\right) \tag{7.7}$$

where x_j, y_j denote the distance to the corresponding source location of F_j.

To obtain estimates of source emission rates F_j from measured vertical columns $V(x,y)$, a linear optimal estimation scheme can be used. However, in this study, additionally the stability parameter a is retrieved so that an iterative scheme has to be applied due to the

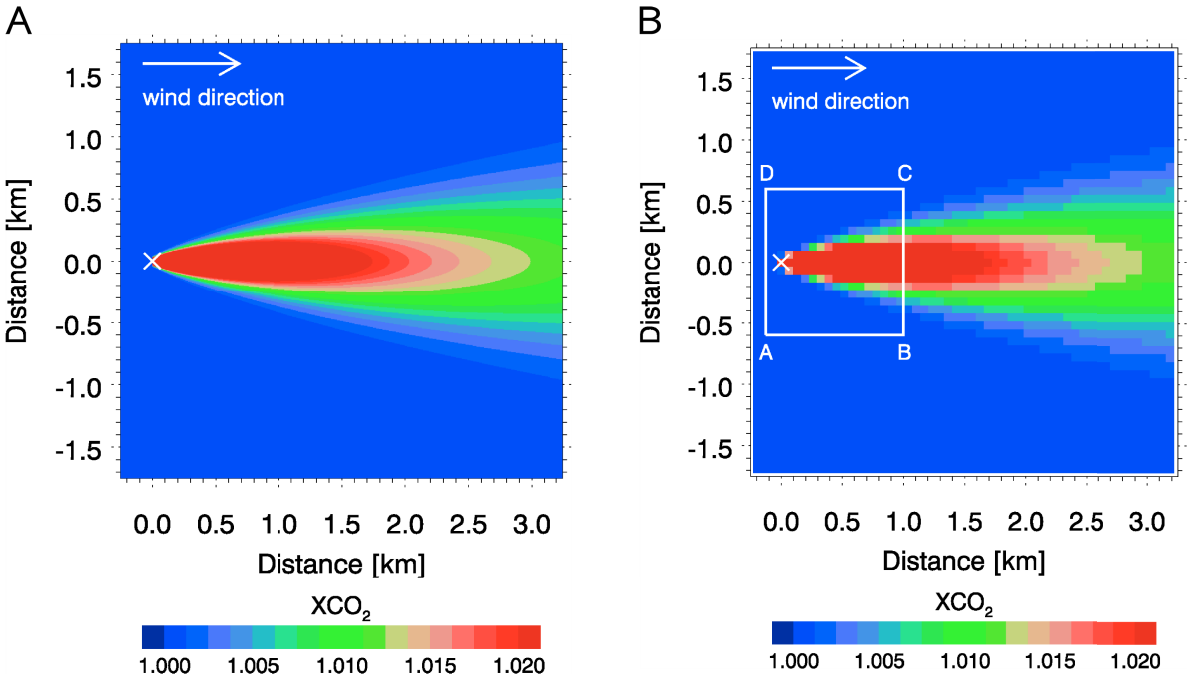

Figure 7.1: Gaussian plume dispersion simulation for a point source (denoted by a white cross) with an emission rate of F =10 Mt CO_2 yr^{-1}. Panel A: High resolution simulation of XCO_2 scaling factors relative to background mole fractions. Panel B: Sampling at approximate resolution of the MAMAP instrument (65 m × 65 m). The white rectangle denotes example boundaries for a Gaussian integral inversion approach. For the simulations, wind speed was set to 4 m s^{-1} and the atmospheric stability to moderately unstable (stability class B). Source width was 50 m.

non-linearity of the inverse problem. A detailed description of theory and application of optimal estimation methods can be found in the textbook of Rodgers (2000). In general, a forward model is fitted to data with respect to given a priori information. Here, optimal estimation finds the solution of maximum probability by minimising the following cost function χ for all F_j and a simultaneously:

$$\chi = \left(\mathbf{V}_{\text{meas}} - \mathbf{V}_{\text{mod}}\right)^T \mathbf{S}_\epsilon^{-1} \left(\mathbf{V}_{\text{meas}} - \mathbf{V}_{\text{mod}}\right) + \left(\mathbf{R} - \mathbf{R}_a\right)^T \mathbf{S}_a^{-1} \left(\mathbf{R} - \mathbf{R}_a\right) \tag{7.8}$$

where $\mathbf{R}$ is the state vector with entries F_j, a to be retrieved. Note that $V(x, y)$ has been re-indexed to a 1-dimensional vector with entries V_i. Furthermore, $\mathbf{V}_{\text{meas}}$ denotes the measured columns with the error covariance matrix $\mathbf{S}_\epsilon$, and $\mathbf{R_a}$ the a priori information of source emission rates and atmospheric stability with the associated covariance matrix $\mathbf{S_a}$. The forward model $\mathbf{V}_{\text{mod}}(\mathbf{R})$ is a function of the state vector elements F_j and a according to Equations (7.7) and (7.5).

If there was no a priori information, and hence, the uncertainties in $\mathbf{S_a}$ were arbitrarily large, Equation (7.8) would lead to a general weighted least squares solution as it was used in Bovensmann et al. (2010) for single point source satellite applications for CarbonSat. However, a priori information may become necessary for an increasing number of sources F_j, especially if they are located close to each other. To avoid unphysical ambiguities resulting in negative emission rates of individual sources, the a priori information can be used to constrain the emission rates to non-negative values. In the presence of strong

sinks, this has to be reconsidered, but for the targets of interest in this work, source strengths exceed possible sinks by several orders of magnitudes. Another possibility to avoid unphysical results is to couple the emissions, for example, by assuming emissions from each stack of a power plant to be equal.

The iterative maximum a posteriori solution $\mathbf{R}_{n+1}$ minimising Equation (7.8) and using an initial value $\mathbf{R}_n$ is given by Rodgers (2000):

$$\mathbf{R}_{n+1} = \mathbf{R}_a + \left(\mathbf{S}_a^{-1} + \mathbf{K}_n^T \mathbf{S}_\epsilon^{-1} \mathbf{K}_n\right)^{-1} \mathbf{K}_n^T \mathbf{S}_\epsilon^{-1} \cdot \left[\mathbf{V}_{\text{meas}} - \mathbf{V}_{\text{mod}}\left(\mathbf{R}_n\right) + \mathbf{K}_n\left(\mathbf{R}_n - \mathbf{R}_a\right)\right] \tag{7.9}$$

with the according covariance matrix:

$$\mathbf{S}_{n+1} = \left(\mathbf{K}_n^T \mathbf{S}_\epsilon^{-1} \mathbf{K}_n + \mathbf{S}_a^{-1}\right)^{-1} \tag{7.10}$$

where $\mathbf{K}$ is the Jacobian or weighting function matrix with entries $K_{i,j} = \partial V_i / \partial R_j$ and the index n denotes the iteration step number. For the present study, convergence is determined to be reached when:

$$\left(\mathbf{R}_{n+1} - \mathbf{R}_n\right)^T \mathbf{S}_{n+1}^{-1} \left(\mathbf{R}_{n+1} - \mathbf{R}_n\right) < \frac{N+1}{100} \tag{7.11}$$

If sufficient data are available in time and space, this statistical treatment will also mitigate the fact, that the Gaussian plume model is a good approximation only on average, but may be a bad representation for a snapshot in time.

7.2 Gaussian integral method

Another way to obtain estimates for emission rates of sources in a distinct area is to take advantage of the Gaussian divergence theorem. It states that the integrated flux F of a vector field $\mathbf{G}$ through the closed surface of region U is equal to the emission rate, which can be positive or negative indicating a source or a sink, respectively:

$$F = \iiint_U \operatorname{div} \mathbf{G}\, dU = \iint_S \mathbf{G} \cdot d\mathbf{S} \tag{7.12}$$

Here, the vector field is defined as:

$$\mathbf{G} = V\, \mathbf{u} \tag{7.13}$$

where V denotes the vertical column of the according trace gas and $\mathbf{u}$ the wind speed. With $\mathbf{n}$ being the normal unit vector on the boundary S, Equation (7.12) becomes in a discrete form:

$$F = \iint_S V\, \mathbf{u} \cdot \mathbf{n}\, dS \approx \sum_i V_i\, \mathbf{u} \cdot \mathbf{n_i}\, \Delta S_i \tag{7.14}$$

where ΔS_i is a scalar measure for the length of the boundary segment under consideration. In practice, the boundaries are generally chosen to form a polygonal shape in a horizontal projection which simplifies calculations. In Figure 7.1 (Panel B), for example, the four

boundary parts $\overline{AB}$, $\overline{BC}$, $\overline{CD}$ and $\overline{DA}$ form a rectangle. The length of segments ΔS_i for each boundary part are selected in a way that they represent the spatial resolution of the measurements. Boundary parts parallel to wind direction do not contribute in Equation (7.14) and can be omitted. For the example shown in Figure 7.1 (Panel B), this applies to the segments $\overline{AB}$ and $\overline{CD}$.

Since V is a measure for the whole column, no vertical transport has to be explicitly accounted for. Note that no horizontal diffusion is taken into account for this very simple approximation.

The boundaries for the actual inversion for emission rates have been chosen manually according to upwind and downwind flight tracks. Measurements along these boundaries have been assigned by a nearest neighbour approach. The upwind component offers potentially the advantage to distinguish between the sources of interest and upwind sources which might increase the background level of the trace gas under investigation.

8

Carbon dioxide from power plants

Large parts of this chapter have been published in Krings et al. (2011). The data presented in this chapter were recorded before the instrument improvement mentioned in Section 4.4 and Section 6.2.

8.1 Target description

During a test flight with a Cessna 207T aircraft (operated by the Free University, Berlin, Germany) close to Berlin on 26 July 2007, several overpasses with the MAMAP instrument were performed over the coal-fired power plants Jänschwalde and Schwarze Pumpe, both operated by the Vattenfall Europe Generation AG, Cottbus, Germany. The power plants are situated south-east of Berlin in the Lausitz lignite mining district exhibiting rather flat topography and with a distance of about 35 km in between (see Figure 8.1, Panel A).

Jänschwalde is a 3000 MW power plant consisting of 6 units, each producing 500 MW of energy mainly via burning of lignite. Flue gas is emitted through 6 out of a total of 9 cooling towers along with 600 t hr^{-1} water vapour per tower formerly trapped in the lignite, from burning hydrogen and from the flue gas desulphurisation (D. Heinze, central immission control representative, Vattenfall Europe Generation AG, personal communication, 2008). The remaining 3 cooling towers only emit water vapour. Annual CO_2 emissions are about 27.4 Mt CO_2 yr^{-1} and Jänschwalde power plant is listed among the top 10 of CO_2 producing power plants (data from CARMA, www.CARMA.org). The cooling towers reach about 113 m height.

The power plant Schwarze Pumpe is also fired with lignite and produces a total of 1600 MW of energy from two units. Two huge cooling towers emit water vapour and the flue gas. Schwarze Pumpe has annual emissions of about 11.9 Mt CO_2 yr^{-1} (data from CARMA, www.CARMA.org). The cooling towers have a ground diameter of 130 m and are about 140 m high.

For both power plants, all flue gases are released through cooling towers along with water vapour and not as in the past through separate high chimneys which in case of

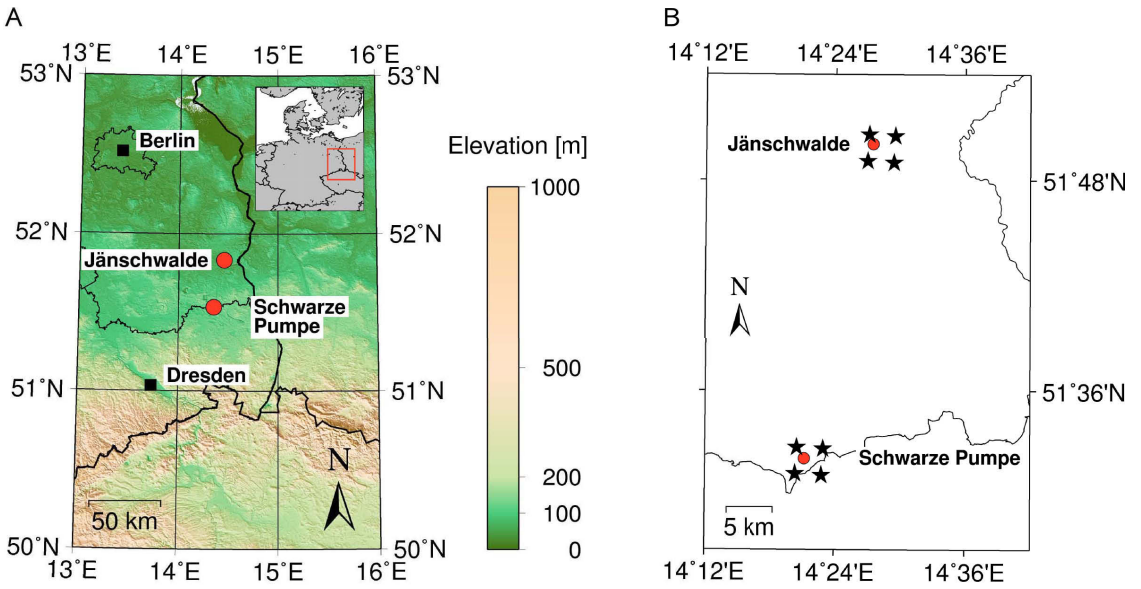

Figure 8.1: Panel A: Map of locations of power plants Jänschwalde and Schwarze Pumpe in eastern Germany close to Berlin. The distance between the two power plants is about 35 km. Panel B: Map showing the four nearest neighbours (black stars) of the power plants Jänschwalde and Schwarze Pumpe (red circle). Each of the power plants has a South-West, South-East, North-West and a North-East nearest neighbour according to the COSMO-DE data grid. (Maps in UTM projection. Topographic data were obtained from the Shuttle Radar Topography Mission (SRTM) version 2.1 (http://dds.cr.usgs.gov/srtm/version2_1/), a collaborative effort from NASA, NGA as well as the German and Italian Space Agencies.)

Jänschwalde were dismantled after installing effective SO_x (sulphur oxides) filters.

The day of measurement had favourable weather conditions characterised by clear sky with only slight cirrus and low to medium wind speeds close to ground. Clouds resulting from condensation of released water vapour were forming only directly above the cooling towers and disappeared in short distances from the power plants (see Figure 8.2).

Detailed information on the power plants' emission rates were obtained from data collected routinely by Vattenfall with a temporal resolution of 15 minutes for the time of the overpasses (see Tables 8.1 and 8.2). According to the German greenhouse gas emissions trading law TEHG (Deutscher Bundestag, 2004), CO_2 emissions are derived from power generation via emission factors for the respective power plants Jänschwalde (about $1.162\,\mathrm{t\,CO2\,MWh^{-1}}$) and Schwarze Pumpe (about $1.048\,\mathrm{t\,CO2\,MWh^{-1}}$). These emission factors are recalculated on a monthly basis and represent the monthly average. Due to the low variations in the combusted coal quality and due to the fact that the power plants were working on base load during the measurements, no significant deviations from the monthly mean were to be expected (D. Heinze, Vattenfall, personal communication, 2008). The error on power generation is generally about 1 % (D. Heinze, Vattenfall, personal communication, 2008). However, actual errors on CO_2 emission rates may potentially be significantly larger. In a study by Evans et al. (2009), for example, CO_2 emissions from different coal fired power plants derived from emission factors were found to be 15 % (and more) lower compared to estimates using continuous emission monitoring systems (CEMS) in combination with gas flow meters. Thereby, the uncertainty of concentrations

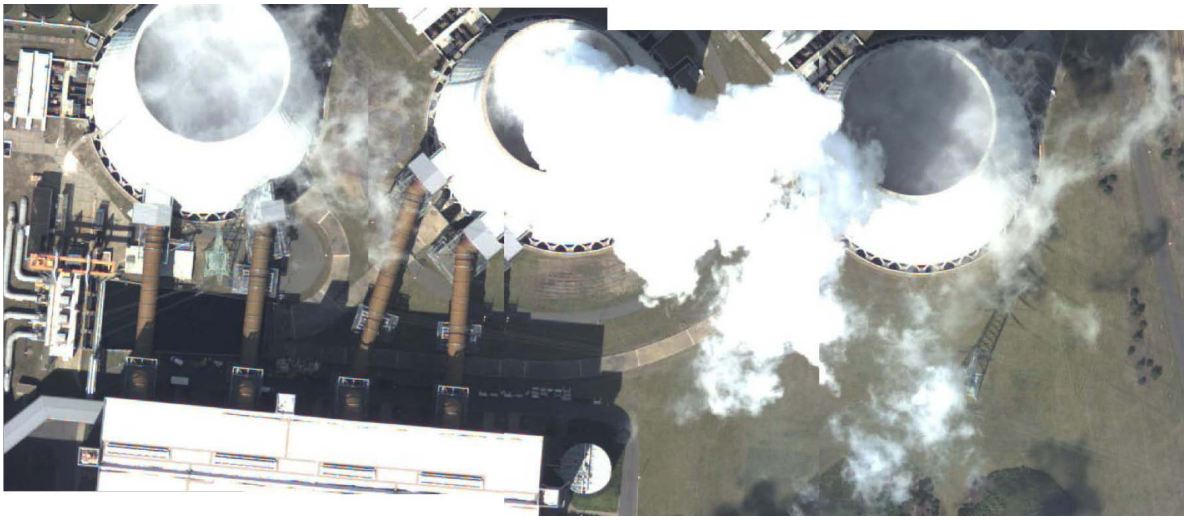

Figure 8.2: Combined images taken by the MAMAP pointing camera over the power plant Jänschwalde during measurements on 26 July 2007. The image consists of four separate photographs.

measured by CEMS is typically lower than 1 % and for the flow meters lower than 5 % (Evans et al., 2009, and references therein).

8.2 Measurement data

The measurements for Jänschwalde and Schwarze Pumpe power plant are displayed in Figure 8.3 and 8.4, respectively. The coordinates were converted from a latitude/longitude format to rectangular Universal Transverse Mercator projection coordinates (see Appendix F). This has the advantage that distances are directly interpretable and geometrical operations, like rotating data points, are easily possible. The data were normalised to the regional background (determined from total flight data) and smoothed by a 3-point moving average. The figures stress the conceptual advantage of using the proxy method over the single gas data. While for both power plants the CO_2 plume is clearly visible in the CO_2 data alone, the data become less noisy for $XCO_2(CH_4)$. Errors largely cancel when using the ratio of CO_2 with simultaneously retrieved CH_4, for example, during turns of the aircraft which tilts the instrument and extends the light path accordingly. General atmospheric effects mostly cancel as investigated in Section 5.3.

To ensure a high level of data quality, MAMAP dark current corrected data were filtered prior to the inversion. First of all, very low signals (maximum signal being below 3000 counts which is 5% of the full well capacity) and signals close to saturation (maximum signal at 55 000 counts which is 85% of the full well capacity, or higher) were rejected.

Subsequently, the quality of the fit has been assured by applying a filter on the RMS (root-mean-square) between fit and model. In Figure 8.5, the RMS values have been ordered by size and plotted. The threshold on the square root of the co-added, squared RMS values for CO_2 and CH_4 was set to 0.95 to reject outliers:

$$\sqrt{\mathrm{RMS}(CO_2)^2 + \mathrm{RMS}(CH_4)^2} < 0.95 \tag{8.1}$$

Table 8.1: Energy production and CO_2 emission rates for power plant Jänschwalde for 26 July 2007 computed using an emission factor of 1.162 t CO_2 MWh^{-1} (D. Heinze, Vattenfall, personal communication, 2008). CEST denotes the Central European Summer Time and UTC the coordinated universal time. In the last column, the 15 minute values are upscaled to yearly emissions for comparison.

Time		Power generation	Energy production	CO_2 emissions	
CEST	UTC	[MW]	[MWh]	[t/15 min]	[Mt/year]
08:30–08:44	06:30–06:44	2387.4	596.85	693.54	24.302
08:45–08:59	06:45–06:59	2395.8	598.95	695.98	24.387
09:00–09:14	07:00–07:14	2382.6	595.65	692.15	24.253
09:15–09:29	07:15–07:29	2370.0	592.50	688.49	24.125
09:30–09:44	07:30–07:44	2373.0	593.25	689.36	24.155
09:45–09:59	07:45–07:59	2370.6	592.65	688.67	24.131
10:00–10:14	08:00–08:14	2355.0	588.75	684.13	23.972
10:15–10:29	08:15–08:29	2355.6	588.90	684.30	23.978
10:30–10:44	08:30–08:44	2354.4	588.69	683.95	23.966
10:45–10:59	08:45–08:59	2360.4	590.19	685.70	24.027
11:00–11:14	09:00–09:14	2355.6	588.99	684.30	23.978
11:15–11:29	09:15–09:29	2364.0	591.09	686.74	24.063

Table 8.2: As Table 8.1 but for power plant Schwarze Pumpe using an emission factor of 1.048 t CO_2 MWh^{-1} (D. Heinze, Vattenfall, personal communication, 2008).

Time		Power generation	Energy production	CO_2 emissions	
CEST	UTC	[MW]	[MWh]	[t/15 min]	[Mt/year]
08:30–08:44	06:30–06:44	1419.784	354.95	371.98	13.034
08:45–08:59	06:45–06:59	1434.544	358.64	375.85	13.170
09:00–09:14	07:00–07:14	1437.696	359.42	376.68	13.199
09:15–09:29	07:15–07:29	1476.672	369.17	386.89	13.557
09:30–09:44	07:30–07:44	1488.192	372.05	389.91	13.662
09:45–09:59	07:45–07:59	1487.120	371.78	389.63	13.652
10:00–10:14	08:00–08:14	1478.820	369.71	387.45	13.576
10:15–10:29	08:15–08:29	1491.476	372.87	390.77	13.692
10:30–10:44	08:30–08:44	1497.332	374.33	392.30	13.746
10:45–10:59	08:45–08:59	1489.268	372.32	390.19	13.672
11:00–11:14	09:00–09:14	1482.968	370.74	388.54	13.614
11:15–11:29	09:15–09:29	1489.920	372.48	390.36	13.678

Generally MAMAP measurements are conducted in bursts of 10 single, sequential measurements. Each burst was selected to compute its average only if more than half of the measurements (that is 6 or more) passed the RMS and signal threshold criteria.

The Gaussian plume inversion has shown to be very stable against variation of the RMS threshold reflecting the effective statistical treatment by the optimal estimation method. A variation of the threshold of ± 0.1 leads to a variation of only $-0.4\,\%/+1.2\,\%$ on the

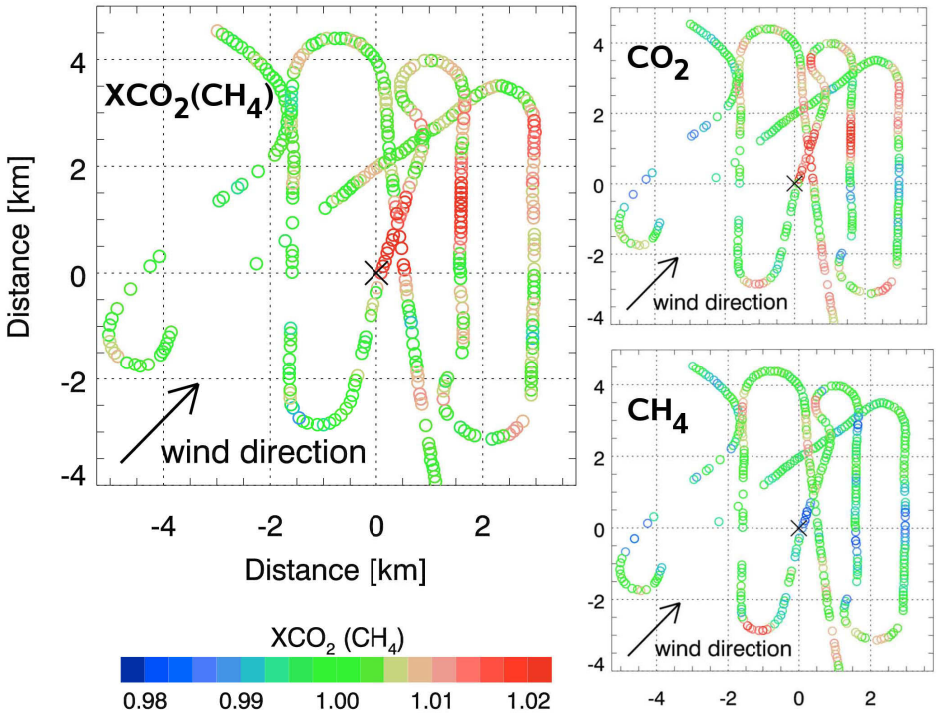

Figure 8.3: MAMAP data from Jänschwalde power plant. The left picture shows the column-averaged dry air mole fractions $X\mathrm{CO}_2(\mathrm{CH}_4)$ relative to background. The upper right picture shows that the CO_2 emissions can already be detected by the CO_2 measurements directly and are not features introduced by the proxy method due to possible errors in the CH_4 measurements (lower right). The single gas pictures (right) also show errors that occur for both measurements, for example, when the aircraft is turning. All data were normalised by the total mean of the complete flight and smoothed by a 3-point moving average. (Note that data on figures to the right do not represent dry columns and were additionally offset corrected for displaying reasons. They do not have the same scale as the ratios shown on the left.)

inversion result in case of Jänschwalde and $-3\,\%/-4\,\%$ in case of Schwarze Pumpe which has a weaker emission rate. For the Gaussian integral, the variation of the inversion is about $+2.3\,\%$ for Jänschwalde and $-1.9\,\%$ for Schwarze Pumpe when the RMS threshold is increased by $+0.1$. A reduction of the threshold causes rather large data gaps which, in combination with the nearest neighbour approach (see Section 7.2), does not lead do meaningful results.

The Gaussian integral is apparently more affected by the filter threshold. This is also due to the fact that less measurements are taken into account compared to the optimal plume estimation method so that single outliers can have a major effect on the inversion result. This is enhanced by the simple nearest neighbour approach that was chosen as a first approach leading to a nonlinear and partly erratic behaviour in case of sparse data. A dedicated flight pattern for measurements can mitigate the effect in future campaigns.

Finally, all data were corrected by the conversion factor k according to Equation (5.12). In the following, $X\mathrm{CO}_2(\mathrm{CH}_4)$ always refers to the altitude corrected mole fractions $X\mathrm{CO}_2(\mathrm{CH}_4)^{\mathrm{corrected}}$ (see Equation (5.13)) and is usually given as scaling factor relative to background.

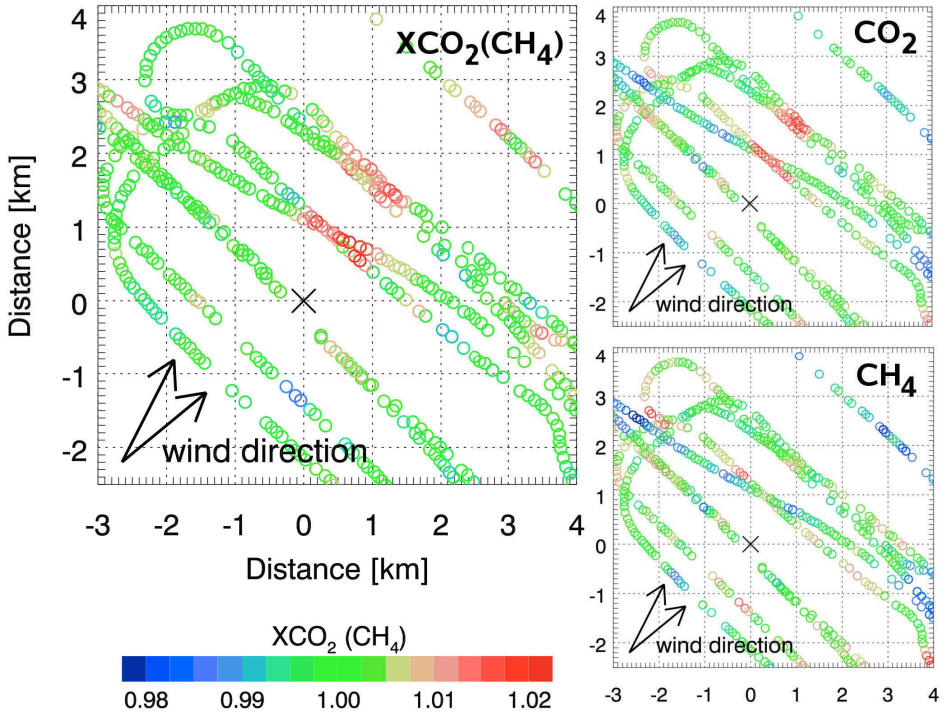

Figure 8.4: Same as Figure 8.3 but for Schwarze Pumpe power plant. Again, the power plant emission plume is already clearly visible in the CO_2 measurement (before $XCO_2(CH_4)$ is computed).

8.3 Wind data

Wind speed is a key parameter entering linearly into Equation (7.7), that is, an error of for example 5 % on the knowledge of the wind speed in the respective altitudes will result in a 5 % error on the emission rates. Hence, detailed knowledge of wind speed and also wind direction is essential. Since the flight over the power plants was designed as instrumental performance test, no on-site information of wind speed was acquired. Instead, wind information from the routine analysis of the numerical weather prediction model COSMO-DE operated by the German Weather Service (DWD) based on the COSMO model (Doms, 2011) was used to analyse the data obtained in terms of emission rates.

COSMO-DE has a spatial resolution of 0.025° × 0.025°. Taking into account that the model computes on a rotated latitude-longitude grid (the north pole is rotated to 170° west and 40° north, see also Appendix E), this results in a resolution of about 2.8 km × 2.8 km. For this study, the hourly wind data were only available interpolated to pressure levels (1000 hPa, 950 hPa, 850 hPa, 700 hPa, etc.). In principle, COSMO-DE output can also be taken directly from the model levels which have a higher vertical resolution with an increasing vertical spacing from 20 m near ground to about 300 m at 700 hPa (see Section 9).

For the inversion process using the integral and the plume method, it is necessary to have knowledge of wind speed at different altitude levels, since the plume rises as a function of distance from the source. The wind speed applied in Equation (7.7) refers to an average wind speed throughout the plume extension as required for the quasi stationary

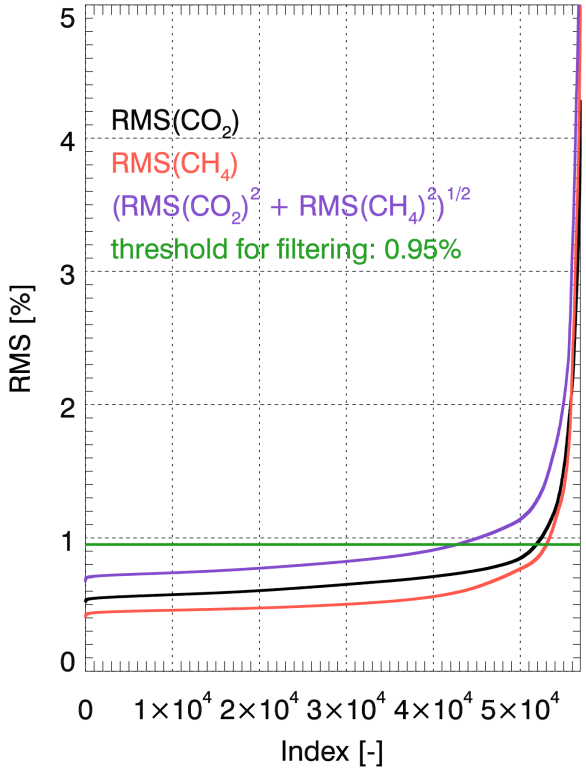

Figure 8.5: Root mean square (RMS) of the difference between fit and model for the dataset used for the inversion, ordered by value. The green vertical line shows the filter threshold which was set to 0.95 % for the analysis.

assumptions that were made.

Wind directions and wind speeds for different altitudes and at relevant times for the overpasses are depicted in Figures 8.6 and 8.7, respectively, for the four nearest neighbour data points according to the COSMO-DE model grid of each power plant (see Figure 8.1, Panel B).

Jänschwalde

From Figure 8.6 (Panel A), it can be seen that according to the COSMO-DE model during the time of the overflight 08:55–09:20 UTC, the wind direction in the lower layers was fairly stable at about 235°–245° for all four nearest neighbours of Jänschwalde power plant. Thereby, 180° refers to wind blowing from south, and 270° to wind blowing from west. This modelled wind direction fits the recorded data, which show a plume extension in the wind direction of about 228°, within a few degrees (see Figure 8.3). The deviation might be due to instationarity effects or caused by regional biases in the model and the coarse temporal resolution not capturing variations below one hour.

To obtain an average wind speed from the model data (Figure 8.7, Panel A) estimated for the whole CO_2 plume regarding both vertical and horizontal extension, a typical plume height of about 1.2 km ($\sigma_z \approx 300$ m) was assumed, since turbulences downwind of the power plant could be observed from the plane up to more than 1.0 km. Furthermore, the

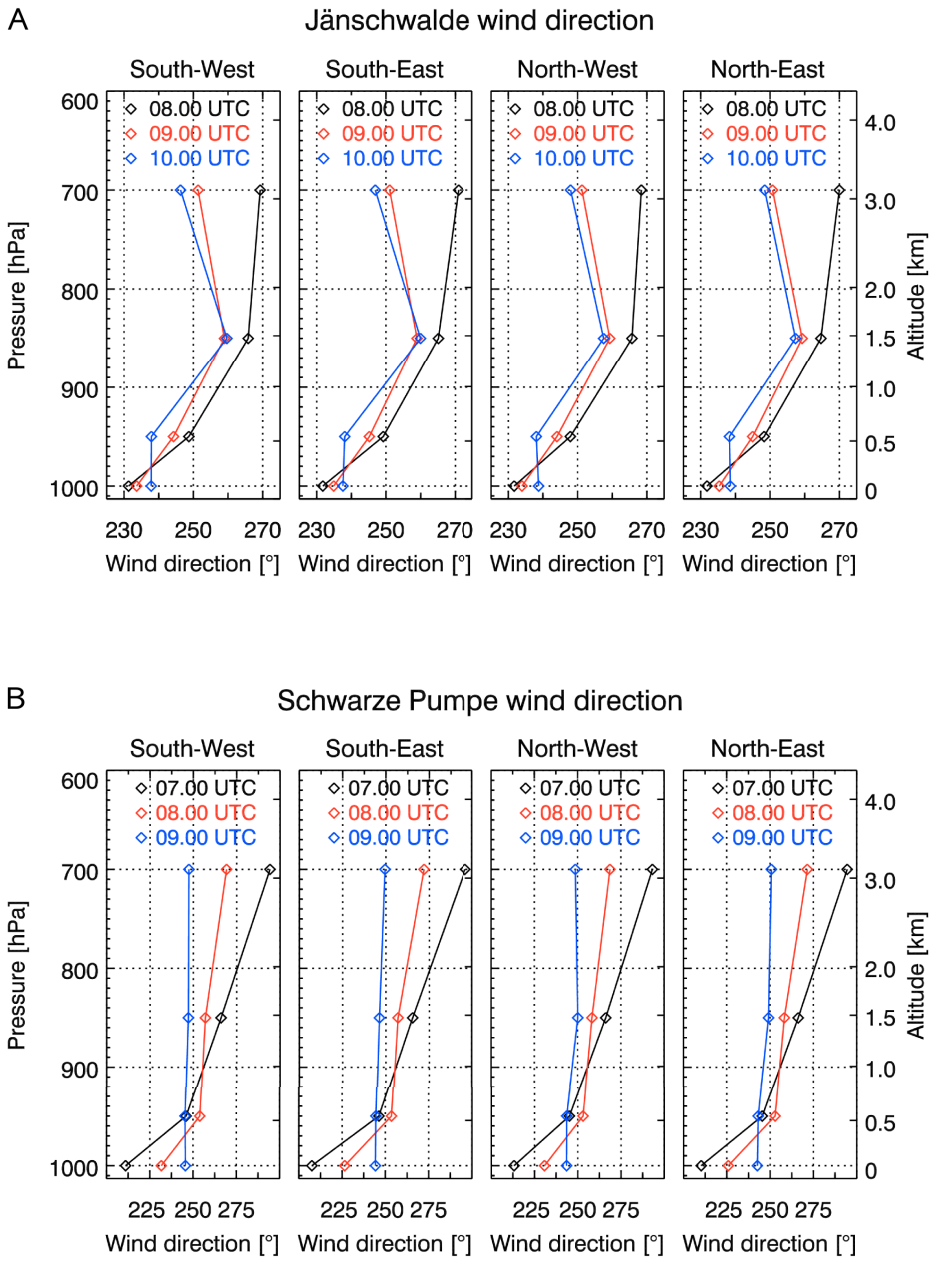

Figure 8.6: Figure of wind directions at the sites of the four nearest neighbours according to the COSMO-DE model grid of the power plants Jänschwalde (Panel A) and Schwarze Pumpe (Panel B) according to the COSMO-DE model as used for the inversion process.

CO_2 distribution was assumed to follow a vertical Gaussian profile $C(z)$ with the origin at stack height and which is reflected from the ground (see, for example, Pasquill, 1971; Beychok, 2005):

$$C(z) = \frac{1}{\sigma_z \sqrt{2\pi}} \left[\exp\left(-\frac{1}{2} \left(\frac{z-h}{\sigma_z} \right)^2 \right) + \exp\left(-\frac{1}{2} \left(\frac{z+h}{\sigma_z} \right)^2 \right) \right] \tag{8.2}$$

with the stack height $h = 113\,\mathrm{m}$. This confines about $k_0 = 56\,\%$ of the CO_2 to the

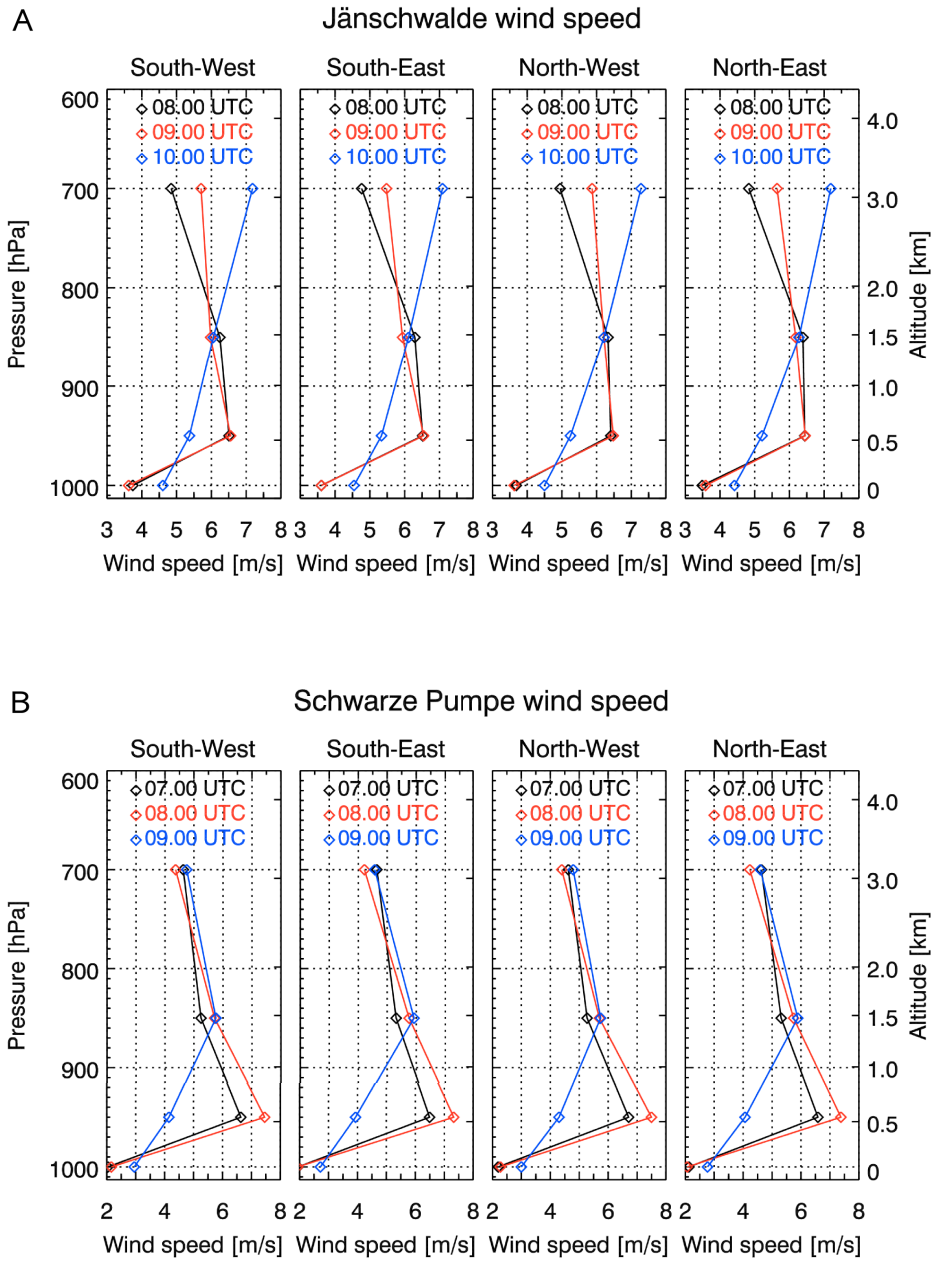

Figure 8.7: Figure of wind speeds at the sites of the four nearest neighbours according to the COSMO-DE model grid of the power plants Jänschwalde (Panel A) and Schwarze Pumpe (Panel B) according to the COSMO-DE model as used for the inversion process.

lowermost 250 m and about $k_1 = 44\,\%$ to the layer between 250 m and 1200 m. An average wind speed for the plume was then computed as follows:

$$\begin{aligned} \overline{u_{\mathrm{jw}}} &= \left[\left(k_0 \cdot \frac{1}{u_{p=1000\,\mathrm{hPa}}} \right) + \left(k_1 \cdot \frac{1}{u_{p=950\,\mathrm{hPa}}} \right) \right]^{-1} \\ &\approx \left[\left(56\ \% \cdot \frac{1}{3.6\,\mathrm{m\,s^{-1}}} \right) + \left(44\ \% \cdot \frac{1}{6.5\,\mathrm{m\,s^{-1}}} \right) \right]^{-1} \approx 4.5\,\mathrm{m\,s^{-1}} \end{aligned} \tag{8.3}$$

Schwarze Pumpe

Where for Jänschwalde wind conditions were sufficiently stationary, wind direction and wind speed were significantly changing for power plant Schwarze Pumpe at 08:10–08:45 UTC (see Figure 8.6 and 8.7, Panels B) causing problems for the inversion. Figure 8.8 shows that the change of wind directions is visible in the MAMAP data. To correct for that to some extent, the data were rotated to the first wind direction and then bent to fit the second wind direction. Obviously, this is in violation of the quasi stationary conditions needed for Gaussian plume assumptions and will affect the inversion result.

The wind directions and the distance from where to bend the data were identified empirically from the data, but are in agreement with wind data from the COSMO-DE model. 210° was assumed for the first wind direction and 234° for the second. The bending point was determined to be located about 1350 m downwind of the power plant.

An average wind speed was computed similarly as for the power plant Jänschwalde (see Section 8.3). Accounting for the corresponding model wind speeds (Figure 8.7, Panel B) and the greater stack height ($h \approx 140$ m) the average wind velocity is:

$$\begin{aligned} \overline{u_{\mathrm{sp}}} &= \left[\left(k_0 \cdot \frac{1}{u_{p=1000\ \mathrm{hPa}}} \right) + \left(k_1 \cdot \frac{1}{u_{p=950\ \mathrm{hPa}}} \right) \right]^{-1} \\ &\approx \left[\left(55\ \% \cdot \frac{1}{2.5\ \mathrm{m\,s^{-1}}} \right) + \left(45\ \% \cdot \frac{1}{5.6\ \mathrm{m\,s^{-1}}} \right) \right]^{-1} \approx 3.3\ \mathrm{m\,s^{-1}} \end{aligned} \tag{8.4}$$

8.4 Inversion results

Besides the wind direction and velocity, which have to be defined before any inversion can be performed (see Section 8.3), the atmospheric stability and the according stability factor a (see Equation 7.3) are also of importance for the Gaussian plume model inversion and are directly retrieved from the data. The measurements over the two power plants were performed in summer in the morning under almost cloud free conditions and hence strong solar insolation. Additionally, the flue gas containing the CO_2 is considerably warmer than the surrounding air masses leading to observed turbulences in up to 1.0 km altitude. Consequently, for the inversion, the a priori atmospheric stability was set to very unstable (stability class A, $a = 213.0$, see Section 7.1) with an uncertainty of ± 100.0.

In agreement with the information that all blocks of each power plant were running at the same level, emissions from all CO_2 emitting exhaust stacks were assumed to be equal for each power plant.

For the radiative transfer simulation, the aircraft altitude was in a very good approximation (± 35 m) assumed to be constant at 1250 m, the spectral albedo constant at 0.18 and the aerosol scenario was an OPAC urban scenario as defined in Section 5.3. The altitude correction factor is then $k = 0.475$ (see Table 5.1).

Figure 8.9 shows power plant stacks (black crosses), the measurement data gridded to boxes of 120 m × 120 m and the plume model inversion result as contour lines of total column scaling factors 1.020, 1.010 and 1.005. Only data between the dashed black lines were taken into account for the Gaussian plume inversion to obtain a more stable result for the stability parameter a which can be strongly influenced by outliers outside the plume

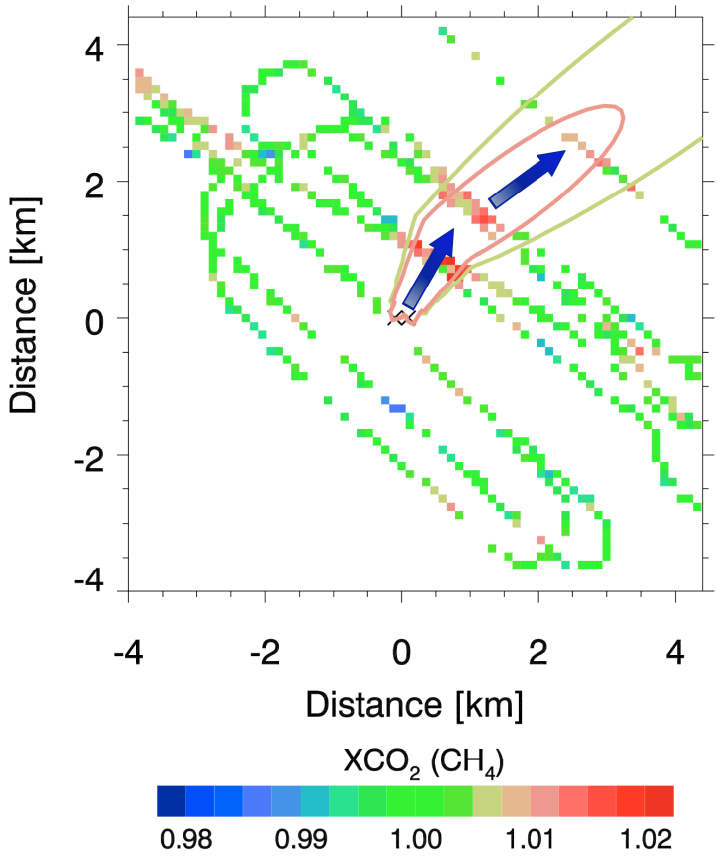

Figure 8.8: Figure showing gridded MAMAP data of the CO_2 plume from Schwarze Pumpe power plant. The blue arrows denote the change in direction of propagation of the plume. The contour lines indicate a simulated plume bend based on the reported emissions. The wind directions were estimated to about 234 ° and 210 °.

area. With an enhanced instrumental precision, this may become unnecessary in the future. A rather good graphical agreement of model and measurement can be observed for both Jänschwalde and Schwarze Pumpe power plant. This is confirmed by the cross sections along the solid black lines (Figures 8.10 and 8.11). The black lines in Figures 8.10 and 8.11 show the result of the measurement always using the nearest neighbour to a point on the line. A good agreement between measurements and simulations based on the Gaussian plume model can be achieved. However, the peak values in vicinity of the power plant exceed the measurement, whereas far from the power plant, the model generally underestimates the emissions. This may be connected to a non-constant stability parameter, for example, due to cooling of the flue gas. Despite the nonstationary wind conditions in case of Schwarze Pumpe, the model fits the data very well.

The solid black lines in Figure 8.9 downwind of the power plant stacks also indicate the boundaries chosen for the Gaussian integral approach. Although potentially useful (see Section 7.2), the upwind boundaries were not used for the inversion and are for visual purposes only. This is because data quality upwind of the power plants turned out to be rather poor. In case of Jänschwalde, sheets of water result in a low signal to noise ratio and a poor fit. Rejection of data from the already very low number of measurements

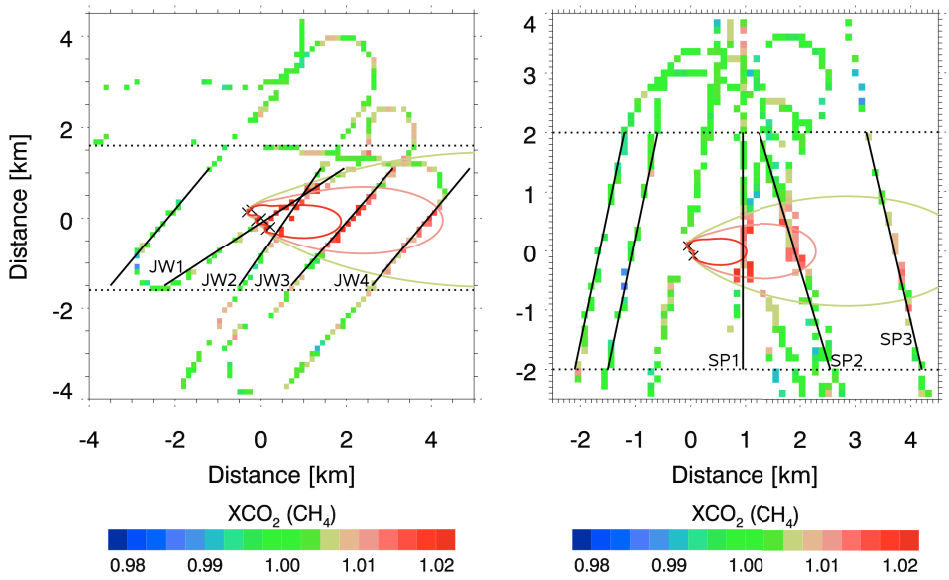

Figure 8.9: Gridded MAMAP data for power plants Jänschwalde (Panel A) and Schwarze Pumpe (Panel B) rotated and bent (only Schwarze Pumpe) to wind direction. $XCO_2(CH_4)$ refers to the altitude corrected dry air mole fractions relative to background. The solid black lines (JW1, JW2, ... and SP1, ...) indicate boundaries used for the Gaussian integral inversion, whereas the contour lines show the fit result of the Gaussian plume model inversion. The dashed black lines show the area which was taken into account for the Gaussian plume inversion.

upwind of the power plant can then lead to strong biases. Since the data were normalised and due to the fact that no CO_2 source of the order of magnitude of the power plant itself can be expected, the upwind component was set to background in a first approach. This can be avoided in the future when dedicated flight patterns are performed.

The same accounts for power plant Schwarze Pumpe where the very inhomogeneous area upwind of the power plant very likely leads to inhomogeneity effects as have been described in Gerilowski et al. (2011). The sensor modification (see Section 4.4) may avoid these problems in future, similar campaigns.

The result of the inversions are given in Table 8.3. The plume model inversion results for Jänschwalde and Schwarze Pumpe are in good agreement with the emission rate reported by the power plant operator (+8.3 % and −9.0 %). For Schwarze Pumpe, the change in wind conditions leading to an unpredictable distribution of the plume and violating the quasi stationary conditions is partly compensated by applying the differential rotation to the data and by fitting the stability parameter which takes into account plume broadening. For both power plants, the retrieved stability parameter is rather large indicating a dispersion corresponding to very unstable conditions. The statistical errors based on the optimal estimation inversion are 7.0 % and 12.4 % for Jänschwalde and Schwarze Pumpe, respectively, and are based mainly on the instrument precision and number of observations. Note that the reported emissions based on emission factors are not free of error either. However, thorough analysis of uncertainties on emission factors and hence the computed emissions are not available.

The measurement error used for the plume inversion was determined from the

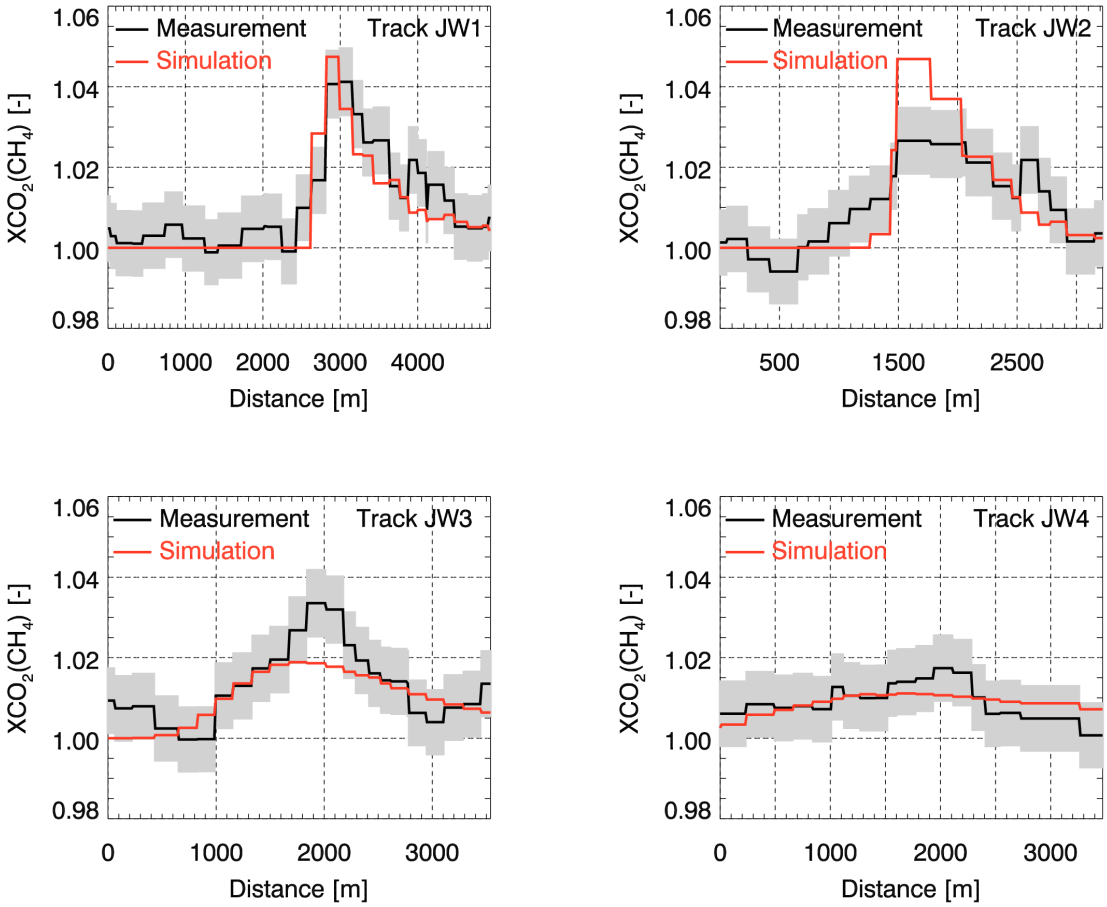

Figure 8.10: The figure shows model data (red) computed from the inversion result for the Gaussian plume model and measurements (black) in case of Jänschwalde power plant along horizontal cross sections through the CO_2 plume. The 1σ measurement uncertainty range based on the instrument precision is shown in grey. For the track numbers see Figure 8.9.

instrument precision given in Section 6.1 and Gerilowski et al. (2011) for the CO_2 profile scaling factor ratios: $\sigma_{\text{prof}} = 1.74\,\%$. Assuming an increase below the aircraft only, that is, using the conversion factor for subcolumn retrieval for the present configuration ($k = 0.475$, see Table 5.1), this results in a standard deviation of $\sigma = 0.83\,\%$ for XCO_2.

For the Gaussian integral, the results are about 0.2 % and 9.9 % below the reported emissions for Jänschwalde and Schwarze Pumpe, respectively, and hence in good agreement. These results assume that there is no systematic error on the inversion result due to the flight track. This assumption is valid for the Gaussian plume model fit but may depend strongly on the flight track pattern for the integral method (see Section 8.5.2).

8.5 Error discussion

8.5.1 Wind and stability

One of the largest uncertainties on the inversion results is caused by the uncertainty of the wind speed. Since wind speed is entering linearly into Equation (7.2), the relative

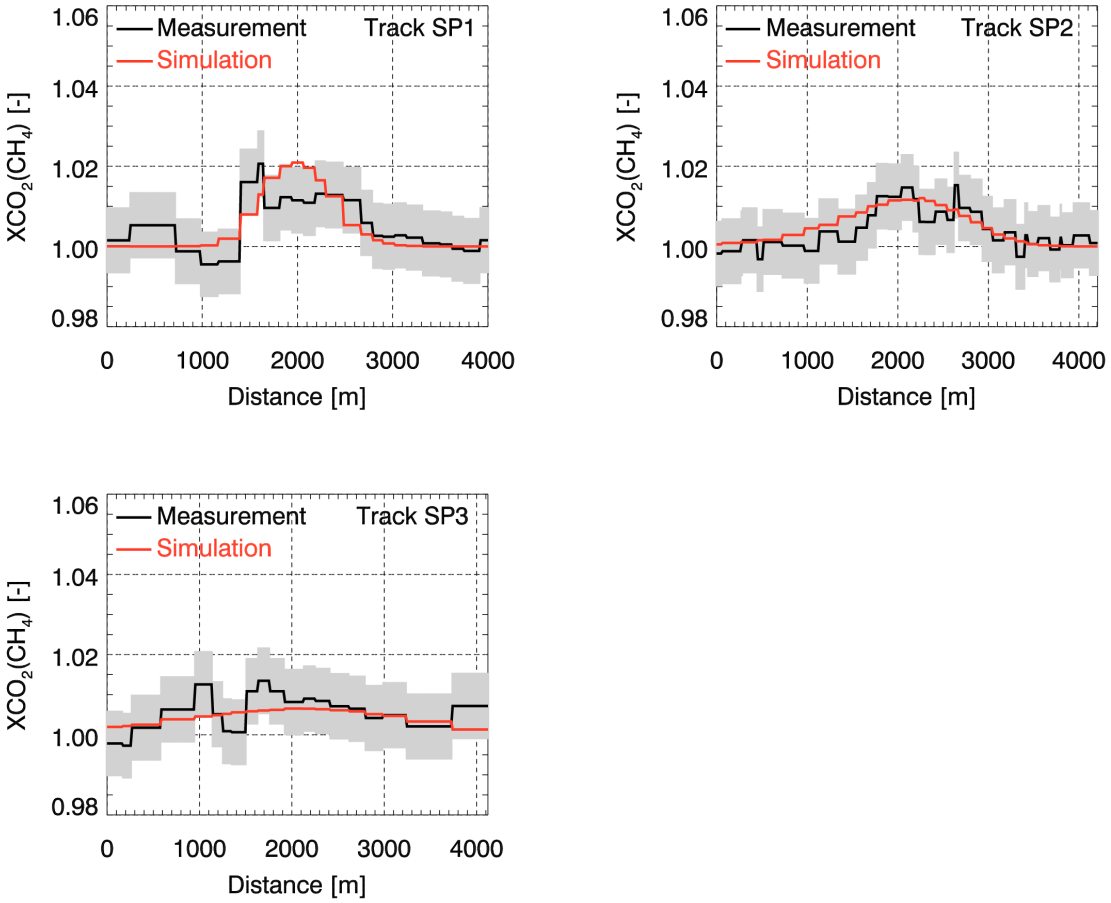

Figure 8.11: The figure shows model data (red) computed from the Gaussian plume inversion and measurements (black) in case of Schwarze Pumpe power plant along horizontal cross sections through the CO_2 plume. The 1σ measurement uncertainty range based on the instrument precision is shown in grey. For the track numbers see Figure 8.9.

error directly translates into a relative error for the inversion. For the morning of 26 July 2007 and the air layers of interest, the data of the COSMO-DE model have a root-mean-square-error of about $0.9\,\mathrm{m\,s^{-1}}$ compared to wind profiler data from the Lindenberg Observatory (Berlin) and virtually no bias (see Appendix G). The accuracy of the wind profilers used for the comparison can be assumed to be about $\approx 0.4\,\mathrm{m\,s^{-1}}$ (R. Leinweber, DWD, Lindenberg Observatory, personal communication, February 2011). Considering the root-mean-square-error, the uncertainty on the inversion result is 20 % for Jänschwalde and 27.3 % for Schwarze Pumpe power plant, based on the average wind speed of $4.5\,\mathrm{m\,s^{-1}}$ and $3.3\,\mathrm{m\,s^{-1}}$, respectively.

Also the uncertainty of the wind direction imposes an error on the inversion. For the wind direction, the root-mean-square-error of the COSMO-DE model data for the according date and time is about 11° with a bias of −9° (see Appendix G). The wind profilers have an accuracy of about ≈5° (R. Leinweber, DWD, Lindenberg Observatory, personal communication, February 2011). However, the wind direction can also be derived from the measured data directly like it was done for this study.

A special simulation set up was chosen to assess the influence of the wind direction

Table 8.3: CO_2 emission rate results for the power plants Jänschwalde and Schwarze Pumpe using the Gaussian plume model and the Gaussian integral inversion methods. For the Gaussian plume model, the result for the retrieved stability parameter a and the statistical errors according to Equation (7.10) are also given.

	Reported emissions	Plume inversion				Integral inversion	
Power plant	$[\mathrm{Mt\,yr^{-1}}]$	absolute $[\mathrm{Mt\,yr^{-1}}]$	relative to reported $[-]$	# pixels used for inversion	stability parameter $[-]$	absolute $[\mathrm{Mt\,yr^{-1}}]$	relative to reported $[-]$
Jänschwalde	24.125	26.131 ±1.838	1.083 ±7.03 %	174	327.4 ±10.2 %	24.066	0.998
Schwarze Pumpe	13.035	11.865 ±1.473	0.910 ±12.41 %	209	357.3 ±13.6 %	11.748	0.901

on the inversion result in the special case of the measurements over Jänschwalde and Schwarze Pumpe power plant presented here. To keep the simulation as realistic as possible, the inversion uses simulated measurements only at points where the MAMAP sensor actually recorded high quality data during the overflight. Simulated data were produced assuming a wind direction of 228° (Jänschwalde) and 210° (Schwarze Pumpe), whereas the inversion was run assuming several different wind directions. The results are summarised in Table 8.4. It can be seen that for the present flight pattern, the inversion bias is not symmetric as regards the change of wind direction. For example, in case of Jänschwalde, errors in wind direction of ±5° can result in an inversion error of +5.3 % and −4.5 % for the plume fit, and +8.3 % and −9.1 % for the integral approach, respectively. For Schwarze Pumpe, the errors are −1.8 % and −1.7 % for the plume inversion, and −2.0 % and +1.3 % for the integral method. In general, the denser the measurements are in quasi-stationary conditions, the more precisely the wind direction can be determined from the measurements due to a characteristic mismatch of measurement data and model fit (see Bovensmann et al., 2010).

8.5.2 Flight pattern and Gaussian integral

In theory, the flight pattern does not matter for the Gaussian plume inversion when computing the emission rate. It will only reduce the uncertainty on the final result. This has also been confirmed by inversion of simulated data. For the Gaussian integral, however, the flight pattern is of crucial importance. When simulating a plume and applying the flight patterns actually flown over Jänschwalde and Schwarze Pumpe for the inversion, the Gaussian integral does not give the source emission rate. From Figure 8.9, it can already be seen that flight paths for Jänschwalde are rather unfortunate for applying the integral method. Not only is one path of the aircraft running between the power plant stacks, but also the track to the very east was not long enough to cover the full horizontal plume extent. Under this condition, the assumption that there is no CO_2 transport perpendicular to the wind direction is not reasonable. This is also confirmed by the simulation which yields an emission rate of about 82.3 % of the true emission rate. This is a systematic error

Table 8.4: Systematic errors in emission rate and stability parameter a caused by choosing a wrong wind direction for plume model and Gaussian integral inversion of simulations of the Jänschwalde and Schwarze Pumpe power plant overflight. Default wind direction for the simulated data was 228 ° (Jänschwalde) and 210 ° (Schwarze Pumpe), default stabilities assumed for the simulation were the same as the retrieved stabilities for Jänschwalde and Schwarze Pumpe in Table 8.3. The results for the integral inversion are already corrected for the systematic error due to the flight pattern.

Δ wind direction	Jänschwalde			Schwarze Pumpe		
[°]	Δ emission rate [%]		Δ stability	Δ emission rate [%]		Δ stability
	Plume	Integral	Retrieved [%]	Plume	Integral	Retrieved [%]
0	+0.0	+0.0	+0.0	+0.0	+0.0	+0.0
+1	+0.5	+1.7	+1.2	+0.3	−0.3	+0.1
−1	−0.4	−1.8	−1.1	−0.2	+0.3	+0.0
+2	+3.2	+3.4	+5.0	+0.0	−0.7	+0.6
−2	−2.7	−3.6	−2.4	−0.6	+0.6	+0.3
+3	+3.1	+5.1	+6.9	−0.8	−1.1	+0.3
−3	−1.9	−5.4	−0.3	−0.2	+0.9	+0.9
+5	+5.3	+8.3	+10.9	−1.8	−2.0	+1.3
−5	−4.5	−9.1	−0.6	−1.7	+1.3	+1.6
+10	+1.7	+15.9	+15.8	−4.7	−4.8	+8.0
−10	−6.1	−18.9	+16.8	−3.7	+1.8	+7.5

that will also appear in the inversion of the real measurements. Hence, the result may have to be corrected for this flight track error by multiplying the final result with a factor of ≈1.22.

For Schwarze Pumpe, the flight tracks are more suitable, since they were long enough at appropriate distances to the power plant. Here, the simulation result is at about 96.9 % compared to the true emission rate, showing that there is almost no systematic error resulting from the choice of flight pattern in this case.

It is of importance for future measurements to apply appropriate flight patterns like, for example, the one at Schwarze Pumpe. More sophisticated interpolation methods compared to the nearest neighbour approach (which was used for this study) may also lead to improved inversion results in case of data gaps or unsuitable flight patterns.

8.5.3 Aerosol sensitivity for the inversion at Jänschwalde power plant

To assess the influence of aerosols on the inversion results, model simulations adapted to MAMAP measurements over the power plant Jänschwalde were performed, where atmospheric conditions were more favourable (more stable) compared to Schwarze Pumpe power plant.

Coal-fired power plants are known to release aerosols, that is, dust consisting mainly of gypsum, SiO_2, Al_2O_3 and SO_3 (D. Heinze, Vattenfall, personal communication, 2011) along with the carbon dioxide. Actual amounts vary depending, for example, on fuel composition and particle removal equipment (electrostatic precipitators (ESPs) or fabric

filters) efficiently removing 90 % – 99.9 % of particles from the flue gas (EPA–CICA Fact Sheet: Wet Electrostatic Precipitators, ESP). Prasad et al. (2006) find for coal-fired power plants in India typical enhancements in optical thickness of about 0.2–0.5 using MODIS satellite data. However, these results may not be representative for power plants with modern particle removal equipment. For example, a modernisation of a 50 year old coal-fired 160 MW power plant in India achieved a reduction in particulate matter emission by a factor of 50 (Prasad et al., 2006, and references therein).

There exist different approaches to estimate aerosol optical thickness (AOT) from mass concentrations of particulate matter (PM). Bovensmann et al. (2010) show that using the assumption of well mixed aerosols in a 2 km vertical column and applying the relation of Péré et al. (2009) between surface aerosol concentrations with diameter less than 10 µm (PM_{10}) and AOT, this results in a conservative estimate of an increase in AOT of about 0.5 per 1 % increase in total column CO_2.

The estimate for PM_{10} release from power plants of $1\,g\,PM_{10}\,kW\,h^{-1}$ given in Bovensmann et al. (2010, and references therein) is too conservative for modern lignite coal-fired power plants like the ones under consideration in this study. The US National Renewable Energy Laboratory (NREL) states emission factors of $41.6\,mg\,PM_{10}\,kWh^{-1}$ for PM_{10} and $0.714\,kg\,CO_2\,kWh^{-1}$ for carbon dioxide averaged over all electric power generation facilities including gas and nuclear power plants in the US (Deru and Torcellini, 2006, revised 2007). For the state of North Dakota which produces 91.8 % of its electrical energy from lignite coal, the average emission factor is $138\,mg\,PM_{10}\,kW\,h^{-1}$ and $1.18\,kg\,CO_2\,kW\,h^{-1}$. Hence, there is a release of about $120\,mg\,PM_{10}\,kg^{-1}\,CO_2$. Assuming a perfect spatial correlation between PM_{10} and CO_2 and additionally taking into account that the CO_2 background column is about $6\,kg\,m^{-2}$ (see Section 6.2), this results in an increase of roughly $\approx 10\,mg\,PM_{10}\,m^{-2}$ per 1 % columnar CO_2 increase.

By using mass extinction coefficients as used by Trier et al. (1997) ($4.93\,m^2\,g^{-1}$ at 550 nm for urban aerosol $PM_{2.5}$) and integrating over the full height or, alternatively, by applying the equation of Raut and Chazette (2009) relating urban PM_{10} concentrations to the extinction coefficient $\alpha_{ext,\,355nm}$ at 355 nm derived from LIDAR measurements ($PM_{10} = 0.217\,g\,m^{-2} \cdot \alpha_{ext,\,355\,nm}$), an increase in AOT due to a 1 % increase in CO_2 of about 0.05 can be estimated.

To model the aerosol impact on the inversion result more realistically, both CO_2 and the aerosol were distributed horizontally and in different height layers via a 3-dimensional Gaussian plume model depending on distance in wind and off-wind direction and height with the origin at the stack locations at the corresponding emission heights. To yield a conservative, general estimate, the stability was set to class B (moderately unstable) allowing for stronger aerosol accumulation compared to very unstable environments. For each ground scene, the according radiative transfer was computed including aerosol load and its height distribution according to Equations (7.4) and (8.2).

The results for the CO_2 over CH_4 ratios are shown in Figure 8.12. The maximum error in a measurement pixel is about +0.03 % occurring close to the power plant where aerosol load will be the largest. This, however, has only a minor effect on the plume inversion giving rise to a bias of +0.4 % on the emission rate after inversion. For the integral inversion, the bias is about +0.3 % compared to an inversion which does not account for a particular aerosol distribution. Hence, impact of aerosol scattering and absorption for coal-fired power plants equipped with modern filter mechanism is insignificant for the

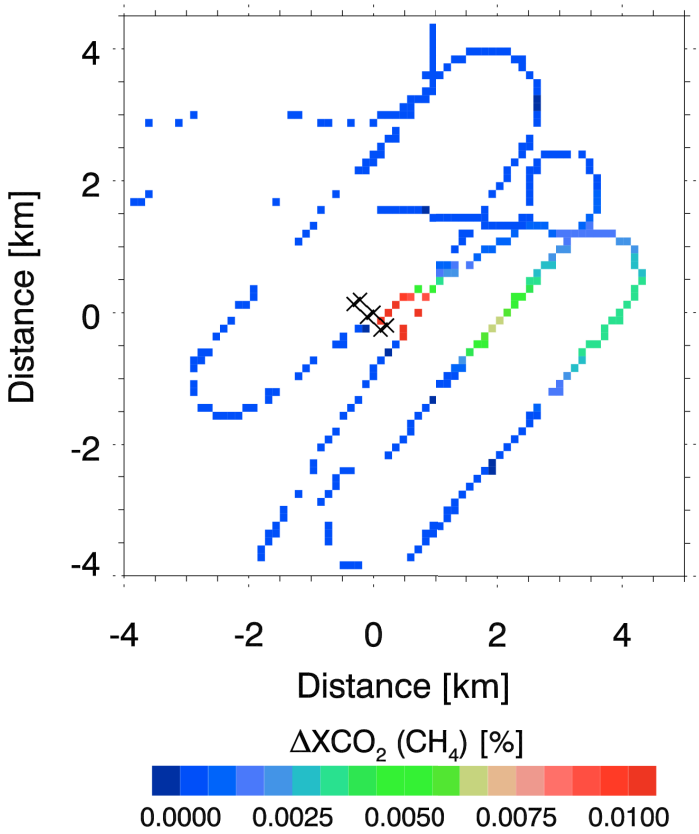

Figure 8.12: Systematic biases due to aerosol alone at the example of Jänschwalde power plant. Maximum error in close vicinity to the power plant is about +0.03 % relative to the background column. The overall plume model inversion is only biased by about +0.4 % of the true emission rate.

retrieval and the subsequent inversions applied here.

The power plants Jänschwalde and Schwarze Pumpe emit even less particulate matter than was assumed for this sensitivity study (D. Heinze, Vattenfall, personal communication, 2011). The actual emission for both power plants is less than 20 mg dust $kW\,h^{-1}$ and about 17 mg PM_{10} $kW\,h^{-1}$, while the specific CO_2 emissions for Jänschwalde are 1.15 kg CO_2 $kW\,h^{-1}$ and for Schwarze Pumpe 1.0 kg CO_2 $kW\,h^{-1}$.

8.5.4 Sensitivity to the conversion factor for Jänschwalde power plant

The conversion factor k accommodating for a CO_2 increase below the aircraft (see Section 5.2) depends not only on the aircraft altitude but also on the distribution of emitted CO_2 below the aircraft, because the averaging kernels are not constant with height. The distribution and plume height, however, are generally not well known, so that the conversion factor is only used as an average value for the subcolumn. Figure 8.13 shows the systematic errors resulting from using the average conversion factor on a Gaussian distributed CO_2 plume in case of Jänschwalde power plant. However, the highest deviation of the retrieved enhancement from the true enhancement is only about +0.06 % relative

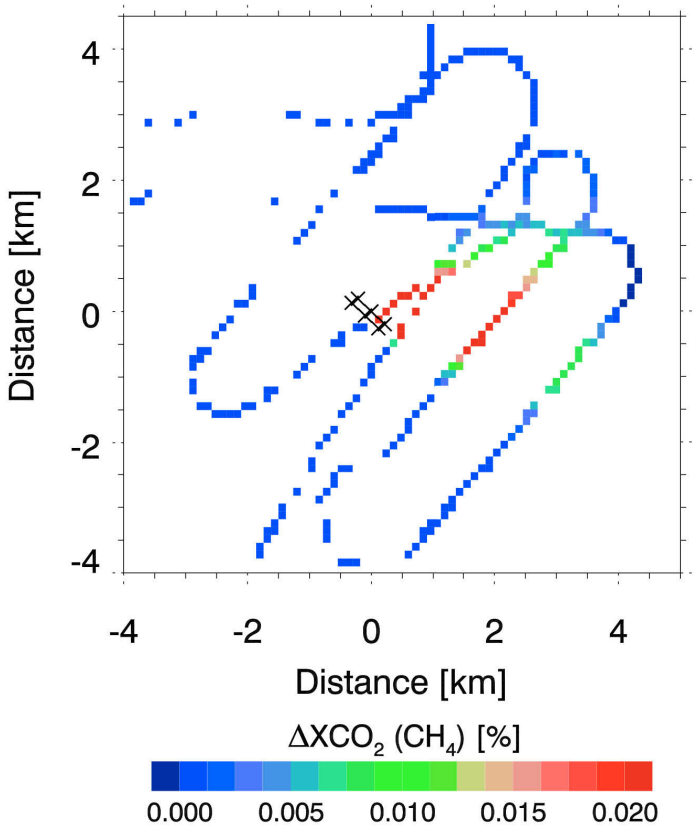

Figure 8.13: Propagated error on the retrieval result due to error on the conversion factor because of insufficient knowledge of the plume height and vertical distribution. Highest deviation from the true value is about +0.06 % relative to the background column. The error of the conversion factor estimates leads to a bias of +1.33 % of the true emission rate using the plume inversion method.

to background occurring close to the power plant, leading to a bias on the plume inversion of +1.3 % of the estimated emission rate. For the integral inversion, the bias is +0.9 % relative to the result with an adapted conversion factor k depending on the vertical CO_2 distribution.

8.5.5 Summary of inversion uncertainties

Generally, the inversion results are in good agreement with the reported values (Table 8.3). Table 8.5 summarises typical error sources and resulting uncertainties for the inverted emission rates of the two power plants. The errors are clearly dominated by uncertainties on wind information. The root-mean-square-error of the model wind speed (0.9 m s^{-1}) for the respective day and time of day are used for the uncertainty on the wind data in this case. In subsequent campaigns, on-site wind information was used to validate the model and to better assess the according error (see Section 9).

Wind directions were derived empirically from the data but due to violation of the stationarity assumption for the Gaussian plume model in case of Schwarze Pumpe, results of the inversion can be expected to have a larger bias. The correction applied by differential

Table 8.5: Overall uncertainty on the final emission rate estimates for the power plants Jänschwalde (JW) and Schwarze Pumpe (SP). Note that Schwarze Pumpe has a higher assumed uncertainty on the wind direction (±10°) due to nonstationary conditions.

	Uncertainty on emission rate [%]			
	Plume inversion		Gaussian integral	
Parameter	JW	SP	JW	SP
Statistical error	7.0	12.4	*	*
Wind speed ($\pm 0.9\,\mathrm{m\,s^{-1}}$)	20.0	27.3	20.0	27.3
Wind direction (±5° resp. ±10°)	5.3	4.7	9.1	4.8
Aerosol	0.4	*	0.3	*
Conversion factor k	1.3	*	0.9	*
Flight pattern (can be accounted for)	–	–	−17.7	−3.1

* according values not determined
– parameter not important for method

rotation of the data and retrieval of the stability parameter a can only partly compensate for that. To account for this additional issue, the error on wind direction is assumed higher for Schwarze Pumpe (±10°) than for Jänschwalde (±5°).

The errors introduced by additional aerosol load resulting from power plant emissions and by variations of the conversion factor k are rather small compared to the other error sources. The flight pattern imposes an error for the Gaussian integral method but can be mitigated by performing appropriate flight patterns during measurements.

It might be argued that the amount of CH_4 removed from the background concentrations in the flue gas by oxidation inside the power plant may potentially impose an additional error on the result of the CH_4 proxy method. However, simple approximations show that this effect is negligible (see Appendix H).

The total uncertainty, assuming errors to be independent and taking the root of the sum of squared errors, leads to uncertainties of the order of 20–30 %. The result is dominated by the uncertainties on wind information.

The uncertainty on the reported emission rate has been disregarded for this comparison so far. The emission factor estimate can be assumed to have a precision of about 1.5 % (in accordance with the EU guidelines, European Commission, 2007), but the accuracy may be significantly worse (Evans et al., 2009).

9 Methane from coal mine ventilation shafts

Parts of this chapter have been published in Krings et al. (2012).

9.1 Research campaign and platform

Coal mine ventilation shafts as an example of a methane source were surveyed on 4 June 2011 as part of the AIRMETH 2011 campaign, a joint research project of the Institute of Environmental Physics, University of Bremen (IUP-Bremen), the Alfred Wegener Institute for Polar and Marine Research (AWI) and the Helmholtz Centre Potsdam, German Research Centre for Geosciences (GFZ). The experiments were performed using the AWI airborne research platform Polar 5. The Polar 5 is based on a DC-3T aircraft refurbished by Basler Turbo Conversions to a BT-67 and further modified for scientific purposes.

Of the basic sensor suite, particularly the AIMMS-20 (Aircraft Integrated Meteorological Measurement System) turbulence probe added as compared to previous MAMAP campaigns is of interest for the retrieval of MAMAP XCH_4 (or XCO_2) because it delivers independent wind information at 30 Hz temporal resolution. This enhances the knowledge of the wind provided from meteorological models. The study of local and regional methane sources were the focus of this campaign. In addition to the MAMAP instrument, the aircraft payload comprised a LGR Los-Gatos Research Inc. RMT-200 fast CH_4 in-situ analyser. The analyser was equipped with an external pump to deliver fast in-situ methane measurements with a temporal resolution of 10 Hz at flight altitude. Furthermore, an imaging DOAS system monitoring NO_2 columns was installed.

As part of the AIRMETH 2011 campaign, methane measurements above ventilation shafts of the RAG Anthrazit Ibbenbüren GmbH coal mine in western Germany were conducted on 4 June 2011 and are analysed in this chapter. Another target of the AIRMETH 2011 campaign was a natural gas blowout site in the North Sea that will be presented in Section 10.

9.2 Mine gas

Mine gas is naturally produced during the slow transformation of plant matter to coal. Prerequisites for this coalification process are high pressure, high temperature and seclusion from oxygen. Generally, mine gas consists of methane, carbon dioxide and nitrogen. Additionally, also hydrogen, water vapour, ethane (C_2H_6) and hydrogen sulfide (H_2S) can occur (EnergieAgentur.NRW, 2009).

About 90 % of the mine gas in coal seams is trapped by adsorption, the rest in pores and caverns. During the time since the beginning of the coalification, about 95 % of the original mine gas has already escaped. For coal seams in the German district of North Rhine-Westphalia, the remaining gas content per ton coal is typically 0–22 m^3. In case of an active mine, the composition by volume is about 25–60 % CH_4 (coal seam methane, CSM), 1–6 % CO_2, 0.1–0.4 % CO, 7–17 % O_2, 4–40 % N_2 and traces of higher hydrocarbon compounds (EnergieAgentur.NRW, 2009).

German safety regulations require that CH_4 mixing ratios in German hard coal mines remain below 1–1.5 % (§35 BVOSt[1]) because methane is explosive in air mixing ratios of 4.4–16.5 % (1013.25 hPa, 20 °C) (EnergieAgentur.NRW, 2009). As a consequence, mine gas has to be extracted using ventilation and direct suction systems (ventilation air methane, VAM). Due to the variability of mine gas in different active mining areas of the same mine, gas production can vary by an order of magnitude during the year. This largely unpredictable temporal variation in conjunction with variation in composition also complicates the usage in combined heat and power units. Nevertheless, in 2007, about 75 % (54 Mt) of extracted methane content in mine gas were utilised referring to the German Ruhr mining area. Furthermore, the gas production varies during the course of the week. It is generally highest on Friday evening and lowest on Monday morning because there is often no coal extraction during weekends and gas production in active mines is tightly linked to cutting of fresh coal (EnergieAgentur.NRW, 2009). However, an abandoned coal mine continues to emit CH_4 with a half-life of 10–20 years (Dones et al., 2007, and references therein).

Lignite still includes large fractions of volatile compounds besides carbon (low degree of coalification) so that the actual mine gas content is usually lower than for hard coal. In addition, lignite is typically situated rather shallow enabling a more effective degassing. The CH_4 fraction in lignite mine gas is very low. This is because due to its shallowness, temperatures hardly reach 80 °C which are necessary for methanogenesis (Dones et al., 2007, and references therein). Large methane contents are therefore mainly expected for hard coal and anthracite.

9.3 Target description

The RAG Anthrazit Ibbenbüren GmbH coal mine is located in western Germany close to the city of Ibbenbüren (see Figure 9.1). Here, anthracite coal with a high degree of coalification and a comparably low content of volatile components[2] is extracted. In

[1] "Bergverordnung für die Steinkohlenbergwerke (BVOSt), vom 10. Januar 2000, in der Fassung vom 1.5.2001."

[2] 5–6 % volatile components, http://www.dsk-anthrazit-ibbenbueren.de/index.php?navi=2&haupt=produkte/index&bild=prod_anthrazit.gif, last access: May 2012.

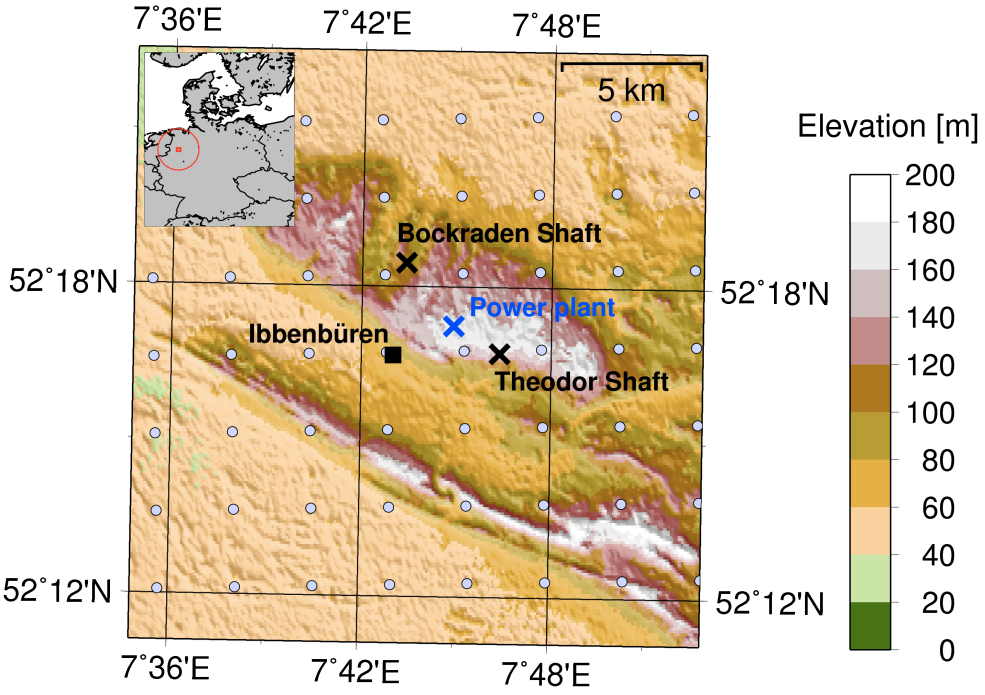

Figure 9.1: Map showing the location of the anthracite mine and the corresponding ventilation shafts that release CH_4 to the atmosphere: Bockraden Shaft and Theodor Shaft. The shafts are close to the city of Ibbenbüren. Light blue circles denote the COSMO-DE model data grid. (Map in UTM projection. Topographic data were obtained from the Shuttle Radar Topography Mission (SRTM) version 2.1 (http://dds.cr.usgs.gov/srtm/version2_1/), a collaborative effort from NASA, NGA as well as the German and Italian Space Agencies.)

comparison to other coal fields, the Ibbenbüren anthracite has a rather high content of mine gas (originally 21 $m^3\,t^{-1}$). This is attributed to a warming of rocks in geologically younger times presumably resulting from its larger depth compared to coal seams of the Ruhr area (EnergieAgentur.NRW, 2009).

The mine gas is released through two ventilation shafts about 4.5 km apart, the Theodor Shaft ("Theodorschacht") and the Bockraden Shaft ("Bockradener Schacht"). Each ventilation shaft is approximately 15 m high and has a diameter of about 7 m. Potential co-release of CO_2 does not hamper CH_4 measurements using MAMAP due to the by far higher sensitivity for CH_4 (see Section 6.2) and the low content of CO_2. There is a small coal fired power plant about half way between the shafts. It produces about 800 MW of power[3] and in 2010 emitted 4.97 Mt CO_2 according to the E-PRTR[4]. However, its CO_2 plume is not significantly interfering with the methane emissions as a result of the spatial separation.

The area around the ventilation shafts is characterised by hilly topography that is shown strongly exaggerated in Figure 9.1. According to the SRTM data, Theodor Shaft is located at an altitude of about 150 m, Bockraden Shaft at about 106 m and the power plant at about 174 m above sea level.

[3]RWE POWER AG, http://www.rwe.com/web/cms/de/55748/rwe-power-ag/standorte/kw-ibbenbueren/, last access: May, 2012.

[4]European Pollutant Release and Transfer Register, http://prtr.ec.europa.eu/, last access: May, 2012.

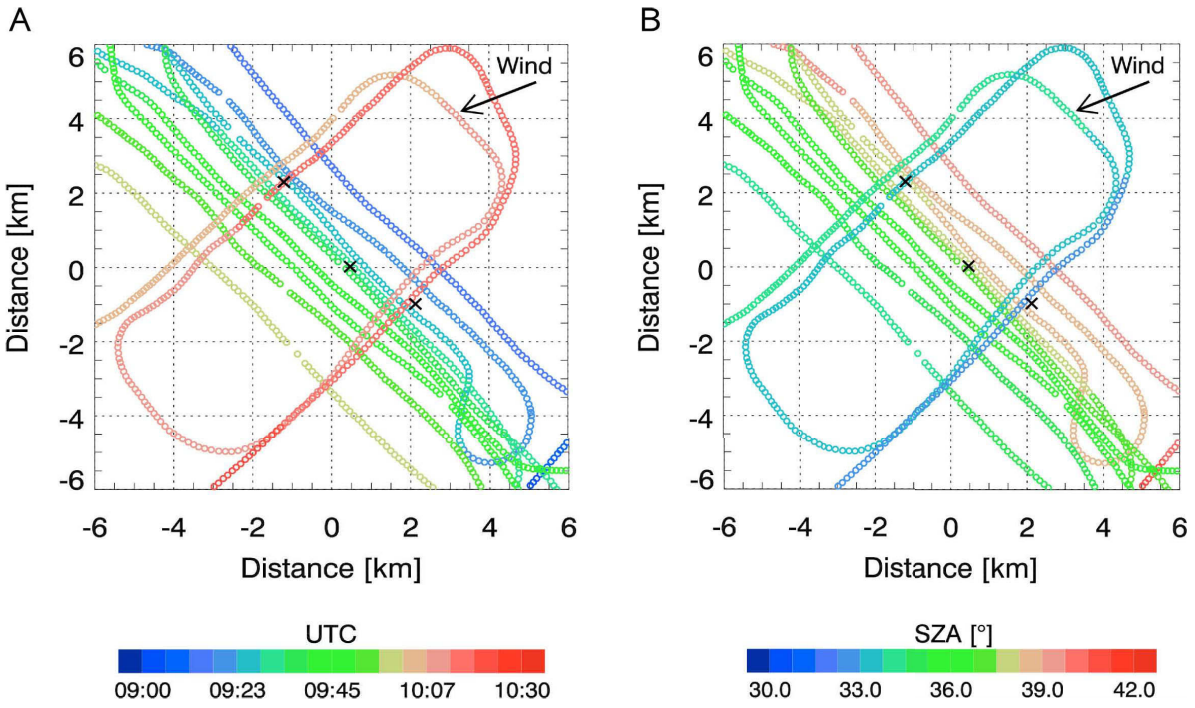

Figure 9.2: Panel A: Time of measurement for each pixel. Panel B: Change of solar zenith angle (SZA) during measurement.

The overflight on 4 June 2011 took place at 09:00–10:20 UTC (Figure 9.2, Panel A) during clear sky and sunny conditions. For the target area, local time was UTC+2 h.

9.4 Measurement data

The column-averaged dry air mole fractions $X\mathrm{CH_4}$ were retrieved using the algorithm and $\mathrm{CO_2}$ proxy method described in Section 5. The background profiles determining the linearisation point are based on the U.S. Standard Atmosphere (U.S. Committee on Extension to the Standard Atmosphere, 1976) shifted to actual concentrations. For $\mathrm{CO_2}$, a background profile of 390 ppm $X\mathrm{CO_2}$ was assumed. For $\mathrm{CH_4}$, the profile was updated to 1757 ppb $X\mathrm{CH_4}$ (with a surface concentration of 1840 ppb) based on the median value of the in-situ measurements which was about 1840 ppb in the boundary layer for this region. The median is generally more robust in presence of outliers (see, for example, Krings, 2007, and references therein), which in this case are the systematic enhancements in the methane plume. The same methane profile was used as background for the inversion process.

MAMAP data with a relative detector filling of about 5–85 % of the full well capacity (3000–55 000 counts) were selected to avoid low signals or signals close to saturation. For the reference radiative transfer model, an OPAC background aerosol scenario (see Section 5.3), an aircraft altitude of 1100 m, a mean solar zenith angle of 36° (Figure 9.2, Panel B) and an average surface elevation of 0.1 km was assumed. In this configuration, the conversion factor to correct for the altitude sensitivity effect (see Section 5.2) is about

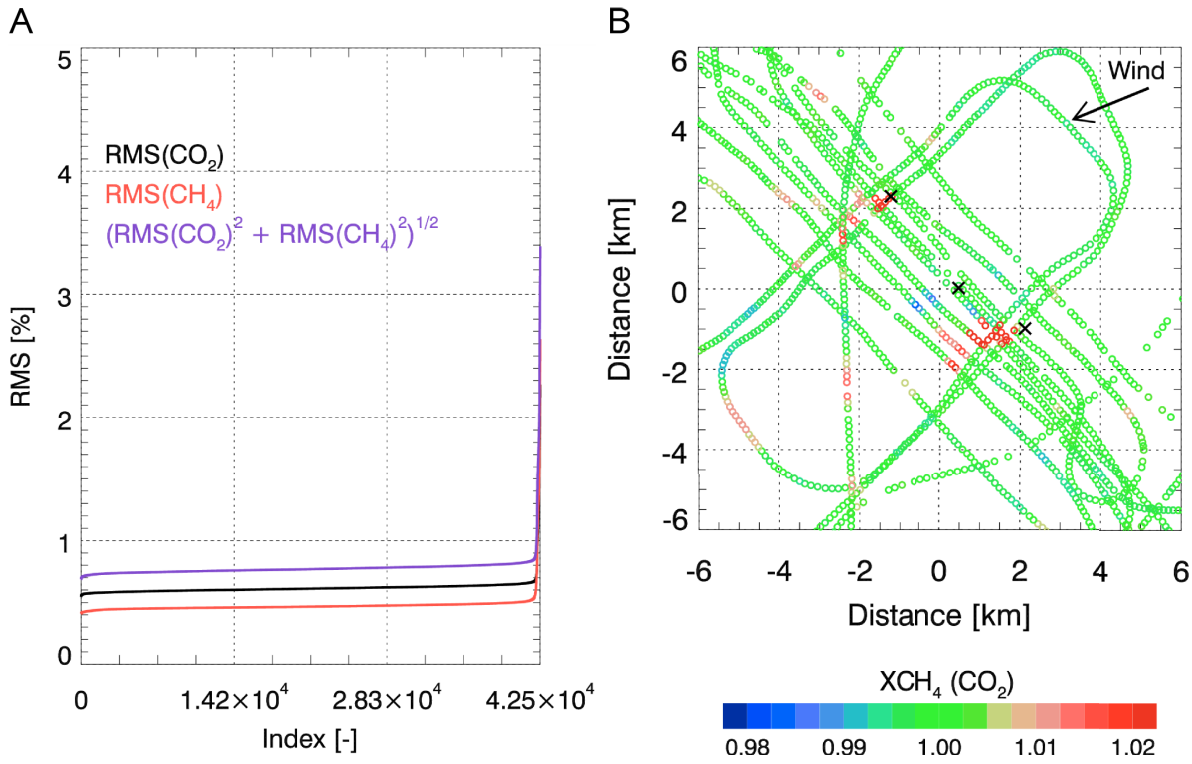

Figure 9.3: Panel A: Fit quality of the measurements ordered by the root-mean-square value of the relative differences between measurement and model after the fit. Panel B: Smoothed and filtered column-averaged dry air mole fractions $XCH_4(CO_2)$ relative to background.

$k = 0.555$.

As for the power plant data (see Section 8.2), each burst of 10 single, sequential measurements was selected to compute its average for one ground scene, provided more than half of the measurements passed the fit quality and signal threshold criteria as well as other potential filter criteria such as the altitude filter (see below).

As a consequence of the instrument modification (see Section 4.4), the fit quality is significantly improved compared to previous data (see Section 8 and Krings et al., 2011) and the inversion result is generally not strongly dependent on a quality filter based on the RMS between model and fit. Figure 9.3 (Panel A) shows the fit quality of the retrieval algorithm before any filters. Compared to data from the power plant overflight (see Figure 8.5) with the old instrument configuration, this is a significant improvement. Only few spectra have a low fit quality, of which 93 % exhibit too low signals and are subsequently rejected by the above mentioned signal filter. The standard deviation (precision) of the XCH_4 data before reaching the measurement area and after leaving the measurement area is below 0.4 %. In the measurement area, the standard deviation naturally is larger because of real atmospheric variations and resulting from flight manoeuvres.

To accommodate for aircraft aperture and mechanical setup, a smaller glass fibre coupled telescope with a focal length of $F \approx 150$ mm but with same f-number as before was installed. This results in a slightly larger MAMAP ground scene size compared to results computed for the improved setup in Section 4.4. For an aircraft altitude of

Table 9.1: Approximate standard deviation σ_θ of wind direction θ at 10 m above ground for different stability conditions (Hanna et al., 1982, and references therein).

Stability	Description	σ_θ [°]
A	very unstable	25
B	moderately unstable	20
C	slightly unstable	15
D	neutral	10
E	slightly stable	5
F	stable	2.5

about 1100 m, a ground speed of 200 km h^{-1} and a total integration time of 0.98 s for 10 co-added measurements, the ground scene is approximately 40 m × 90 m (cross track × along track).

Figure 9.3 (Panel B) shows normalised, smoothed (3-point moving average) and filtered (RMS < 0.8 %) $X\mathrm{CH_4(CO_2)}$ data. Additionally, the data were normalised by a 100-point moving average to remove slowly varying, systematic effects such as changing solar zenith angle. Clearly visible are the two $\mathrm{CH_4}$ plumes being dispersed in downwind direction and with a stronger emission rate for the southern ventilation shaft (Theodor Shaft). Furthermore, a small negative anomaly can be observed originating at the power plant's location. This is caused by the increased $\mathrm{CO_2}$ in the power plant's flue gas that appears in the $X\mathrm{CH_4(CO_2)}$ as a methane depletion due to the proxy method.

The $\mathrm{CH_4}$ plume from the northern ventilation shaft (Bockraden Shaft) exhibits a broken and discontinuous appearance which indicates unstable atmospheric conditions (see Table 9.1) that may be further enhanced by topography effects.

For a subsequent, quantitative analysis of the data, the RMS filter as well as any smoothing was disabled. An altitude filter (allowing 1000–1200 m flight altitude) was added to avoid errors for low flight tracks that intersect the vertical plume extension and that were meant for gathering in-situ data. In these cases, methane molecules above the aircraft would not be correctly attributed by the MAMAP retrieval. The corresponding $X\mathrm{CH_4}$ data superimposed on the topography are displayed in Figure 9.4. Compared to Figure 9.3 (Panel B), one roughly north-south transect in the centre of the figure is missing. This is an in-situ flight track at low altitude.

Figure 9.5 shows the same data zoomed to the area that is relevant for the $\mathrm{CH_4}$ emissions. In addition, the single gas columns of $\mathrm{CH_4}$ and $\mathrm{CO_2}$ are qualitatively displayed. They do not represent dry air mole fractions and are shown at a different scale. The methane plume can be clearly observed already in the single gas $\mathrm{CH_4}$ data. Furthermore, $\mathrm{CH_4}$ and $\mathrm{CO_2}$ generally suffer from systematic errors at the same locations that cancel for the proxy method.

Besides the features that were visible also in the smoothed data, the unsmoothed $X\mathrm{CH_4}$ columns appear slightly more noisy and show additional areas with apparently systematic depletion in $X\mathrm{CH_4(CO_2)}$ (see Figure 9.6). This does not seem to originate from the proxy method (potentially increased $\mathrm{CO_2}$) but arises from the $\mathrm{CH_4}$ spectral region directly (see Figure 9.5). Data at the anomalies have only a slightly decreased fit quality, but it turns

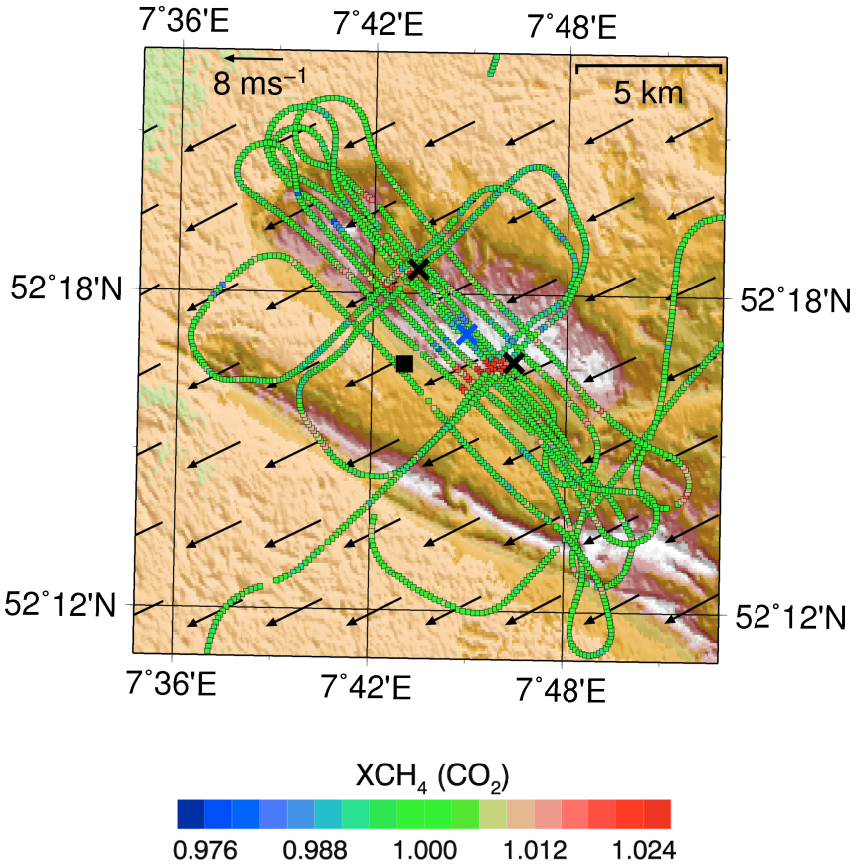

Figure 9.4: Unsmoothed and not RMS-filtered data superimposed on the topography. An altitude filter was applied to obtain quantitatively meaningful $XCH_4(CO_2)$ data. Data were normalised to regional background as observed during the flight. Black arrows denote the wind field at about 256 m altitude above ground at 10:00 UTC.

out that these features spatially coincide with bankings of excavated material from the mine. This is confirmed by aerial imagery (Figure 9.7) and by the pointing camera of the MAMAP instrument (Figure 9.8). Since no plume is obvious downwind of these deposits, this is likely an effect caused by surface properties, namely surface spectral reflectance, and not related to depletion in CH_4 (or increased CO_2).

A possible explanation for this behaviour could be systematic effects that become more relevant for decreased signal strength over ground scenes with reduced surface spectral reflectance such as the excavation material.

Potentially, fluorescence, which is the emission of electromagnetic radiation at wavelengths different from the excitation wavelengths, may contribute to these erroneous signals. Minerals are generally known to exhibit fluorescence (Gaft et al., 2005). This would result in an additive component to the light intensity that cannot be accounted for by the polynomial in Equation (5.1) for the logarithmic fit. A synthetic retrieval confirms that, in case of low surface spectral reflectance, an additive component of about +2 % of the total signal can lead to a spurious decrease in $XCH_4(CO_2)$ which is comparable to the observed decrease over the excavated material. Since these areas are not located close to the dispersion plume of the ventilation shafts, this matter has been disregarded for

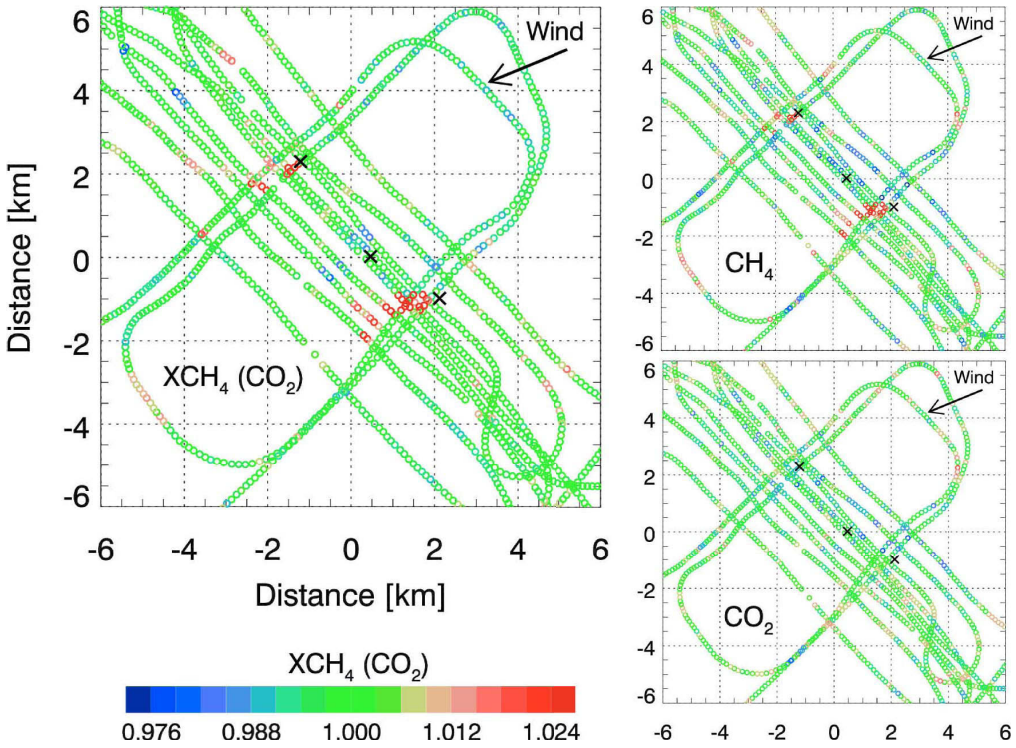

Figure 9.5: Same as Figure 9.4 but zoomed to the area of interest. Upper and lower right show additionally the CH_4 and CO_2 single columns. Note that they do not represent dry air mole fractions and have a different scale than $XCH_4(CO_2)$.

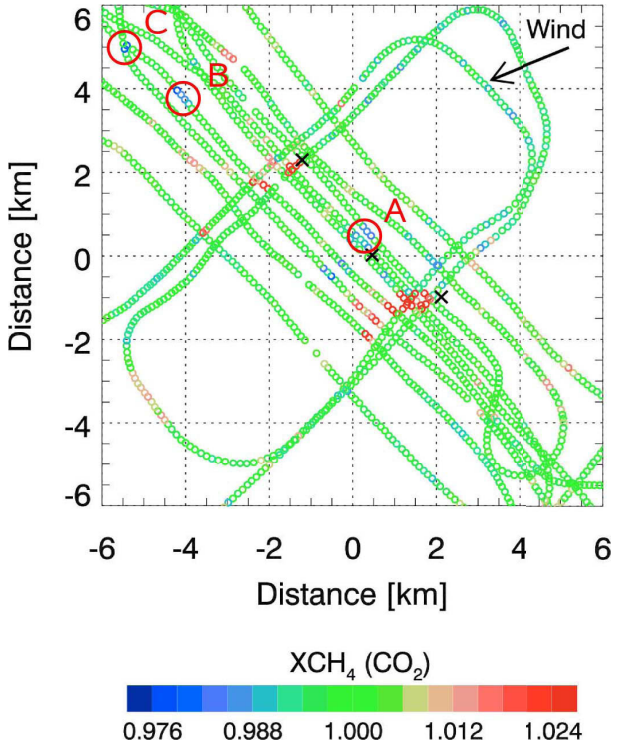

Figure 9.6: Same as Figure 9.5 but with marked anomalies.

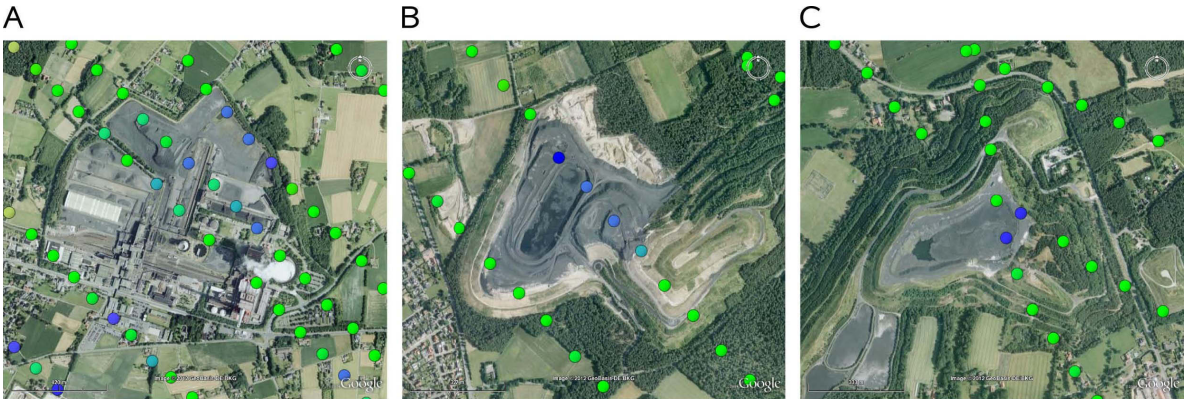

Figure 9.7: MAMAP data superimposed on Google Earth aerial imagery of anomaly locations. As can be seen, low $XCH_4(CO_2)$ (blue circles) correlates with areas of excavated material (grey). Panels A, B and C denote the anomalies marked in Figure 9.6. Compare also Figure 9.8. Data points denote the centre position of measured areas and are not to scale with observed ground scenes which are about twice as large and of rectangular shape.

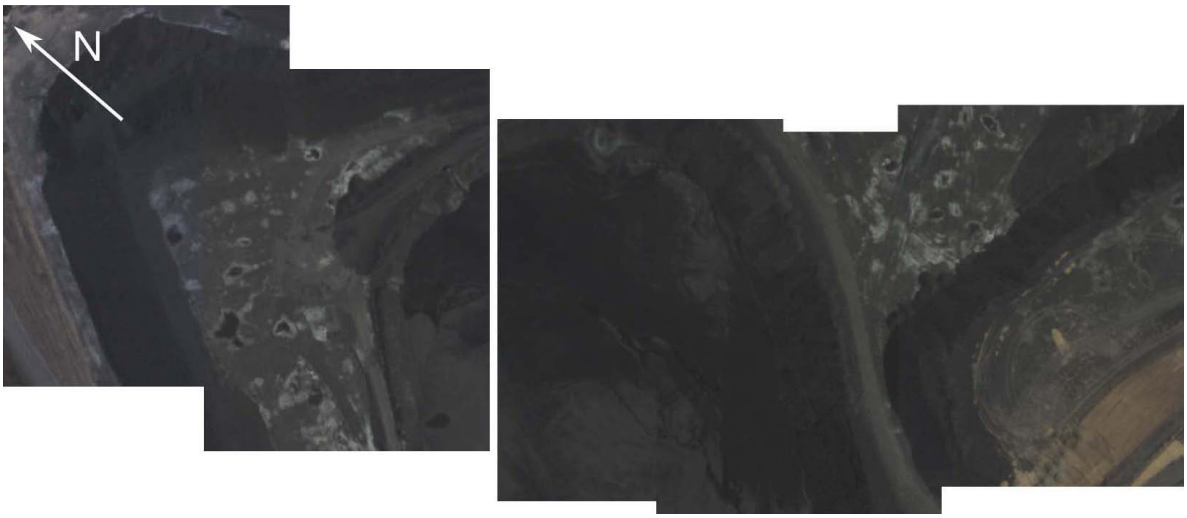

Figure 9.8: Pictures of the area below the aircraft taken by the MAMAP pointing camera. The figure shows exemplarily the excavated material at the location of anomaly B (see Figures 9.6 and 9.7) and is composed of 5 independent pictures.

further data processing. However, the precise origin of the above effect requires further investigation with additional measurements.

9.5 Wind data

Similar to before (see Section 8.3), wind information for the air layers of interest was obtained from the routine analysis of the numerical weather prediction model COSMO-DE

Table 9.2: Model layer altitudes and corresponding altitudes of layer centres above ground at the model grid position east of Theodor Shaft (52.2794 °N, 7.7540 °E). The first line of the table refers to the surface elevation.

Layer	Altitude above sea level [m]		Altitude above ground [m]	
	Layer centre	Layer boundary	Layer centre	Layer boundary
		114.5		0.0
50	124.4		9.9	
		134.3		19.8
49	149.9		35.4	
		165.4		50.9
48	186.8		72.3	
		208.2		93.7
47	235.6		121.1	
		263.0		148.5
46	296.6		182.1	
		330.2		215.7
45	370.1		255.6	
		410.1		295.6
44	456.6		342.1	
		503.1		388.6
43	556.2		441.7	
		609.4		494.9
42	669.6		555.1	
		729.7		615.2
41	796.8		682.3	
		864.0		749.5
40	938.4		823.9	
		1012.9		898.4
39	1094.7		980.2	
		1176.6		1062.1
38	1266.0		1151.5	
		1355.4		1240.9
37	1452.7		1338.2	
		1549.9		1435.4

(see Appendix E). In this case, however, model data were obtained that are given on model levels granting the same horizontal resolution (2.8 km × 2.8 km) but increased vertical resolution. These coordinates are terrain following. The lowest model layer (number 50) is approximately 10 m above ground. For the model grid point west of Theodor Shaft, surface elevation and model layer centre altitudes are exemplarily given in Table 9.2.

Wind fields for model layers 50, 45 and 40 for UTC times 09:00, 10:00 and 11:00 are shown in Figure 9.9. The model wind is rather uniform in speed and direction with no significant influence of the topography at model resolution. Wind speed is increasing with altitude and the direction is turning clockwise. This is to be expected as wind becomes geostrophic with decreasing surface friction due to the Coriolis force. Later, the difference between surface and aloft decreases as the mixed layer grows (see also Section 1.2).

The evolution of the mixed layer can be better seen from profiles at the two nearest neighbours of Theodor Shaft and Bockraden Shaft, respectively (Figure 9.10). The mixed layer grows from about 350 m thickness at 08:00 UTC to about 1100 m at 11:00 UTC characterised by the step in wind speed and direction at the transition to the free troposphere. The upper boundary of the mixed layer acts as a lid and gas plumes from sources within this layer are not likely to extend beyond it. In close vicinity to Theodor Shaft, wind speed is ranging from 6 m s^{-1} to 9 m s^{-1} for the mixed layer and wind direction from 55° to 65°, only slowly varying with time apart from changes introduced by the mixed layer evolution. For Bockraden Shaft, wind speeds are slightly lower ranging from 5 m s^{-1} to 9 m s^{-1} in the mixed layer with wind directions similar to Theodor Shaft.

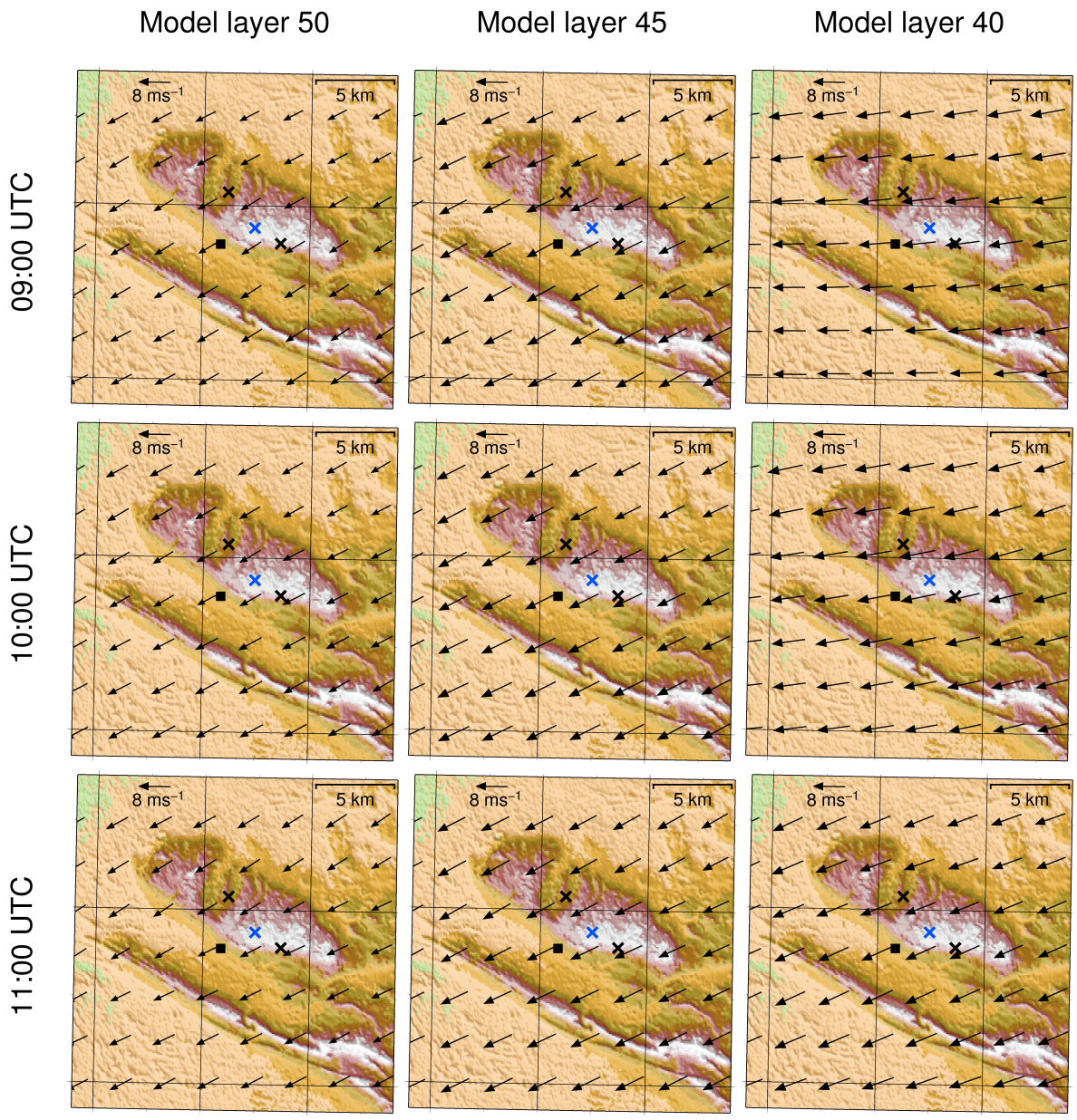

Figure 9.9: Wind fields for different times (rows) and model layers (columns). Model layers 50, 45 and 40 thereby refer to altitudes above ground of approximately 10 m, 256 m and 824 m, respectively, slightly depending on the surface elevation. Size of arrows is proportional to absolute wind speed.

All wind data from the COSMO-DE model for the measurement area as displayed, for example, in Figure 9.4 are shown in Figure 9.11. Variations in wind speed across the area are about $\pm 1\,\mathrm{m\,s^{-1}}$ at 09:00 UTC decreasing to about $\pm 0.5\,\mathrm{m\,s^{-1}}$ at 11:00 UTC. The great scatter in wind speed at about 450 m altitude across the area at 09:00 UTC is due to the different depth of the mixed layer for different model locations mainly depending on surface elevation. Wind direction varies by about $\pm 5°$ and shows the same scattering at the mixed layer boundary.

To compare the COSMO-DE model data with wind information acquired at flight

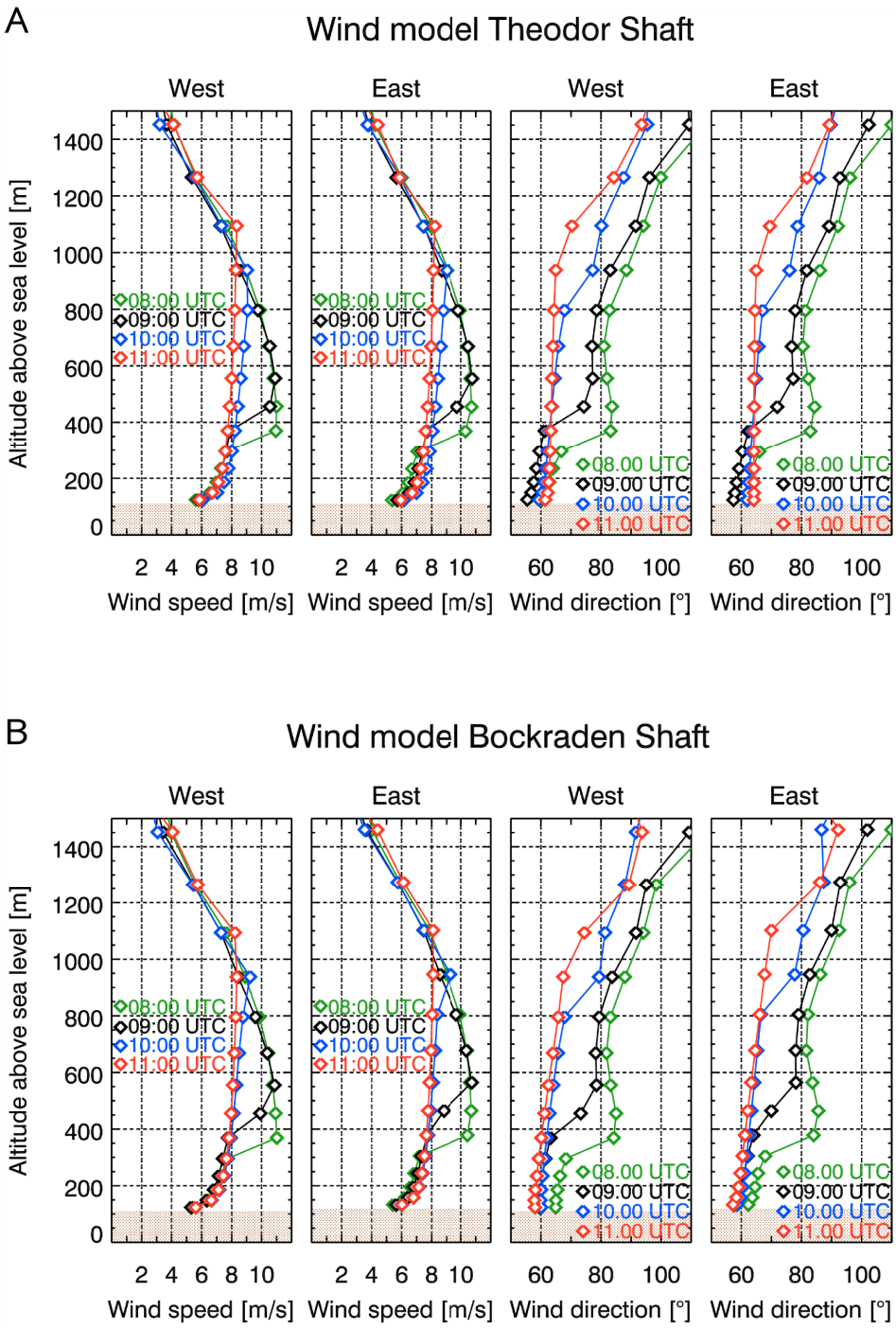

Figure 9.10: Panel A: Wind speed and direction for the model grid points west (52.2794 °N, 7.7540 °E) and east (52.2801 °N, 7.7948 °E) of the location of Theodor Shaft. Panel B: Same as Panel A but for model grid points east (52.3036 °N, 7.7120 °E) and west (52.3043 °N, 7.7528 °E) of Bockraden Shaft. Local time was UTC+2 h.

altitude over the measurement area using the AIMMS-20 turbulence probe, model data from the whole area were fitted by a 6th-order polynomial for altitudes covered by the overflight (Figure 9.11). Wind components in north-south and east-west direction were

fitted separately before wind speeds and directions were computed. The comparison between fitted model data and measurements from the turbulence probe is shown in Figure 9.12 (Panel A). The measurements were smoothed by a 1000 point moving average representing approximately 1 minute averages. Observation times of both, measurement and model data, are indicated by the colour scale.

The agreement for the altitudes of the remote sensing measurements (1000–1200 m) are good. The scatter for the measured data is higher than for the model data, which are given only on an hourly time scale. For lower altitudes, where the actual plume is located, the averaged model data seem to systematically overestimate the wind speed. For a more quantitative analysis, however, model and measurement have to be compared at the same location.

This can be accomplished using data from a descent-ascent profile reaching about 70 m above ground at the airport Münster/Osnabrück located approximately 17 km south-southwest of Theodor Shaft, which is compared to in-situ wind data at the airport's weather station (EDDG) and the COSMO-DE model in Figure 9.12 (Panel B). At this location, the systematic, negative bias of the model can be confirmed. Model data at the airport's closest grid point at 11:00 UTC are on average about $0.7\,\mathrm{m\,s^{-1}}$ higher for the mixed layer taking into account the altitudes from the lowest measurement (118 m) to 600 m. Considering the accuracy of the AIMMS-20 instrument for the horizontal wind of $0.5\,\mathrm{m\,s^{-1}}$ by specification (see, for example, Beswick et al., 2008) or better, this bias is significant. In-situ wind data measured at 10 m above ground every 20–30 minutes also indicate an overestimation of wind speeds by the model. Therefore, the data from the turbulence probe of the profile were used to calibrate the model applying a correction of $-0.7\,\mathrm{m\,s^{-1}}$. This correction is still within the error range of the wind model of about $0.9\,\mathrm{m\,s^{-1}}$ as estimated for the power plant overflight (see Section 8.5.1 and Appendix G).

Wind direction between model and measurements agree within the uncertainties, although the weather station data indicate a high variability in wind direction of $\pm 20°$ not captured by the model.

Effective wind speed

To compute an effective wind speed from the model data, it is assumed that the plume is approximately terrain following with respect to the vertical coordinate. This is, for example, a good approximation for smooth hills in neutral stability conditions (Hunt and Snyder, 1982). Additional turbulence is possible but was not considered explicitly for this work. Part of it will be compensated by the stability fit of the plume inversion (see Section 9.6) which cannot distinguish between diffusion and turbulent mixing on somewhat larger scales. The release height in case of Theodor Shaft was set to the surface elevation according to the SRTM model of 150 m plus the stack height of 15 m. However, since the COSMO-DE model elevation grid has a lower resolution, the model elevation at the Theodor Shaft location is only about 115 m when evaluating the nearest neighbour grid point.

The effective wind speed was computed using the vertical wind profile of north-south and east-west components weighted by the concentration enhancement according to Equation (8.2) for the modelled vertical dispersion. In case of Theodor Shaft, two effective

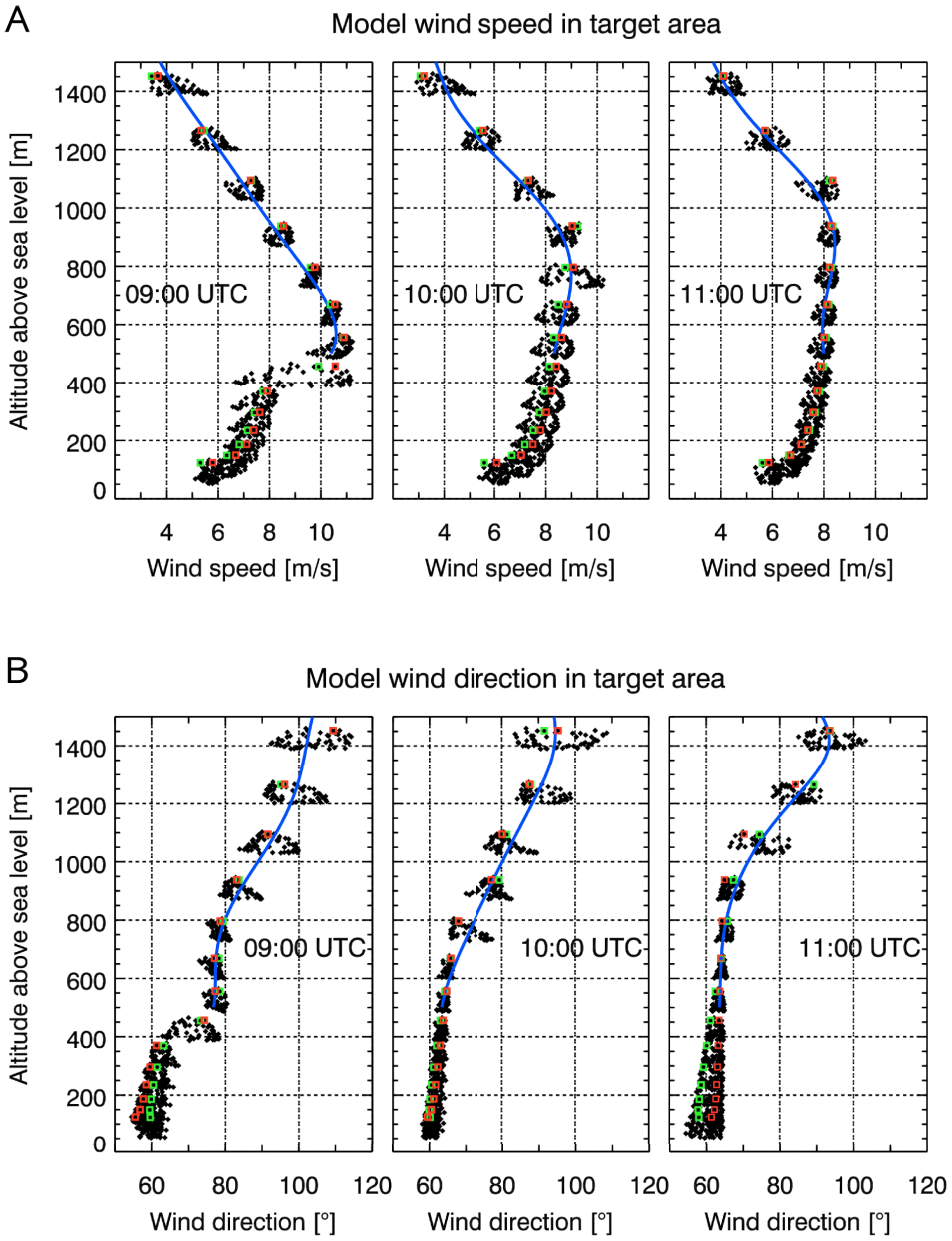

Figure 9.11: Wind speed (Panel A) and direction (Panel B) from the COSMO-DE model throughout the measurement area as shown in Figure 9.4. Red squares denote data from the location east of Theodor Shaft and green squares data east of Bockraden Shaft. The blue line indicates a 6th-order polynomial fit from about 500 m to 1500 m corresponding to flight altitudes during the survey.

wind speeds were computed. The first corresponding to the close vicinity and the near part of the plume, taking into account the mean wind profile of the two nearest model grid locations (east and west of the ventilation shaft location). The vertical dispersion coefficient σ_z was computed according to Equation (7.4) assuming a mean distance from the shaft of 1 km. The approximate stability class can be determined according to Table 7.2. Considering a mean solar zenith angle of about 36° (moderate solar insolation) and a wind speed around 6 m s^{-1} (see Figure 9.11), this results in stability classes D (neutral) or C

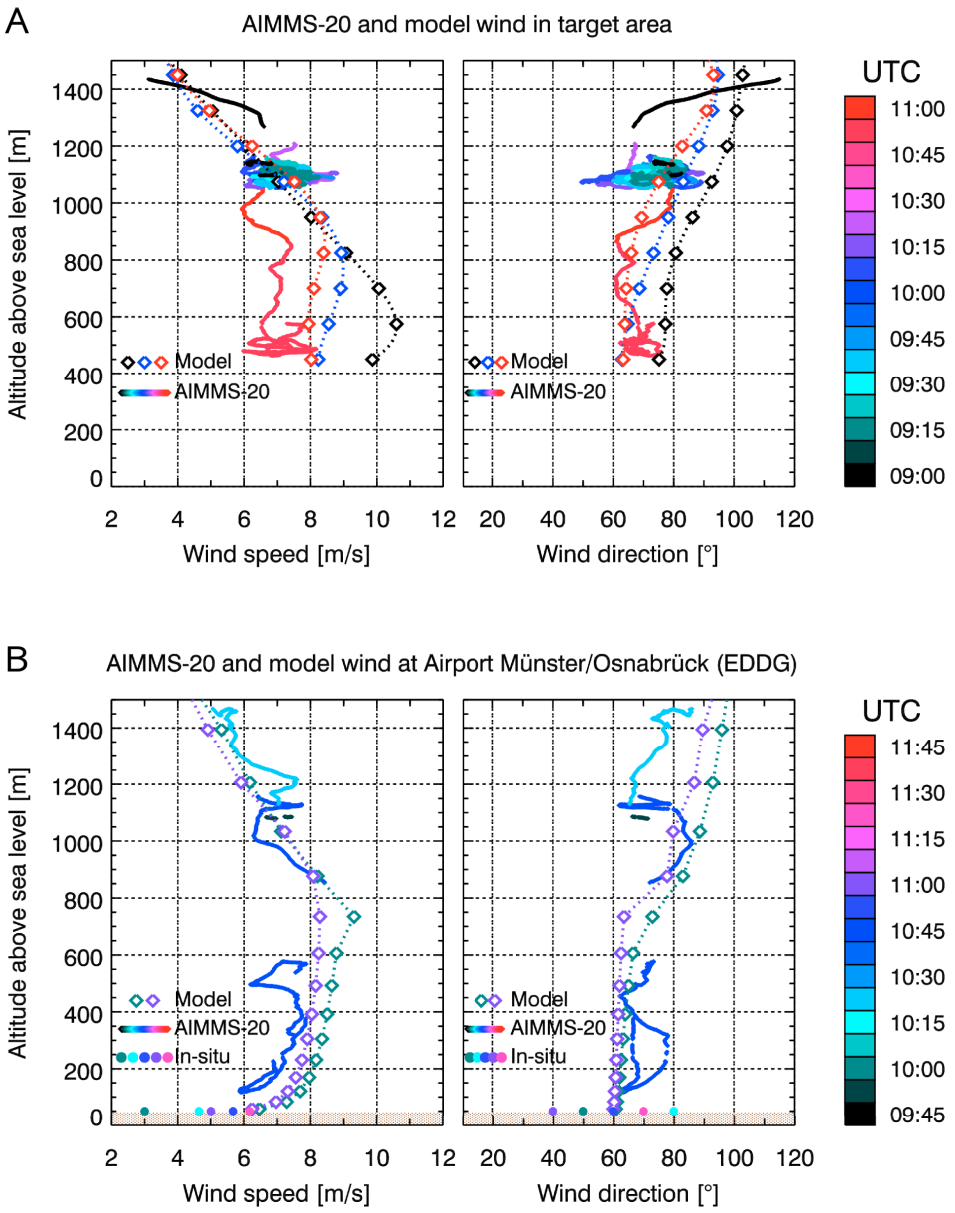

Figure 9.12: Panel A: Comparison between mean model data (diamonds) for times 09:00, 10:00 and 11:00 UTC and AIMMS-20 turbulence probe wind data (thick line). The colour indicates the time according to the colour bar to the right. The left plot shows wind speed, the right plot wind direction. Panel B: AIMMS-20 wind data from a dive at the airport Münster/Osnabrück and the surrounding area compared with model data at a grid point less than 100 m away from the airport (52.1279 °N, 7.6800 °E). Additionally, in-situ data from the weather station (EDDG) are shown. Time of measurements are according to the colour bar on the right. In-situ data from the weather station at the Airport Münster/Osnabrück (EDDG) were obtained from Weather Underground (http://www.wunderground.com/, May 2012).

(slightly unstable) with corresponding parameters for the determination of σ_z according to Table 7.1. This is confirmed in the inversion process (see below) which for the far and undisturbed plume results in a stability parameter a that corresponds to a stability class between C and D. Taking into account that topography may create an additional turbulent

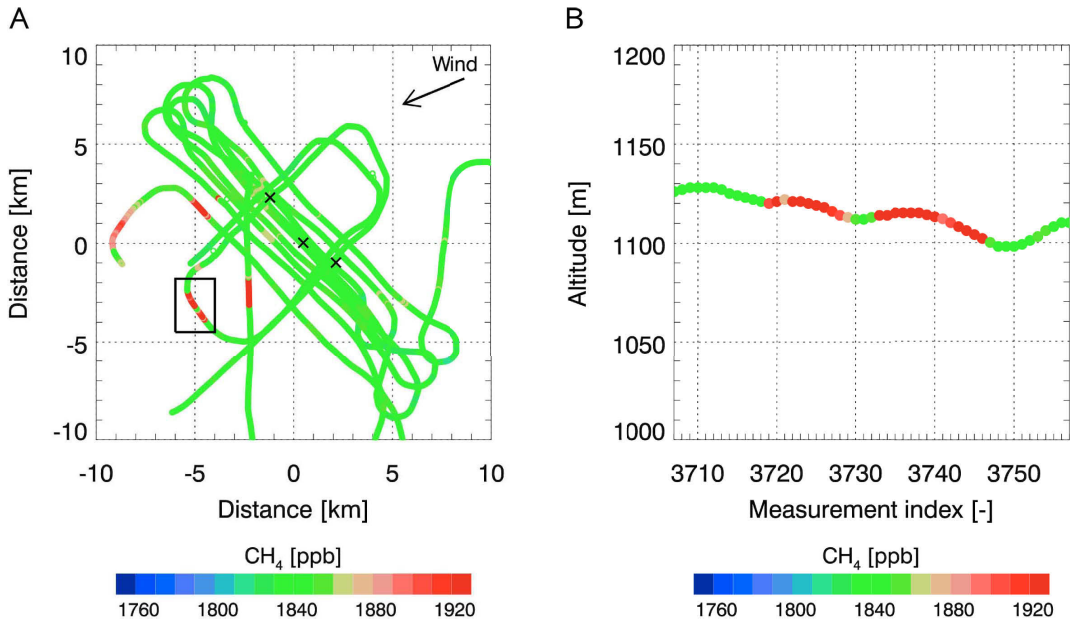

Figure 9.13: Panel A: Methane data from the in-situ probe averaged for 1 second. Data from the furthest part of the plume as indicated by the black box are shown in Panel B. In-situ data provided by J. Hartmann, Alfred Wegener Institute for Polar and Marine Research (AWI).

diffusion and considering that for the far part of the plume, the in-situ sensor picked up an average CH_4 enhancement of about 80 ppb (see Figure 9.13), which can only be modelled using stability class C (see below), the slightly unstable case C was used for computing the effective wind speed.

For the near part of Theodor Shaft, this yields $\sigma_z = 61$ m and about 18 % of the emitted CH_4 is confined to the surface layer (layer 50 according to the COSMO-DE model). The next layers share 27 % (layer 49), 30 % (layer 48), 19 % (layer 47), 5 % (layer 46) and 0.3 % (layer 45). Consequently, the corresponding plume height is approximately the upper boundary of layer 45. Taking the altitude profile of the model grid point west of Theodor Shaft as reference, the plume presumably rises to about 296 m above ground. Taking the mean from 09:00 and 10:00 UTC, the effective wind speed for the near area of Theodor Shaft results in about 6.9 m s^{-1} and the mean wind direction in about 59.8°.

The second effective wind speed is evaluated for the far part of the plume in about 8 km distance from Theodor Shaft. Model wind profiles of 8 grid points throughout the plume extension were considered taking into account the real distance to the source when evaluating the vertical dispersion including the dispersion coefficient σ_z – except for one upwind profile east of Theodor Shaft, where the distance to the source was set to 0 km. Model grid points were selected so that no part of the plume is overly represented. The effective wind speed for the far part of the plume is then about 7.7 m s^{-1} and the wind direction about 63.1°. The vertical distribution at 8 km distance, according to these assumptions, is about 4 % (layer 50), 6 % (layer 49), 8 % (layer 48), 10 % (layer 47), 12 % (layer 46), 13 % (layer 45 and 44), 12 % (layer 43), 9 % (layer 42), 7 % (layer 41), 4 % (layer 40), 2 % (layer 39) and less than 0.7 % (layer 38).

The flight altitude corresponds to layer 39 with a share of the total column enhancement

of $s = 2\,\%$. To compare with the in-situ measurements, following assumptions are made: 100 % of the released methane in a vertical column at about 8 km distance correspond to about $\Delta_{\text{tc}} = 1.2\,\%$ of the total background column as seen from MAMAP measurements, where the background column is TC $\approx 3.75 \cdot 10^{19}$ molecules CH_4 cm^{-2}, the air layer is about $d \approx 160$ m thick with an approximate pressure of about $p_1 = 900$ hPa and temperature of $T_1 = 288$ K. Assuming further air to be an ideal gas and using the Loschmidt number $N_L \approx 2.7 \cdot 10^{19}$ molecules cm^{-3} for the number of molecules at standard conditions ($p_0 = 1013.25$ hPa, $T_0 = 273.15$ K), the expected in-situ enhancement $\Delta_{\text{in-situ}}$ is:

$$\Delta_{\text{in-situ}} = \frac{s\ \Delta_{\text{tc}}\ \text{TC}}{N_L\ \frac{p_1 T_0}{p_0 T_1}\ d} \approx 25\,\text{ppb} \tag{9.1}$$

which is in agreement with the measurements that showed about 80 ppb increase, considering involved uncertainties and variability in vertical distribution. For comparison, stability class D (more stable than class C) would yield a mole fraction increase in layer 39 that is too low to be measured (about 10^{11} times lower).

For the northern Bockraden Shaft, only the wind profile from the nearest model grid point was taken into account. It is located about 870 m in downwind direction approximately half way between the ventilation shaft and the maximum, visible plume extent. For slightly unstable stability conditions, as before, and the measurement time 09:00–10:00 UTC, the effective wind speed amounts to about 6.4 m s^{-1} and the average wind direction is about 59.9°. The release height was taken to be the surface elevation according to the SRTM model plus the shaft height of 15 m resulting in 121 m above sea level. This is about 7 m above ground according to the COSMO-DE surface elevation model.

Calibration with wind measurements

Analysis of the measured wind data above has revealed that the wind model is biased by about -0.7 m s^{-1}. So far, this information was not taken into account for the computation of the effective wind speed. Applying the wind speed calibration of -0.7 m s^{-1}, the final effective wind speeds are 6.2 m s^{-1} for the near part of Theodor Shaft, 7.0 m s^{-1} for the far part and 5.7 m s^{-1} for Bockraden Shaft.

9.6 Inversion results

To infer methane emission rates for each ventilation shaft, the Gaussian plume inversion and the integral method (see Section 7) were applied separately for each shaft. Prior to the inversion, the data were rotated so that the wind direction points in positive x-direction and subsequently gridded to regular boxes of 65 m ×65 m covering approximately the same area as a MAMAP ground scene.

Gaussian plume inversion

For the optimal estimation method using the inverse Gaussian plume model (see Section 7.1), the a priori for the stability parameter was set to $a = 120 \pm 120$ only

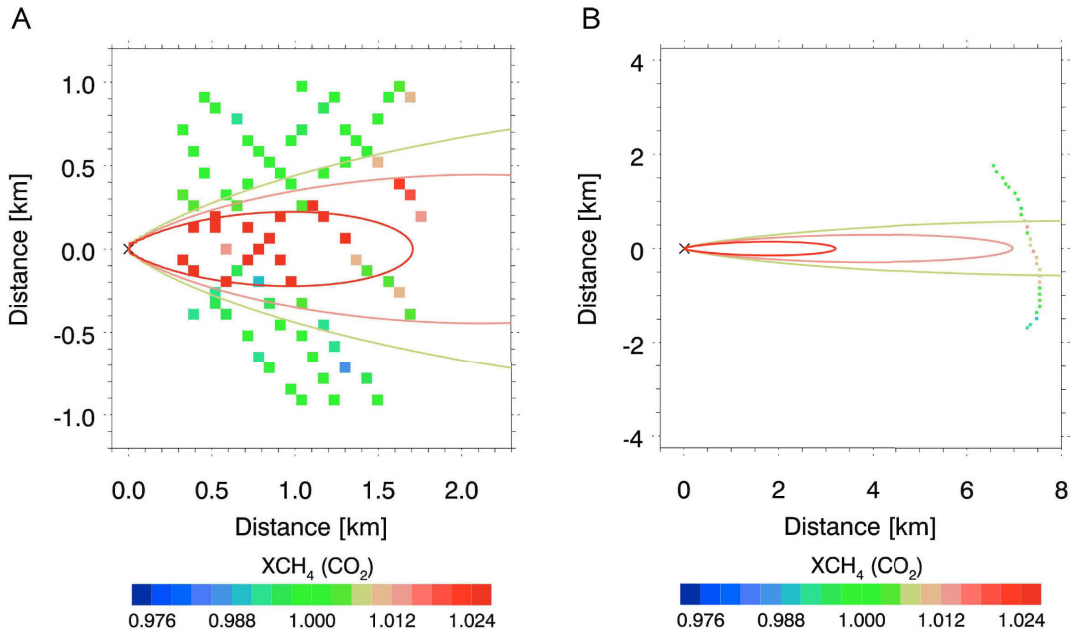

Figure 9.14: Data used for the inversion of the near part of Theodor Shaft (Panel A) and the far part (Panel B). Contour lines indicate the result from the Gaussian plume model inversion.

constraining the stability to the physically meaningful range. Considering only one source, the inversion is statistically stable and does not need an additional constraint on the emission rate to prevent unrealistic results. Hence, no a priori information is needed for the emission rate. The wind direction was not taken from the computation of effective wind speed and direction but from the measured MAMAP data directly. Although the COSMO-DE model shows similar wind directions for the part of the plume in the vicinity of Theodor Shaft and the total plume extend, this is not confirmed by the data. Close to the ventilation shaft, a wind direction of about 85° was empirically found to best fit the data. Whereas the far part alone represents a plume advected by wind coming from 71°.

The measurements in the close vicinity of Theodor Shaft apparently missed the plume which is very narrow so close to the source. To avoid potential interference on the inversion of the near part of the plume, data from the first 300 m downwind were excluded prior to the inversion. Similarly, data were restricted to ±1000 m in across wind direction to avoid the impact of other sources than the one under consideration. Finally, data further than 1800 m away from the ventilation shaft, where the plume appears particularly rugged, were omitted. The selected rotated and gridded data are shown in Figure 9.14 (Panel A) including the contour lines resulting from inferred emission rate and stability parameter.

The far part of the plume is subject to a different effective wind speed and direction. Hence, the plume (and integral) inversion for the near and far part were conducted separately (Figure 9.14, Panel B). The across wind limits were set to ±1800 m accounting for a wider dispersion further from the source.

As for the near part of Theodor Shaft, the data from Bockraden Shaft were restricted to ±1000 m in across wind direction. The wind direction is empirically determined to about 60.0°. In addition, data with a distance of more than 1.9 km from the source, where the plume starts to exhibit a very discontinuous appearance, were rejected for the plume

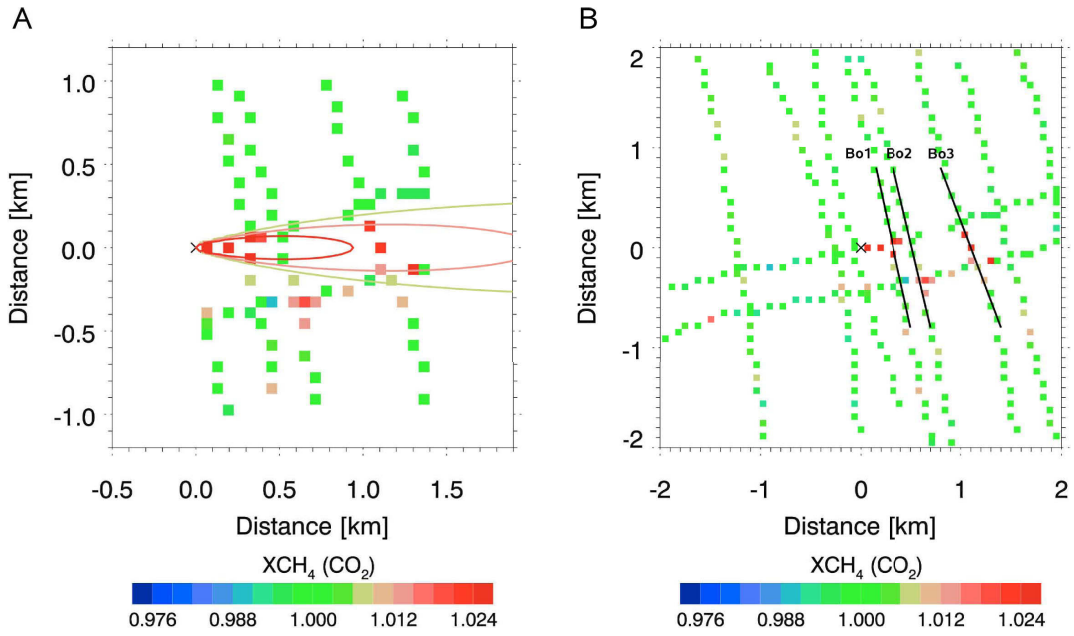

Figure 9.15: Relevant data for the inversion of the emissions from Bockraden Shaft using the inverse Gaussian plume model (Panel A) and the integral method (Panel B). Contour lines (Panel A) indicate the result from the Gaussian plume model inversion, while the black tracks (Panel B) show the boundaries for the integral method.

inversion (Figure 9.15, Panel A).

Gaussian integral inversion

The Gaussian integral method was applied using the same wind directions as for the plume inversion. The boundaries for the method are shown in Figure 9.16 for the plume originating from Theodor Shaft and in Figure 9.15 (Panel B) for the Bockraden plume.

For the power plant measurements in Section 8, data upwind of the plume were too sparse and of relatively poor quality to be used as upwind reference for the integral method (see Section 7.2). Data quality for the coal mines is potentially good enough. In case of Theodor Shaft (Figure 9.16), the two nearest upwind tracks show very similar concentrations, but they are both above the regional background (Figure 9.17). When inspecting the topography map (see Figure 9.4), it can be seen that both these tracks are above the highest surface elevation of this region. Remembering that the retrieval was performed assuming an average surface elevation of 100 m and taking into account that the actual elevation upwind is considerably higher, this can partly be explained by the retrieval error on the $X\mathrm{CH}_4$ result (see Table 5.4). Accumulated over the two upwind tracks, respectively, this results in an enhancement above background comparable to the result of the integral method. Assuming the elevation to be 100 m higher than used as input for the radiative transfer, more than 80 % of the above background signal can be explained.

The upwind reference data were therefore not used. Instead, it was assumed that there are no additional CH_4 sources of significant strength upwind of the two ventilation shafts.

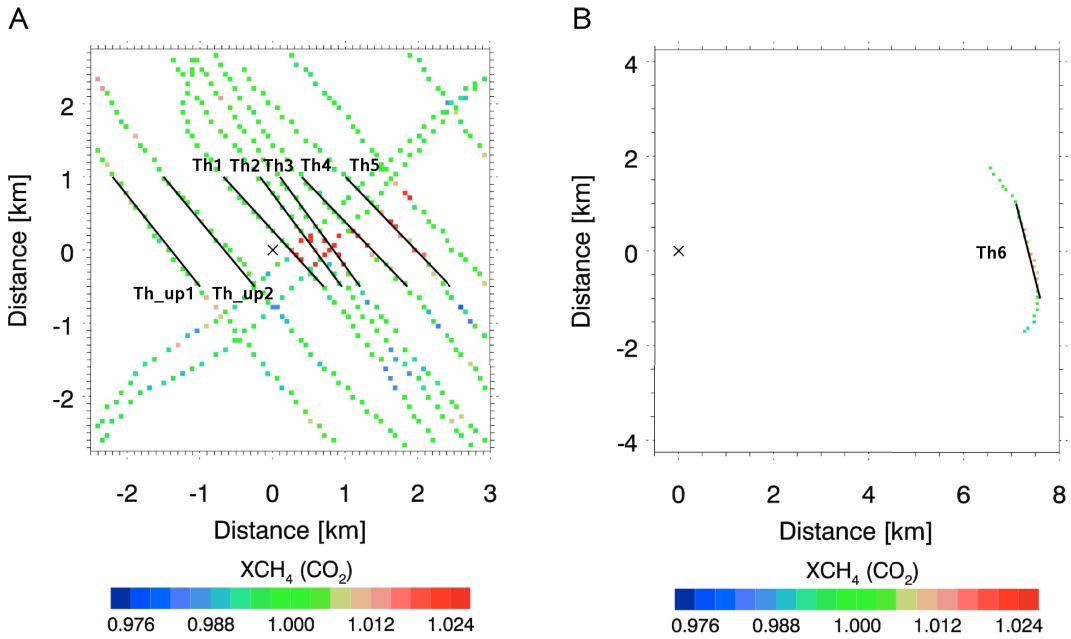

Figure 9.16: Boundaries for the integral inversion for near (Panel A) and far (Panel B) part of Theodor Shaft.

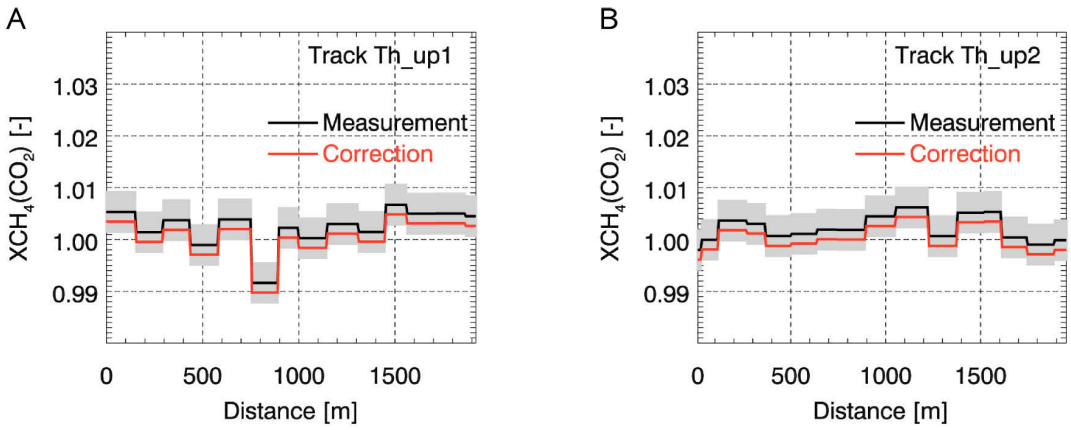

Figure 9.17: Measurements along horizontal cross sections upwind of Theodor Shaft (black). Additionally the 1σ uncertainty range based on the instrument precision (grey) and a topography correction is shown (red). See Figure 9.16 for position of the cross sections.

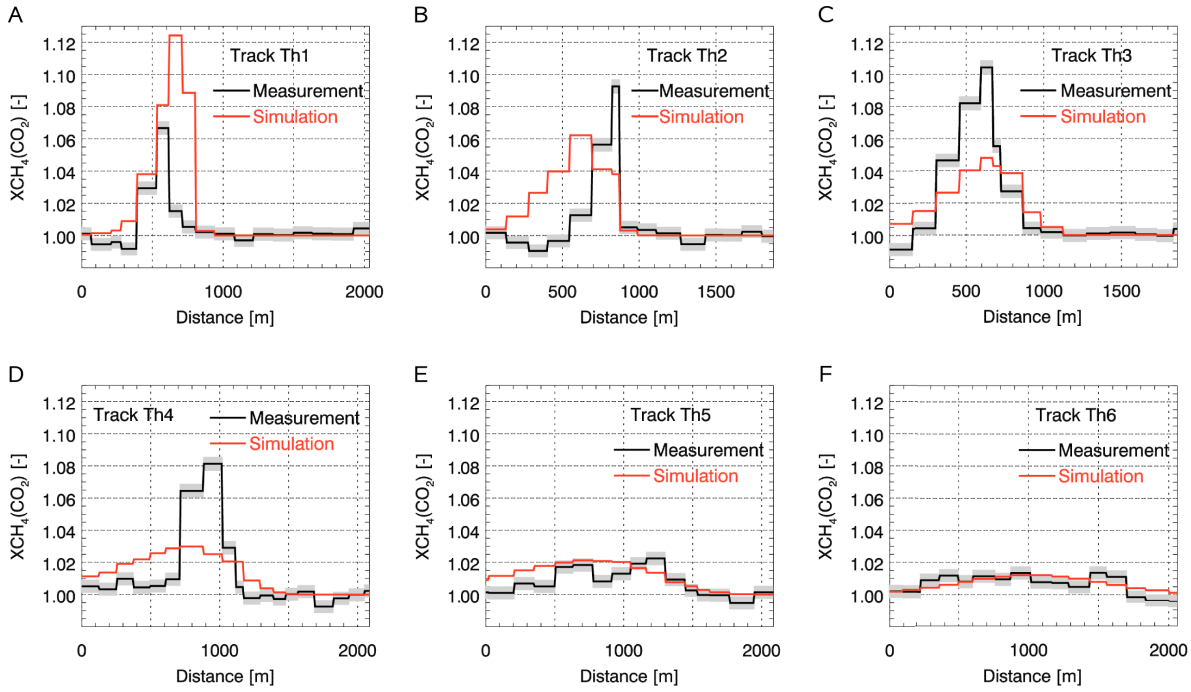

Figure 9.18: Measurement (black) with according precision (grey) and plume model simulations (red) based on the inversion results along horizontal cross sections through the CH_4 plume originating at Theodor Shaft. The position of the cross section tracks is specified in Figure 9.16.

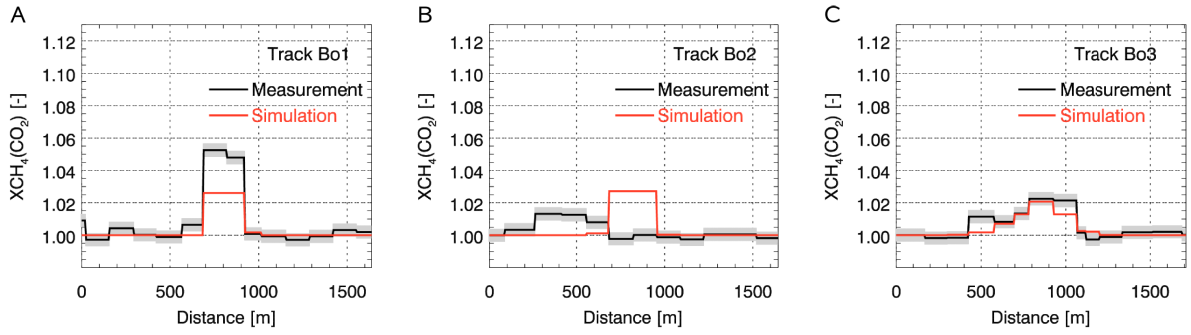

Figure 9.19: As Figure 9.18 but for Bockraden Shaft. Figure 9.15 (Panel B) shows the position of the cross sections.

Downwind cross sections of measurements and plume inversion result are shown in Figures 9.18 and 9.19. Thereby, the model simulations use the same nearest neighbour approach to the cross section tracks to ensure comparability between model and measurements. For Theodor Shaft, the model overestimates the concentrations in the near part, where in the mid range measurements exceed the model. In the far part, model simulation and measurements have a flat Gaussian shape and agree very well.

In case of Bockraden Shaft (Figure 9.19), the furthest measurements agree nicely with the model simulations based on the inversion. Whereas in the mid part, a change in wind direction with respect to the modelled direction is apparent.

Flight pattern and Gaussian integral

As pointed out in Section 8.5.2, the flight pattern and patchy data can lead to systematic errors for the inversion result of the integral method. Simulations based on the emission rate as resulting from the integral inversion and the stability parameters a obtained from the respective plume fits were performed. The systematic errors for the near and far part of Theodor Shaft and for the Bockraden Shaft are about $-3.8\,\%$ (caused by parts of the plume not captured in the lower part (negative y-direction) which cannot be observed for the measurements since the measured plume exhibits a slight bend in positive y-direction), $-4.6\,\%$ (plume not completely captured in its horizontal extend) and $-1.2\,\%$. Note that the potential systematic error is generally improved compared to the data from power plant Jänschwalde. This can mainly be attributed to less data gaps and a denser flight pattern. The flight pattern error was corrected for in the inversion results.

Results

Results of the inversion are given in Table 9.3. The rather large stability parameter of 227.5 for the near part of Theodor Shaft indicates possible additional broadening by changing wind directions or topography. Whereas stability for the far part (84.5) and for Bockraden Shaft (120.1) is in the range to be expected for stability class C.

While the integral inversions and the plume inversion of the far part of Theodor Shaft give a rather similar result of about $31\,\mathrm{kt\,CH_4\,yr^{-1}}$, the plume inversion of the near part indicates a significantly higher emission rate of about $43\,\mathrm{kt\,CH_4\,yr^{-1}}$ with a much lower statistical error partly due to the higher number of observations that were used.

The inferred emission rate for Bockraden Shaft is significantly lower as could already be expected from a qualitative analysis of the data. The emission estimate from the integral method ($16\,\mathrm{kt\,CH_4\,yr^{-1}}$) using 3 tracks is larger than for the plume inversion ($12\,\mathrm{kt\,CH_4\,yr^{-1}}$)

9.7 Error discussion

Several potential sources of error on the inversion are discussed in the following. Aerosol is not assumed to be a major contributor as it already proved to be insignificant for the assessment of emissions from coal fired power plants where much more aerosol variations are expected (see Section 8.5.3).

Table 9.3: CH_4 emission rate results in kt CH_4 yr^{-1} for the coal mine ventilation shafts Theodor Shaft and Bockraden Shaft using the Gaussian plume model and the Gaussian integral inversion methods. For the Gaussian plume model, the result for the retrieved stability parameter a and the statistical errors according to Equation (7.10) are also given. The data from Theodor Shaft were inverted separately for the near and far part of the plume.

	Plume inversion			Integral inversion	
Ventilation shaft	emission $[\mathrm{kt\,yr^{-1}}]$	# pixels used for inversion	stability parameter $[-]$	emission $[\mathrm{kt\,yr^{-1}}]$	# tracks used for inversion
Theodor Shaft (near)	43.125 ±1.065	80	227.5 ±3.0 %	31.151	5
Theodor Shaft (far)	31.830 ±5.233	28	84.5 ±18.8 %	30.819	1
Bockraden Shaft	12.363 ±0.419	74	120.1 ±6.8 %	16.088	3

9.7.1 Effective wind speed and stability

Not considering the additional 35 m altitude according to the high resolution topography from SRTM relative to the COSMO model and just taking the COSMO model elevation plus 15 m shaft height for Theodor Shaft, results in a by −2 % decreased effective wind speed for both the near and far part of the plume. This gives an indication for the possible magnitude of the uncertainty induced by the topography and its limited representation in the model. The insignificant difference between SRTM and COSMO-DE elevation model of −8 m at Bockraden Shaft results only in a negligible variation in effective wind speed. However, Bockraden Shaft is located in a shallow valley which may have a slight trapping effect on the CH_4 plume.

As discussed in Section 9.5, the wind model was calibrated by measured data which have an accuracy of about $0.5\,\mathrm{m\,s^{-1}}$. This uncertainty was adopted for the error estimation resulting in a relative error of about 8 %, 7 % and 9 % for the wind speeds in case of Theodor Shaft near ($6.2\,\mathrm{m\,s^{-1}}$), Theodor Shaft far ($7.0\,\mathrm{m\,s^{-1}}$) and Bockraden Shaft ($5.7\,\mathrm{m\,s^{-1}}$). The relative error translates directly into an uncertainty on the inferred emission rate.

9.7.2 Wind direction

The impact on the inversion result originating from uncertainty on the knowledge of the wind direction was examined by testing wind directions that differ from the assumed wind direction. The knowledge of average wind direction for the far part is assumed to be better (±1.5°) than for the near parts of the plumes (±5°), simply by noting that a changed wind direction leads to a larger spatial displacement in the distance. The different wind directions were applied to inversion procedures of actual measurements and simulations (Table 9.4). The sensitivities vary significantly for different plumes and methods.

For the integral method, when not changing the actual tracks, the modified wind direction impacts only the angle between wind and track normal vector so that the effect

Table 9.4: Error on simulated and measured inversion results due to uncertainty on wind direction.

		Δ inversion [%]			
	Δ wind	Simulation		Measurement	
Ventilation shaft	direction [°]	Plume	Integral	Plume	Integral
Theodor (near)	−5.0	−5.3	+7.1	−3.9	+7.0
	+5.0	+0.04	−7.9	+1.4	−7.8
Theodor (far)	−1.5	+0.36	+0.62	−5.9	+0.62
	+1.5	−0.44	−0.69	−1.5	−0.69
Bockraden	−5.0	−5.3	+2.0	−29.5	+2.0
	+5.0	+6.9	−2.8	+25.5	−2.8

for measurement and simulation are essentially equal and is of the order of a few percent.

This is not the case for the plume inversion method, where measurements close to the source may drastically change the result. Here, the plume shape is particularly dependent on changing wind directions. This is less significant in case of the near part of Theodor Shaft, where the first 300 m of measurements were omitted. However, this was not done for the sparser methane enhancements at Bockraden Shaft at the expense of a rather large uncertainty with respect to the assumed wind direction.

9.7.3 Restriction to relevant measurement area

For the plume inversion of the near part of Theodor Shaft, influence on the inversion result of the restriction to ±1000 m in across wind direction is insignificant (less than 0.05 %) when extended by 1000 m in each direction. The exclusion of the very near and mid part of the plume is physically reasonable to avoid short term wind changes affecting the overall result. However, when the data area for the near part of the plume is reduced by 50 % (−750 m) the inversion result changes by +1.7 %, and when extended by 50 % the inversion yields −6.0 % less suffering visibly from changing wind directions. This apparent variability in wind direction lead to the choice of the relevant measurement area in the first place.

In case of the far part of the Theodor plume, extending the across wind direction extension by +1000 m in either direction reduces the plume inversion result by about −1.4 %, while extension in along wind direction in either direction does not make sense, since only the furthest track is under investigation.

Also for the Bockraden Shaft the plume inversion is stable regarding increase of the across wind direction extension by +1000 m, where no significant change of the inversion result occurs. Extending the range in wind direction by +500 m results in a decrease by −1.3 %. This is a very low sensitivity considering the scattering of the plume. When the relevant area is not beginning at the source but at +300 m downwind distance from the source, the result is by −4.9 % lower.

For the integral method in case of the near part of Theodor Shaft, extending or shortening at the lower ends of all tracks by ±200 m in y-direction changes the inversion

result by −5.4 % and +0.4 % respectively. Extension of the track might potentially be sensitive to the CO_2 emissions of the nearby power plant. Extending or shortening at the upper ends of all tracks by ±200 m in y-direction changes the inversion result by −0.9 % and −0.4 %, respectively.

The impact of the same procedure on the Bockraden integral result is +0.8 %, −0.7 %, −0.4 %, −2.2 %.

Extending or shortening the integral path for the far part of the plume is not useful because the straight part of the track is not long enough, and shortening would lead to clear cutting of the plume.

9.7.4 Conversion factor, non-linearity and plume height issues

The uncertainty of the conversion factor was determined as in Section 8.5.4 by synthetic retrievals of simulated data taking into account also vertical dispersion according to Equations (7.4) and (8.2) and assuming slightly unstable conditions (stability class C).

The far part inversion is biased by about −0.5 % for the plume and the integral method. At this distance, the vertical extension of the simulated plume slightly exceeds the aircraft altitude leading to a small underestimation of the source strength.

In case of Bockraden Shaft (Figure 9.20, Panel A), the integral inversion is biased by +0.1 % whereas the plume inversion is biased by −1 %. The negative bias of the plume inversion is due to a relatively large deviation from the true column (−0.19 % maximum) for measurement pixels close to the source where highest concentrations can be found. This is potentially due to non-linearity effects not considered in the WFM-DOAS algorithm for large deviations from the fixed linearisation point mole fractions. Further away from the source, where methane concentrations are lower, this effect is lower than the effect from the conversion factor that generally slightly overestimates column concentrations when the plume is not equally distributed below the aircraft but lower to the ground.

For the near part of Theodor Shaft (Figure 9.20, Panel B), the inversion of the methane columns retrieved from simulated data is biased by −0.3 % for the plume inversion and integral method relative to the simulated emission rate. The reasons for the negative bias are similar as for Bockraden Shaft. However, by omitting the first 300 m for the plume inversion, where highest columnar increase can be found, the effect is smaller.

Hence, the overall contribution of these effects to the total uncertainty on the inversion result is rather low in all cases and is in line with results obtained for CO_2 inversions for the power plant experiment (Section 8.5.4).

9.7.5 Uncertainty of the methane background column

Uncertainties in the assumed background column of methane have direct impact on the inversion results. For this study, the background column was constrained using the in-situ absolutely calibrated data to scale a U.S. Standard profile. The resulting column-averaged dry air mole fraction is about $X\mathrm{CH}_4 = 1757$ ppb. Assuming a ±1 % uncertainty this gives a range of about 1740–1774 ppb which is realistic for the area of interest. The resulting uncertainty propagated to the inverted emission rate is then also ±1 %.

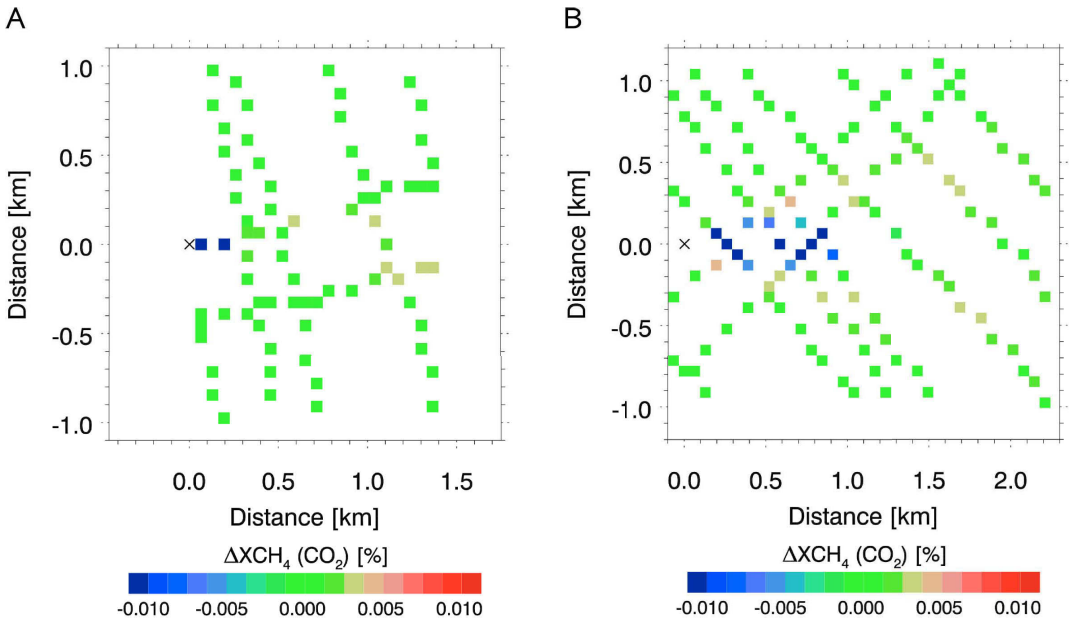

Figure 9.20: Column error relative to background from simulated methane retrievals using a vertical distribution according to a three dimensional Gaussian dispersion model for the actual flight pattern and inverted source strength and stability of Bockraden Shaft (Panel A) and Theodor Shaft (Panel B), respectively.

9.8 Comparison with reported data

To obtain a total emission rate for the mine, a weighted mean was computed from the individual results. In case of Theodor Shaft, first the mean of the plume inversion results of near and far part weighted by the inverse error, and the mean of the integral method weighted by the number of tracks (see Table 9.3) was calculated. The arithmetic mean of both gives the final result for Theodor Shaft (36.155 kt CH_4 yr^{-1}). Whereas for Bockraden Shaft, the final result is the arithmetic mean between integral and plume inversion method (14.226 kt CH_4 yr^{-1}).

The results were compared with data as reported by the mine showing an astonishingly good agreement (see Table 9.5). The difference between the mean inversion model result and the total reported emissions is less than 1 %. For the individual shafts, the inversion result is about 4 % lower compared to the reported emissions for Theodor Shaft and about 16 % higher in case of Bockraden Shaft.

Overall inversion errors

Uncertainties for individual inversion methods and ventilation shafts were propagated to the individual and total emission rates taking into account the calculation specification for obtaining the weighted mean (Table 9.6). This is straight forward for the independent statistical error from the plume inversion using Gaussian error propagation. In case of wind direction, the – compared to the simulations – larger variations for the measurements are considered to give a conservative error estimate. To account for the non-random behaviour

Table 9.5: Comparison between reported and inferred CH_4 emission rates. For Theodor Shaft, the two lines indicate the near and far part of the plume. The total result refers to the weighted mean of the inversion results according to involved uncertainties. See main text for more information. Reported values were kindly provided by the district government of Arnsberg (*Bezirksregierung Arnsberg, Abteilung Bergbau und Energie in NRW*).

Ventilation shaft	Emission rate $[\mathrm{kt\,CH_4\,yr^{-1}}]$			
	Reported	Inversion result		
		Plume inversion	Integral inversion	(Weighted) Mean
Theodor Shaft	37.690	43.125±1.065 31.830±5.233	31.151 30.819	36.155
Bockraden Shaft	12.274	12.363±0.419	16.088	14.226
Total	49.964			50.381

Table 9.6: Uncertainties by parameter on the inversion results for the individual ventilation shafts and for the total coal mine.

Parameter	Uncertainty [%]		
	Theodor Shaft	Bockraden Shaft	Total
Wind speed ($\pm 0.5\,\mathrm{m\,s^{-1}}$)	±7.9	±8.8	±8.2
Wind direction (±5°)	±5.2	±14.4	±7.8
Statistical error	±7.4	±2.9	±5.4
Considered measurement area	±5.0	±3.4	±4.6
Topography representation	±2.0	–	±1.4
CH_4 background column (±1 %)	±1.0	±1.0	±1.0
Conversion factor k	±0.5	±0.5	±0.5
Total uncertainty	±13.2	±17.2	±13.5

in this case, no Gaussian propagation was applied but a maximum error estimation, that is, a linear accumulation of the absolute values of errors taking into account the largest errors for each shaft and method. This gives a reasonable worst case estimate. Same accounts for uncertainties due to wind speed, considered measurement area, conversion factor and topography representation.

By computing the root of the sum of the squared individual, independent errors listed in Table 9.6, the approximate total uncertainty on the inferred total emission result becomes about 13.5 % and for the individual shafts 13.2 % (Theodor) and 17.2 % (Bockraden). Thereby, the total uncertainty comprises all random and systematic error components. The resulting uncertainties are strongly reduced compared to the power plant experiment. This is predominantly based on the reduced error in wind speed due to calibration with measurements by the AIMMS-20 instrument and generally higher wind speeds in the

boundary layer that reduce the relative error. However, uncertainty on wind information still dominates the error budget.

10

Survey of a marine, natural gas blowout site

Beside coal mine ventilation shafts, a natural gas seep at a former blowout site in the North Sea was surveyed within the scope of the AIRMETH 2011 campaign (see Section 9.1). Compared to the instrumental setup for terrestrial targets, the application over sea requires additional precautions. The low reflectance of water in the SWIR range of the electromagnetic spectrum for a nadir geometry involves comparably lower signal to noise ratios for a fixed exposure time. Longer exposure can potentially mitigate this effect but involves a deterioration in spatial resolution and hence also in the detection limit considering the larger ground scene.

This can be avoided when pointing the instrument off nadir towards the bright specular reflection of the sunlight, the so-called sunglint or glitter. To keep a constant viewing direction towards the sunglint in the moving aircraft, the instrument optics were mounted on a gyro-stabilised, hydraulic platform (see Figure C.2 in Appendix C) that automatically retains a preset direction.

While the complete data analysis (Gerilowski et al., 2012) involves information and measurements from various additional sources which are partly not publicly available, this chapter concentrates on results of the MAMAP measurements.

10.1 Target description

In 1990, a shallow, natural gas reservoir was accidentally hit during offshore oil exploration in the North Sea about 200 km off the coast of Scotland followed by strong gas flow (blowout) to the sea surface. The drilling accident at well 22/4b with no reported injuries took place under direction of Mobil North Sea LLC, which was a subsidiary company of ExxonMobil. Subsequently, the respective claims were returned to the UK government.

Since then, the blowout crater at about 57.9° N 1.6° E has been subject of few research campaigns (compare, for example, Rehder et al., 1998; IFM-GEOMAR, 2011). Methane

emission rate estimates are mainly based on analysis of water samples or sonar scans of the underwater bubble plume originating from the sea floor at about 100 m depth. Documented emission estimates range between 70 and 300 kt CH_4 yr^{-1} with a very high degree of uncertainty (Deutscher Bundestag – 17. Wahlperiode, 2010). It can further be assumed that about one third reaches the atmosphere as direct emissions to the atmosphere through ascending bubbles like observed for example by Leifer et al. (2006a) for a seep at 250 m depth. The remainder is dissolved in the ocean or oxidised to CO_2 of which parts can lead to indirect, diffuse emissions over larger spatial scales.

The actual amount of methane released to the atmosphere is relevant for the UK emissions inventory which includes greenhouse gas leakage due to exploration in its territory under the Kyoto protocol. Note that the European Emissions Trading Scheme is not applicable, since it currently does not cover methane nor emissions from fossil fuel exploration. So far, emissions from the blowout are unaccounted for in the UK greenhouse gas budget due to incompleteness of emission information (Deutscher Bundestag – 17. Wahlperiode, 2010).

The survey with the Polar 5 aircraft took place on 3 June 2011, between 09:10 UTC and 12:10 UTC during clear sky conditions. MAMAP data for quantification of the direct atmospheric emissions during the time of the overflight were acquired upwind and downwind of the blowout position at a constant altitude of about 650 m. In-situ measurements were performed downwind down to altitudes of about 100 m above sea level restricted by aircraft safety regulations.

Remote sensing flight patterns were optimised preflight for an assumed direct atmospheric input of about 10 kt CH_4 yr^{-1} at the lower range of prior emission estimates and forecasted wind speeds of 3 m s^{-1} according to the Global Forecast System (GFS) model for the given time.

10.2 Measurement data

Column-averaged dry air mole fractions $XCH_4(CO_2)$ were retrieved using a reference radiative transfer scenario for background aerosol load, 40° solar zenith angle and 35° off nadir viewing angle limited by the aircraft aperture. The off nadir pointing was sufficient to capture the sun glitter area. In a simplified approach, glint was simulated by setting the spectral albedo to 0.6. Polarisation effects which may occur for ocean specular reflection were not explicitly addressed, since the MAMAP optics include depolarising elements in the optical path. While for CO_2 the reference profile for the linearisation point was the same as for the coal mine ventilation shafts, for CH_4, the U.S. Standard profile was shifted to yield a background column-averaged mole fraction of 1738 ppb with 1820 ppb at the surface.

Figure 10.1 shows relevant atmospheric data acquired by the AIMMS-20 probe. Wind speeds were mainly at about 4–6 m s^{-1} blowing from 190°–230°. This could be confirmed by environmental buoy 62164 data measured at 30 m altitude about 100 km south-west of the target area. The recorded temperatures indicate that the boundary layer height was about 150 m from where temperatures start to decrease towards the sea surface. The flight altitude was hence well above a possible CH_4 plume. Temperature data for comparison were not available for buoy 62164 and was taken from buoy 62120 (measuring at sea

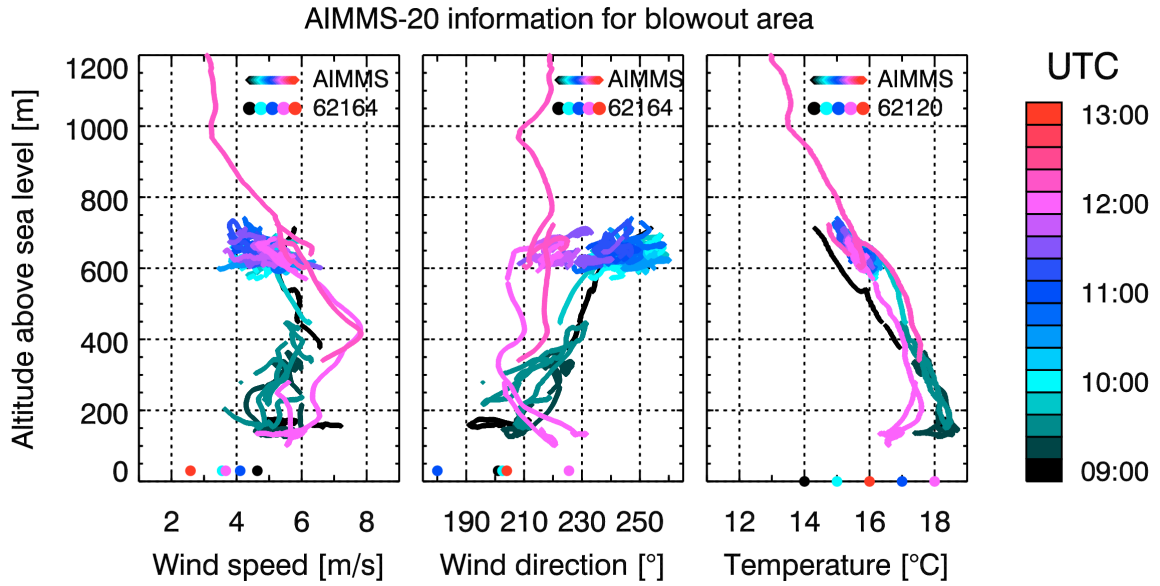

Figure 10.1: Atmospheric data from the AIMMS-20 probe: Wind speed, wind direction and air temperature. Data from buoys 62164 and 62120 were obtained from Weather Underground (http://www.wunderground.com/, August 2012). Time of measurement is given by the colour scale to the right.

level) about 170 km south of the blowout location.

By computing the gradient in potential temperature between sea surface and adjacent air layer, the atmospheric stability can be estimated according to Hasse and Weber (1985). Ocean temperatures at the blowout location and the nearby Sleipner field (about 50 km north) were approximately 11.5 °C for the time period of the overflight (IFM-GEOMAR, 2011). Considering a sea surface pressure of about 1036 hPa measured by the environmental buoys, the difference in potential temperature between sea and air is roughly 4 K. For wind speeds of about 5 m s^{-1}, this results in stability class E (slightly stable) which was used as input for plume model simulations.

Figure 10.2 (Panel A) shows the retrieved MAMAP remote sensing data from the blowout location gridded to 50 m × 50 m boxes equivalent to the approximate ground scene size of MAMAP for an altitude of 650 m. The flight pattern was right on target as could be confirmed by an onboard camera which captured the plume at the expected position (see Figure 10.3). Observed dimensions are in agreement with ship based observations which report a bubble plume diameter of about 20 m (IFM-GEOMAR, 2011). Additionally to a fit quality filter (RMS $\leq$ 0.798 %), MAMAP measurements were filtered with respect to variations in the inclination of the viewing direction. Usually, for high inclinations, the sun glint spot was missed and received signal strengths were too low for subsequent processing.

The results show no significantly enhanced methane levels as would be expected for a source with 10 kt CH_4 yr^{-1} direct atmospheric input and a diameter of about 20 m at the present atmospheric conditions. A corresponding simulation using the actually performed flight track and adding a random noise component of 0.25 % (1 σ) equal to the precision of the filtered data but no CH_4 sources is shown in Figure 10.2 (Panel B). Measurement and simulation are basically indistinguishable.

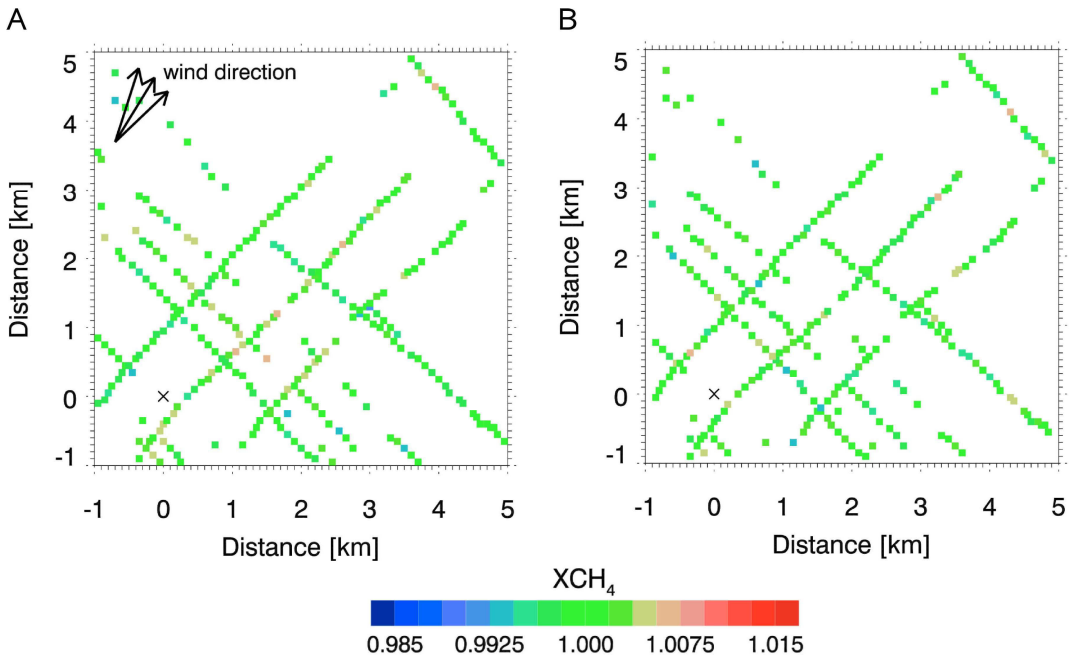

Figure 10.2: MAMAP data (Panel A) and simulation with a random noise component of 0.25 % (1 σ) in the absence of any sources (Panel B). Pixels are plotted with approximately doubled edge length for better visibility.

Diffuse release of CO_2 as resulting from oxidised CH_4 causes only a minor error for $XCH_4(CO_2)$ based on the CO_2 proxy method: Of an assumed 70 kt CH_4 yr^{-1} source at the seabed, about two thirds (see above) or 47 kt yr^{-1} of CH_4 could potentially be oxidised to 128 kt CO_2 yr^{-1}. Due to the 500 times higher sensitivity of MAMAP for CH_4 than for CO_2 (Section 6.2), the proxy method could lead to a bias of less than 2.6 % relative to the measured CH_4 enhancement in case of coincidental release of CH_4 and CO_2. A real CH_4 enhancement of 1 % relative to background, for example, could appear as an enhancement of 0.974 % in MAMAP measurements. This is a negative bias of −0.026 % relative to background and can hence be neglected considering that the instrument precision is about 0.4 % (Section 6.2). Generally, the conditions will be more favourable than in this conservative assumption. For example, not all CH_4 can be immediately oxidised and released at the same location as the CH_4.

10.3 Comparison with simulations

By comparing simulations for different emission rates and atmospheric parameters with the actual measurements, an upper limit constraint for direct atmospheric emissions originating from ascending bubbles at the blowout location at the given time can be determined. The simulations cover wind directions from 200°–245° and various emission rates for a conservatively high wind speed of 5.5 m s^{-1}. Figures 10.4 and 10.5 show simulated emissions of 7.5 kt CH_4 yr^{-1} and 5.0 kt CH_4 yr^{-1}, respectively. The simulations support the conclusion that the direct atmospheric emissions at the time of the overflight were likely below 7.5 kt CH_4 yr^{-1} and potentially below 5.0 kt CH_4 yr^{-1}. Lower emissions

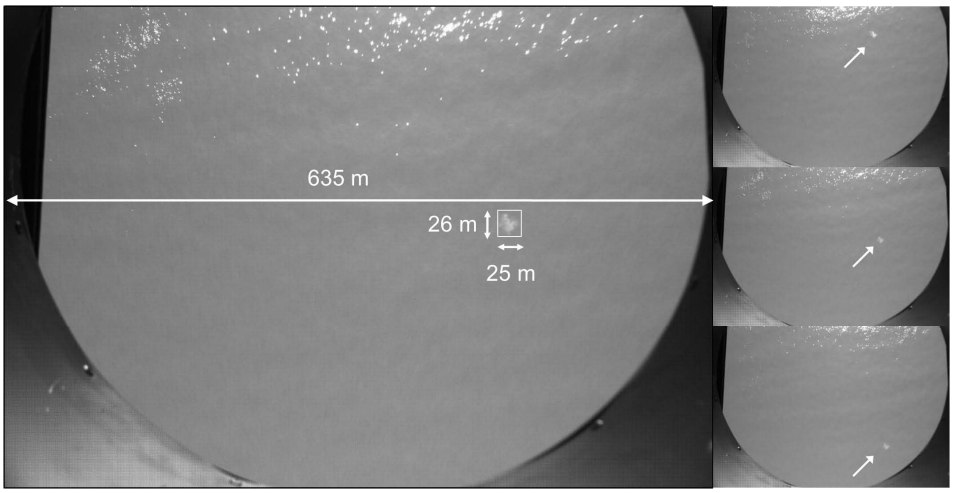

Figure 10.3: A sequence of photographs looking nadir at the position of the blowout during the measurement overflight. The approximate extension of the bubble plume at the surface is about 25 m. (Figure courtesy of A. Schönhardt.)

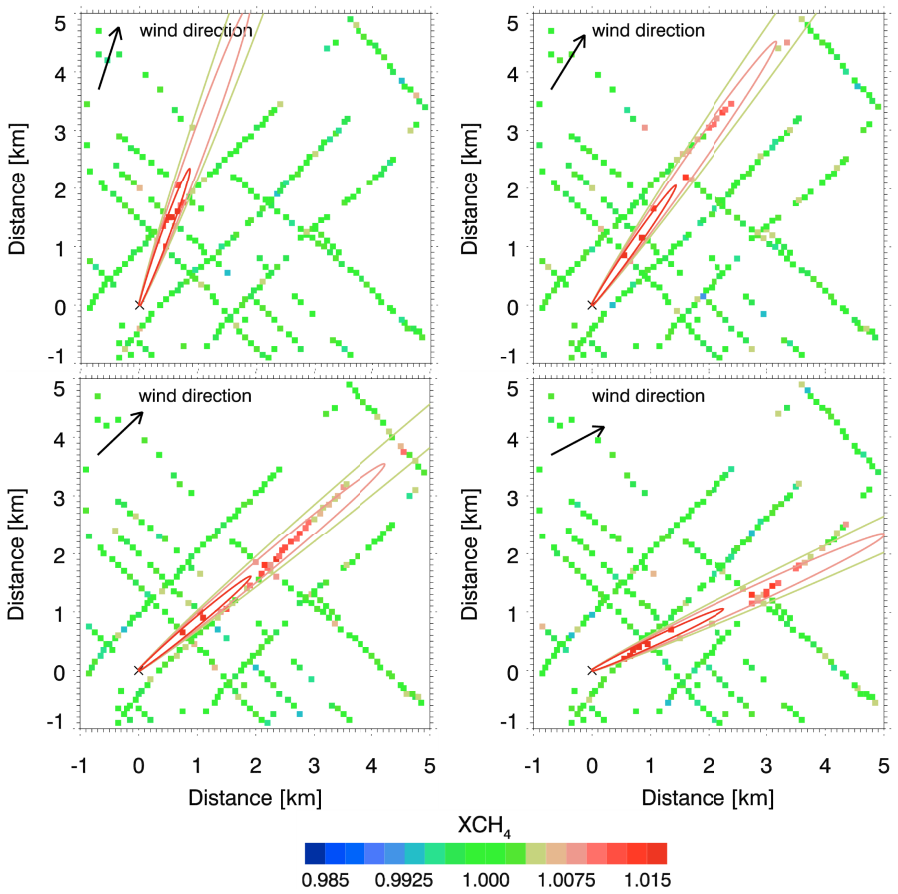

Figure 10.4: Gaussian plume forward model simulations for a source of about 20 m in diameter and an emission rate of 7.5 kt CH_4 yr^{-1} at the origin of the coordinate system. Simulations were performed for four different wind directions between 200 ° (upper left) and 245 ° (lower right). Wind speed was set to 5.5 m s^{-1}.

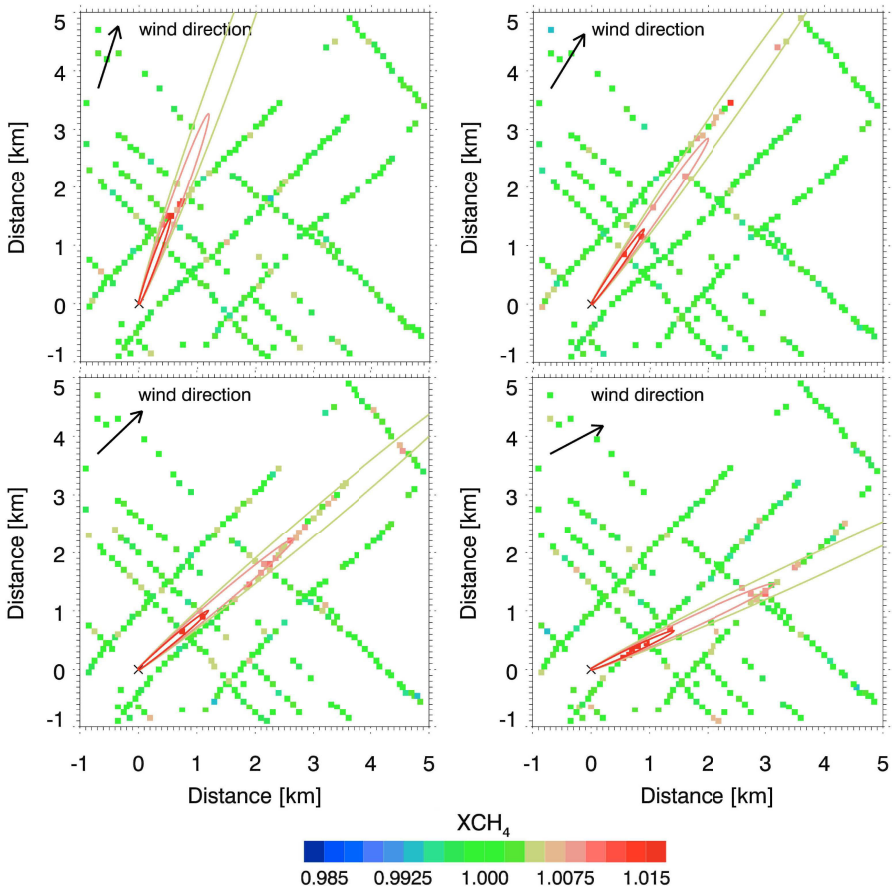

Figure 10.5: As Figure 10.4 but for an emission rate of 5.0 kt CH_4 yr^{-1}.

of 2.5 kt CH_4 yr^{-1} would have been close to MAMAP's detection limit.

Even though MAMAP data do not show the expected methane plume, the present analysis is an example of extracting useful geophysical information by providing an upper limit constraint. To confirm that the blowout emissions are below MAMAP's detection limit, additional measurements with a denser flight pattern are required.

One limitation of the method applied is that it cannot capture diffuse degassing, only point source emissions due to direct ebullition (via bubbles) can be measured. The diffuse degassing on the other hand may occur on a wide area and even with highly accurate in-situ measurements is difficult to distinguish from the natural, background degassing which for the total UK continental shelf ranges between 0.1 and 3.5 Mt CH_4 yr^{-1} (Judd et al., 1997).

11
Summary and conclusions

Knowledge of the strength and distribution of sources and sinks of greenhouse gases is essential to be able to understand and predict future climate change. While this knowledge currently has significant gaps, the present work presented and evaluated possibilities to accurately quantify emission rates from point sources releasing the greenhouse gases methane (CH_4) and carbon dioxide (CO_2) using airborne remote sensing data.

Retrieval algorithm

The Methane Airborne MAPper instrument (MAMAP) proved to be a versatile tool to map greenhouse gas plumes onboard various airborne platforms with different measurement geometries. In the context of this work, a pre-existing, preliminary retrieval algorithm based on WFM-DOAS for SCIAMACHY satellite data converting measured spectra to column-averaged dry air mole fractions $X\mathrm{CH}_4$ and $X\mathrm{CO}_2$ was revised to accommodate for the special requirements of MAMAP.

The algorithm modification included the introduction of a conversion factor that takes into account the altitude sensitivity for a passive remote sensing instrument situated within the atmosphere and relying on solar backscatter. The conversion factor is applicable under the assumption that relevant changes of the trace gas of interest are predominantly occurring below the aircraft, which is reasonable for point and localised sources. Based on the measurement geometry, about twice the sensitivity is achieved below the aircraft compared to the remaining greenhouse gas column above. Extensive studies were performed to assess the sensitivity of the retrieval result to changes in measurement geometry and different atmospheric parameters. The column-averaged dry air mole fractions $X\mathrm{CO}_2(\mathrm{CH}_4)$ and $X\mathrm{CH}_4(\mathrm{CO}_2)$ derived from ratios of retrieved CO_2 and CH_4 columns were shown to be robust against variations of, for example, aerosol content, cirrus clouds, topography, aircraft altitude and solar zenith angle. Biases may be large for the single gas columns but mostly cancel for the ratios leading to a significantly enhanced data quality. Typical accuracies that may generally be expected for the retrieval

of $X\mathrm{CH_4}(\mathrm{CO_2})$ and $X\mathrm{CO_2}(\mathrm{CH_4})$ are about 0.24 % relative to background. If additionally the altitude correction factor is applied, the accuracy is further improved.

Based on this algorithm, the precision of the instrument in its original setup, as inferred from the data directly, is about 1.74 % for the profile scaling factor ratios over inhomogeneous land scenes (Gerilowski et al., 2011). This yields a precision of about 0.83 % for $X\mathrm{CO_2}(\mathrm{CH_4})$ and 1.0 % for $X\mathrm{CH_4}(\mathrm{CO_2})$ for typical instrument altitudes of about 1.25 km, a solar zenith angle of 40° and assuming $\mathrm{CO_2}$ and $\mathrm{CH_4}$ variations to occur mainly below the aircraft. The introduction of a spatial scrambler unit (technical modification not part of this work, for more information see Gerilowski et al., 2011) significantly improved the precision by a factor of three to about 0.6 % for the profile scaling factor ratios as could be determined from data in this work. Or, taking into account the altitude sensitivity factor, the precision is about 0.35 % for $X\mathrm{CH_4}(\mathrm{CO_2})$ and 0.3 % for $X\mathrm{CO_2}(\mathrm{CH_4})$. With respect to the precision, 3-σ-detection limits can be defined as $\pm$1.05 % for $X\mathrm{CH_4}(\mathrm{CO_2})$ and $\pm$0.9 % for $X\mathrm{CO_2}(\mathrm{CH_4})$.

Inversion for point source emission rates

To obtain $\mathrm{CO_2}$ and $\mathrm{CH_4}$ emission rates for the localised sources under investigation in this work (coal fired power plants and coal mine ventilation shafts), two inversion approaches were applied: the Gaussian plume inversion and the Gaussian integral inversion method.

For the plume inversion, a Gaussian plume model is fitted to the retrieved dry column information using an optimal estimation approach. A priori information is used to restrict the data to a physically meaningful range. This is helpful in the presence of several sources with overlapping emission plumes that are inverted at once, but generally not required for a single source inversion.

The integral inversion is based on the Gaussian divergence theorem which states that the integrated flux through the boundaries of an area is equal to the emission rate. The upwind and downwind boundaries were selected manually, while boundaries parallel to wind direction do not contribute when diffusion is neglected.

One of the most important input parameters for both inversion models is the wind speed. It enters linearly into the equations for both methods, and hence a 10 % uncertainty on wind speed translates into a 10 % uncertainty on the greenhouse gas emission estimates. Another very important factor is the flight pattern performed over the point source to be assessed. For the Gaussian integral method, systematic errors can be significant, but they can be almost completely avoided if an appropriate flight pattern is performed. In particular, the flight tracks should be long enough to cover the entire plume. For the Gaussian plume model, the flight pattern is not of that importance. It mainly reduces the statistical error. However, it is of advantage to densely sample the plume centre with highest values above background and accordingly high signal to noise ratio.

In direct comparison, both inversion methods, the Gaussian plume inversion and the Gaussian integral method, are able to deliver accurate results. The Gaussian plume method requires more parameters, but it can incorporate all available data resulting in a reduced statistical uncertainty. In cases where atmospheric and other parameters are not well defined, the Gaussian integral method may be of advantage, for example, because of its independence of the atmospheric stability and the lower sensitivity on variations of wind direction. On the other hand, the integral method can be strongly biased by a few outliers,

especially when the data are rather patchy. With the modified instrument, however, almost all data are of high quality leading to a continuous observation pattern.

Based on simulations, the minimum emission rate to allow for an accurate inversion is about 3–5 kt CH_4 yr^{-1} or 2–3 Mt CO_2 yr^{-1} for typical conditions. In favourable atmospheric conditions, for example, low wind speeds, weaker sources can be quantified accordingly.

Carbon dioxide from power plants

MAMAP measurements over the coal fired power plants Jänschwalde and Schwarze Pumpe, located near Berlin, Germany, performed on 26 July 2007 showed distinct CO_2 plumes that originate at the power plants' stack locations. Applying the Gaussian plume model and the integral inversion to the retrieved $XCO_2(CH_4)$, CO_2 emission rates could be inferred. Relative to reported values, the emission rates of Jänschwalde power plant (about 24 Mt CO_2 yr^{-1}) were overestimated by 8.3 % for the plume model and underestimated by 0.2 % for the Gaussian integral. For Schwarze Pumpe power plant (yearly emissions of about 13 Mt CO_2 yr^{-1}), the emission rate was underestimated by 9.0 % (Gaussian plume model) and by about 9.9 % (Gaussian integral), respectively. In case of Schwarze Pumpe, non-stationary wind conditions complicated the inversion process. The total uncertainties of 20–30 % were dominated by the uncertainty on wind information (approximately $\pm 0.9\,m\,s^{-1}$). In an extensive simulation, the error caused by aerosol scattering and absorption as well as the error on the conversion factor on the inversion have turned out to be not significant.

For the analysis of the power plant measurements, wind data of the routine analysis of the numerical weather prediction model COSMO-DE of the German Weather Service (DWD) were used. Although COSMO-DE has a rather high horizontal resolution of 2.8 km compared to other models and an hourly output, wind information with higher resolution in space and time is desirable to increase the accuracy of the final results which was already similar to uncertainties in power plant CO_2 emissions as presented by Ackerman and Sundquist (2008).

Methane from coal mine ventilation shafts

A dedicated survey of two coal mine ventilation shafts of an anthracite mine near Ibbenbüren, Germany, was conducted on 4 June 2011 with the modified MAMAP instrument. After the experience gained with the data analysis from the power plant test flight, great importance had been attached to acquiring more precise wind information. Therefore, a vertically higher resolved version of the COSMO-DE model output as well as a turbulence probe integrated to the aircraft were utilised for the data analysis. Measured wind data enabled calibration of the model against measurements reducing the approximate uncertainty on wind speed to about $\pm 0.5\,m\,s^{-1}$. Furthermore, data from an additional in-situ CH_4 analyser were used for an improved data interpretation.

The total CH_4 release due to mine gas emissions was estimated to about 50.4 kt CH_4 yr^{-1} with an uncertainty of ±13.5 %. This was within 1 % of the emission rate reported by the mine operator to the district government.

Although significantly reduced, the uncertainty of the wind information was still the largest contributor (about ±8 %) to the error budget but was in this case of similar

magnitude as other error sources such as the statistical uncertainty based on the measurement error (about ±5 %).

Marine gas seep

In cases where no plume structure with increased column concentrations is visible, MAMAP data can still be useful. For example, data recorded at a natural gas blowout site in the North Sea on 3 June 2011 were compared to simulations of a CH_4 source with different emission rates under various atmospheric conditions. Based on the actual flight pattern, an upper limit constraint for direct atmospheric CH_4 emissions for the time of the overflight could be obtained. In this case, emissions were likely below 7.5 kt CH_4 yr^{-1} and potentially below 5.0 kt CH_4 yr^{-1}.

Outlook

The focus of this work was to give a detailed analysis and characterisation of data from MAMAP's SWIR channel at about 1600 nm and associated possibilities in the data processing. The NIR channel covering the O_2-A absorption band at about 760 nm can deliver valuable additional information about clouds and aerosol and in particular also for cases where CO_2 and CH_4 sources coincide, but it has not been investigated in depth during this work. However, the retrieval algorithm, that has been optimised for CO_2 and CH_4 retrieval, can also be used for the O_2 retrieval. Few optimisations may be of advantage to account for the specific setup of the O_2-A channel, for example, regarding the preliminary wavelength calibration (see Appendix I).

Of great interest is the development of an imaging MAMAP instrument with a wider swath but same or smaller ground scene size. Many snapshots of plumes can be recorded in very little time reducing the influence of atmospheric variations and the time necessary for surveys. Moreover an imaging MAMAP instrument has the potential to significantly reduce the inversion limit by delivering substantially more data as was shown by simulations.

The methods developed and assessed in this work are valuable and relevant also to analysis of satellite data with sufficient spatial resolution and precision such as expected for CarbonSat (Bovensmann et al., 2010; Velazco et al., 2011). Based on the progress in deriving emission rate estimates using measurements of the airborne instrument MAMAP presented in this work, the Gaussian plume inversion in a slightly modified form has been simulated for satellite applications in an Observing System Simulation Experiment (OSSE) for CarbonSat (Bovensmann et al., 2010). The goal of the potential satellite mission CarbonSat is the quantification of natural and anthropogenic greenhouse gas fluxes from space. Satellite observations offer the opportunity of global coverage in a few days also over targets where accessibility or permissioning may be delicate for aircraft. Furthermore, repeated measurements over the same targets reduce the statistical uncertainty and may help to monitor a temporal development.

Part IV

Appendix

A

Henyey-Greenstein phase function

While generally for Mie scattering the analytical determination of the phase function is difficult due to complex interplay with the particle's microphysical properties, it can be approximated by a Henyey-Greenstein function (Henyey and Greenstein, 1941):

$$P_{\mathrm{HG}}(\theta, g) = \frac{1 - g^2}{\left(1 + g^2 - 2g\cos\theta\right)^{3/2}} \tag{A.1}$$

where θ is the scattering angle and g the asymmetry factor. An asymmetry factor of $g = +1$ means that all radiation is scattered forward whereas $g = 0$ corresponds to an isotropic distribution of scattered radiation.

The forward peak is generally well reproduced compared to the Mie phase function but the agreement is less good for the backward peak. A mitigation technique is to use a double Henyey-Greenstein phase function (Goody and Yung, 1989):

$$P(\theta) = bP_{\mathrm{HG}}(\theta, g_1) + (1 - b)P_{\mathrm{HG}}(\theta, g_2) \tag{A.2}$$

where $0 \leq b \leq 1$ and g_2 accounting for a backward peak when assigned a negative value.

B

Instrumental slit function

The slit function f is necessary for the forward model to simulate radiances with limited resolution as observed with the MAMAP instrument. The simulated measurements at instrument resolution are obtained by convolution of the slit function with the simulated monochromatic radiances.

In the short-wave infrared channel where CO_2 and CH_4 are observed, the slit function is best described by the sum of two Gaussian functions that are slightly shifted:

$$f_{\mathrm{SWIR}}(\lambda-\lambda_0) = a_{\mathrm{SWIR}} \cdot \left[0.9 \cdot \exp\left(-\left(2\sqrt{\ln 2}\,\frac{(\lambda-\lambda_0)}{\mathrm{FWHM}} \right)^2 \right) + 0.1 \cdot \exp\left(-\left(2\sqrt{\ln 2}\,\frac{(\lambda-\lambda_0+0.6\ \mathrm{FWHM})}{2.5\ \mathrm{FWHM}} \right)^2 \right) \right] \tag{B.1}$$

where λ is the actual wavelength, λ_0 the centre wavelength (of a detector pixel) and a is a normalisation factor defined by the inverse of the numerical integral of the slit function sampled according to the wavelength grid. The approximate full width at half maximum (FWHM) for the SWIR channel is thereby 0.82 nm.

For the near infrared channel, where O_2 is measured, the slit function has been preliminarily fitted by a single Gaussian function with a FWHM of 0.46 nm.

$$f_{\mathrm{NIR}}(\lambda-\lambda_0) = a_{\mathrm{NIR}} \cdot \exp\left(-\left(2\sqrt{\ln 2}\,\frac{(\lambda-\lambda_0)}{\mathrm{FWHM}} \right)^2 \right) \tag{B.2}$$

MAMAP instrumental slit functions for both channels are displayed in Figure B.1.

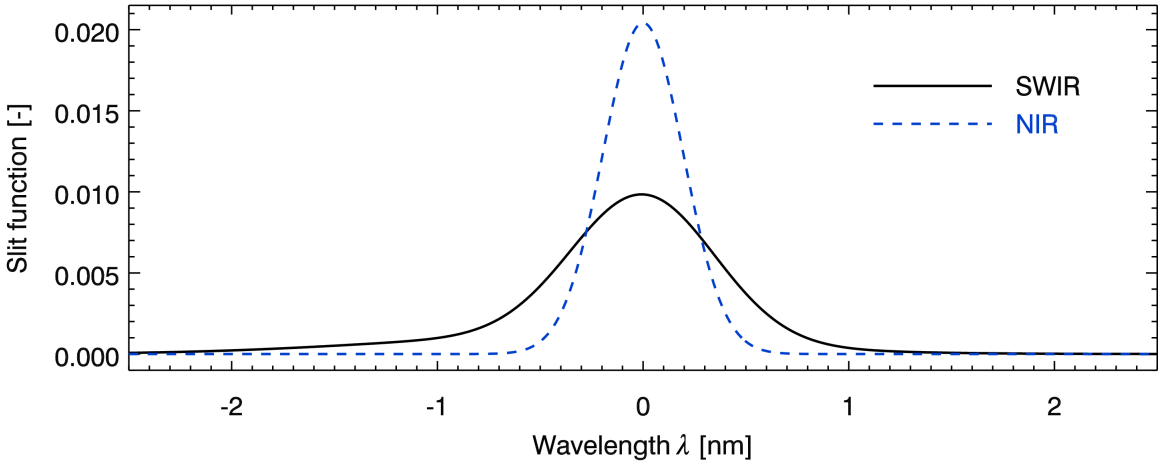

Figure B.1: MAMAP instrumental slit functions as used for the short-wave infrared (SWIR) and near infrared (NIR) channel. For the NIR channel, the slit function is preliminary. The centre wavelength in this figure is $\lambda_0 = 0\,\text{nm}$.

C
MAMAP photographs

This appendix shows additional photographs of the MAMAP instrument and its integration to aircraft. The measurements above the coal mine ventilation shafts (see Section 9) and above the natural gas blowout in the North Sea (see Section 10) were conducted onboard the Polar 5 aircraft (Figure C.1, Panel A), whereas the power plant overflights (see Section 8) were performed using a Cessna 207T (Figure C.1, Panel B).

For the blowout measurements, the instrument optics were mounted on a gyro-stabilised, hydraulic platform shown from inside the cabin (Figure C.2, Panel A) and from below the aircraft (Figure C.2, Panel B).

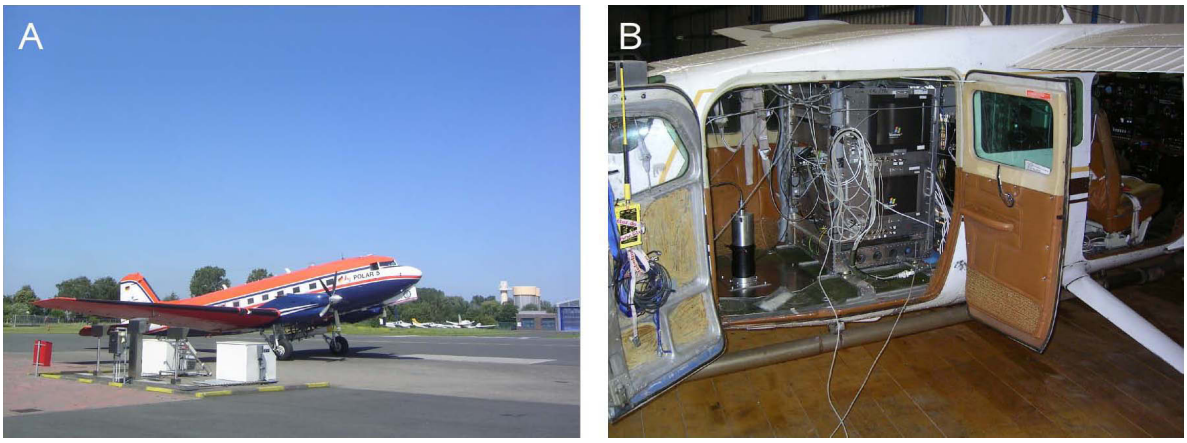

Figure C.1: . Panel A: Polar 5 aircraft of the Alfred Wegener Institute for Polar Research, Germany (AWI). The Polar 5 is based on a Douglas DC-3T built in 1942 and has been refurbished to a Basler BT-67 in 2007. Panel B: MAMAP instrument integrated in the Cessna 207T operated by the Free University, Berlin, Germany. The computer rack is on the right and the glass fibre coupled telescope including the spatial scrambler unit sits on top of a nadir port in the back of the aircraft. The spectrometer unit is to the right of the computer rack but not visible.

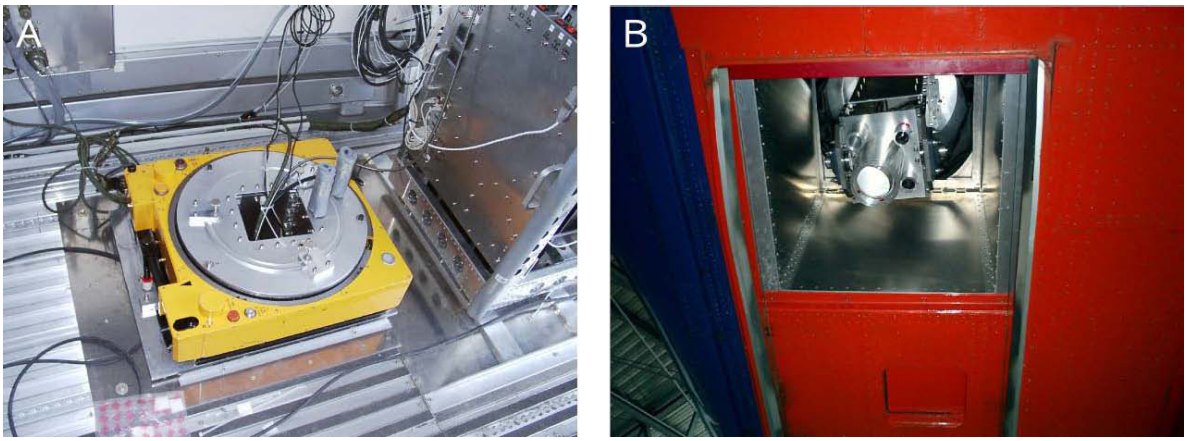

Figure C.2: Stabilisation platform with mounted, external optics (Panel A) connected to the zenith sky inlet of MAMAP via glass fibre as installed in the Polar 5 aircraft. The MAMAP optics as well as outlets for an additional imaging DOAS instrument for NO_2 measurements (operated in the UV) and two observer CCD-cameras are better visible from below the aircraft (Panel B). (Photograph Panel A taken by S. Krautwurst, photograph Panel B taken by A. Schönhardt.)

D

MAMAP conversion factors

In this appendix, additional conversion factors (see Section 5.2) for various aircraft altitudes, solar zenith angles, spectral albedos and aerosol scenarios are given (Table D.1).

Table D.1: MAMAP conversion factors for retrieval output assuming all deviations from standard mean column occurred below the aircraft.

Aircraft altitude [m]	Solar zenith angle [°]	Surface albedo [−]	Aerosol type	Conversion factor [−]	
				CH_4	CO_2
850	40	0.01	urban	0.582	0.476
			background	0.573	0.468
		0.1	urban	0.561	0.458
			background	0.563	0.459
		0.18	urban	0.559	0.456
			background	0.562	0.459
		0.25	urban	0.557	0.455
			background	0.561	0.458
		0.4	urban	0.555	0.453
			background	0.560	0.457
850	50	0.01	urban	0.607	0.489
			background	0.598	0.481
		0.1	urban	0.584	0.470
			background	0.586	0.472
		0.18	urban	0.582	0.468
			background	0.585	0.471
		0.25	urban	0.581	0.467
			background	0.585	0.470
		0.4	urban	0.578	0.465
			background	0.583	0.469

Table D.1: MAMAP conversion factors for retrieval output – continued.

Aircraft altitude [m]	Solar zenith angle [°]	Surface albedo [−]	Aerosol type	Conversion factor [−]	
				CH_4	CO_2
850	60	0.01	urban	0.639	0.508
			background	0.628	0.498
		0.1	urban	0.612	0.485
			background	0.614	0.486
		0.18	urban	0.610	0.483
			background	0.613	0.485
		0.25	urban	0.608	0.482
			background	0.612	0.484
		0.4	urban	0.606	0.480
			background	0.611	0.483
1250	40	0.01	urban	0.606	0.499
			background	0.594	0.489
		0.1	urban	0.580	0.477
			background	0.582	0.478
		0.18	urban	0.578	0.475
			background	0.581	0.477
		0.25	urban	0.577	0.474
			background	0.580	0.477
		0.4	urban	0.575	0.472
			background	0.579	0.476
1250	50	0.01	urban	0.630	0.512
			background	0.618	0.501
		0.1	urban	0.603	0.488
			background	0.604	0.489
		0.18	urban	0.600	0.487
			background	0.603	0.488
		0.25	urban	0.599	0.485
			background	0.602	0.488
		0.4	urban	0.597	0.484
			background	0.601	0.487
1250	60	0.01	urban	0.662	0.530
			background	0.647	0.517
		0.1	urban	0.629	0.502
			background	0.630	0.502
		0.18	urban	0.626	0.500
			background	0.628	0.501
		0.25	urban	0.625	0.498
			background	0.628	0.501
		0.4	urban	0.622	0.497
			background	0.626	0.500

Table D.1: MAMAP conversion factors for retrieval output – continued.

Aircraft altitude [m]	Solar zenith angle [°]	Surface albedo [−]	Aerosol type	Conversion factor [−]	
				CH_4	CO_2
3000	40	0.01	urban	0.693	0.585
			background	0.676	0.571
		0.1	urban	0.661	0.558
			background	0.661	0.557
		0.18	urban	0.658	0.556
			background	0.659	0.557
		0.25	urban	0.657	0.555
			background	0.659	0.556
		0.4	urban	0.656	0.554
			background	0.658	0.555
	50	0.01	urban	0.709	0.591
			background	0.695	0.580
		0.1	urban	0.677	0.564
			background	0.677	0.564
		0.18	urban	0.675	0.563
			background	0.676	0.563
		0.25	urban	0.674	0.562
			background	0.675	0.563
		0.4	urban	0.672	0.560
			background	0.674	0.562
	60	0.01	urban	0.732	0.602
			background	0.718	0.591
		0.1	urban	0.696	0.572
			background	0.696	0.572
		0.18	urban	0.693	0.570
			background	0.694	0.571
		0.25	urban	0.692	0.569
			background	0.693	0.570
		0.4	urban	0.690	0.568
			background	0.693	0.569
4500	40	0.01	urban	0.743	0.639
			background	0.733	0.630
		0.1	urban	0.718	0.618
			background	0.718	0.618
		0.18	urban	0.716	0.616
			background	0.717	0.617
		0.25	urban	0.716	0.616
			background	0.716	0.616
		0.4	urban	0.714	0.615
			background	0.716	0.616

Table D.1: MAMAP conversion factors for retrieval output – continued.

Aircraft altitude [m]	Solar zenith angle [°]	Surface albedo [−]	Aerosol type	Conversion factor [−]	
				CH_4	CO_2
4500	50	0.01	urban	0.755	0.642
			background	0.747	0.636
		0.1	urban	0.730	0.622
			background	0.730	0.622
		0.18	urban	0.729	0.620
			background	0.729	0.621
		0.25	urban	0.728	0.619
			background	0.729	0.620
		0.4	urban	0.727	0.619
			background	0.728	0.620
	60	0.01	urban	0.770	0.647
			background	0.765	0.643
		0.1	urban	0.744	0.626
			background	0.744	0.626
		0.18	urban	0.742	0.624
			background	0.743	0.624
		0.25	urban	0.741	0.623
			background	0.742	0.624
		0.4	urban	0.740	0.622
			background	0.741	0.623

E

Rotated coordinate system of the wind model

The COSMO[1] non-hydrostatic numerical weather prediction models that have been used for this work are based on the "Lokal-Modell" (LM) of the German Weather Service[2] (Doms, 2011). It features terrain following coordinates on a rotated latitude-longitude grid. The north pole is rotated to λ_N =170°W and φ_N =40°N (see Figure E.1). This leads to equator and prime meridian running through Germany. In Germany and central Europe the grid is then almost rectangular leading to a more homogeneous distribution of grid points compared to an unrotated grid.

The transformation from rotated (λ, φ) to geographical coordinates (λ_g, φ_g) is given by (Baldauf et al., 2011):

$$\lambda_g = \lambda_N - \arctan\left(\frac{\cos\varphi \sin\lambda}{\sin\varphi \cos\varphi_N - \sin\varphi_N \cos\varphi \cos\lambda}\right) \tag{E.1}$$

$$\varphi_g = \arcsin\left(\sin\varphi \sin\varphi_N + \cos\varphi \cos\lambda \cos\varphi_N\right) \tag{E.2}$$

and for the back transformation:

$$\lambda = \arctan\left(\frac{-\cos\varphi_g \sin\left(\lambda_g - \lambda_N\right)}{-\cos\varphi_g \sin\varphi_N \cos\left(\lambda_g - \lambda_N\right) + \sin\varphi_g \cos\varphi_N}\right) \tag{E.3}$$

$$\varphi = \arcsin\left(\sin\varphi_g \sin\varphi_N + \cos\varphi_g \cos\varphi_N \cos\left(\lambda_g - \lambda_N\right)\right) \tag{E.4}$$

The horizontal wind components u, v of the model output refer to the rotated grid and have to be converted to the corresponding geographical wind components u_g, v_g via:

$$u_g = u\cos\delta + v\sin\delta \tag{E.5}$$

$$v_g = -u\sin\delta + v\cos\delta \tag{E.6}$$

[1] COSMO: Consortium for Small-Scale Modelling

[2] Deutscher Wetterdienst (DWD)

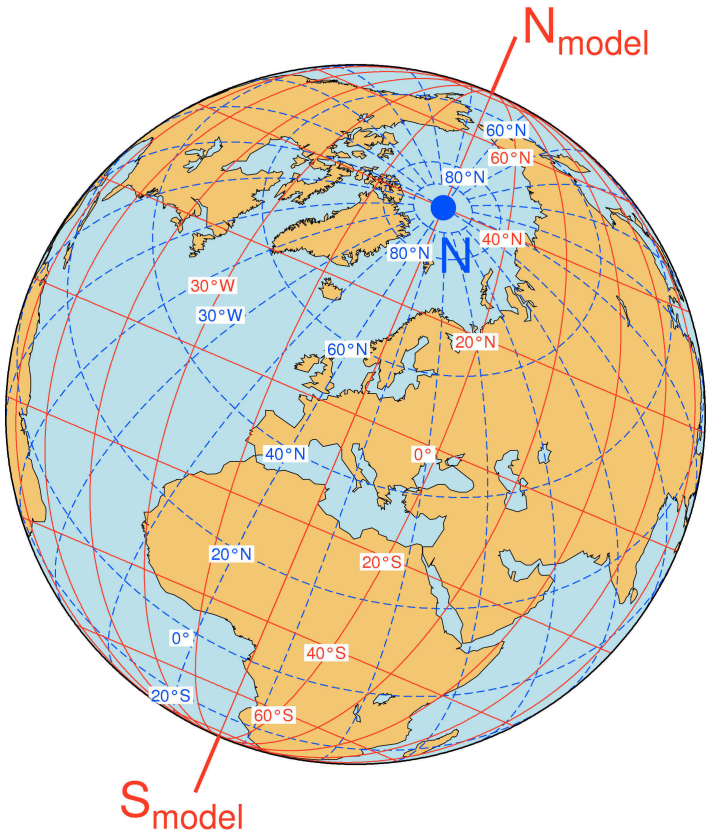

Figure E.1: Geographical (blue) and rotated grid (red) for the COSMO models. The model north pole is at λ_N =170°W and φ_N =40°N. The equator of the model grid runs through Germany.

and backwards:

$$u = u_g \cos\delta - v_g \sin\delta \tag{E.7}$$

$$v = u_g \sin\delta + v_g \cos\delta \tag{E.8}$$

where δ is the angle between meridians in the geographical system and in the rotated system:

$$\delta = \arctan\left(\frac{\cos\varphi_N \sin\left(\lambda_N - \lambda_g\right)}{\cos\varphi_g \sin\varphi_N - \sin\varphi_g \cos\varphi_N \cos\left(\lambda_N - \lambda_g\right)}\right) \tag{E.9}$$

The German Weather Service runs two different COSMO models. The COSMO-DE[3] has a resolution of about $\Delta\varphi = \Delta\lambda = 0.025° \approx 2.8$ km on an area that is defined by the geographical corner points given in Table E.1 and illustrated in Figure E.2 (Panel A). COSMO-DE provides 50 altitude levels with an increasing spacing from 20 m near ground to about 300 m at 700 hPa (Baldauf et al., 2011).

The COSMO-EU[4] model covers a wider area (see Table E.1 and Figure E.2, Panel B) with a reduced horizontal resolution of $\Delta\varphi = \Delta\lambda = 0.0625° \approx 7$ km and a reduced vertical resolution providing 40 altitude layers (Schulz and Schättler, 2009).

[3]COSMO-DE was formerly named Lokal-Modell-Kürzestfrist (LMK).
[4]COSMO-EU was formerly named Lokal-Modell-Europa (LME).

Table E.1: Corner coordinates for the model area of the COSMO-DE and and the COSMO-EU model (Baldauf et al., 2011; Schulz and Schättler, 2009).

Corner	COSMO-DE		COSMO-EU	
	λ_g	φ_g	λ_g	φ_g
south-west	2.98°E	44.77°N	9.14°W	27.70°N
south-east	17.72°E	44.72°N	34.67° E	26.12°N
north-west	1.04°E	56.20°N	34.24°W	65.58°N
north-east	19.84°E	56.14°N	63.47° E	62.40°N

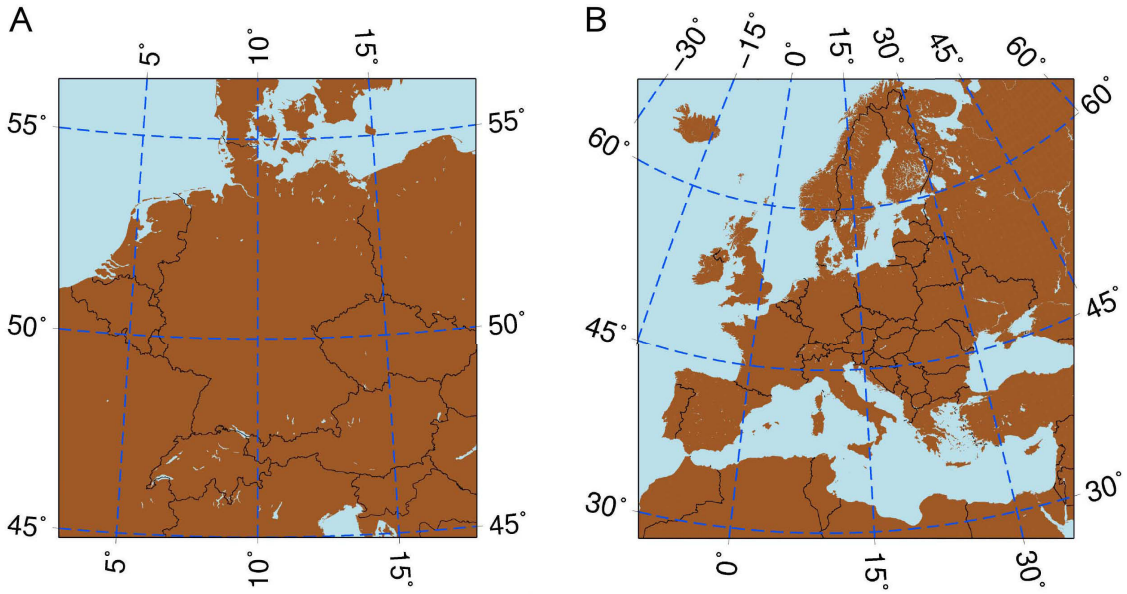

Figure E.2: Model area covered by the COSMO-DE model (Panel A) and the COSMO-EU model (Panel B) according to Table E.1.

For wind information on these vertically high resolved model surfaces, data are computed on an Arakawa-C-Grid that exhibits numerical advantages but requires interpolation since u and v components are not given at coinciding locations (compare Baldauf et al., 2011; Schulz and Schättler, 2009). Wind information on vertical pressure coordinates, that partly have been used also for this work, is already interpolated on the regular COSMO-DE or COSMO-EU grid.

F

Universal Transverse Mercator coordinates

While MAMAP data are geolocated by latitude and longitude information via GPS, it is convenient to transform the horizontal geographical location into a conformal projection that preserves shapes and angles. In this way, distances can be better evaluated and operations on the data, such as rotations, can be conducted easily.

Such a projection is the Universal Transverse Mercator (UTM) projection. The normal Mercator projection, first presented by G. Mercator in 1569 (compare, for example, Snyder, 1987), is a cylindrical projection with the projection cylinder aligned with the Earth's rotational axis and touching Earth at the equator. The projection is conformal, that is, the north-south scale equals the east-west scale and local shapes are conserved. While for the equator areas are truly projected, this leads to large areal distortions (exaggerations) at higher latitudes. Historically important is that sailing routes (with constant angle towards north) are shown as straight lines (loxodrome, rhumb line), but are usually longer than the great circle, which is the shortest possible connection between two points on a sphere (orthodrome). However, the advantage of loxodromes is the avoidance of constant navigational change of course. Loxodromes and orthodromes are equal following a meridian or the equator.

The "simple" latitude-longitude projection, or Plate Carrée projection, which is often used in remote sensing is also a cylindrical projection with strong scale differences in north-south and east-west directions at higher latitudes.

For the transverse Mercator projection, the cylinder is aligned perpendicular to the rotational axis touching the globe at the prime meridian with the advantage of the central meridian being true to scale, and the scale error being a function only of the distance to the central meridian. In its spherical form, the transverse Mercator was introduced by Lambert (1772), while the ellipsoidal form was first explicitly developed by Gauss in 1822 to allow a geodetic measurement of the kingdom of Hannover. However, it was first orderly described and expanded by Krueger (1912).

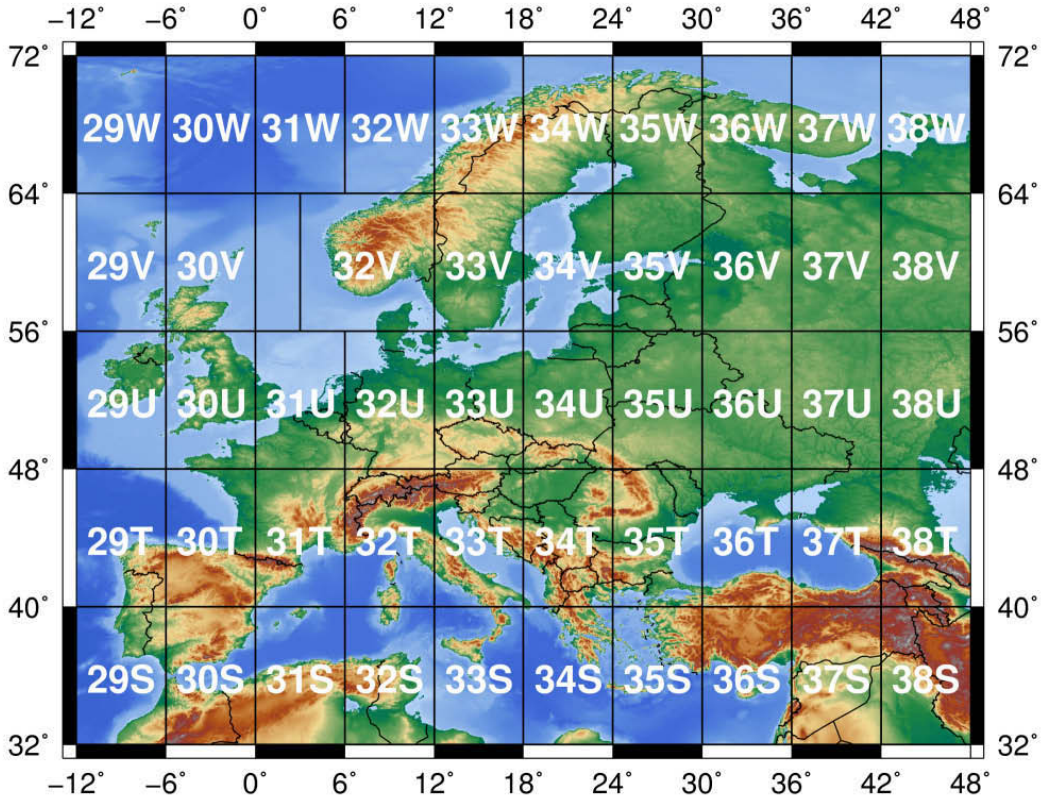

Figure F.1: Grid zone notation for the Universal Transverse Mercator projection over Europe. Most parts of Germany are covered by the 32U and the 33U zone. The zone 32V zone is expanded compared to the regular 6° so that it covers all Norway. This is at the expense of zone 31V which has been shrunk to 3°. (Topography from ETOPO2v2 Global Gridded 2-minute Database, National Geophysical Data Center, National Oceanic and Atmospheric Administration, U.S. Dept. of Commerce, http://www.ngdc.noaa.gov/mgg/global/etopo2.html.)

To avoid the great distortions in the transverse Mercator projections far from the central meridian, the Earth is piecewise projected for the UTM system. The UTM projection has been adopted by the U.S. military in 1947 (Snyder, 1987) and has since been applied by numerous civilian organisations including, for example, the U.S. Geological Survey (USGS) and has recently been implemented by German mapping agencies by adopting the European Terrestrial Reference System (ETRS 89). It divides the globe into zones of 6° latitude and 8° longitude between 80°S and 84°N with few exceptions. Each longitude band has its own central meridian and is designated a number from 1–60 beginning at 180°W. the latitudinal bands are noted by letters from C–X beginning at 80°S but omitting I and O due to potential confusion with numbers 1 and 0. The polar regions are projected separately by Universal Polar Stereographic Projections. The notation of zones for the relevant areas in this work are shown in Figure F.1.

The central meridional scale has been deliberately reduced by a factor of 0.9996 to reduce errors on average for the area. This results in two lines true to scale parallel to the central meridian in about 180 km distance. The maximum scale variations in grid zones at the equator, where distortions are largest, amount to about 0.001 of the true

Table F.1: Several reference ellipsoids and their parameters (Snyder, 1987). The UTM system generally uses the WGS 84 reference ellipsoid where WGS stands for *World Geodetic System*.

Reference ellipsoid	Date	Equatorial radius a [m]	Polar radius b [m]
Bessel	1841	6 377 397.2	6 356 079.0
Clarke	1866	6 378 206.4	6 356 583.8
Krasovsky	1940	6 378 245	6 356 863.0
WGS 72	1972	6 378 135	6 356 750.5
GRS 80	1980	6 378 137	6 356 752.3
WGS 84	1984	6 378 137	6 356 752.3

scale (Snyder, 1987).

The centre of the coordinate system for the projection is the intersection of central meridian and equator. The x-coordinate (easting) and the y-coordinate (northing) have been given offsets to avoid negative numbers (false easting, false northing). For the northern hemisphere: $x_0 = 500\,000\,\text{m}$, $y_0 = 0\,\text{m}$; and for the southern hemisphere $x_0 = 500\,000\,\text{m}$ and $y_0 = 10\,000\,000\,\text{m}$.

The projection formulae are dependent on the reference ellipsoid. For the present work, the WGS 84 datum convention has been applied (see Table F.1). In the following, the series solution equations used for the projection as given in Thomas (1952); Snyder (1987) and Hager et al. (1989) are shown. Note that in this work, only relative distances are of importance so that coordinates in graphs are always given relative to a designated centre point.

Defining fundamental parameters:

φ	latitude (in rad)	(F.1)
λ	longitude (in rad)	(F.2)
a	equatorial radius	(F.3)
b	polar radius	(F.4)
$k_0 = 0.9996$	UTM scale factor	(F.5)
$f = \dfrac{a-b}{a}$	flattening/ellipticity	(F.6)
$e^2 = \dfrac{a^2-b^2}{a^2}$	squared first eccentricity	(F.7)
$e'^2 = \dfrac{a^2-b^2}{b^2}$	squared second eccentricity	(F.8)
$n = \dfrac{a-b}{a+b}$		(F.9)
$\rho = \dfrac{a(1-e^2)}{(1-e^2\sin^2\varphi)^{3/2}}$	radius of curvature of the Earth in the meridian plane	(F.10)

$$\nu = \frac{a}{(1-\mathrm{e}^2\sin^2\varphi)^{1/2}} \quad \text{radius of curvature perpendicular to the meridian plane} \tag{F.11}$$

$$\Delta\lambda = \lambda - \lambda_0 \quad \text{difference of longitude from central meridian } \lambda_0 \tag{F.12}$$

Defining auxiliary parameters for computing the meridional arc S (true meridional distance on the ellipsoid from the equator):

$$A' = a\left(1 - n + \frac{5}{4}\left(n^2 - n^3\right) + \frac{81}{64}\left(n^4 - n^5\right) + \ldots\right) \tag{F.13}$$

$$B' = \frac{3}{2}a\left(n - n^2 + \frac{7}{8}\left(n^3 - n^4\right) + \frac{55}{64}n^5 + \ldots\right) \tag{F.14}$$

$$C' = \frac{15}{16}a\left(n^2 - n^3 + \frac{3}{4}\left(n^4 - n^5\right) + \ldots\right) \tag{F.15}$$

$$D' = \frac{35}{48}a\left(n^3 - n^4 + \frac{11}{16}n^5 + \ldots\right) \tag{F.16}$$

$$E' = \frac{315}{512}a\left(n^4 - n^5 + \ldots\right) \tag{F.17}$$

Then, S can be computed as:

$$S = A'\varphi - B'\sin 2\varphi + C'\sin 4\varphi - D'\sin 6\varphi + E'\sin 8\varphi \tag{F.18}$$

Additional auxiliary parameters:

$$T_1 = Sk_0 \tag{F.19}$$

$$T_2 = \frac{\nu k_0 \sin\varphi\cos\varphi}{2} \tag{F.20}$$

$$T_3 = \frac{\nu k_0 \sin\varphi\cos^3\varphi}{24}\left(5 - \tan^2\varphi + 9e'^2\cos^2\varphi + 4e'^2\cos^4\varphi\right) \tag{F.21}$$

$$\begin{aligned} T_4 = \frac{\nu k_0 \sin\varphi\cos^5\varphi}{720}\big(&61 - 58\tan^2\varphi + \tan^4\varphi + 270e'^2\cos^2\varphi - 330e'^2\tan^2\varphi\cos^2\varphi \\ &+ 445e'^4\cos^4\varphi + 324e'^6\cos^6\varphi - 680e'^4\tan^2\varphi\cos^4\varphi \\ &+ 88e'^8\cos^8\varphi - 600e'^6\tan^2\varphi\cos^6\varphi - 192e'^8\tan^2\varphi\cos^8\varphi\big) \end{aligned} \tag{F.22}$$

$$T_5 = \frac{\nu k_0 \sin\varphi\cos^7\varphi}{40320}\left(1385 - 3111\tan^2\phi + 543\tan^4\varphi - \tan^6\varphi\right) \tag{F.23}$$

$$T_6 = \nu k_0 \cos\varphi \tag{F.24}$$

$$T_7 = \frac{\nu k_0 \cos^3\varphi}{6}\left(1 - \tan^2\varphi + e'^2\cos^2\varphi\right) \tag{F.25}$$

$$\begin{aligned} T_8 = \frac{\nu k_0 \cos^5\varphi}{120}\big(&5 - 18\tan^2\varphi + \tan^4\varphi + 14e'^2\cos^2\varphi - 58e'^2\tan^2\varphi\cos^2\varphi + 13e'^4\cos^4\varphi \\ &+ 4e'^6\cos^6\varphi - 64e'^4\tan^2\varphi\cos^4\varphi - 24e'^6\tan^2\varphi\cos^6\varphi\big) \end{aligned} \tag{F.26}$$

$$T_9 = \frac{\nu k_0 \cos^7\varphi}{5040}\left(61 - 479\tan^2\varphi + 179\tan^4\varphi - \tan^6\varphi\right) \tag{F.27}$$

$$T_{10} = \frac{\tan\varphi'}{2\rho\nu k_0^2} \tag{F.28}$$

$$T_{11} = \frac{\tan\varphi'}{24\rho\nu^3 k_0^4}\left(5 + 3\tan^2\varphi' + e'^2\cos^2\varphi' - 4e'^4\cos^4\varphi' - 9e'^2\tan^2\varphi'\cos^2\varphi'\right) \tag{F.29}$$

$$\begin{aligned} T_{12} = \frac{\tan\varphi'}{720\rho\nu^5 k_0^6}\big(&61 + 90\tan^2\varphi' + 46e'^2\cos^2\varphi' + 45\tan^4\varphi' - 252e'^2\tan^2\varphi'\cos^2 \\ &- 3e'^4\cos^4\varphi' + 100e'^6\cos^6\varphi' - 66e'^4\tan^2\varphi'\cos^4\varphi' \\ &- 90e'^2\tan^4\varphi'\cos^2\varphi' + 88e'^8\cos^8\varphi' + 225e'^4\tan^4\varphi'\cos^4\varphi' \\ &+84e'^6\tan^2\varphi'\cos^6\varphi' - 192e'^8\tan^2\varphi'\cos^8\varphi'\big) \end{aligned} \tag{F.30}$$

$$T_{13} = \frac{\tan\varphi'}{40320\rho\nu^7 k_0^8}\left(1385 + 3633\tan^2\varphi' + 4095\tan^4\varphi' + 1575\tan^6\varphi'\right) \tag{F.31}$$

$$T_{14} = \frac{1}{\nu k_0 \cos\varphi'} \tag{F.32}$$

$$T_{15} = \frac{1}{6\nu^3 k_0^3 \cos\varphi'}\left(1 + 2\tan^2\varphi' + e'^2\cos^2\varphi'\right) \tag{F.33}$$

$$\begin{aligned} T_{16} = \frac{1}{120\nu^5 k_0^5 \cos\varphi'}\big(&5 + 6e'^2\cos^2\varphi' + 28\tan^2\varphi' - 3e'^4\cos^4\varphi' + 8e'^2\tan^2\varphi'\cos^2\varphi' \\ &+24\tan^4\varphi' - 4e'^6\cos^6\varphi' + 4e'^4\tan^2\varphi'\cos^4\varphi' + 24e'^6\tan^2\varphi'\cos^6\varphi'\big) \end{aligned} \tag{F.34}$$

$$T_{17} = \frac{1}{5040\nu^7 k_0^7 \cos\varphi'}\left(61 + 662\tan^2\varphi' + 1320\tan^4\varphi' + 720\tan^6\varphi'\right) \tag{F.35}$$

Geographical to UTM coordinates

The conversion from geographical coordinates (latitude φ, longitude λ) is then given by:

$$x = x_0 + T_1 + \Delta\lambda^2 T_2 + \Delta\lambda^4 T_3 + \Delta\lambda^6 T_4 + \Delta\lambda^8 T_5 \tag{F.36}$$

$$y = y_0 + \Delta\lambda T_6 + \Delta\lambda^3 T_7 + \Delta\lambda^5 T_8 + \Delta\lambda^7 T_9 \tag{F.37}$$

where the easting x is relative to the central meridian λ_0 of the projection.

UTM to geographical coordinates

Instead of an iterative solution that is often found in UTM transformation, here, the backward transformation is accomplished using the rectifying latitude μ to find the

footpoint latitude φ'. Thereby, the rectifying latitude corresponds to the normalised meridional distance requiring a value of $\pi/2$ at the poles and the footpoint latitude corresponds to the meridional distance at ($x = 0$, y):

$$\mu = \frac{M}{1 - \frac{1}{4}e^2 - \frac{3}{64}e^4 - \frac{5}{256}e^6 - \dots} \tag{F.38}$$

where $M = y/k_0$ denotes the meridional arc. The footpoint latitude is then given by (Snyder, 1987):

$$\begin{aligned}\varphi' = \mu &+ \left(\frac{3}{2}n - \frac{27}{32}n^3 + \dots\right)\sin(2\mu) + \left(\frac{21}{16}n^2 - \frac{55}{32}n^4 + \dots\right)\sin(4\mu) \\ &+ \left(\frac{151}{96}n^3 - \dots\right)\sin(6\mu) + \left(\frac{1097}{512}n^4 - \dots\right)\sin(8\mu) + \dots\end{aligned} \tag{F.39}$$

For the conversion from UTM to geographical coordinates this yields:

$$\varphi = \varphi' - (x - x_0)^2 T_{10} + (x - x_0)^4 T_{11} - (x - x_0)^6 T_{12} + (x - x_0)^8 T_{13} \tag{F.40}$$

$$\lambda = \lambda_0 + (x - x_0) T_{14} - (x - x_0)^3 T_{15} - (x - x_0)^5 T_{16} - (x - x_0)^7 T_{17} \tag{F.41}$$

These equations are valid within a specific UTM zone and are accurate to 0.01 m for grid coordinates and to 0.001″ for geographical coordinates (Hager et al., 1989).

Very similar to UTM coordinates are the Gauss-Krüger coordinates that rely on smaller grid cells of 3° width and that can dispense the use of a scaling factor. They were used as standard, for example, in Germany before being replaced by the ETRS 89 with UTM coordinates. The Gauss-Krüger system was used in conjunction with the Bessel Ellipsoid.

G
Error of the wind model

The preferable quantity to evaluate the error of the wind model would be a systematic comparison between measured and model data at the location where wind data are required. However, in case of the COSMO model, such an assessment is not available. An estimation of the error on wind speed and direction has therefore been obtained by using data from the wind profiler radar of the Lindenberg Observatory operated by the German Weather Service (DWD) close to Berlin. Thereby, the accuracy of the measurement can be assumed to be about $\approx 0.4\,\mathrm{m\,s^{-1}}$ for wind speed and about $\approx 5°$ for wind direction (R. Leinweber, DWD, Lindenberg Observatory, personal communication, February 2011).

Figures G.1–G.3 show the result of this comparison as provided by the German Weather Service[1]. Figure G.1 shows the comparison of radar data and the COSMO-DE wind data from the analysis run valid for the day of the power plant overflights on July 26, 2007. The upper panels refer to wind direction and the lower panels to wind speed. From left to right, the panels refer to times 07:00, 08:00, 09:00 and 10:00 UTC. In Figure G.2, the same data are shown as deviation from the observation. Figure G.3 shows the bias (left panels) and root mean square error (right panels) for wind direction (upper panels) and wind speed (lower panels) as mean value for the time from 07:00–10:00 UTC where also the profiler data from the half-hourly data at 07:30, 08:30 and 09:30 is included although not displayed in Figures G.1 and G.2. On the right hand side of each graphic in Figure G.3 is the number of observations for the respective altitude layer. From the lower right graphic, it can be seen that the root mean square error is roughly $0.9\,\mathrm{m\,s^{-1}}$ for the lower atmosphere and is on average almost free of bias (lower left panel). The root mean square error on the wind direction (upper right panel) is about 11° with a bias of −9° (upper left panel). However, the error on wind direction is generally less problematic since wind direction can be deducted from the data directly.

[1] U. Pflüger, German Weather Service (DWD), Offenbach (Verifikation des operationellen Wettervorhersagemodells COSMO DE, Deutscher Wetterdienst, Offenbach, Referat Interpretation und Verifikation, Abteilung Meterorlogische Analyse und Modellierung), personal communication, July 2011.

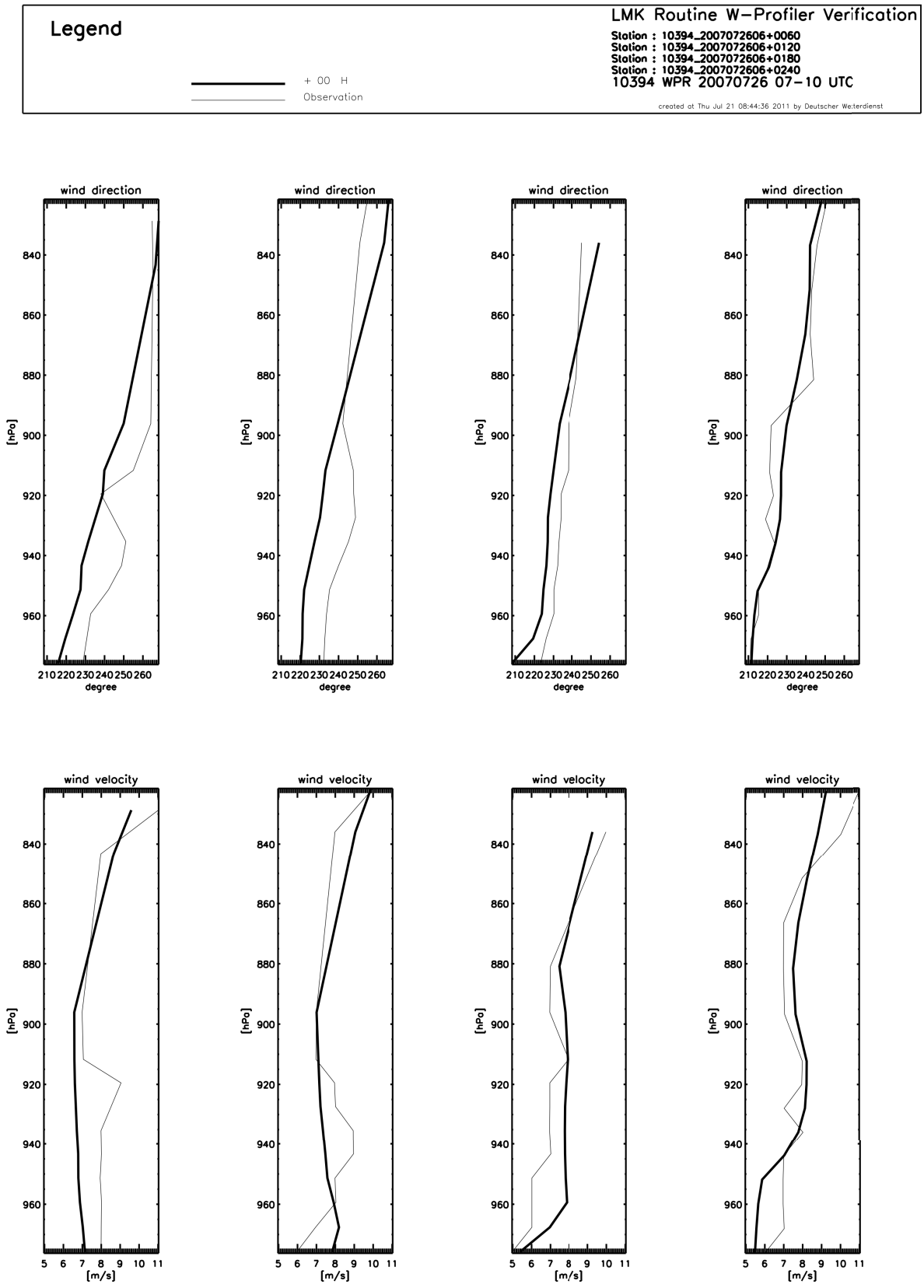

Figure G.1: Comparison between absolute values of wind data from the COSMO-DE analysis model and wind profiler measurements at Lindenberg observatory. See text for description. Figure courtesy of U. Pflüger, German Weather Service (DWD).

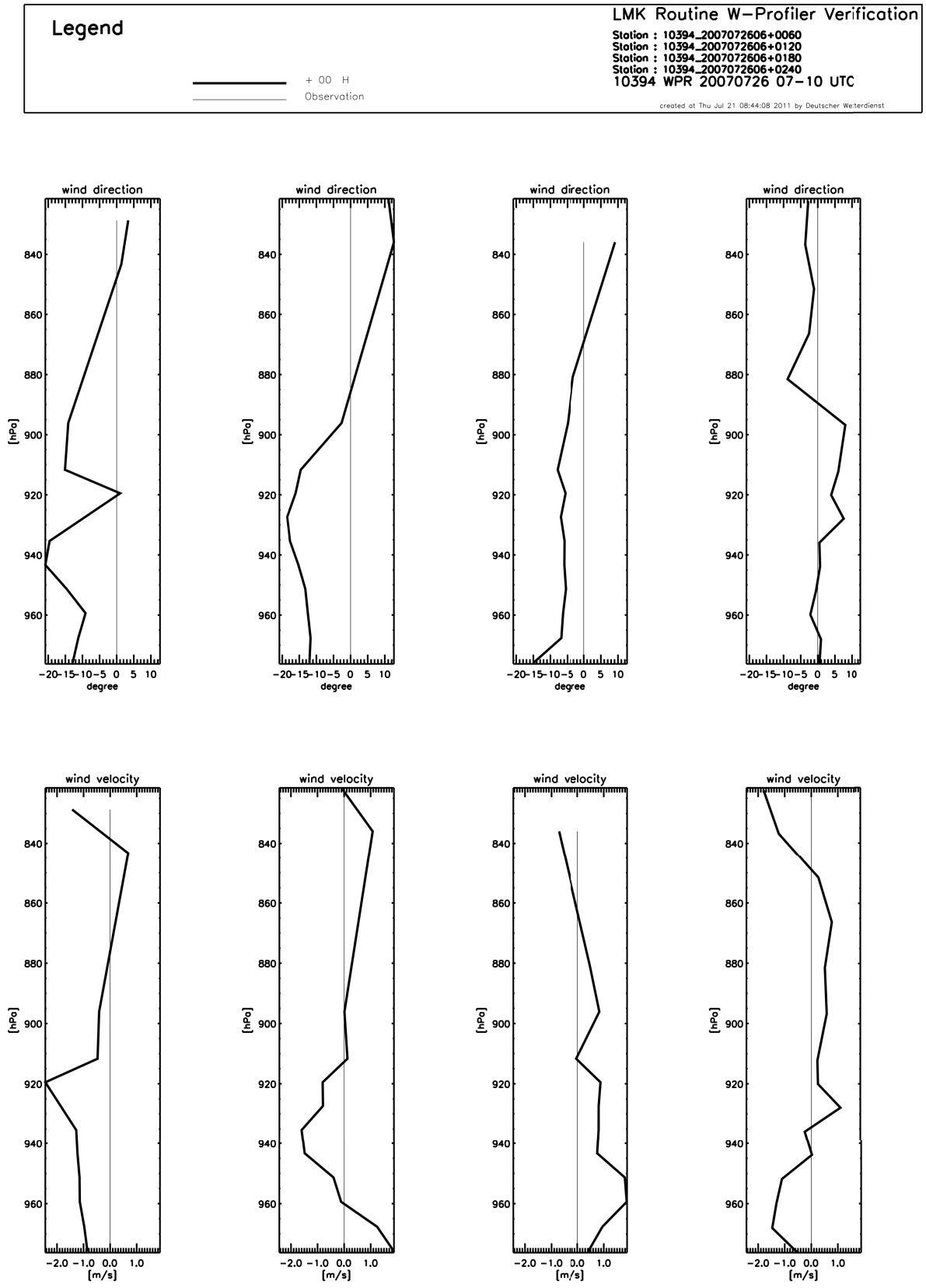

Figure G.2: Deviations of the COSMO-DE analysis model wind information relative to profiler data at Lindenberg observatory. See text for description. Figure courtesy of U. Pflüger, German Weather Service (DWD).

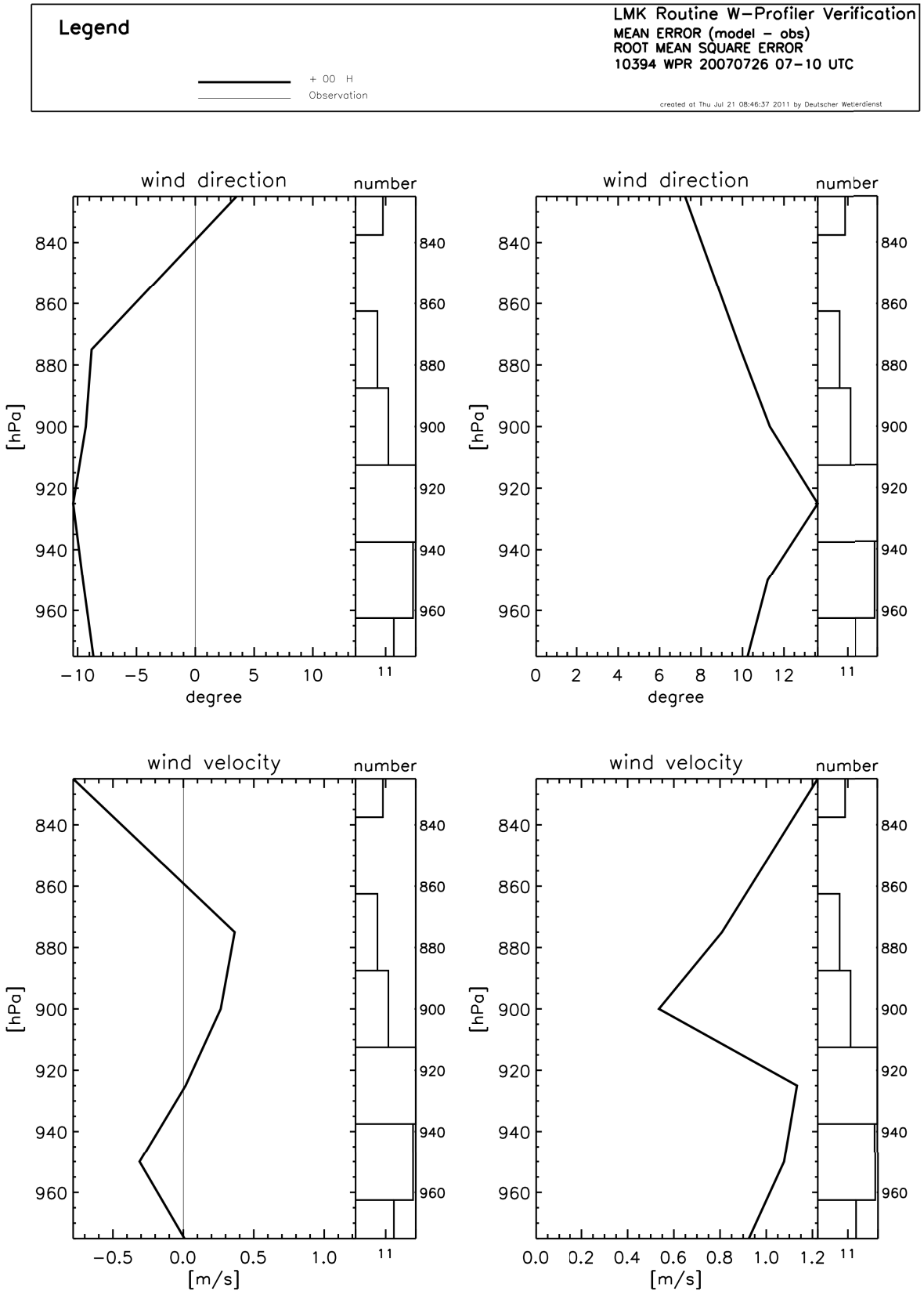

Figure G.3: Mean bias (left panels) and root mean square error (right panels) for the COSMO-DE analysis wind data relative to wind profiler data at Lindenberg observatory for 07:00–10:00 UTC on July 26, 207. See text for description. Figure courtesy of U. Pflüger, German Weather Service (DWD).

H

Methane depletion in power plant flue gas

In the following, a simple estimation is performed for a potential error resulting from removal of background CH_4 amounts from a power plant's flue gas due to oxidation. This is conducted at the example of power plant Jänschwalde.

The modern, lignite fired power plant Boxberg III operated by Vattenfall Europe Generation AG (70 km from Dresden, 50 km from power plant Jänschwalde) produces flue gas of a volume of $6 \cdot 10^6\,\mathrm{m^3\,hr^{-1}}$ (Römer, 1996). Where Boxberg III has two 500 MW units, Jänschwalde has six of them. Assuming the same flue gas volume per unit, Jänschwalde emits roughly:

$$F = 3 \cdot \left(6 \cdot 10^6\,\mathrm{m^3\,hr^{-1}}\right) \tag{H.1}$$

$$= 18 \cdot 10^6\,\mathrm{m^3\,hr^{-1}} \tag{H.2}$$

$$= \ 5000\,\mathrm{m^3\,s^{-1}} \tag{H.3}$$

Taking into account also the amount of water vapour emitted ($600\,\mathrm{t\,hr^{-1}}$ water vapour per tower, D. Heinze, Vattenfall, personal communication, 2008), the total flue gas including water vapour is about:

$$F = 5000\,\mathrm{m^3\,s^{-1}} + \frac{600\,\mathrm{t\,hr^{-1}}}{\rho_{\mathrm{H_2O}}} \tag{H.4}$$

$$\approx 5300\,\mathrm{m^3\,s^{-1}} \tag{H.5}$$

with water vapour density $\rho_{\mathrm{H_2O}} = 0.6\,\mathrm{kg\,m^{-3}}$.

The diameter of the six flue gas emitting stacks is about 50 m. Hence, the volume can be expressed as:

$$F \approx 5300\,\mathrm{m^3\,s^{-1}} \tag{H.6}$$

$$= \underbrace{6 \cdot 50\ \mathrm{m} \cdot 50\ \mathrm{m}}_{\text{volume base area}} \ \cdot \ \underbrace{0.35\ \mathrm{m}}_{\text{volume height}} \ \cdot \mathrm{s^{-1}} \tag{H.7}$$

Assuming a wind speed of $2\,\mathrm{m\,s^{-1}}$, an air parcel passes the stack diameter in about 25 s. The accumulation time, during which the air parcel is loaded with flue gas, is then about 25 s. The same air parcel could pass over more than one stack one after another which would enhance the depletion of CH_4 in the parcel. This depends on wind direction and location of the individual stacks and was not accounted for in this calculation.

Over the corresponding area of $50\,\mathrm{m} \times 50\,\mathrm{m}$, the flue gas plume reaches a height of about:

$$h = 0.35\,\mathrm{m\,s^{-1}} \cdot 25\,\mathrm{s} \tag{H.8}$$
$$\approx 10\,\mathrm{m} \tag{H.9}$$

Assuming now that all CH_4 in the flue gas has been combusted in the power plant as a secondary effect and assuming also that this flue gas air parcel completely replaces the old air, this results in a column of 10 m which does not include any CH_4. With a number n_{air} (Loschmidt constant) of air molecules at standard pressure and temperature of:

$$n_{\mathrm{air}} = 2.7 \cdot 10^{19}\,\mathrm{molecules\,cm^{-3}} \tag{H.10}$$

and a CH_4 background concentration close to the surface of:

$$c = 1.78\,\mathrm{ppm} \tag{H.11}$$

this results in an absolute CH_4 depletion of:

$$\Delta_{\mathrm{CH_4}} = -n_{\mathrm{air}} \cdot c \cdot h \tag{H.12}$$
$$\approx -0.48 \cdot 10^{17}\,\mathrm{molecules\,cm^{-2}} \tag{H.13}$$

Taking into account the total column of CH_4 molecules of $N_{\mathrm{CH_4}} = 3.67 \cdot 10^{19}\,\mathrm{molecules\,cm^{-2}}$, this is equivalent to a relative change of:

$$\Delta_{\%,\mathrm{CH_4}} = -\frac{n_{air} \cdot c \cdot h}{N_{\mathrm{CH_4}}} \tag{H.14}$$
$$\approx -\frac{0.48 \cdot 10^{17}\ \mathrm{molecules\,cm^{-2}}}{3.67 \cdot 10^{19}\ \mathrm{molecules\,cm^{-2}}} \tag{H.15}$$
$$\approx -0.13\,\% \tag{H.16}$$

This is the approximate worst case scenario for MAMAP (ground scene about $29\,\mathrm{m} \times 33\,\mathrm{m}$) in close vicinity to the power plant. For a bigger ground scene than MAMAP exhibits, for example, for a possible CarbonSat ground scene of $2\,\mathrm{km} \times 2\,\mathrm{km}$, the effect is smaller because not the whole ground scene area will be covered by the flue gas.

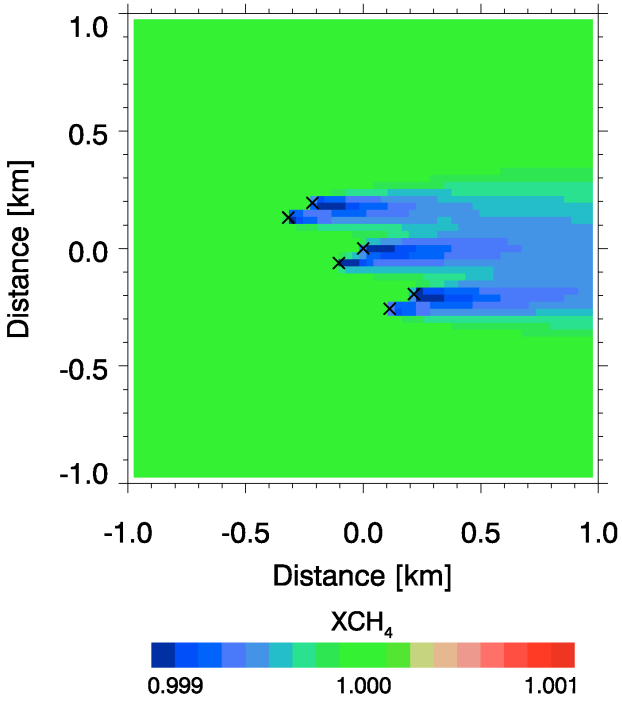

Figure H.1: Depletion of CH_4 in the Jänschwalde flue gas plume computed for an approximate MAMAP ground scene of 30 m × 30 m, a slightly unstable atmosphere and a wind speed of 2 m s^{-1}. The crosses indicate flue gas and water vapour emitting stacks.

Alternative description via Gaussian plume model

An estimate of the depletion of CH_4 can also be obtained by calculating the "negative CH_4 emission rate", corresponding to the missing CH_4 in the released flue gas:

$$F'_{CH_4} = -F \cdot n_{air} \cdot c \cdot \frac{1}{N_A} \cdot M \tag{H.17}$$

$$= -5300\ \mathrm{m^3\,s^{-1}} \cdot 2.7 \cdot 10^{19}\ \mathrm{molecules\,cm^{-3}} \cdot 1.78\ \mathrm{ppm} \cdot \frac{1}{6.022 \cdot 10^{23}\ \mathrm{mol^{-1}}} \cdot 16\ \mathrm{g\,mol^{-1}} \tag{H.18}$$

$$= -6.8\ \mathrm{g\,s^{-1}} \tag{H.19}$$

where $M = 16\,\mathrm{g\,mol^{-1}}$ is the molar mass of CH_4 and $N_A = 6.022 \cdot 10^{19}\,\mathrm{mol^{-1}}$ Avogadro's constant. This emission rate can be used as input for a Gaussian plume model (see Section 7.1) showing the spatial distribution CH_4 depletion for stationary conditions (see Figures H.1 and H.2). The maximum depletion is about −0.14 % for a 30 m × 30 m ground scene and hence somewhat larger than the first estimate since plumes of different stacks overlap. For a 2 km × 2 km ground scene, the maximum depletion is about −0.017 %.

Implications

Possible implications for the interpretation of $XCO_2(CH_4)$ based on the ratio CO_2/CH_4 are addressed in the following. Assuming the worst case CH_4 depletion of −0.14 % and

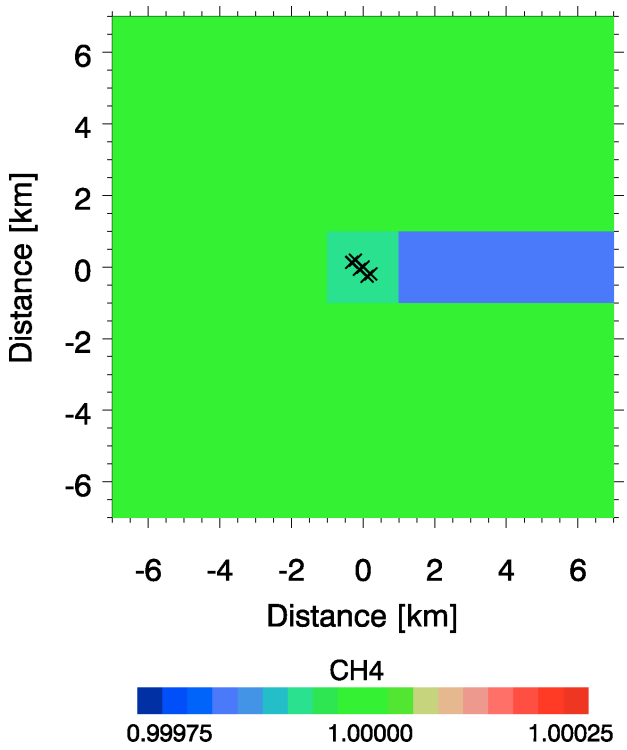

Figure H.2: As Figure H.1 but for a potential satellite ground scene of 2 km × 2 km, a slightly unstable atmosphere and a wind speed of 2 m s^{-1}.

ignoring any other CH_4 variations or additional errors as well as the altitude sensitivity effect, this would result in a spurious relative CO_2 increase of:

$$\frac{V_{CO_2} \,/\, \overline{V_{CO_2}}}{V_{CH_4} \,/\, \overline{V_{CH_4}}} = \frac{V_{CO_2}}{\overline{V_{CH_4}} \cdot (1 - 0.0014)} \cdot \frac{\overline{V_{CH_4}}}{\overline{V_{CO_2}}} \tag{H.20}$$

$$\approx 1.0014 \cdot \frac{V_{CO_2}}{\overline{V_{CO_2}}} \tag{H.21}$$

$$= (1 + \Delta^{\text{error}}_{\%,CO_2}) \frac{V_{CO_2}}{\overline{V_{CO_2}}} \tag{H.22}$$

$$\Rightarrow \Delta^{\text{error}}_{\%,CO_2} = 0.14\,\% \tag{H.23}$$

Where V denotes measured vertical columns of CO_2 or CH_4 and $\overline{V}$ the total background column. $\Delta^{\text{error}}_{CO_2} = 0.14\,\%$ is the spurious increase in CO_2 relative to background due to CH_4 depletion. This value is rather small compared to the expected true CO_2 increase over such a power plant. Hence, the relative error on the measured CO_2 increase can be neglected, in particular, when taking into account that not all background CH_4 will be removed in the combustion process.

Preliminary fit results for the near infrared channel

MAMAP's near infrared channel was not the focus of this work, but the described WFM-DOAS retrieval algorithm (see Section 5) can also be applied to retrieval of oxygen from the O_2-A band. Figure I.1 shows a preliminary O_2-A fit result using data from the near infrared channel recorded on 26 July 2007, during the power plant overflight analysed in Section 8. The calibration of the wavelength axis is only preliminary and needs to be revised for a routine O_2 retrieval.

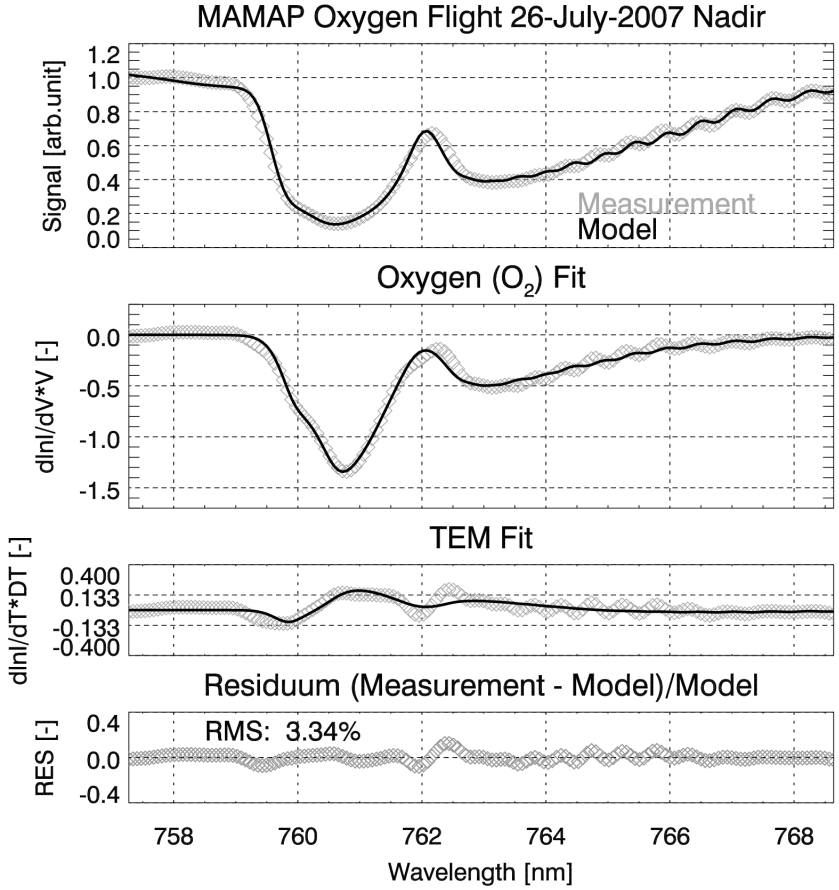

Figure I.1: Example fits of the MAMAP WFM-DOAS algorithm applied to a single O_2 spectrum using a preliminary wavelength calibration. Data were obtained on 26 July 2007, during the power plant overflight treated in Section 8. The top panel shows a MAMAP nadir spectrum (grey symbols) and the solid line the fitted, linearised radiative transfer model. The bottom panel shows the fit residuum which is the difference between measurement and simulation after the fit (the root-mean-square (RMS) of the fit residuum (RES) is 3.34 %). The second panel shows details of the O_2 fit. The solid line is the scaled derivative of the radiance with respect to a change of the oxygen vertical column. The grey symbols show the O_2 fit residuum which is identical with the black curve except that the spectral fit residuum has been added.

Bibliography

Ackerman, K. V. and Sundquist, E. T.: Comparison of Two U.S. Power-Plant Carbon Dioxide Emissions Data Sets, Environ. Sci. Technol., 42, 5688–5693, doi:10.1021/es800221q, 2008.

Albert, S., Bauerecker, S., Boudon, V., Brown, L. R., Champion, J., Loëte, M., Nikitin, A., and Quack, M.: Global analysis of the high resolution infrared spectrum of methane $^{12}CH_4$ in the region from 0 to 4800 cm^{-1}, Chem. Phys., 356, 131–146, doi:10.1016/j.chemphys.2008.10.019, 2009.

Amat, G. and Pimbert, M.: On Fermi Resonance in Carbon Dioxide, J. Mol. Spectrosc., 16, 278–290, doi:10.1016/0022-2852(65)90123-2, 1965.

Andres, R. J., Boden, T. A., Bréon, F.-M., Ciais, P., Davis, S., Erickson, D., Gregg, J. S., Jacobson, A., Marland, G., Miller, J., Oda, T., Olivier, J. G. J., Raupach, M. R., Rayner, P., and Treanton, K.: A synthesis of carbon dioxide emissions from fossil-fuel combustion, Biogeosciences Discuss., 9, 1299–1376, doi:10.5194/bgd-9-1299-2012, 2012.

Ångström, A.: On the Atmospheric Transmission of Sun Radiation and on Dust in the Air, Geogr. Ann., 11, 156–166, 1929.

Arrhenius, S.: XXXI. On the influence of carbonic acid in the air upon the temperature of the ground, Philosophical Magazine Series 5, 41, 237–276, doi:10.1080/14786449608620846, 1896.

Arrhenius, S.: Die vermutliche Ursache der Klimaschwankungen, Meddelanden från K. Svenska Betenskapsakademiens Nobelinstitut, 1, 1–10, 1906.

Australian Government: Department of Climate Change and Energy Efficiency, Australian National Greenhouse Accounts, National Inventory Report 2009, Volume 1, The Australian Government Submission to the UN Framework Convenction on Climate Change, April 2011, 304 pp., 2011.

Aydin, M., Verhulst, K. R., Saltzman, E. S., Battle, M. O., Montzka, S. A., Blake, D. R., Tang, Q., and Prather, M. J.: Recent decreases in fossil-fuel emissions of ethane and methane derived from firn air, Nature, 476, 198–201, doi:10.1038/nature10352, 2011.

Babcock, H. D. and Herzberg, L.: Fine Structure of the Red System of Atmospheric Oxygen Bands, Astrophys. J., 108, 167–190, doi:10.1086/145062, 1948.

Babilotte, A., Lagier, T., Fiani, E., and Taramini, V.: Fugitive Methane Emissions from Landfills: Field Comparison of Five Methods on a French Landfill, Journal of Environmental Engineering, 136, 777–784, doi:10.1061/(ASCE)EE.1943-7870.0000260, 2010.

Baldauf, M., Förstner, J., Klink, S., Reinhardt, T., Schraff, C., Seifert, A., and Stephan, K.: Kurze Beschreibung des Lokal-Modells Kürzestfrist COSMO-DE (LMK) und seiner Datenbanken, Technical Report, Deutscher Wetterdienst, Geschäftsbereich Forschung und Entwicklung, 80 pp., 2011.

Banwell, C. N.: Fundamentals of Molecular Spectroscopy, 339 pp., McGRAW-HILL Book Company Europe, Maidenhead, Berkshire, England, 3rd edn., 1983.

Barkley, M. P., Monks, P. S., Frieß, U., Mittermeier, R. L., Fast, H., Körner, S., and Heimann, M.: Comparisons between SCIAMACHY atmospheric CO_2 retrieved using (FSI) WFM-DOAS to ground based FTIR data and the TM3 chemistry transport model, Atmos. Chem. Phys., 6, 4483–4498, doi:10.5194/acp-6-4483-2006, 2006.

Bergamaschi, P., Krol, M., Dentener, F., Vermeulen, A., Meinhardt, F., Graul, R., Ramonet, M., Peters, W., and Dlugokencky, E. J.: Inverse modelling of national and European CH_4 emissions using the atmospheric zoom model TM5, Atmos. Chem. Phys., 5, 2431–2460, doi:10.5194/acp-5-2431-2005, 2005.

Bergamaschi, P., Frankenberg, C., Meirink, J. F., Krol, M., Dentener, F., Wagner, T., Platt, U., Kaplan, J. O., Körner, S., Heimann, M., Dlugokencky, E. J., and Goede, A.: Satellite chartography of atmospheric methane from SCIAMACHY on board ENVISAT: 2. Evaluation based on inverse model simulations, Journal of Geophysical Research, 112, 501–511, doi:10.1029/2006JD007268, 2007.

Bergamaschi, P., Frankenberg, C., Meirink, J. F., Krol, M., Villani, M. G., Houweling, S., Dentener, F., Dlugokencky, E. J., Miller, J. B., Gatti, L. V., Engel, A., and Levin, I.: Inverse modelling of global and regional CH_4 emissions using SCIAMACHY satellite retrievals, J. Geophys. Res., 114, D22 301, doi:10.1029/2009JD012287, 2009.

Berk, A., Anderson, G. P., Acharya, P. K., Chetwynd, J. H., Bernstein, L. S., Shettle, E. P., Matthew, M. W., and Adler-Golden, S. M.: MODTRAN USER's MANUAL, 98 pp., Air Force Research Laboratory, Space Vehicles Directorate, Hanscom AFB, MA 01731-3010, U.S.A., 1999, Last revised 17 April, 2000.

Bertagnolio, P. P.: Mapping of Tropospheric Greenhouse Gases using Airborne Near-Infrared/Shortwave-Infrared Spectroscopy, Master Thesis, 119 p., Postgraduate Programme Environmental Physics (PEP), Institute of Environmental Physics (IUP), University of Bremen, Germany, 2008.

Beswick, K. M., Gallagher, M. W., Webb, A. R., Norton, E. G., and Perry, E.: Application of the Aventech AIMMS20AQ airborne probe for turbulence measurements during the Convective Storm Initiation Project, Atmos. Chem. Phys., 8, 5449–5463, doi:1doi:10.5194/acp-8-5449-2008, 2008.

Beychok, M. R.: Fundamentals of Stack Gas Dispersion, Milton R. Beychok, 4th edn., 2005.

Bischof, W., Fabian, P., and Borchers, R.: Decrease in CO_2 mixing ratio observed in the stratosphere, Nature, 288, 347–348, doi:10.1038/288347a0, 1980.

Börjesson, G., Danielsson, Å., and Svennson, B. H.: Methane Fluxes from a Swedish Landfill Determined by Geostatistical Treatment of Static Chamber Measurements, Environ. Sci. Technol., 34, 4044–4050, 2000.

Boudon, V., Rey, M., and Loëte, M.: The vibrational levels of methane obtained from analyses of high-resolution spectra, J. Quant. Spectrosc. Radiat. Transfer, 98, 394–404, doi:10.1016/j.jqsrt.2005.06.003, 2006.

Bousquet, P., Ciais, P., Miller, J. B., Dlugokencky, E. J., Hauglustaine, D. A., Prigent, C., Van der Werf, G. R., Peylin, P., Brunke, E.-G., Carouge, C., Langenfelds, R. L., Lathière, J., Papa, F., Ramonet, M., Schmidt, M., Steele, L. P., Tyler, S. C., and White, J.: Contribution of anthropogenic and natural sources to atmospheric methane variability, Nature, 443, 25–27, doi:10.1038/nature05132, 2006.

Bovensmann, H., Burrows, J. P., Buchwitz, M., Frerick, J., Noël, S., and Rozanov, V. V.: SCIAMACHY: Mission Objectives and Measurement Modes, J. Atmos. Sci., 56, 127–150, 1999.

Bovensmann, H., Buchwitz, M., Burrows, J. P., Reuter, M., Krings, T., Gerilowski, K., Schneising, O., Heymann, J., Tretner, A., and Erzinger, J.: A remote sensing technique for global monitoring of power plant CO_2 emissions from space and related applications, Atmos. Meas. Tech., 3, 781–811, doi:10.5194/amt-3-781-2010, 2010.

Bradley, E. S., Leifer, I., Roberts, D. A., Dennison, P. E., and Washburn, L.: Detection of marine methane emissions with AVIRIS band ratios, Geophys. Res. Lett., 38, L10 702, doi:10.1029/2011GL046729, 2011.

Brasseur, G. P. and Solomon, S.: Aeronomy of the Middle Atmosphere – Chemistry and Physics of the Stratosphere and Mesosphere, Springer, P.O. Box 17, 3300 AA Dordrecht, The Netherlands, 3rd edn., 2005.

Bréon, F.-M. and Ciais, P.: Spaceborne remote sensing of greenhouse gas concentrations, Comptes Rendus Geoscience, 342, 412–424, doi:10.1016/j.crte.2009.09.012, 2010.

Buchwitz, M.: Strahlungstransport- und Inversions-Algorithmen zur Ableitung atmosphärischer Spurengasinformationen aus Erdfernerkundungsmessungen in Nadirgeometrie im ultravioletten bis nahinfraroten Spektralbereich am Beispiel SCIAMACHY, PhD thesis, Berichte aus dem Institut für Umweltphysik, Volume 4, Logos-Verlag, Berlin, 2000.

Buchwitz, M., Rozanov, V. V., and Burrows, J. P.: A near-infrared optimized DOAS method for the fast global retrieval of atmospheric CH_4, CO, CO_2, H_2O, and N_2O total column amounts from SCIAMACHY Envisat-1 nadir radiances, J. Geophys. Res., 105, 15 231–15 245, 2000.

Buchwitz, M., de Beek, R., Burrows, J. P., Bovensmann, H., Warneke, T., Notholt, J., Meirink, J. F., Goede, A. P. H., Bergamaschi, P., Körner, S., Heimann, M., and Schulz, A.: Atmospheric methane and carbon dioxide from SCIAMACHY satellite data: initial comparison with chemistry and transport models, Atmos. Chem. Phys., 5, 941–962, doi:10.5194/acp-5-941-2005, 2005a.

Buchwitz, M., de Beek, R., Noël, S., Burrows, J. P., Bovensmann, H., Bremer, H., Bergamaschi, P., Körner, S., and Heimann, M.: Carbon monoxide, methane and carbon dioxide columns retrieved from SCIAMACHY by WFM-DOAS: year 2003 initial data set, Atmos. Chem. Phys., 5, 3313–3329, doi:10.5194/acp-5-3313-2005, 2005b.

Burrows, J. P., Hölzle, E., Goede, A. P. H., Visser, H., and Fricke, W.: SCIAMACHY–Scanning Imaging Absorption Spectrometer for Atmospheric Chartography, Acta Astronautica, 35, 445–451, 1995.

Chambers, A. and Strosher, M.: DIAL Measurements of Fugitive Emissions from Natural Gas Plants and the Comparison with Emission Factor Estimates, 15th Annual Emission Inventory Conference, US Environmental Protection Agency New Orleans, May 15-18, 2006a.

Chambers, A. and Strosher, M.: Refinery Demonstration of Optical Technologies for Measurement of Fugitive Emissions and for Leak Detection, Final Report, Environment Canada, Ontario Ministry of the Environment and Alberta Environment, 2006b.

Charpentier, A. D., Bergerson, J. A., and MacLean, H. L.: Understanding the Canadian oil sands industry's greenhouse gas emissions, Environ. Res. Lett, 4, 014 005 (11pp.), doi:10.1088/1748-9326/4/1/014005, 2009.

Chédin, A., Serrar, S., Scott, N. A., Crevoisier, C., and Armante, R.: First global measurement of midstropospheric CO_2 from NOAA polar satellites: Tropical zone, J. Geophys. Res., 108(D18), 4581, doi:10.1029/2003JD003439, 2003.

CMP: The Conference of the Parties serving as the meeting of the Parties to the Kyoto Protocol, Draft decision -/CMP.7, Outcome of the work of the Ad Hoc Working Group on Further Commitments for Annex I Parties under the Kyoto Protocol at its sixteenth session, 9 pp., 2011.

COP: The Conference of the Parties, Draft decision -/CP.17, Establishment of an Ad Hoc Working Group on the Durban Platform for Enhanced Action, Proposal by the President, 2 pp., 2011.

Cormier, J. G., Hodges, J. T., and Drummond, J. R.: Infrared water vapor continuum absorption at atmospheric temperatures, J. Chem. Phys., 122, 114 309, doi:10.1063/1.1862623, 2005.

Craig, H.: The Natural Distribution of Radiocarbon and the Exchange Time of Carbon Dioxide Between Atmosphere and Sea, Tellus, 9, 1–17, doi:10.1111/j.2153-3490.1957.tb01848.x, 1957.

Crevoisier, C., Chedin, A., and Scott, N. A.: AIRS channel selection for CO_2 and other trace-gas retrievals, Q. J. R. Meteorol. Soc., 129, 2719–2740, doi:10.1256/qj.02.180, 2003.

Crevoisier, C., Nobileau, D., Fiore, A. M., Armante, R., Chédin, A., and Scott, N. A.: Tropospheric methane in the tropics - first year from IASI hyperspectral infrared observations, Atmos. Chem. Phys., 9, 6337–6350, doi:10.5194/acp-9-6337-2009, 2009.

Crisp, D., Atlas, R. M., Breon, F.-M., Brown, L. R., Burrows, J. P., Ciais, P., Connor, B. J., Doney, S. C., Fung, I. Y., Jacob, D. J., Miller, C. E., O'Brien, D., Pawson, S., Randerson, J. T., Rayner, P., Salawitch, R. J., Sander, S. P., Sen, B., Stephens, G. L., Tans, P. P., Toon, G. C., Wennberg, P. O., Wofsy, S. C., Yung, Y. L., Kuang, Z., Chudasama, B., Sprague, G., Weiss, B., Pollock, R., Kenyon, D., and Schroll, S.: The Orbiting Carbon Observatory (OCO) mission, Adv. Space Res., 34, 700–709, doi:10.1016/j.asr.2003.08.062, 2004.

Crisp, D., Miller, C., Bréon, F., Boesch, H., Braverman, A., Brown, L., Bruegge, C., Burrows, J., Chevallier, F., Ciais, P., Connor, B., Doney, S., Engelen, R., Fung, I., Griffith, D., Jacob, D., Michalak, A., Natraj, V., Notholt, J., O'Brien, D., O'Dell, C., Palmer, P., Pawson, S., Pollock, R., Polonsky, I., Randerson, J., Rayner, P., Rogers, M., Salawitch, R., Sander, S., Stephens, G., Tans, P., Toon, G., Wennberg, P., Wofsy, S., Wunch, D., and Yung, Y.: The Need for Atmospheric Carbon Dioxide Measurements from Space: Contributions from a Rapid Reflight of the Orbiting Carbon Observatory, 54 pp., http://www.nasa.gov/pdf/363474main_OCO_Reflight.pdf, last access: October, 2012, 2009.

Davies, J. H. and Davies, D. R.: Earth's surface heat flux, Solid Earth, 1, 5–24, doi:10.5194/se-1-5-2010, 2010.

Denman, K. L., Brasseur, G., Chidthaisong, A., Ciais, P., Cox, P. M., Dickinson, R. E., Haglustaine, D., Heinze, C., Holland, E., Jacob, D., Lohmann, U., Ramachandran, S., da Silva Dias, P. L., Wofsy, S. C., and Zhang, X.: Couplings Between Changes in the Climate System and Biogeochemistry. In: *Climate Change 2007: The Physical Science Basis. Contribution of Working Group I to the Fourth Assessment Report of the Intergovernmental Panel on Climate Change* [Solomon, S., D. Qin, M. Manning, Z. Chen, M. Marquis, K.B. Averyt, M.Tignor and H.L. Miller (eds.)], Cambridge University Press, Cambridge, United Kingdom and New York, NY, USA, 2007.

Deru, M. and Torcellini, P.: Source Energy and Emission Factors for Energy Use in Buildings, Technical Report NREL/TP-550-38617, National Renewable Energy Laboratory, Midwest Research Institute, Battelle, 2006, revised 2007.

Deutscher Bundestag – 17. Wahlperiode: Erdgas-Blowout vor der Küste Schottlands, Drucksache 17/4342, 2010.

Deutscher Bundestag: Gesetz zur Umsetzung der Richtlinie 2003/87/EG über ein System für den Handel mit Treibhausgasemissionszertifikaten in der Gemeinschaft, Artikel 1, Gesetz über den Handel mit Berechtigungen zur Emission von Treibhausgasen (Treibhausgas-Emissionshandelsgesetz – TEHG), Bundesgesetzblatt, Jahrgang 2004 Teil I, 1578–1590, 2004.

Dlugokencky, E. J., Steele, L. P., Lang, P. M., and Masarie, K. A.: The growth rate and distribution of atmospheric methane, J. Geophys. Res., 99, 17 021–17 043, doi:10.1029/94JD01245, 1994.

Dlugokencky, E. J., Bruhwiler, L., White, J. W. C., Emmons, L. K., Novelli, P. C., Montzka, S. A., Masarie, K. A., Lang, P. M., Crotwell, A. M., Miller, J. B., and Gatti, L. V.: Observational constraints on recent increases in the atmospheric CH_4 burden, Geophys. Res. Lett., 36, L18 803, doi:10.1029/2009GL039780, 2009.

Doms, G.: A Description of the Nonhydrostatic Regional COSMO-Model, Deutscher Wetterdienst, Technical Report (http://www.cosmo-model.org/), last access: October 2012, 2011.

Dones, R., Bauer, C., and Röder, A.: Kohle. In: *Sachbilanzen von Energiesystemen: Grundlagen für den ökologischen Vergleich von Energiesystemen und den Einbezug von Energiesystemen in Ökobilanzen für die Schweiz. Final report ecoinvent No. 6-VI* [Dones, R. (Ed.) et al.], Paul Scherrer Institut Villigen, Swiss Centre for Life Cycle Inventories, Dübendorf, CH, 2007.

Ellerman, A. D. and Buchner, B. K.: The European Union Emissions trading Scheme: Origins, Allocations, and Early Results, Review of Environmental Economics and Policy, 1, 66–87, doi:10.1093/reep/rem003, 2007.

Elsner, J. B., Trepanier, J. C., Strazzo, S. E., and Jagger, T.: Sensitivity of limiting hurricane intensity to ocean warmth, *in press*, Geophys. Res. Lett., doi:10.1029/2012GL053002, 2012.

EnergieAgentur.NRW: Grubengas. Ein Energieträger in Nordrhein-Westfalen. Ministerium für Wirtschaft, Mittelstand und Energie des Landes Nordrhein-Westfalen, 36 pp., 1, 2009.

Environment Canada: National Inventory Report 1990–2009: Greenhouse Gas Sources and Sinks in Canada, The Canadians Government's Submission to the UN Framework Convention on Climate Change, Part 1, 224 pp., 2011.

Ershov, O.: Pergam-Suisse ALMA System Inspection of pipelines from helicopter in the North part of Italy–Report, Pergam-Suisse AG Talacker 42 Zürich 8001, Switzerland, 2007.

Etiope, G.: Natural emissions of methane from geological seepage in Europe, Atmospheric Environment, 43, 1430–1443, doi:10.1016/j.atmosenv.2008.03.014, 2009.

European Commission: Decision 2002/358/CE, concerning the approval, on behalf of the European Community, of the Kyoto Protocol to the United Nations Framework Convention on Climate Change and the joint fulfilment of commitments thereunder, Official Journal of the European Union, L 130, 1–3, 2002.

European Commission: Decision 2007/589/EC, establishing guidelines for the monitoring and reporting of greenhouse gas emissions pursuant to Directive 2003/87/EC of the European Parliament and of the Council, Official Journal of the European Union, L 229, 1–85, 2007.

European Commission: Decision 2011/638/EU, on benchmarks to allocate greenhouse gas emission allowances free of charge to aircraft operators pursuant to Article 3e of Directive 2003/87/EC of the European Parliament and of the Council, Official Journal of the European Union, L 252, 20–21, 2011a.

European Commission: Decision 2011/278/EU, determining transitional Union-wide rules for harmonised free allocation of emission allowances pursuant to Article 10a of Directive 2003/87/EC of the European Parliament and of the Council, Official Journal of the European Union, L 130, 1–45, 2011b.

European Parliament and Council of the European Union: Directive 2003/87/EC, establishing a scheme for greenhouse gas emission allowance trading within the Community and amending Council Directive 96/61/EC, Official Journal of the European Union, L 275, 32–46, 2003.

European Parliament and Council of the European Union: Directive 2009/29/EC amending Directive 2003/87/EC so as to improve and extend the greenhouse gas emission allowance trading scheme of the Community, Official Journal of the European Union, L 140/63, 1–25, 2009.

Evans, S., Deery, S., and Bionda, J.: How Reliable are GHG Combustion Calculations and Emission Factors, Presented at the CEM 2009 Conference, September 23-25, Milan, Itlay, 2009.

Foken, T.: Angewandte Meteorologie, Mirkometeorologische Methoden, 325 pp., Springer-Verlag, Berlin, Heidelberg, New York, 2nd edn., 2006.

Forster, P., Ramaswamy, V., Artaxo, P., Berntsen, T., Betts, R., Fahey, D. W., Haywood, J., Lean, J., Lowe, D. C., Myhre, G., Nganga, J., Prinn, R., Raga, G., Schulz, M., and Dorland, R. V.: Changes in Atmospheric Constituents and in Radiative Forcing. In: *Climate Change 2007: The Physical Science Basis. Contribution of Working Group I to the Fourth Assessment Report of the Intergovernmental Panel on Climate Change* [Solomon, S., D. Qin, M. Manning, Z. Chen, M. Marquis, K.B. Averyt, M.Tignor and H.L. Miller (eds.)], Cambridge University Press, Cambridge, United Kingdom and New York, NY, USA, 2007.

Frankenberg, C., Meirink, J. F., van Weele, M., Platt, U., and Wagner, T.: Assessing Methane Emissions from Global Space-Borne Observations, Science, 308, 1010–1014, doi:10.1126/science.1106644, 2005a.

Frankenberg, C., Platt, U., and Wagner, T.: Iterative maximum a posteriori (IMAP)-DOAS for retrieval of strongly absorbinb trace gases: Model studies for CH_4 and CO_2 retrieval from near infrared spectra of SCIAMACHY onboard ENVISAT, Atmos. Chem. Phys., 5, 9–22, doi:10.5194/acp-5-9-2005, 2005b.

Frankenberg, C., Warneke, T., Butz, A., Aben, I., Hase, F., Spietz, P., and Brown, L. R.: Pressure broadening in the $2\nu_3$ band of methane and its implication on atmospheric retrievals, Atmos. Chem. Phys., 8, 5061–5075, doi:10.5194/acp-8-5061-2008, 2008.

Fu, Q., Hu, Y., and Yang, Q.: Identifying the top of the tropical tropopause layer from vertical mass flux analysis and CALIPSO lidar cloud observations, Geophys. Res. Lett., 34, L14 813, doi:10.1029/2007GL030099, 2007.

Gaft, M., Reisfeld, R., and Panczer, G.: Modern Luminescence Spectroscopy of Minerals and Materials, 368 pp., Springer-Verlag, Berlin, Heidelberg, 2005.

Geibel, M.: Measurement of climate-relevant trace gases via infrared spectroscopy, Technical Reports 23, 247 pp., Max-Planck-Institut für Biogeochemie, Jena, Germany, 2011.

Geibel, M. C., Gerbig, C., and Feist, D. G.: A new fully automated FTIR system for total column measurements of greenhouse gases, Atmos. Meas. Tech., 3, 1363–1375, doi:10.5194/amt-3-1363-2010, 2010.

Gerilowski, K., Tretner, A., Krings, T., Buchwitz, M., Bertagnolio, P. P., Belemezov, F., Erzinger, J., Burrows, J. P., and Bovensmann, H.: MAMAP – a new spectrometer system for column-averaged methane and carbon dioxide observations from aircraft: Instrument description and performance analysis, Atmos. Meas. Tech., 4, 215–243, doi:10.5194/amt-4-215-2011, 2011.

Gerilowski, K., Krings, T., and Bovensmann, H.: Qualitative methane flux upper limit constraints from airborne remote sensing data acquired over the 22/4B emission site, Final Report, IFE-FR-KGTKHB-24052012-BO_EXXON_R2.0, University of Bremen, 26. pp, 2012.

Gettelman, A., Salby, M. L., and Sassi, F.: Distribution and influence of convection in the tropical tropopause region, J. Geophys. Res., 107, D104 080, doi:10.1029/2001JD001048, 2002.

Gillette, R. H. and Eyster, E. H.: The Fundamental Rotation-Vibration Band of Nitric Oxide, Phys. Rev., 56, 1113–1119, doi:10.1103/PhysRev.56.1113, 1939.

Goody, R. M. and Yung, Y. L.: Atmospheric Radiation, Theoretical Basis, 519 pp., Oxford University Press, New York, Oxford, 2nd edn., 1989.

Görlach, B., Gagelmann, F., Junge, C., Kühleis, C., Landgrebe, J., Lünenbürger, B., Oeverdieck, C., and Schreyögg, A.-P.: Carbon Leakage, Die Verlagerung von Produktion und Emissionen als Herausforderung für den Emissionshandel?, Deutsche Emissionshandelsstelle (DEHSt) im Umweltbundesamt, 2008.

Gössling, S. and Upham, P.: (eds.), Climate Change and Aviation – Issues, Challenges and Solutions, Earthscan, 2009.

Grainger, J. F. and Ring, J.: Anomalous Fraunhofer Line Profiles, Nature, 193, 762, doi:10.1038/193762a0, 1962.

Hager, J. W., Behensky, J. F., and Drew, B. W.: The Universal Grids: Universal Transverse Mercator (UTM) and Universal Polar Stereographic (UPS), Defense Mapping Agency Technical Manual 8358.2, 49 pp., United States Government Printing Office, Washington, 1989.

Haken, H. and Wolf, H. C.: Molekülphysik und Quantenchemie, 528 pp., Springer-Verlag, Berlin, Heidelberg, New York, 4th edn., 2003.

Hanna, S. R., Briggs, G. A., and Hosker, Jr., R. P.: Handbook on Atmospheric Diffusion, 110 pp., Atmospheric Turbulence and Diffusion Laboratory, National Oceanic and Atmospheric Administration, Technical Information Center, U.S. Department of Energy, 1982.

Hartmann, J., Tran, H., and Toon, G. C.: Influence of line mixing on the retrievals of atmospheric CO_2 from spectra in the 1.6 and 2.1 μm regions, Atmos. Chem. Phys., 9, 7303–7312, doi:10.5194/acp-9-7303-2009, 2009.

Hartmann, J.-M., Boulet, C., and Robert, D.: Collisional effets on molecular spectra, Laboratory Experiments and Models, Consequences for Applications, 411 pp., Elsevier Science, Amsterdam, 1st edn., 2008.

Hasse, L. and Weber, H.: On the conversion of Pasquill categories for use over sea, Boundary-Layer Meteorol., 31, 177–185, doi:10.1007/BF00121176, 1985.

Hegerl, G. C., Zwiers, F. W., Braconnot, P., Gillett, N. P., Luo, Y., Marengo Orsini, J. A., Nicholls, N., Penner, J. E., and Stott, P. A.: Understanding and Attributing Climate Change. In: *Climate Change 2007: The Physical Science Basis. Contribution of Working Group I to the Fourth Assessment Report of the Intergovernmental Panel on Climate Change* [Solomon, S., D. Qin, M. Manning, Z. Chen, M. Marquis, K.B. Averyt, M.Tignor and H.L. Miller (eds.)], Cambridge University Press, Cambridge, United Kingdom and New York, NY, USA, 2007.

Helm, D.: Sins of Emission, The Wall Street Journal, Europe, 13 March, 2008.

Henyey, L. G. and Greenstein, J. L.: Diffuse radiation in the galaxy, Astrophys. J., 93, 70–83, doi:10.1086/144246, 1941.

Herzberg, G.: Molecular Spectra and Molecular Structure, I. Infrared and Raman Spectra of Diatomic Molecules, 632 pp., D. van Nostrand Company, Inc., Princeton, New Jersey, New York, Toronto, London, 2nd edn., 1950.

Herzberg, G.: Molecular Spectra and Molecular Structure, II. Infrared and Raman Spectra of Polyatomic Molecules, 632 pp., D. van Nostrand Company, Inc., Princeton, New Jersey, New York, Toronto, London, 1956.

Hess, M., Koepke, P., and Schult, I.: Optical Properties of Aerosols and Clouds: The Software Package OPAC, Bull. Am. Meteorol. Soc., 79, 831–844, doi:10.1175/1520-0477(1998)079<0831:OPOAAC>2.0.CO;2, 1998.

Hewitt, C. N. and Jackson, A. V.: (edts.), Atmospheric Science for Environmental Scientists, John Wiley & Sons Ltd, 2009.

Hoffmann, A., Clifford, D., Aulinas, J., Carton, J. G., Deconinck, F., Esen, B., Hüsing, J., Kern, K., Kox, S., Krejci, D., Krings, T., Lohrey, S., Romano, P., Topham, R., and Weitnauer, C.: A Novel Satellite Mission Concept for Upper Air Water Vapour, Aerosol and Cloud Observations Using Integrated Path Differential Absorption LiDAR Limb Sounding, Remote Sensing, 4, 867–910, doi:10.3390/rs4040867, 2012.

Houghton, R. A., van der Werf, G. R., DeFries, R. S., Hansen, M. C., House, J. I., Le Quéré, C., Pongratz, J., and Ramankutty, N.: Chapter G2 Carbon emissions from land unse and land-cover change, Biogeosciences Discuss., 9, 835–878, doi:10.5194/bgd-9-835-2012, 2012.

Hunt, J. C. R. and Snyder, W. H.: Experiments on stably and neutrally stratified flow over a model three-dimensional hill, J. Fluid Mech., 96, 671–704, doi:10.1017/S0022112080002303, 1982.

IFM-GEOMAR: RV Alkor Fahrtbericht / Cruise Report AL374, ECO_2, Sub-seabedCO_2 Storage: Impact on Marine Ecosystems, 29.05. – 14.06.2011, Kiel – Kiel (Germany), Berichte aus dem Leibniz-Institut für Meereswissenschaften an der Christian-Albrechts-Universität zu Kiel Nr. 51, Ed.: P. Linke, 65 pp., 2011.

International Energy Agency: Key World Energy Statistics, 81 pp., http://www.iea.org/publications/, last access: October, 2012, 2011.

IPCC: Climate Change 2007: The Physical Science Basis. Contribution of Working Group I to the Fourth Assessment Report of the Intergovernmental Panel on Climate Change [Solomon, S., D. Qin, M. Manning, Z. Chen, M. Marquis, K.B. Averyt, M. Tignor and H.L. Miller (eds.)], Cambridge University Press, Cambridge, United Kingdom and New York, NY, USA, 996 pp., 2007.

IUPAC: Compendium of Analytical Nomenclature. Definitive Rules 1997. Prepared for publication by J. Inczédy, T. Lengyel, A. M. Ure, http://old.iupac.org/publications/analytical_compendium/, last access: October, 2012, 3rd edn., 1997.

Jagovkina, S. V., Karol, I. L., Zubov, V. A., Lagun, V. E., Reshetnikov, A. I., and Rozanov, E. V.: Reconstruction of the methane fluxes from the west Siberia gas fields by the 3D regional chemical transport model, Atmospheric Environment, 34, 5319–5328, doi:10.1016/S1352-2310(00)00347-2, 2000.

Jenkins, F. A. and White, H. E.: Fundamentals of Optics, 746 pp., The Mcgraw-Hill Companies, Inc., New York, 4th edn., 2001.

Jones, P. D., New, M., Parker, D. E., Martin, S., and Rigor, I. G.: Surface air temperature and its changes over the past 150 years, Rev. Geophys., 37, 173–199, doi:10.1029/1999RG900002, 1999.

Joughin, I. and Alley, R. B.: Stability of the West Antarctic ice sheet in a warming world, Nature Geosci., 4, 506–513, doi:10.1038/ngeo1194, 2011.

Judd, A., Davies, G., Wilson, J., Holmes, R., Baron, G., and Bryden, I.: Contributions to atmospheric methane by natural seepages on the UK continental shelf, Marine Geology, 137, 165–189, 1997.

Kai, F. M., Tyler, S. C., Randerson, J. T., and Blake, D. R.: Reduced methane growth rate explained by decreased Northern Hemisphere microbial sources, Nature, 476, 194–197, doi:10.1038/nature10259, 2011.

Katsman, C. A. and van Oldenborgh, G. J.: Tracing the upper ocean's "missing heat", Geophys. Res. Lett., 38, L14 610, doi:10.1029/2011GL048417, 2011.

Keeling, C. D. and Heimann, M.: Meridional Eddy Diffusion Model of the Transport of Atmospheric Carbon Dioxide 2. Mean Annual Carbon Cycle, J. Geophys. Res., 91, 7782–7796, doi:10.1029/JD091iD07p07782, 1986.

Keeling, C. D., Bacastow, R. B., Bainbridge, A. E., Ekdahl, C. A., Guenther, P. R., and Waterman, L. S.: Atmospheric carbon dioxide variations at Mauna Loa Observatory, Hawaii, Tellus, 28, 538–551, doi:10.1111/j.2153-3490.1976.tb00701.x, 1976.

Keeling, C. D., Piper, S. C., Bacastow, R. B., Wahlen, M., Whorf, T. P., Heimann, M., and Meijer, H. A.: Atmospheric CO_2 and $^{13}CO_2$ Exchange with the Terrestrial Biosphere and Oceans from 1978 to 2000: Observations and Carbon Cycle Implications. In: *A History of Atmospheric CO2 and its effects on Plants, Animals, and Ecosystems* [J.R. Ehleringer, T.E. Cerling, and M.D. Dearing (eds.)], 83–213, Springer Verlag, New York, 2005.

Keeling, C. D., Piper, S. C., Whorf, T. P., and Keeling, R. F.: Evolution of natural and anthropogenic fluxes of atmospheric CO_2 from 1957 to 2003, Tellus B, 63, 1–22, doi:10.1111/j.1600-0889.2010.00507.x, 2011.

Kiemle, C., Quatrevalet, M., Ehret, G., Amediek, A., Fix, A., and Wirth, M.: Sensitivity studies for a space-based methane lidar mission, Atmos. Meas. Tech., 4, 2195–2211, doi:10.5194/amt-4-2195-2011, 2011.

King, L. V.: On the Complex Anisotropic Molecule in Relation to the Dispersion and Scattering of Light, 104, 333–357, 1923.

Kleipool, Q. L., Jongma, R. T., Gloudemans, A. M. S., Schrijver, H., Lichtenberg, G. F., van Hees, R. M., Maurellis, A. N., and Hoogeveen, R. W. M.: In-flight proton-induced radiation damage to SCIAMACHY's extended-wavelength InGaAs near-infrared detectors, Inf. Phys. Tech., 50, 30–37, doi:10.1016/j.infrared.2006.08.001, 2007.

Kneizys, F. X., Shettle, E. P., Abreu, L. W., Chetwynd, J. H., Anderson, G. P., Gallery, W. O., Selby, J. E. A., and Clough, S. A.: Users Guide to LOWTRAN 7, Environmental Research Papers, No. 1010, Technical Report, AFGL-TR-88-0177, Air Force Geophysics Laboratory, Hanscom AFB, MA 01731, 1988.

Kokhanovsky, A. A.: Cloud Optics, 276 pp., Atmospheric and Oceanographic Sciences Library, Vol. 34, Springer, Dordrecht, 2nd edn., 2006.

Krings, T.: The influence of robust statistics, remote reference, and horizontal magnetic transfer functions on data processing in magnetotellurics, Universität Münster, Diploma Thesis, University of Münster, 107 pp., 2007.

Krings, T., Gerilowski, K., Buchwitz, M., Reuter, M., Tretner, A., Erzinger, J., Heinze, D., Pflüger, U., Burrows, J. P., and Bovensmann, H.: MAMAP – A new spectrometer system for column-averaged methane and carbon dioxide observations from aircraft: retrieval algorithm and first inversions for point source emission rates, Atmos. Meas. Tech., 4, 1735–1758, doi:10.5194/amt-4-1735-2011, 2011.

Krings, T., Gerilowski, K., Buchwitz, M., Hartmann, J., Sachs, T., Erzinger, J., Burrows, J. P., and Bovensmann, H.: Quantification of methane emission rates from coal mine ventilation shafts using airborne remote sensing data, Atmos. Meas. Tech. Discuss., 5, 7383–7429, doi:10.5194/amtd-5-7383-2012, 2012.

Krueger, L.: Konforme Abbildung des Erdellipsoids in der Ebene, Königlich Preuszisches geodätisches Institut, 182 pp., Potsdam, Neue Folge Nr. 52, Teubner, Leipzig, doi:10.2312/GFZ.b103-krueger28, 1912.

Lambert, J. H.: Anmerkungen und Zusätze zur Entwerfung der Land- und Himmelscharten. In: Beiträge zum Gebrauche der Mathematik und deren Anwendung III, 336 pp., 1772.

Leifer, I., Luyendyk, B. P., Boles, J., and Clark, J. F.: Natural marine seepage blowout: Contribution to atmospheric methane, Global Biogechemical cycles, 20, doi:10.1029/2005GB002668, 2006a.

Leifer, I., Roberts, D., Margolis, J., and Kinnaman, F.: In situ sensing of methane emissions from natural marine hydrocarbon seeps: A potential remote sensing technology, Earth Planet. Sci. Lett., 245, 509–522, doi:10.1016/j.epsl.2006.01.047, 2006b.

Lemke, P., Ren, J., Alley, R. B., Allison, I., Carrasco, J., Flato, G., Fujii, Y., Kaser, G., Mote, P., Thomas, R. H., and Zhang, T.: Observations: Changes in Snow, Ice and Frozen Ground. In: *Climate Change 2007: The Physical Science Basis. Contribution of Working Group I to the Fourth Assessment Report of the Intergovernmental Panel on Climate Change* [Solomon, S., D. Qin, M. Manning, Z. Chen, M. Marquis, K.B. Averyt, M.Tignor and H.L. Miller (eds.)], Cambridge University Press, Cambridge, United Kingdom and New York, NY, USA, 2007.

Liou, K. N.: An introduction to Atmospheric Radiation, 583 pp., International Geophysics Series, Volume 84, Academic Press, San Diego, London, 2nd edn., 2002.

Liu, C. and Zipser, E. J.: Global distribution of convection penetrating the tropical tropopause, J. Geophys. Res., 110, D23 104, doi:10.1029/2005JD006063, 2005.

Livingston, W. and Wallace, L.: An atlas of the solar spectrum in the infrared from 1850 to 9000 cm^{-1} (1.1 to 5.4 μm), National Solar Observatory, Tech. rep. 91-001, 1991.

Lloyd, J., Francey, R. J., Mollicone, D., Raupach, M. R., Sogachev, A., Arneth, A., Byers, J. N., Kelliher, F. M., Rebmann, C., Valentini, R., Wong, S.-C., Bauer, G., and Schulze, E.-D.: Vertical profiles, boundary layer budgets, and regional flux estimates for CO_2 and its $^{13}C/^{12}C$ ratio and for water vapor above a forest/bog mosaic in central Siberia, Global Biogeochem. Cycles, 15, 267–284, doi:10.1029/1999GB001211, 2001.

Martin, D. O.: The Change of Concentration Standard Deviations with Distance, J. Air Poll. Control Assoc., 26, 145–147, doi:10.1080/00022470.1976.10470238, 1976.

Martin, P. E. and Barker, E. F.: The Infrared Absorption Spectrum of Carbon Dioxide, Phys. Rev., 41, 291–303, doi:10.1103/PhysRev.41.291, 1932.

Masters, G. M.: Introduction to Environmental Engineering and Science, Prentice-Hall, Inc., 2nd edn., 1998.

McCluskey, C. W. and Stoker, D. S.: Raman observations of quantum interference in the $\nu_1/2\nu_2$ Fermi dyad region of carbon dioxide, arXiv:physics/0601182v1 [physics.chem-ph], pp. 1–10, 2006.

Meyer, O., Busack, V., Haepe, S., Theopold, F., and Heimes, F. J.: HELPCOS The Helicopter Based Pipeline Control System of VGN–Verbundnetz AG, 23rd World Gas Conference, Amsterdam, 2006.

Mie, G.: Beiträge zur Optik trüber Medien, speziell kolloidaler Metallösungen, Ann. Phys., 330, 377–455, doi:10.1002/andp.19083300302, 1908.

Moosmüller, H.: Optical absorption in nitrogen due to spontaneous Raman scattering, J. Opt. Soc. Am. B, 11, 286–289, doi:10.1364/JOSAB.11.000286, 1994.

Morino, I., Uchino, O., Inoue, M., Yoshida, Y., Yokota, T., Wennberg, P. O., Toon, G. C., Wunch, D., Roehl, C. M., Notholt, J., Warneke, T., Messerschmidt, J., Griffith, D. W. T., Deutscher, N. M., Sherlock, V., Connor, B., Robinson, J., Sussmann, R., , and Rettinger, M.: Preliminary validation of column-averaged volume mixing ratios of carbon dioxide and methane retrieved from GOSAT short-wavelength infrared spectra, Atmos. Meas. Tech., 4, 1061–1076, doi:10.5194/amt-4-1061-2011, 2011.

Mörner, N.-A. and Etiope, G.: Carbon degassing from the lithosphere, Global Planet. Change, 33, 185–203, doi:10.1016/S0921-8181(02)00070-X, 2002.

Nassar, R., Jones, D. B. A., Suntharalingam, P., Chen, J. M., Andres, R. J., Wecht, K. J., Yantosca, R. M., Kulawik, S. S., Bowman, K. W., Worden, J. R., Machida, T., and Matsueda, H.: Modeling global atmospheric CO_2 with improved emission inventories and CO_2 production from the oxidation of other carbon species, Geosci. Model Dev., 3, 689–716, doi:10.5194/gmd-3-689-2010, 2010.

Nisbet, E. and Weiss, R.: Top-Down Versus Bottom-Up, Science, 328, 1241–1243, doi:10.1126/science.1189936, 2010.

NRC: National Research Council (NRC) – Committee on Methods for Estimating Greenhouse Gas Emissions, Verifying Greenhouse Gas Emissions: Methods to Support International Climate Agreements, ISBN 0-309-15212-7, available from http://www.nap.edu/catalog/12883.html, last access: October, 2012, 2010.

Olivier, J. G. J., Van Aardenne, J. A., Dentener, F. J., Pagliari, V., Ganzeveld, L. N., and Peters, J. A. H. W.: Recent trends in global greenhouse gas emissions: regional trends 1970–2000 and spatial distribution of key sources in 2000, Environmental Sciences, 2, 81–99, doi:10.1080/15693430500400345, 2005.

Olivier, J. G. J., Janssens-Maenhout, G., Peters, J. A. H. W., and Wilson, J.: Long-term trend in global CO_2 emissions. 2011 report, The Hague: PBL/JRC, 2011.

Oppenheimer, M.: Global warming and the stability of the West Antarctic Ice Sheet, Nature, 393, 325–332, 1998.

Pasquill, F.: Atmospheric dispersion of pollution, Quat. J. R. Met. Soc., 97, 369–395, doi:10.1002/qj.49709741402, 1971.

Péré, J.-C., Pont, V., Mallet, M., and Bessagnet, B.: Mapping of PM10 surface concentrations derived from satellite observations of aerosol optical thickness over South-Eastern France, Atmos. Res., 91, 1–8, doi:10.1016/j.atmosres.2008.05.001, 2009.

Pine, A. S.: Line Mixing Sum Rules for the Analysis of Multiplet Spectra, J. Quant. Spectrosc. Radiat. Transfer, 57, 154–155, doi:10.1016/S0022-4073(96)00129-X, 1997.

Prasad, A. K., Singh, R. P., and Kafatos, M.: Influence of coal based thermal power plants on aerosol optical properties in the Indo-Gangetic basin, Geophys. Res. Lett., 33, L05 895, doi:doi:10.1029/2005GL023801, 2006.

Randel, W. J., Shine, K. P., Austin, J., Barnett, J., Claud, C., Gillett, N. P., Keckhut, P., Langematz, U., Lin, R., Long, C., Mears, C., Miller, A., Nash, J., Seidel, D. J., Thompson, D. W. J., Wu, F., and Yoden, S.: An update of observed stratospheric temperature trends, J. Geophys. Res., 114, D02 107, doi:doi:10.1029/2008JD010421, 2009.

Raut, J.-C. and Chazette, P.: Assessment of vertically-resolved PM_{10} from mobile lidar observations, Atmos. Chem. Phys., 9, 8617–8638, doi:10.5194/acp-9-8617-2009, 2009.

Rayleigh, Lord.: (Strutt, J.W.), On the Light from the Sky, its Polarization and Colour, Phil. Mag., 41, 107–120, 274–279, 1871.

Régalia-Jarlot, L., Zéninari, V., Parvitte, B., Grossel, A., Thomas, X., von der Heyden, P., and Durry, G.: A complete study of the line intensities of four bands of CO_2 around 1.6 and 2.0 μm: A comparison between Fourier transform and diode laser measurements, J. Quant. Spectrosc. Radiat. Transfer, 101, 325–338, doi:10.1016/j.jqsrt.2005.11.021, 2006.

Rehder, G., Keir, R. S., Suess, E., and Pohlmann, T.: The Multiple Sources and Patterns of Methane in North Sea Waters, Aquatic Geochemistry, 4, 403–427, 1998.

Reuter, M., Buchwitz, M., Schneising, O., Heymann, J., Bovensmann, H., and Burrows, J. P.: A method for improved SCIAMACHY CO_2 retrieval in the presence of optically thin clouds, Atmos. Meas. Tech, 3, 209–232, doi:10.5194/amt-3-209-2010, 2010.

Reuter, M., Bovensmann, H., Buchwitz, M., Burrows, J. P., Connor, B. J., Deutscher, N. M., Griffith, D. W. T., Heymann, J., Keppel-Aleks, G., Messerschmidt, J., Notholt, J., Petri, C., Robinson, J., Schneising, O., Sherlock, V., Velazco, V., Warneke, T., Wennberg, P. O., and Wunch, D.: Retrieval of atmospheric CO_2 with enhanced accuracy and precision from SCIAMACHY: Validation with FTS measurements and comparison with model results, J. Geophys. Res., 116, Do4301, doi:10.1029/2010JD015047, 2011.

Richter, A. and Wagner, T.: The Use of UV, Visible and Near IR Solar Back Scattered Radiation to Determine Trace Gases. In: *The Remote Sensing of Tropospheric Composition from Space* [J.P. Burrows, U. Platt and P. Borrell (eds.)], 219–283, Springer-Verlag Berlin Heidelberg, doi:10.1007/978-3-642-14791-3_2, 2011.

Rigby, M., Prinn, R. G., Fraser, P. J., Simmonds, P. G., Langenfelds, R. L., Huang, J., Cunnold, D. M., Steele, L. P., Krummel, P. B., Weiss, R. F., O'Doherty, S., Salameh, P. K., Wang, H. J., Harth, C. M., Mühle, J., and Porter, L. W.: Renewed growth of atmospheric methane, Geophys. Res. Lett., 35, L22 805, doi:10.1029/2008GL036037, 2008.

Rignot, E., Bamber, J. L., van den Broeke, M. R., Davis, C., Li, Y., van de Berg, W. J., and van Meijgaard, E.: Recent Antarctic ice mass loss from radar interferometry and regional climate modelling, Nature Geosci., 1, 106–110, doi:10.1038/ngeo102, 2008.

Ringeval, B., de Noblet-Ducoudré, N., Ciais, P., Bousquet, P., Prigent, C., Papa, F., and Rossow, W. B.: An attempt to qunatify the impact of changes in wetland extent on methane emissions on the seasonal and interannual time scales, Global Biogeochem. Cycles, 24, GB2003, doi:10.1029/2008GB003354, 2010.

Ritter, K. J. and Wilkerson, T. D.: High-Resolution Spectroscopy of the Oxygen A Band, J. Mol. Spectrosc., 121, 1–19, doi:10.1016/0022-2852(87)90167-6, 1987.

Rodgers, C. D.: Inverse Methods for Atmospheric Sounding: Theory and Practice, Series on Atmospheric, Oceanic and Planetary Physics – Vol. 2, World Scientific Publishing, 2000.

Roedel, W. and Wagner, T.: Physik unserer Umwelt: Die Atmosphäre, Springer-Verlag Berlin Heidelberg, 4th edn., doi:10.1007/978-3-642-15729-5, 2011.

Römer, W.: Boxberg III - erfolgreiche Nachrüstung eines ostdeutschen Braunkohlekraftwerkes, Nicrofer 5923 hMo - alloy 59, VDM Case History, 2, 1996.

Rothman, L. S., Jaquemart, D., , Barbe, A., Benner, D. C., Birk, M., Brown, L. R., Carleer, M. R., Jr, C. C., Chance, K., Coudert, L. H., Dana, V., Devi, V. M., Flaud, J., Gamache, R. R., Goldman, A., Hartmann, J., Jucks, K. W., Makim, A. G., Mandin, J., Massie, S. T., Orphalh, J., Perrin, A., Rinsland, C. P., Smith, M. A. H., Tennyson, J., Tolchenov, R. N., Toth, R. A., Auwera, J. V., Varanasi, P., and Wagner, G.: The *HITRAN* 2004 molecular spectroscopic database, Journal of Quantitative Spectroscopy & Radiative Transfer, 96, 139–204, doi:10.1016/j.jqsrt.2004.10.008, 2005.

Rothman, L. S., Gordon, I. E., , Barbe, A., Benner, D., Bernath, P. F., Birk, M., Boudon, V., Brown, L. R., Campargue, A., Champion, J., Chance, K., Coudert, L. H., Dana, V., Devi, V. M., Fally, S., Flaud, J., Gamache, R. R., Goldman, A., Jacquemart, D., Kleiner, I., Lacome, N., Lafferty, W. J., Mandin, J., Massie, S. T., Mikhailenko, S. N., Miller, C. E., Moazzen-Ahmadi, N., Naumenko, O. V., Nikitin, A. V., Orphal, J., Perevalov, V. I., Perrin, A., Predoi-Cross, A., Rinsland, C. P., Rotger, M., Šimečková, M., Smith, M. A. H., Sung, K., Tashkun, S. A., Tennyson, J., Toth, R. A., Vandaele, A. C., and Auwera, J. V.: The *HITRAN* 2008 molecular spectroscopic database, Journal of Quantitative Spectroscopy & Radiative Transfer, 110, 533–572, doi:10.1016/j.jqsrt.2009.02.013, 2009.

Rozanov, A., Rozanov, V., Buchwitz, M., Kokhanovsky, A., and Burrows, J. P.: SCIATRAN 2.0 – A new radiative transfer model for geophysical applications in the 175–2400 nm spectral region, Adv. Space. Res., 36, 1015–1019, doi:DOI: 10.1016/j.asr.2005.03.012, 2005.

Rozanov, V. V.: User's Guide for the Software Package SCIATRAN (Radiative Transfer Model and Retrieval Algorithm), Version 3.2, 156 pp., Institute of Remote Sensing University of Bremen, Germany, 2012.

Sakaizawa, D., Kawakami, S., Nakajima, M., Tanaka, T., Morino, I., and Uchino, O.: An airborne amplitude-modulated 1.57 μm differential laser absorption spectrometry: simultaneous measurement of partial column-avearged dry air mixing ratio of CO_2 and target range, Atmos. Meas. Tech. Discuss., 5, 4851–4880, doi:10.5194/amtd-5-4851-2012, 2012.

Santer, B. D., Wigley, T. M. L., and Taylor, K. E.: The Reproducibility of Observational Estimates of Surface and Atmospheric Temperature Change, Science, 334, 1232–1233, doi:10.1126/science.1216273, 2011.

Sathyanarayana, D. N.: Vibrational Spectroscopy – Theory and Applications, 2004, Reprint, New Age International Publishers, New Delhi, 2005.

Schneising, O.: Analysis and interpretation of satellite measurements in the near-infrared spectral region: Atmospheric carbon dioxide and methane, PhD thesis, University of Bremen, Institute of Environmental Physics (IUP), Germany, 2009.

Schneising, O., Buchwitz, M., Burrows, J. P., Bovensmann, H., Reuter, M., Notholt, J., Macatangay, R., and Warneke, T.: Three years of greenhouse gas column-averaged dry air mole fractions retreived from satellite – Part 1: Carbon dioxide, Atmos. Chem. Phys., 8, 3827–3853, doi:10.5194/acp-8-3827-2008, 2008.

Schneising, O., Buchwitz, M., Burrows, J. P., Bovensmann, H., Bergamaschi, P., and Peters, W.: Three years of greenhouse gas column-averaged dry air mole fractions retreived from satellite – Part 2: Methane, Atmos. Chem. Phys., 9, 443–465, doi:10.5194/acp-9-443-2009, 2009.

Schneising, O., Buchwitz, M., Reuter, M., Heymann, J., Bovensmann, H., and Burrows, J. P.: Long-term analysis of carbon dioxide and methane column-averaged mole fractions retrieved from SCIAMACHY, Atmos. Chem. Phys. Discuss., 10, 27 479–27 522, doi:10.5194/acpd-10-27479-2010, 2010.

Schneising, O., Buchwitz, M., Reuter, M., Heymann, J., Bovensmann, H., and Burrows, J. P.: Long-term analysis of carbon dioxide and methane column-averaged mole fractions retrieved from SCIAMACHY, Atmos. Chem. Phys., 11, 2863–2880, doi:10.5194/acp-11-2863-2011, 2011.

Schnisa, H.: Investigations on the Smile-Effect for Airborne Spectroscopy of Methane and Carbon Dioxide, Bachelor Thesis, 51 pp., Institute of Environmental Physics (IUP), University of Bremen, Germany, 2009.

Schrader, B. and Moore, D. S.: Laser-based Molecular Spectroscopy for Chemical Analysis: Raman Scattering Processes, Pure Appl. Chem., 69, 1451–1468, doi:10.1351/pac199769071451, 1997.

Schulz, J. and Schättler, U.: Kurze Beschreibung des Lokal-Modells Europa COSMO-EU (LME) und seiner Datenbanken auf dem Datenserver des DWD, Technical Report, Deutscher Wetterdienst, Geschäftsbereich Forschung und Entwicklung, 71 pp., 2009.

Schuster, G. L., Dubovik, O., and Holben, B. N.: Angstrom exponent and bimodal aerosol size distributions, J. Geophys. Res., 111, D07 207, doi:10.1029/2005JD006328, 2006.

Seinfeld, J. H. and Pandis, S. N.: Atmospheric Chemistry and Physics – From Air Pollution to Climate Change, John Wiley, New York, 1998.

Shakhova, N., Semiletov, I., Salyuk, A., Yusupov, V., Kosmach, D., and Gustafsson, Ö.: Extensive Methane Venting to the Atmosphere from Sediments of the East Siberian Arctic Shelf, Science, 327, 1246–1250, doi:10.1126/science.1182221, 2010.

Shindell, D. T., Faluvegi, G., Koch, D. M., Schmidt, G. A., Unger, N., and Bauer, S. E.: Improved Attribution of Climate Forcing to Emissions, Science, 326, 716–718, doi:10.1126/science.1174760, 2009.

Shine, K. P., Bourqui, M. S., de F. Forster, P. M., Hare, S. H. E., Langematz, U., Braesicke, P., Grewe, V., Ponater, M., Schnadt, C., Smith, C. A., Haigh, J. D., Austin, J., Butchart, N., Shindell, D. T., Randel, W. J., Nagashima, T., Portmann, R. W., Solomon, S., Seidel, D. J., Lanzante, J., Klein, S., Ramaswamy, V., and Schwarzkopf, M. D.: A comparison of model-simulated trends in stratospheric temperatures, Q. J. R. Meteorol. Soc., 129, 1565–1588, doi:10.1256/qj.02.186, 2003.

Shu, F. H.: The Physical Universe, An Introduction to Astronomy, 584 pp., A Series of books in astronomy, University Science Books, Sausalito, 1982.

Sneep, M. and Ubachs, W.: Direct measurement of the Rayleigh scattering cross section in various gases, J. Quant. Spectrosc. Radiat. Transfer, 92, 293–310, doi:10.1016/j.jqsrt.2004.07.025, 2005.

Snyder, J. P.: Map Projections – A working Manual, 394 pp., U.S. Geological Survey Professional Paper 1395, United States Government Printing Office, Washington, 1987.

Solanki, S. K. and Krivova, N. A.: Can solar variability explain global warming since 1970?, J. Geophys. Res., 108(A5), 1200, doi:10.1029/2002JA009753, 2003.

Solomon, S., Rosenlof, K. H., Portmann, R. W., Daniel, J. S., Davis, S. M., Sanford, T. J., and Plattner, G.-K.: Contributions of Stratospheric Water Vapor to Decadal Changes in the Rate of Global Warming, Science, 327, doi:10.1126/science.1182488, 2010.

Stephen, D. W. and Moroz, W. J.: Wet plume rise from cooling towers in strong winds, Water Air Soil Pollut., 6, 9–24, doi:10.1007/BF00158711, 1976.

Stephens, B. B., Gurney, K. R., Tans, P. P., Sweeney, C., Peters, W., Bruhwiler, L., Ciais, P., Ramonet, M., Bousquet, P., Nakazawa, T., Aoki, S., Machida, T., Inoue, G., Vinnichenko, N., Lloyd, J., Jordan, A., Heimann, M., Shibistova, O., Langenfelds, R. L., Steele, L. P., Francey, R. J., and Denning, A. S.: Weak Northern and Strong Tropical Land Carbon Uptake from Vertical Profiles of Atmospheric CO_2, Science, 316, 1732–1735, doi:10.1126/science.1137004, 2007.

Strow, L. L., Hannon, S. E., De-Souza Machado, S., Motteler, H. E., and Tobin, D. C.: Validation of the Atmospheric Infrared Sounder radiative transfer algorithm, J. Geophys. Res., 111, D09S06, doi:10.1029/2005JD006146, 2006.

Stull, R. B.: An introduction to boundary layer meteorology, 670 pp., Kluwer Academic Publishers, Dordrecht, The Netherlands, 1988.

Suto, H., Kuze, A., Nakajima, M., Hamazaki, T., Yokota, T., and Inoue, G.: Airborne SWIR FTS for GOSAT validation and calibration (Proceedings Paper), SPIE Proceedings, 7106, doi:10.1117/12.799963, 2008.

Sutton, O. G.: A Theory of Eddy Diffusion in the Atmosphere, Proceedings of the Royal Society of London. Series A, Containing Papers of a Mathematical and Physical Character, 135, 143–165, 1932.

Taylor, J. A. and Orr, J. C.: The natural latitudinal distribution of atmospheric CO_2, Glob. Planet. Change, 26, 375–386, doi:10.1016/S0921-8181(00)00050-3, 2000.

Terao, Y., Mukai, H., Nojiri, Y., Machida, T., Tohjima, Y., Saeki, T., and Maksyutov, S.: Interannual variability and trends in atmospheric methane over the western Pacific from 1994 to 2010, J. Geophys. Res., 116, D14 303, doi:10.1029/2010JD015467, 2011.

The Parliament of the Commonwealth of Australia: Senate 2010–2011, Clean Energy Bill 2011, Revised Explanatory Memorandum, 299 pp., 2011.

Thomas, P. D.: Conformal Projections in Geodesy and Cartography, 152 pp., Special Publication No. 251, U.S. Department of Commerce, Coast and Geodetic Survey, United States Government Printing Office, Washington, 1952.

Thoning, K. W., Tans, P. P., and Komhyr, W. D.: Atmospheric carbon dioxide at Mauna Loa Observatory 2. Analysis of the NOAA GMCC data 1974–1985, J. Geophys. Res., 94, 8549–9565, doi:10.1029/JD094iD06p08549, 1989.

Toth, R. A., Brown, L. R., Miller, C. E., Malathy Devy, V., and Benner, D.: Spectroscopic database of CO_2 line parameters: 4300–7000 cm^{-1}, J. Quant. Spectrosc. Radiat. Transfer, 109, 906–921, doi:10.1016/j.jqsrt.2007.12.004, 2008.

Tran, H., Boulet, C., and Hartmann, J.: Line mixing and collision-induced absorption by oxygen in the A band: Laboratory measurements, model, and tools for atmospheric spectra computations, J. Geophys. Res., 111, D15 210, doi:10.1029/2005JD006869, 2006.

Tran, H., Hartmann, J., Toon, G., Brown, L. R., Frankenberg, C., Warneke, T., Spietz, P., and Hase, F.: The $2\nu_3$ band of CH_4 revisited with line mixing: Consequences fro spectroscopy and atmospheric retrievals at 1.67 μm, J. Quant. Spectrosc. Radiat. Transfer, 111, 1344–1356, doi:10.1016/j.jqsrt.2010.02.015, 2010.

Trenberth, K. E., Jones, P. D., Ambenje, P., Bojariu, R., Easterling, D., Klein Tank, A., Parker, D., Rahimzadeh, F., Renwick, J. A., Rusticucci, M., Soden, B., and Zhai, P.: Observations: Surface and Atmospheric Climate Change. In: *Climate Change 2007: The Physical Science Basis. Contribution of Working Group I to the Fourth Assessment Report of the Intergovernmental Panel on Climate Change* [Solomon, S., D. Qin, M. Manning, Z. Chen, M. Marquis, K.B. Averyt, M.Tignor and H.L. Miller (eds.)], Cambridge University Press, Cambridge, United Kingdom and New York, NY, USA, 2007.

Trenberth, K. E., Fasullo, J. T., and Kiehl, J.: Earth's Global Energy Budget, Bull. Amer. Meteor. Soc, 90, 311–323, doi:10.1175/2008BAMS2634.1, 2009.

Trier, A., Cabrini, N., and Ferrer, J.: Correlations between urban atmospheric light extinction coefficients and fine particle mass concentrations, Atmósfera, 10, 151–160, 1997.

Turner, D. B.: Workbook of Atmospheric Dispersion Estimates, U.S. Department of Health, Education, and Welfare, 95 pp., 1970.

Tzella, A. and Legras, B.: A Lagrangian view of convective sources for transport of air across the Tropical Tropopause Layer: distribution, times and the radiative influence of clouds, Atmos. Chem. Phys., 11, 12 517–12 534, doi:10.5194/acp-11-12517-2011, 2011.

United Nations: Kyoto Protocoll to the United Nations Framework Convention on Climate Change, 21 pp., 1998.

U.S. Committee on Extension to the Standard Atmosphere: U.S. Standard Atmosphere, 1976, National Oceanic and Atmospheric Administration, National Aeronautics and Space Administration, United States Air Force, Washington D.C., 241 pp., 1976.

Vallance Jones, A. and Harrison, A. W.: $^1\Delta_g$–$^3\Sigma_g^-$ O_2 Infrared emission band in the twilight airglow spectrum, J. Atmos. Terr. Phys., 13, 45–60, doi:10.1016/0021-9169(58)90024-2, 1958.

Varandas, A. J. C. and Xu, Z. R.: Permutational Symmetry and Role of Nuclear Spin in Vibrational Spectra. The Alkali Metal Trimers. In: *Introduction to Advanced Topics of Computational Chemistry* [L.A. Montero, L.A. Díaz and R. Bader (eds.)], 219–283, Editorial de la Universidad de La Habana, Havana, 2003.

Velazco, V. A., Buchwitz, M., Bovensmann, H., Reuter, M., Schneising, O., Heymann, J., Krings, T., Gerilowski, K., and Burrows, J. P.: Towards space based verification of CO_2 emissions from strong localized sources: fossil fuel power plant emissions as seen by a CarbonSat constellation, Atmos. Meas. Tech., 4, 2809–2822, doi:10.5194/amt-4-2809-2011, 2011.

Vieitez, M. O., van Duijn, E. J., Ubachs, W., Witschas, B., Meijer, A., de Wijn, A. S., Dam, N. J., and van de Water, W.: Coherent and spontaneous Rayleigh-Brillouin scattering in atomic and molecular gases and gas mixtures, Phys. Rev. A, 82, 043 836, doi:10.1103/PhysRevA.82.043836, 2010.

Villasenor, R., Magdaleno, M., Quintanar, A., Gallardo, J. C., López, M. T., Jurado, R., Miranda, A., Aguilar, M., Melgarejo, L. A., Palmerín, E., Vallejo, C. J., and Barchet, W. R.: An air quality emission inventory of offshore operations for the exploration and production of petroleum by the Mexican oil industry, Atmospheric Environment, 37, 3713–3729, 2003.

Wallace, J. M. and Hobbs, P. V.: Atmospheric Science - An introductory survey, 467 pp., Academic Press, 525 B Street, Suite 1900, San Diego, California 92101–4495, USA, 1977.

Weil, J. C. and Jepsen, A. F.: Evaluation of the Gaussian Plume Model at the Dickerson Power Plant, Atmos. Environ., 11, 901–910, doi:10.1016/0004-6981(77)90019-1, 1977.

Worden, J., Kulawik, S., Frankenberg, C., Payne, V., Bowman, K., Cady-Peirara, K., Wecht, K., Lee, J., and Noone, D.: Profiles of CH_4, HDO, H_2O, and N_2O with improved lower tropospheric vertical resolution from Aura TES radiances, Atmos. Meas. Tech., 5, 397–411, doi:10.5194/amt-5-397-2012, 2012.

Wu, J., Huang, X., Carter, S., and Bowman, J. M.: Tests of MULTIMODE calculations of rovibrational energies of CH_4, Chem. Phys. Lett., pp. 285–289, doi:10.1016/j.cplett.2006.06.024, 2006.

Wuebbles, D. J. and Hayhoe, K.: Atmospheric methane and global change, Earth-Science Reviews, 57, 177–210, doi:10.1016/S0012-8252(01)00062-9, 2002.

Xiong, X., Barnet, C., Maddy, E., Wei, J., Liu, X., and Pagano, T. S.: Seven Years' Observation of Mid-Upper Tropospheric Methane from Atmospheric Infrared Sounder, Remote Sens, 2, 2509–2530, doi:10.3390/rs2112509, 2010.

Yang, E.-S., Cunnold, D. M., Salawitch, R. J., McCormic, M. P., Russel III, J., Zawodny, J. M., Oltmans, S., and Newchurch, M. J.: Attribution in recovery in lower-stratospheric ozone, J. Geophys. Res., 111, D17 309, doi:10.1029/2005JD006371, 2006.

Young, A. T.: Rayleigh Scattering, Appl. Opt., 20, 533–535, doi:10.1364/AO.20.000533, 1980.

Zimig, W. and Ulbricht, M.: CHARM®–The dawn of a new era in checking the tightness of natural gas pipelines, 23rd World Gas Conference, Amsterdam, 2006.

Acknowledgements

I would like to express my gratitude to Michael Buchwitz who advised me during all stages of the research presented here. His comments and scientific insight made this work possible in the first place. I am thankful for the support of Prof. Dr. John P. Burrows who entrusted me with this fascinating topic and who gave advice and motivation on countless occasions. I would like to thank particularly Konstantin Gerilowski for his continuous, critical comments that have significantly improved this work. I am very thankful to Heinrich Bovensmann who always looked at this work from a broader scientific perspective and gave corresponding advice. I would like to thank Prof. J. Notholt for dedicating his time to be second reviewer of this thesis.

MAMAP research activities were conducted in parts in cooperation with Andreas Tretner, Torsten Sachs and Prof. J. Erzinger from the Helmholtz Centre Potsdam – GFZ German Research Centre for Geosciences. For the many successful measurement campaigns, I am thankful to Konstantin Gerilowski, Heinrich Bovensmann, Sven Krautwurst, Carsten Lindemann (FU Berlin), Thomas Ruhtz (FU Berlin), Torsten Sachs (GFZ Potsdam), Jörg Hartmann (AWI Bremerhaven), Anja Schönhardt as well as the team of the Polar 5 research aircraft.

This work has been financed by the University and the State of Bremen. For financial support for summer schools and conference participation, I am additionally thankful to the Postgraduate International Physics Programme (PIP), the European Geosciences Union (EGU), the German Aerospace Center (DLR), the European Space Agency (ESA) and the Austrian Research Promotion Agency (FFG).

I would like to thank all current and former colleagues from the IUP greenhouse gas group, in particular Michael Buchwitz, Maximilian Reuter, Oliver Schneising and Jens Heymann for valuable discussions and support. I am also thankful to the many other colleagues at IUP that shared scientific and non-scientific insight. For great moments at and outside work, I would like to thank especially Maximilian Reuter, Oliver Schneising, Jens Heymann, Ralf Bauer, Florian Ernst, Sebastian Dikty, Sebastian Mieruch, Katja Weigel, Joana Leitão Alexandre, Kai-Uwe Eichmann, Stefan Bötel, Antje Buß and Lena Brinkhoff.

I am thankful to Vladimir Rozanov for support regarding the SCIATRAN radiative transfer model. Furthermore, I am grateful for the insights gained from cooperations with Ulrich Pflüger and Ronny Leinweber from the German Weather Service (DWD) who provided data from wind profilers and from the COSMO-DE model. Cooperations with Dietmar Heinze from Vattenfall Europe Generation AG, Cottbus, Germany and with the district government of Arnsberg (*Bezirksregierung Arnsberg, Abteilung Bergbau und Energie in NRW*) allowed for the detailed comparison with official data as reported within the context of emission inventories. Part of the ground based in-situ data was provided by Weather Underground (http://www.wunderground.com). The MAMAP measurement sketch has been approved to be used in this work by the LEGO group. For taking care of

the many administrative challenges, I am thankful to Petra Horn, Geraldine Schmiechen, Lars Jeschke, Anja Gatzka and Birgit Teuchert. Furthermore, I would like to thank Heiko Schellhorn and Heiko Schröter for IT support.

I would like to especially thank Lena for her continuous support, for being there for me and also for proofreading large parts of this work.

Zu guter Letzt danke ich vor allem meinen Eltern und meiner Schwester, dafür dass sie mir immer unterstützend zur Seite stehen.

Corrections

Page 20, Figure 2.1: figure replaced by the official IPCC errata version of the same plot

Page 28, Table 2.5: corrected values for “Emissions” for “Geological sources” (“5” → “14”) and values for “Range of estimate” for “Geological sources” (“0.4–12.2” → “12–36”) and “Marine Sediments” (“0.2–12.2” → “0.4–12.2”)

Page 28, Equation (2.21): corrected “$CH_4 + O_2 \longrightarrow HCHO + 2\,H_2O$” by “$CH_4 + OH + HO_2 \longrightarrow HCHO + 2\,H_2O$”

Page 34, line 5 and 6: “1.2 µm” → “1.4 µm”, “1.3 µm” → “1.4 µm”

Page 54, footnote: “1.29 µm” → “1.27 µm”

Page 61, Equation (5.3): inserted missing index *j*

Page 63, caption of Figure 5.1: “0.64%” → “0.62%”

Page 64, caption of Figure 5.2: “2.2%” → “1.4%”